University of Strathclyde Glasgow

Computational Haemodynamics in Vascular Networks: Multi-phase Cell-Free Layer Modelling in the Microvasculature, Testicular Microcirculation, and Blood Flow in the Pulmonary Bifurcation

Tanchanok Wisitponchai

Department of Biomedical Engineering

University of Strathclyde

This thesis is submitted for the degree of

Doctor of Philosophy

2025

Declarations

This thesis is the result of the author's original research. It has been composed by the author and has not been previously submitted for examination, which has led to the award of a degree. The copyright of this thesis belongs to the author under the terms of the United Kingdom Copyright Acts as qualified by the University of Strathclyde Regulation 3.50. Due acknowledgement must always be made of the use of any material contained in, or derived from, this thesis.

Signed,

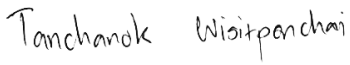

Tanchanok Wisitponchai

Acknowledgement

I would like to express my deepest gratitude to my supervisors, Dr Asimina Kazakidi and Dr Junxi Wu. Dr Asimina provided me with a solid foundation in computational fluid dynamics and engineering methodology, ensuring that the models developed in this thesis were robust and could be applied with confidence. Dr Junxi offered invaluable guidance on the biological applications of these models, broadening my perspective and inspiring the design of the multi-phase framework with consideration of practical use. In addition to their academic mentorship, they encouraged me to become a better presenter at academic events and generously shared advice that has been helpful in my daily life in the UK.

I am also indebted to the members of my research group (Dr Maria Boumpouli, Dr James Cowley, Dr Pratik Kandangwa, Aniol Puigdefabregas Nogueras, Sava Popescu) for their support, from navigating software to sharing ideas and experiences beyond the academic setting.

I gratefully acknowledge Siemens STAR-CCM+ for providing access to the simulation platform and ARCHIE-WeSt for the use of supercomputing resources. I extend my thanks to Dr Junxi Wu, Laure Vidal-Roussel, and Ruth Allen for generously supplying images used in the reconstruction studies, and to the departmental staff for their constant support and assistance. I am also grateful for the opportunities provided by conferences and the university, which offered not only platforms to present my research but also opportunities to learn from others, exchange ideas, and grow as a scholar.

I am deeply thankful to the Thai Royal Government for granting me a scholarship, and to the officials who managed the administrative processes with patience and care. Lastly, I extend my heartfelt thanks to my family in Thailand for their constant support, and to my Thai friends in the UK (especially Ratchadawan Dalai), with whom I shared the ups and downs of the PhD journey.

Abstract

Small vessel disease is recognised as a major contributor to serious clinical outcomes, including ischaemia, stroke, cardiac insufficiency, renal dysfunction and organ atrophy, due to the associated disruption in the microvascular blood flow. The precise cause-and-effect relationship between localised haemodynamics and clinical outcomes in such diseases remains poorly established. For that, it is important to understand the underlying mechanisms of blood flow in microvascular networks. Utilising Computational Fluid Dynamics (CFD) methods, which help quantify haemodynamic parameters not easily measured *in vivo*, this thesis investigates simplified and anatomically correct vessel geometries at various scales.

A key novelty of this work is the development of a novel multi-phase, multi-component continuum-based model using the Eulerian Multiphase (EMP) method, which treats blood as a suspension of red blood cells (RBCs) in plasma. With this, we investigate the behaviour of the cell-free layer (CFL) in arteriolar microvessels, a critical plasma-rich lubricating layer adjacent to the vascular wall that is fundamentally disrupted at bifurcations. This disruption creates a lasting asymmetric flow profile in the daughter vessels that governs overall perfusion in a microvascular network.

The model was validated using a CFL value specific to the haematocrit and diameter of a vessel, to allow assessment of its rheological predictions. The model's predictions were compared with established experimental findings to test its ability to reproduce fundamental non-Newtonian blood characteristics, including shear-thinning behaviour and the non-linear viscosity–haematocrit relationship. The Power-law, Casson, and Carreau–Yasuda models were used as benchmarks, confirming that the EMP approach robustly captured the shear-dependent viscosity of blood and its haematocrit dependence.

Parametric investigations then evaluated the model's robustness, and a range of physiological and geometrical conditions were studied. These conditions included variations in the feeding haematocrit, inflow rate, biased outflow, and bifurcation architecture. The simulations reproduced well-known haemodynamic phenomena in arterioles, such as the haematocrit partitioning (the Zweifach–Fung effect),

asymmetric CFL profiles, and the downstream recovery of flow symmetry. These results provided strong evidence that the EMP model not only reproduces physiologically observed phenomena but also offers a mechanistic insight into their haemodynamic origins.

The framework was then extended to realistic arteriolar microvessel network reconstructions. The multi-phase, multi-component simulations were conducted in testicular bifurcated microvessels with non-planar, tortuous paths. These studies revealed how CFL formation and plasma skimming manifest in physiologically relevant geometries. This work bridges the gap between idealised bifurcations and real vascular architecture, demonstrating the model's capacity to capture the effects of complex geometry on local haemodynamics.

In network scale, the multi-phase, multi-component model was successfully applied to the testicular atrophic network (48 μm). However, its application to the control network (89 μm), which features more extensive branching, was omitted due to the significant meshing challenges, which would require mesh optimisation. The single-phase model was instead used, revealing distinct haemodynamic patterns between control and atrophic morphologies, which translating into functional deficits in perfusion and resistance. To establish a clear contrast with the micro-scale, a separate analysis was performed on a large vessel bifurcation, the pulmonary arteries, where inertial forces are stronger and the CFL effects are negligible. By establishing this macro-scale simulation, the unique and dominant role of multi-phase, multi-component phenomena in microcirculation becomes clearer. Successfully bridging these distinct vascular scales underscores the value of the computational methods employed throughout this thesis.

List of Publications

Oral Conference Presentations

- Wisitponchai, T., Wu, J., Kazakidi, A., A biphasic haemodynamic model in microvascular networks. The 10th International Workshop on Nonequilibrium Thermodynamics (IWNET 2025). 2025, 8 – 11 Jun. Greece.
- Wisitponchai, T., Wu, J., Kazakidi, A., Recovery of the cell-free layer symmetry for arterial microvascular bifurcations. The congress of the European Society of Biomechanics (ESB2024). 2024, 30 Jun – 3 Jul. Edinburgh.
- Wisitponchai, T., Wu, J., Kazakidi, A., A recovery of symmetric flow in multi-branching. The association of Biomedical Engineers, Medical Engineers and Bioengineers (BioMedEng23). 2023, 14-15 Sep Swansea.
- Wisitponchai, T., Wu, J., Kazakidi, A., A recovery of symmetric flow in bifurcations. The congress of the European Society of Biomechanics (ESB2023). 2023, 8 – 3 Jul. Netherlands.

Poster Conference Presentations

- Wisitponchai, T., Wu, J., Kazakidi, A., Two-phase modeling of RBC and CFL dynamics in idealised and subject-Specific Microvessels. The association of Biomedical Engineers, Medical Engineers and Bioengineers (BioMedEng25). 2025, 4-5 Sep. Glasgow.
- Wisitponchai, T., Vidal-Roussel,L., Wu, J., Kazakidi, A., A biphasic flow model in idealised and engineered microvessels. Scottish Fluid Mechanics Meeting (SFMM38). 2025, 28 May. Glasgow.
- Wisitponchai, T., Wu, J., Kazakidi, A., A biphasic blood flow model in Bifurcated microvessels. The 11th Health Challenge Thailand 2025, 3 May. London. [Poster presentation].
- Wisitponchai, T., Wu, J., Kazakidi, A., A biphasic blood flow model in Bifurcated microvessels. The association of Biomedical Engineers, Samaggi Academic Conference and Careers Fair (SACC). 2025, 1 Feb. London. [Poster presentation].
- Wisitponchai, T., Wu, J., Kazakidi, A., A biphasic blood flow model in Bifurcated microvessels. The association of Biomedical Engineers, Medical Engineers and Bioengineers (BioMedEng24). 2024, 5-6 Sep. London. [Poster presentation].

- Wisitponchai, T., Wu, J., Kazakidi, A., Two-phase blood flow downstream of a 3D bifurcation. Scottish Fluid Mechanics Meeting (SFMM38). 2024, 20 May. Edinburgh. [Poster presentation].
- Wisitponchai, T., Wu, J., Kazakidi, A., Blood flow in bifurcations with two-phase model. Scottish Fluid Mechanics Meeting (SFMM37). 2023, 20 May. Glasgow. [Poster presentation].
- Wisitponchai, T., Wu, J., Kazakidi, A., Simulation of blood flow in different branching patterns: bifurcation, trifurcation, and tetrafurcation. Scottish Fluid Mechanics Meeting (SFMM36). 2023, 29 May. Uban. [Poster presentation].

Manuscripts in preparation

- Wisitponchai, T., Wu, J., Kazakidi, A., Recovery of symmetric flow downstream of 3D bifurcated microvessels with two-phase continuum model.
- Wisitponchai, T., Wu, J., Kazakidi, A., Computational fluid dynamics on mouse testicular atrophy.
- Wisitponchai, T., Allen, R., Kazakidi, A., Haemodynamics in the pulmonary arteries of Turner syndrome.

Contents

List of figures

List of Tables

Chapter 1

Introduction

1.1 Motivation

Microvascular ischaemia, a condition of inadequate blood supply to tissues, is a primary driver of organ damage, dysfunction and atrophy, contributing to a substantial global health burden. While clinicians can observe outcomes such as elevated blood viscosity and haematocrit [1, 2], the specific haemodynamic events that initiate and propagate perfusion deficits remain poorly understood. A significant challenge lies in understanding how subtle, local changes in flow dynamics accumulate across a vascular network to produce a clinically significant deficit.

The transition from functional to dysfunctional flow is critically influenced by the behaviour of blood at bifurcations, the fundamental branching points of the vascular network. In straight microvessels, blood into a central core of red blood cells (RBCs) surrounded by a lubricating, plasma-rich cell-free layer (CFL) that reduces flow resistance. This characteristic is disturbed at bifurcations, where the RBC core becomes skewed at inner wall and the enlarged CFL is in the outer wall of the daughter entrance. The disrupted RBC core gradually reorganises, allowing the CFL to recover and reform, and the flow to regain symmetry at a significant distance downstream [3, 4].

Investigating these phenomena presents significant methodological challenges. Direct *in vivo* observation is restricted by the microscopic scale and optical accessibility, preventing detailed measurement of parameters such as CFL thickness and flow profiles. Computationally, single-phase models fail to capture the essential particulate nature of blood (CFL formation and uneven RBC distribution to daughter branches), while high-fidelity particle-resolved simulations, which track individual RBCs, are too computationally expensive to model in network-level.

Particle-based and hybrid models show that CFL formation results from RBC migration driven by haemodynamic forces, with thickness influenced by haematocrit, deformability, and aggregation. At bifurcations, symmetry restoration is delayed, requiring distances of 8D to 25D [3, 5, 6], and varies with geometry, vessel size, and flow conditions. While previous models describe CFL asymmetry and recovery, they do not compute the forces driving RBC redistribution. Mechanisms such as hydrodynamic lift and shear-induced migration are theorised mainly in straight tubes, yet these forces remain unmeasured *in vitro* [7]. Analyses are further limited to simple bifurcations, excluding non-planar or complex networks. This gap limits understanding of network-level haemodynamics and highlights the need for computational frameworks that incorporate these parameters, compute interfacial forces explicitly, and extend analysis to physiologically relevant scales. This creates a methodological void for studying network-level haemodynamics with sufficient physical realism.

This thesis is motivated by the need for a tool that can bridge this gap. We develop, validate, and apply a novel multi-phase, multi-component continuum model using the Eulerian Multiphase (EMP) method, which offers a unique balance of physical fidelity and computational feasibility. The innovative framework is designed to enable the investigation of phenomena arising from blood's particulate nature, representing these characteristics through a continuum-based approach. The EMP framework models blood as an RBC-rich component (RBC-rich phase dispersed in plasma phase) surrounded by a near-wall pure plasma component. By averaging the volume fractions of these components, the model calculates haematocrit and captures plasma skimming without the computational cost of particle-level simulations. Crucially, EMP phase interaction closures compute momentum exchanges, including drag and lift forces, allowing direct analysis of CFL dynamics and downstream reformation. This capability provides mechanistic insight into CFL-related phenomena such as viscosity and haematocrit distribution.

The model is applied to both idealised and testicular bifurcations (20 μm), while a contrasting single-phase analysis of a large pulmonary artery bifurcation (2 cm) to establish a clear contrast with the micro-scale. Parametric studies on idealised bifurcations clarify the role of geometric and flow parameters in shaping CFL development and associated effects such as plasma skimming. Meanwhile, simulations of the testicular bifurcation and its network extend this analysis to non-planar and intricate vascular structures, offering a more physiologically representative perspective on microvascular flow dynamics.

While the multi-component, multi-phase model offers a practical balance between physical realism and computational cost, its continuum assumption limits applicability in scenarios where particulate behaviour is dominant. Within the EMP framework, CFL dynamics and global flow characteristics are represented through phase distribution rather than explicit cell morphology or clustering. Phenomena such as RBC aggregation (rouleaux formation) [8, 9] and deformability [10, 11] occur at the microscale and disease conditions and therefore require particle-level resolution or additional rheological parameters for accurate representation. Because EMP employs volume-averaging at the RBC-plasma interface, it cannot directly depict rouleaux stacks or shape alterations. Future developments should integrate rheological parameters governing aggregation and elasticity or adopt hybrid particle–continuum strategies to achieve both physical fidelity and computational tractability.

1.2 Clinical background

Abnormal haemodynamics often manifest as increased blood viscosity contributes to major ischemia conditions including heart disease (16% of global deaths) and stroke (11%) (WHO, 2019 [12]) , defined as the resistance of blood to flow [1, 13]. One of the most significant factors determining the viscosity is an elevated haematocrit, the volume fraction of red blood cells to the whole blood [1, 2]. A haematocrit increase of around 11% may boost blood viscosity by up to 20%, as demonstrated by controlled haemodilution experiments using capillary viscometry [1]. According to Poiseuille's law, this elevation in viscosity reduces flow by roughly 16-17%, which triggers

compensatory mechanisms such as 20% rise in blood pressure or 4-5% vasodilation to preserve normal circulation [1].

In individuals with arteriosclerosis, impaired vasodilation limits this response, leaving tissues at greater risk of ischemia due to hyperviscosity. This is particularly critical in sickle cell disease, where chronic anaemia leads to a paradoxically low haematocrit and low whole blood viscosity under normal oxygen conditions [14]. The subnormal viscosity can reduce the shear stress on vessel walls, which is linked to endothelial activation and damage.

Abnormal haemodynamics are particularly impactful in the microcirculation, where the geometry of the vessels and the properties of the blood may create unique pathological conditions [15, 16]. The architecture of vascular branching points, or bifurcations, creates regions that are inherently vulnerable to ischaemia [17]. Branching in small arterioles creates vulnerable zones where the uneven distribution of red blood cells leads to a significant drop in metabolites and the formation of oxygen-deficient 'plasma channels' during an occlusion. An acute occlusion of a single arteriole triggers a complex response: upstream vessels may dilate to reroute flow, while downstream vessels constrict due to the drop in pressure [18]. This can lead to the 'no reflow' phenomenon, where blood flow fails to resume after a blockage, is cleared due to localised haemoconcentration and poor blood rheology [19].

During an acute ischaemic stroke in the brain, abnormal blood flow resulting from high viscosity and haematocrit is likely to lead to poor clinical outcomes [2, 13]. Ischaemic stroke patients exhibit significantly higher viscosity than those with stroke mimics [20]. This hyperviscosity is particularly damaging in the ischaemic penumbra, where it impairs perfusion by increasing resistance after failure of the autoregulation mechanism [2]. A high haematocrit is linked to poor reperfusion and predicts a larger final infarct with less salvaged brain tissue [2, 21]. At the microvascular level, even a single blocked arteriole causes a cognitive deficit [22]. Multiple microinfarcts can subsequently merge, accelerating brain injury through a progressive collapse of the surrounding microcirculation, characterised by vessel constriction and obstruction [15, 22].

Extending this concept to the reproductive system, testicular bifurcation points within its arterial network represent critical loci where haemodynamic disturbances can initiate microvascular pathology, ultimately predisposing to tissue atrophy and impaired spermatogenesis. Under normal conditions, centripetal and radiating arteries supported by anastomoses maintain uniform perfusion and heat exchange [23-25]. However, pathological states such as varicocele-induced reflux or hypertensive remodelling disrupt this architecture, reducing arterial inflow and creating zones of hypoxia [26, 27]. These deficits impair Sertoli cell function and compromise the blood–testis barrier, triggering germ cell loss and tubular degeneration. Progressive vascular lesions, including sclerosis and hyalinisation, further increase resistance, perpetuating perfusion failure. The outcome is a measurable reduction in testicular volume, clinically recognised as atrophy [26, 28-33].

Distal structural changes in pulmonary microvessels, such as reduced density and compliance, profoundly influence global haemodynamics, elevating pressure and altering wave reflection patterns [34]. In turn, macrovascular forces, including cyclic stretch and shear stress, propagate adverse stimuli that accelerate microvascular fibrosis [35]. Evidence from computational sensitivity analyses confirms that microvascular parameters dominate haemodynamic variability, while proximal stiffness exerts secondary effects. This bidirectional relationship cannot be captured by single-scale models; therefore, multiscale integration of micro- and macrovascular domains is essential to reproduce the mechanistic continuum and improve predictive accuracy.

The multi-component multi-phase model advances translational impact by linking particulate blood behaviour to clinically relevant outcomes across physiologically realistic, non-planar vascular networks. For example, the model's ability to predict plasma skimming and asymmetric CFL reformation provides a platform to investigate why single-capillary occlusions trigger the blood-brain barrier leakage observed by Zhu et al. (2023) [16]. This capability informs the clinical inquiry into identifying high-risk critical vascular junctions or regions in neurodegenerative diseases such as Alzheimer's. Sucato et al. (2020) highlight Ischaemia with Non-Obstructive Coronary Arteries (INOCA) as a condition where microvascular dysfunction drives angina

despite normal angiograms [36]. By simulating feeding haematocrit and diameter asymmetry, the EMP framework can quantify microvascular resistance and plasma skimming, offering a non-invasive alternative measure for invasive indices. This informs the decision problem: can EMP-derived flow heterogeneity explain anginal symptoms and guide personalised therapy in INOCA patients? By explicitly computing the RBC-rich and plasma phase interactions, the EMP framework can inform decision problems regarding no-reflow and leakage (Zhao et al., 2023) [37]. The framework can also identify how network geometry and interstitial edema (Kloka et al., 2023) disrupt the endothelial barrier [38], ultimately predicting the risk of post-reperfusion heart failure.

1.3 Microvascular networks

The microvasculature encompasses vessels with diameters ranging from 5 to 100 μm, that is arterioles (the focus of this investigation), venules and capillaries [39, 40] (Fig. 1.1). The networks have a significant degree of organisation due to a considerable amount of irregularity, randomness, non-uniformity and tortuosity. The geometry of blood vessels including their position, size and branching pattern is highly organised to regulate flow resistance and perfusion, rather than serving solely as a passive conduit for blood distribution [41].

An organ's microcirculatory bed is principally concerned with three functions: regulation of blood flow, exchange of nutrients and gases and circulatory shunting [40]. The regulation of blood distribution is mediated by arterioles, whose muscular walls facilitate vasomotor responses to neural, hormonal and local chemical stimuli, such as nitric oxide. The critical function of exchange occurs within the capillaries; their thin, permeable walls and narrow diameter are structurally adapted for the efficient transfer of oxygen and other materials between blood and tissues, forcing erythrocytes into single file. After traversing the capillaries networks, blood drains in thin-walled venules. Finally, the bypass mechanism is provided by arteriolar-venular anastomoses, which act as shunts to divert blood from the capillary network, thereby enabling rapid control of thermoregulation and vascular resistance [42].

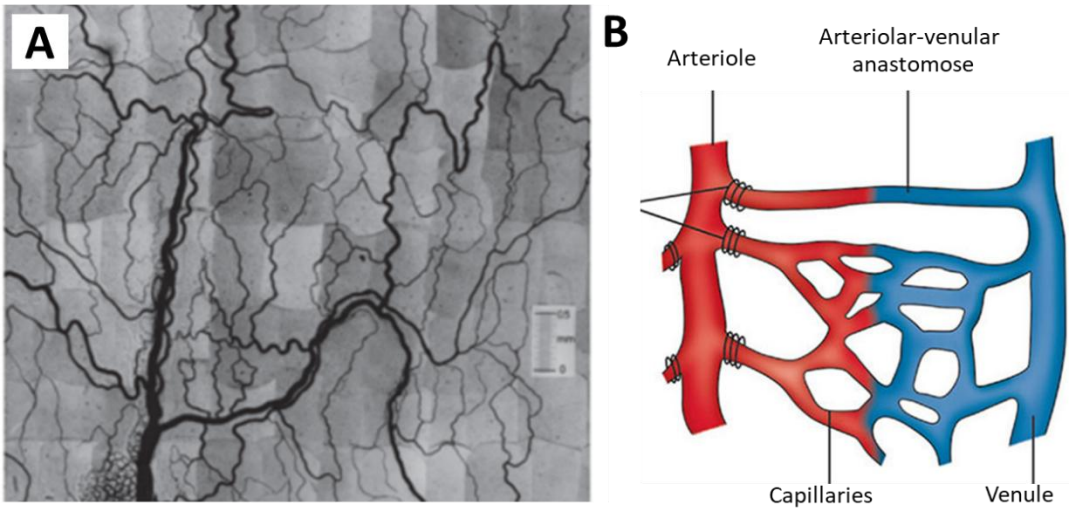

Figure 1.1: Microvascular network. (A) Microvasculature in the rat mesentery [39]. (B) A microcirculatory bed illustrating arterioles branching into capillaries and connecting to venules, with arteriolar-venular anastomoses [42].

1.4 Blood flow in microvessels

In microvessels, blood behaves as a complex, non-homogeneous fluid because the red blood cells (RBCs) are comparable in size to the microvascular diameter. Although blood consists of plasma and various cells, its rheology is overwhelmingly determined by the high concentration of RBCs, which make up 40-45% of its volume, with other cells making up approximately 1% [43]. As major components of blood, RBCs significantly influence blood rheology through aggregation and deformability. Blood exhibits non-Newtonian properties such as shear-thinning effects and viscoelasticity due to RBC interactions, resulting in a complex, nonlinear relationship between viscosity and shear rate.

Blood flow in arterioles is governed by several complex factors, including two particular significant phenomena : the formation of a cell-free layer (CFL) and unequal cell partitioning at branches [44]. Shear forces in vessels with diameters of a few microns push RBCs towards the vessel centre, creating the CFL and an RBC-rich core that reduces local viscosity. This lateral migration results in a nonuniform radial distribution of RBCs and contributes to several important haemodynamic phenomena,

including altered local haematocrit, viscosity reduction and unequal partitioning of red blood cells at vascular bifurcations.

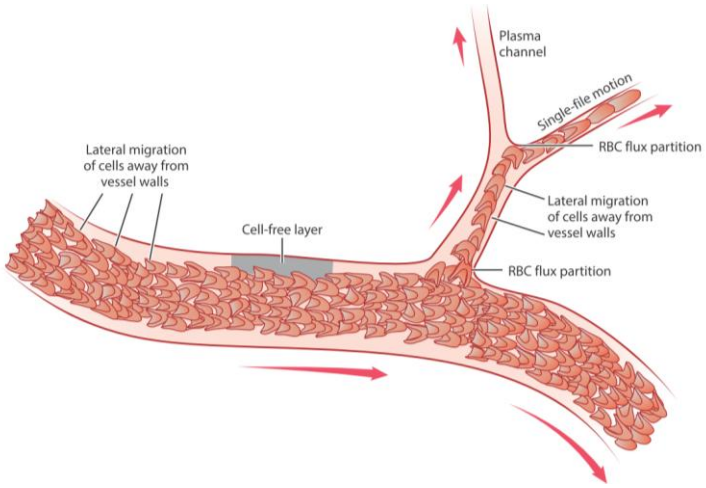

Figure 1.2**:** Fluid distribution of blood in bifurcated microvessels. Red blood cells migrate centrally, creating a cell-free layer (CFL), and preferentially enter high-flow branches at bifurcations. This causes uneven haematocrit, potential plasma channels, and single-file flow in capillaries [10].

1.4.1 Blood Rheology

1.4.1.1 Vascular resistance

Microvascular resistance is a key factor in regulating pressure and blood flow. To ensure adaptive tissue perfusion, microvascular resistance is precisely controlled through complex cellular and rheological interactions, rather than by simple hydrostatic pressure alone [10, 39]. The deformability and aggregation of red blood cells, combined with the vessel's own autoregulatory responses, collectively determine the resistance in each segment. This governs the local pressure gradients that drive flow, creating a dynamic system far more complex than the idealised relationship between pressure, flow, and resistance described by Poiseuille's law [45]. However, Poiseuille's Law is based on idealised conditions, it provides a vital baseline for understanding pressure-flow dynamics and hydraulic resistance. Its utility is in providing a baseline to quantify the impact of complex phenomena, such as the Fahraeus-Lindqvist effect [46, 47] and CFL formation.

In idealised tube flow, the relationship between pressure gradient (ΔP), volumetric flow rate (Q), and vascular resistance (R) is described by Poiseuille's law [45].

$$Q = \frac{\pi}{128}\frac{\Delta P D^4}{L\mu} \tag{1.1}$$

$$Q = \Delta P/R \tag{1.2}$$

$$R = \frac{\Delta P}{Q} = \frac{128\mathrm{L}\mu}{\pi D^4} \tag{1.3}$$

where D is diameter, μ is viscosity and L is length. According to Eq. 1.3, the flow resistance depends on the pressure gradient (ΔP), vessel length and blood viscosity. This means even small changes in vessel diameter can greatly affect the resistance, thereby helping control blood flow perfusion to tissues. Such quick adjustments in diameter occur through the rapid contraction and relaxation of smooth muscle in the arteriolar walls [48].

Because microvessels *in vivo* are not ideal cylinders, their resistance is higher than predicted, highlighting the need to account for vessel geometry, branching, and cell–wall interactions [49]. Smaller vessels (~5 μm) show more size variation than larger ones (~60 μm), which can raise the local resistance by up to 23% and the overall flow resistance (total pressure drop) by approximately 7–13.5% [49].

1.4.1.2 Blood pressure

A central finding from direct measurements in microvascular networks is that the maximum resistance to flow occurs in precapillary arterioles [50]. As shown in Fig. 1.3, there is a characteristic pattern where arterial pressure drops sharply as vessel diameters get smaller. This is the opposite of what Poiseuille's law would predict, which suggests that maximum resistance should occur in the smallest vessels [50, 51]. Despite the heterogenous nature of vascular tissue architectures, a consistent trend is the conservation of total blood flow, evidenced by red blood cell velocity decreasing through the branching arterioles and increasing in the converging venules [50].

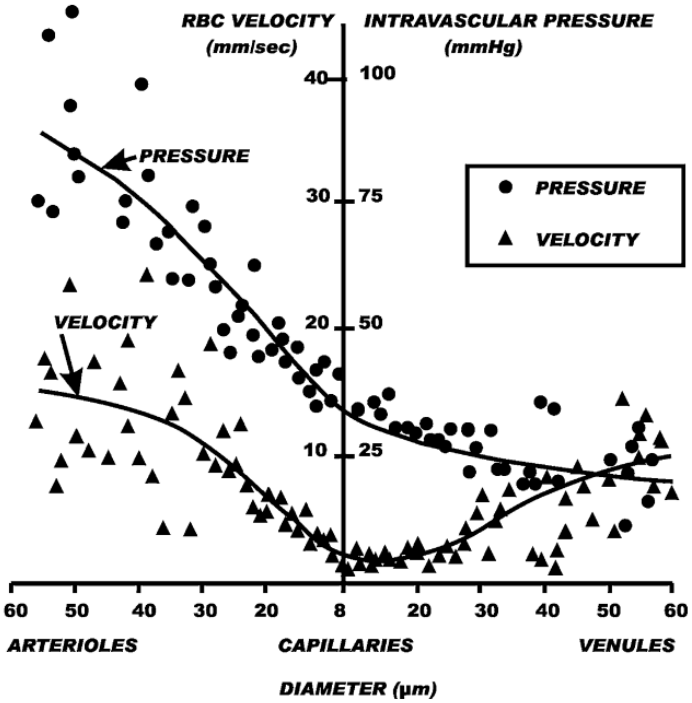

Figure 1.3: Intravascular pressure and RBC velocity across microcirculation obtained from arterioles to venules in cat mesentery [51].

1.4.1.3 Blood viscosity

Poiseuille's Law can be inverted to define an apparent or effective viscosity (μ_{app}):

$$\mu_{app} = \frac{\pi}{128}\frac{\Delta P D^4}{LQ} \tag{1.4}$$

$$\mu_{rel} = \mu_{app}/\mu_p \tag{1.5}$$

where μ_{rel} is the relative viscosity and μ_p is the plasma viscosity. The apparent viscosity is the internal resistance of a fluid to deformation from shear forces. This property is often expressed as a relative value by dividing it by the viscosity of the suspending medium (such as plasma, μ_p), a relationship defined as the relative apparent viscosity (μ_{rel}) in Eq. 1.5 [10].

While plasma exhibits Newtonian characteristics, the whole blood is inherently non-Newtonian, displaying phenomena such as shear-thinning, thixotropy, viscoelasticity

and occasionally yield stress, particularly at low shear rates [52]. These behaviours arise from RBC aggregation, deformability and alignment with flow at higher shear rates. At shear rates below 1 s^{-1}, blood has high apparent viscosity that decreases with increasing shear [52]. First described by Chien et al. in the 1960s [53, 54], these effects have been modelled using power-law, Cross and Carreau models, with later subsequent refinements improving accuracy [55].

1.4.1.4 Fåhræus effect

Blood's particulate behaviour in microvessels gives rise to the Fåhraeus effect [46, 47], where the local RBC concentration within a specific vessel segment (tube haematocrit; HT) is lower than the discharge haematocrit (HD), which is the volume fraction of blood flowing into or out of the same segment. This occurs because RBCs tend to migrate towards the centre of the vessel, forming a near-wall CFL [39, 56]. When RBCs aggregate or flow under low velocities, the CFL expands, increasing the average RBC velocity (u_c) relative to the bulk blood velocity (u_b). This disparity in velocity means RBCs pass through the tube faster, reducing their transit time and thus lowering HT compared to HD. The relationship between HT and HD is mathematically described by the covariance of the radial profiles of velocity $u(r)$ and haematocrit $H(r)$ with radial position r between 0 at the vessel axis and a at the vessel wall, as shown in Eq. 1.6. Empirical studies have yielded a parametric relationship [57], Eq. 1.7, which quantifies the HT/HD ratio based on *in vitro* experiments with human RBC suspensions in glass tube of varying vessel diameter D.

$$\frac{\mathrm{HT}}{\mathrm{HD}} = \frac{\int_0^a u(r) r dr \cdot \int_0^a H(r) r dr}{\int_0^a u(r) H(r) r dr \cdot \int_0^a r dr} \tag{1.6}$$

$$\frac{\mathrm{HT}}{\mathrm{HD}} = \mathrm{HD} + (1 - \mathrm{HD}) \cdot (1 + 1.7e^{-0.415D} - 0.6)e^{-0.011D} \tag{1.7}$$

1.4.1.5 Fåhræus–Lindqvist effect

The Fåhræus–Lindqvist effect provides an explanation for the observed nonlinear changes in blood viscosity and haematocrit with varying vessel diameters.

Specifically, this phenomenon describes how the apparent viscosity of blood diminishes when it flows through progressively smaller tubes. This relationship was shown by Pries et al. (1992) [56, 58], who used experimental data to calculate the relative apparent in vitro viscosity μ_{rel} as a function of vessel diameter and discharge HD:

$$\mu_{rel} = 1 + (\mu_{45} - 1)\frac{(1-HD)^C - 1}{(1-0.45)^C - 1} \tag{1.8}$$

$$\mu_{45} = 220\exp(-1.3D) + 3.2 - 2.4\exp(-0.06D^{0.645}) \tag{1.9}$$

$$\mathrm{C} = (0.8 + e^{-0.075D})(-1 + \frac{(1-HD)^C - 1}{(1+10^{-11}+D^{12}} + \frac{(1-HD)^C - 1}{(1+10^{-11}+D^{12}} \tag{1.10}$$

where μ_{45} is the apparent blood viscosity relative to that of the suspending medium for a discharge haematocrit HD of 0.45. The coefficient C describes the dependence on haematocrit.

During 1990 to 1994 [57, 59], Pries et al. examined the blood flow in an animal model and developed an empirical relationship for the apparent viscosity:

$$\mu_{rel} = 1 + (\mu_{45} - 1)\frac{(1-HD)^C - 1}{(1-0.45)^C - 1}\left(\frac{D}{D-1.1}\right)^2 \tag{1.11}$$

$$\mu_{45} = 6\exp(-0.085D) + 3.2 - 2.44\exp(-0.06D^{0.645}) \tag{1.12}$$

The presence of near-wall CFL is considered the primary cause of Fahraeus-Lindqvist effect [39]. Secomb et al. (1995) [60] introduced this concept using a two-phase model where a central, cell-rich core (with viscosity μ_c) is enveloped by a layer of plasma (with lower viscosity μ_p). The location of this plasma layer in the high-shear region near the wall is crucial, as it lowers viscous energy dissipation and reduces the overall apparent viscosity [39]. A larger CFL results in a lower apparent viscosity; however, this effect is dependent on the core remaining centred, as displacement can cause resistance to rise [39].

1.4.1.6 Aggregation

RBCs in humans and some mammals normally form aggregates called rouleaux, described as closely packed stacks of cells arranged face-to-face. Unlike clots, rouleaux readily coalesce in low-flow or static conditions. While normally dispersed by the shear forces of healthy blood flow, their persistence in pathological conditions such as diabetes can lead to the occlusion of microvessels [8]. This reversible aggregation causes excessive rouleaux formation and a blunted velocity profile. Such excessive aggregation is caused by an imbalance where the intrinsic tendency of RBCs to adhere overcomes the disruptive forces of the flow, altering blood velocity profiles.

While RBC aggregation typically increases the viscosity in the bulk flow, it can paradoxically decrease the apparent viscosity in narrow tubes at low flow rates [9]. This is because aggregate formation tends to pull the RBCs away from the vessel wall, thereby widening the low-viscosity CFL and reducing flow resistance [61], as shown in Fig. 1.4A. However, this mechanism is orientation dependent. In horizontal tubes at low flow rates, gravitational sedimentation of RBCs can occur, leading to a marked increase in apparent viscosity as the plasma flows faster than the sedimented cells [62] (Fig. 1.4B).

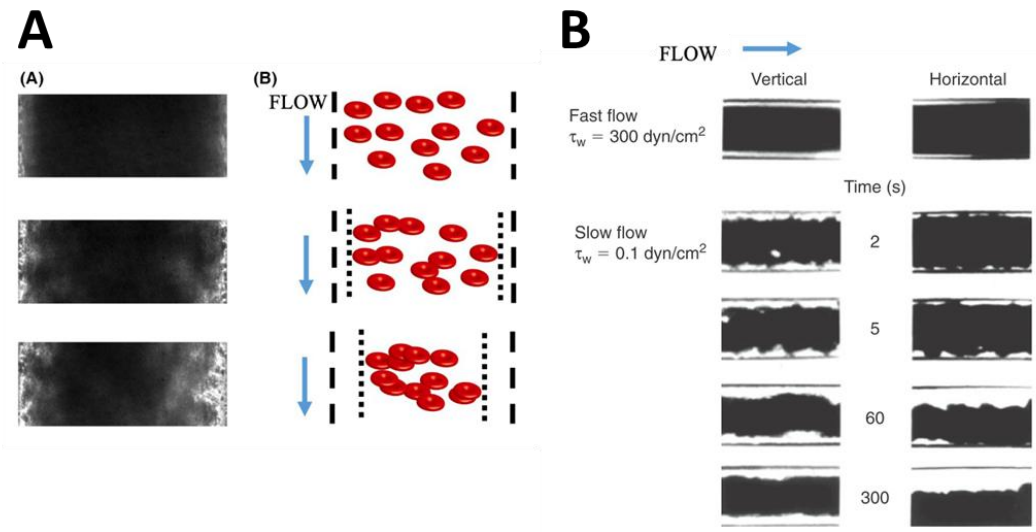

Figure 1.4: Image of RBC aggregation dynamics. (A) A time-lapse sequence demonstrating the aggregation growth immediately after flow cessation from Weber-Fishkin et. al. (2022) [61]. The direction of flow is from top to bottom. (B) The RBC aggregation in a 60-µm tube after a sudden reduction in flow rate, observed by Alonso et al. (1995) [62]. The vertical orientation (left) shows a symmetric RBC core forming,

while the horizontal tube (right) shows how gravity causes sedimentation and an asymmetric distribution of RBCs.

RBC aggregation is most prevalent in low-shear postcapillary venules, as high shear in arterioles and narrow capillary diameters typically prevent it. However, aggregation can influence arteriolar flow under pathological or low-flow conditions. For instance, Ong et al. (2010, 2011) [63, 64] demonstrated that dextran-induced RBC aggregation in arterioles (20–60 μm) enlarges the CFL during reduced flow. Simulations verify that reversible rouleaux dynamics are essential for modelling blood flow, particularly at low shear, where aggregation drives the rise in blood viscosity [65]. Adhesive forces between cells (3.0–7 pN normal and 1.5–3 pN tangential) align with experimental rouleaux disaggregation [65].

1.4.1.7 RBCs deformation

The surface area of biconcave RBCs, measuring approximately 8 μm in diameter and 2 μm thickness, is optimised for efficient gas exchange. This inherent elasticity is crucial, enabling RBCs to reversibly alter their shape to pass through capillaries narrower than their own diameter [10]. Their flow behaviour is determined by vessel size and haematocrit. RBCs move in a single file in capillaries under 6 μm, whereas in 6-10 μm capillaries, their flow can transition from single-file to multi-file as cell concentration increases [39] (Fig. 1.5A&B). RBCs exhibit a dual nature, behaving as both rigid and flexible particles depending on the shear rate. At low shear, their orientations are disordered, while high shear rates cause the cells to stretch and align with the direction of flow [66], as demonstrated in Fig. 1.5C. A slight reduction in the deformability of RBCs leads to significant increase in blood viscosity and microvascular flow resistance across a range of shear rates and at various haematocrit levels (Fig. 1.6). This shear-dependent deformability is crucial for oxygen and carbon dioxide transport, as a reduction in flexibility can obstruct microvessels and lead to diminished blood flow and hypoxia [11].

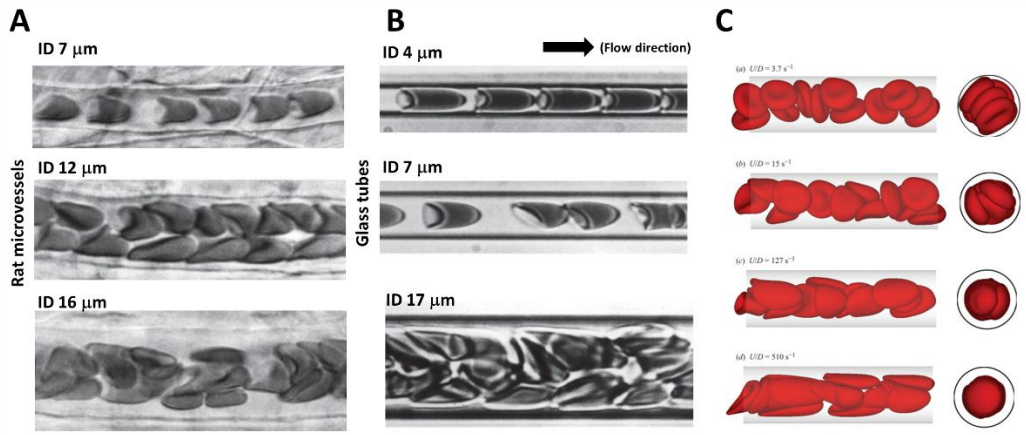

Figure 1.5: Visualisation of RBC flow in a tube. (A, B) RBC flow displaying micrographs from rat mesenteric microvessels and small glass tubes, respectively, with different inner diameters (ID). RBCs behave in single-file and multifile flow [39]. (C) CFD simulation under variation of pseudo shear rate (U/D) [66].

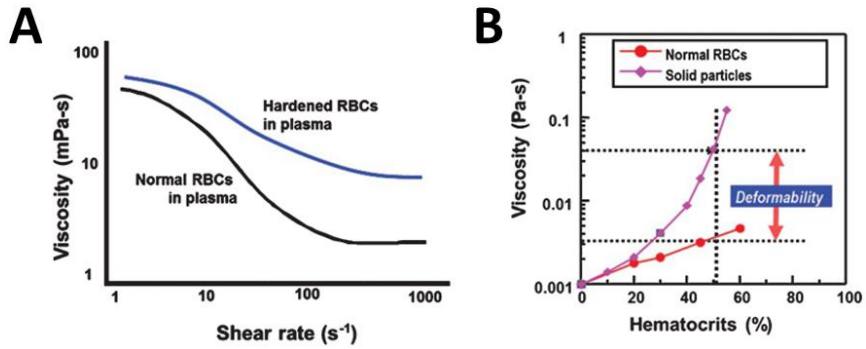

Figure 1.6: The influence of RBC deformation on blood resistance. Comparison of blood viscosity vs (A) shear rate and (B) haematocrit [11].

1.4.1.8 Haematocrit

Haematocrit is a critical determinant of oxygen delivery and flow efficiency, with changes often indicating physiological or pathological states. The value of haematocrit depends entirely on the context of its measurement. A standard blood test from a large vein provides the systemic haematocrit (Hsys), which represents the overall average for the entire body. At a more localised level, discharge haematocrit (HD) measures the RBC proportion in a sample after exiting a vessel. Feeding haematocrit (HF) refers

to the RBC concentration entering a vessel or network at the inlet, serving as the upstream condition for flow. In contrast, tube haematocrit (HT) refers to the instantaneous RBC concentration inside a flowing microvessel. Hsys and HD are typically measured using centrifugation, whereas HT is determined by counting RBCs within a specific vessel volume. As demonstrated by the distribution of tube haematocrit in Fig. 1.7, HT is consistently lower than the systemic average and reaches a minimum within the smallest microvessels. A summary of these haematocrits was provided in Table 1.1.

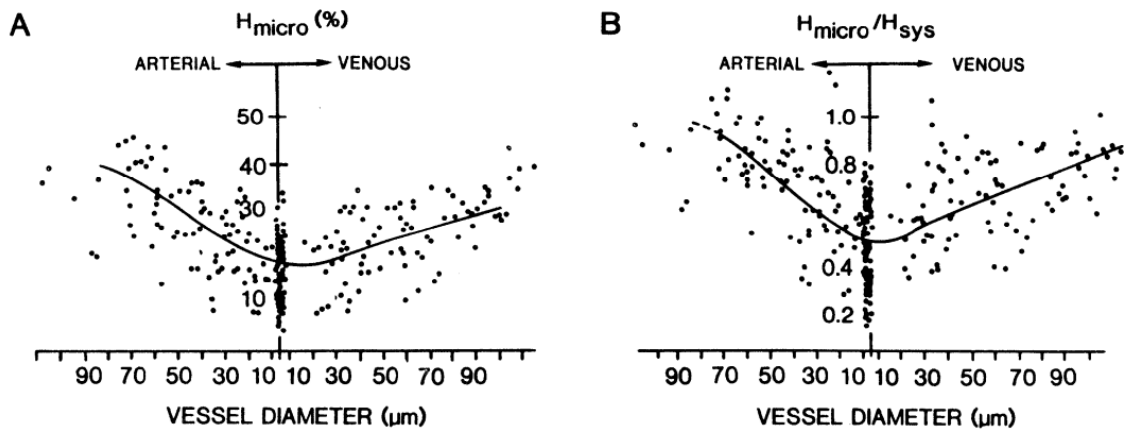

Figure 1.7: Haematocrit distribution. (A) Tube haematocrit or micro-vessel haematocrit (H_{micro}) and (B) HT normalised with respect to its corresponding systemic Haematocrit (H_{sys}) in rat cremaster muscle [67]. The Hsys averages around 36%.

Blood viscosity increases with higher haematocrit, especially at low shear rates due to RBCs aggregation [68]. The axial migration of red blood cells, which travel faster than the peripheral plasma, reduces the HT, thereby lowering the apparent viscosity and increasing the perfusion efficiency, an effect underscored by the HT/HD ratio [67]. This reduction correlates with the velocity difference between the mean RBC velocity (u_{RBC}) and the bulk flow velocity (u_{bulk}), described mathematically as [10]:

$$\frac{HT}{HD} = \frac{u_{bulk}}{u_{RBC}} \tag{1.13}$$

Table 1.1: Definition of haematocrit metrics in microvascular studies

Term	Definition and Validity	Measurement	Ref
Hsys	- Overall RBC volume fraction in the entire blood volume - Represents whole-body average - Used in clinical blood tests	- Centrifugation of venous blood sample	[67] [69] [70]
HD	- RBC proportion in blood exiting a vessel - Valid for microcirculation and experimental setups - Reflects RBC delivery to downstream network	- Collected sample after vessel outflow - Centrifugation or RBC flux calculation	[58] [67] [69] [71]
HF	- RBC proportion in blood entering a vessel - Represents upstream feeding condition for micro vascular flow - a boundary condition in simulation and experiment	- Prepare concentration of the input sample, based on Hsys or HD - inlet blood sample or controlled perfusion setting	[72] [73]
HT	- Instantaneous RBC concentration inside a vessel segment - Used in microvascular studies - Strongly affected by Fahraeus effect and axial migration	Direct RBC counting in a defined volume or image-based estimation	[67] [74] [73] [75] [76]
Hmicro	- interchangeably with HT in literature (Context-specific term)	Same as HT	[67]
Model-based HT/HD	- Calculated from assumed RBC distribution - Used when direct measurement is not feasible	Analytical or computational models	[77] [78]

The flow patterns in certain diameters are demonstrated in Fig. 1.8, which is the diameter-dependent variation in haematocrit [79, 80]. RBCs transition from a single-file to a multifile flow pattern as haematocrit increases, which also increases cell-wall interaction [80]. Moreover, HT was found to have temporal variations that dynamically correlated with spontaneous vasomotion [81].

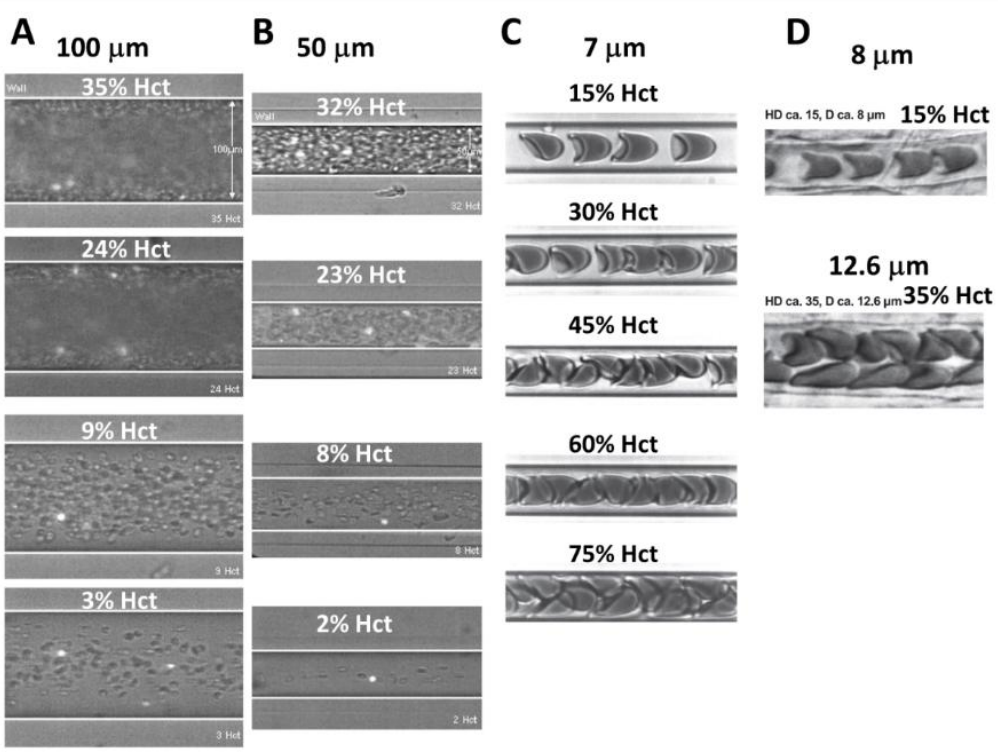

Figure 1.8: The impact of diameter to RBCs distribution. (A, B, C) Microscope images of RBCs distribution in a glass tube [82]. (D) Micrographs of RBCs in rat mesenteric microvessels [39].

The tube haematocrit is calculated directly by counting the number of RBCs that pass through a specific volume over a set period of time ($HT=N_{RBC}*V_{RBC}/V_{bulk}$) in experimental [67, 73, 74, 83] and particle-based computational studies [73, 75]. Meanwhile, the discharge haematocrit is determined by several techniques, including centrifugation, which is a measurement of RBC flux (Q_{RBC}) [73, 83].

$$HD = \frac{Q_{RBC}}{Q_{bulk}} \tag{1.14}$$

Indirect haematocrit estimation can be performed via photometric analysis of the RBCs area fraction. The calculation of haematocrit presented by Ellsworth and Pittman (1986) [77] is a theoretical example, based on assumptions including a Poiseuille velocity profile and symmetrical distribution of RBCs. The radial concentration of RBCs is described by the power law (Eq. 1.15), which is used to calculate the flow-weighted HD (Eq. 1.16) and area-weighted HT (Eq. 1.17):

$$H(r) = H_o \left[1 - \left(\frac{r}{R}\right)^n\right] \tag{1.15}$$

$$\text{HD} = \frac{2\pi \int_0^R H(r)u(r)rdr}{2\pi \int_0^R u(r)rdr} \tag{1.16}$$

$$\text{HT} = \frac{2\pi L \int_0^R H(r)rdr}{2\pi L \int_0^R rdr} \tag{1.17}$$

Rashidi et al. (2023) [78] calculated HT from the area fraction of RBCs ($\emptyset_s$) in *in vivo* images, incorporating the cell volume (V_{RBC}; 56.5 μm^3), the single RBC area (A_{RBC}), and the vessel radius (R_v).

$$\text{HT} = \emptyset_s \frac{V_{RBC}}{A_{RBC}\pi R_v} \tag{1.18}$$

In the two-phase continuum model by Giannokostas et al. (2021) [76], HD and HT are calculated from an assumed RBC concentration, H(r). This profile is a step-function including a constant core haematocrit (Hc) in the centre and zero in the near-wall CFL.

$$\text{HD} = \frac{\int_0^R H(r)u(r)rdr}{\int_0^R u(r)rdr} \tag{1.19}$$

$$\text{HT} = \frac{\int_0^R H(r)rdr}{\int_0^R rdr} \tag{1.20}$$

1.4.1.9 Blood velocity

In a long, cylindrical three-dimensional (3D) vessel with constant diameter, the incompressible, Newtonian, laminar Poiseuille flow obtains a parabolic velocity profile, with zero values at the walls and a maximum value at the centre, twice the average velocity. In the microcirculation, the blood velocity profiles have been reported as being both parabolic [79, 84, 85] and blunt [79, 85, 86], as illustrated in

Fig. 1.9., and influenced by several combined factors. A nearly parabolic profile is observed in a 100 μm straight microtubules at very low haematocrit (~1%) [79], while the profile becomes increasingly blunt in straight arterioles (i.e., diameters of 17-32 μm [86]) as cell concentration rises due to RBCs interactions in shear flow [79, 86]. Meanwhile, a decrease in the degree of blunting is the result of the reduced blood viscosity, which is a consequence of cell disaggregation and deformation [87].

In addition to haematocrit, the blunt profile is a consequence of the influence of shear stress developed at the vessel wall on blood and plasma flow [79, 88]. The flow profile is blunted and lacks a sharp peak because a core of fast-moving RBCs is formed by the lubricating CFL. With increasing flow rates, the profile continues to become more parabolic due to the increase in the shear rate on the RBCs [84, 85]. Furthermore, as illustrated in Fig. 1.9B, RBC and plasma velocities were comparable at the core, both averaging 3.5 mm/s and reaching maxima of 6.9 and 7.0 mm/s, respectively, under conditions of 21% haematocrit and a high wall shear rate of 2.8×10^{-2} s^{-1} in the 100 μm tube [84].

Blood flow velocity is a highly dynamic variable that varies significantly depending on vessel diameter, anatomical location, metabolic demand, systemic blood pressure and blood rheology such as viscosity. Immediately after an arteriole bifurcation, the velocity peaks skewed towards the outer wall, before shifting back to the vessel centre at a long distance [89, 90], as illustrated in Fig. 1.9C&D. Additionally, flow speed is inversely related to the total cross-sectional area. The flow is fastest in the arterioles, slows significantly in the capillaries, and then speeds up again in the venules, although it remains lower than in arterioles [67, 89, 91]. (Fig. 1.3, Fig. 1.10).

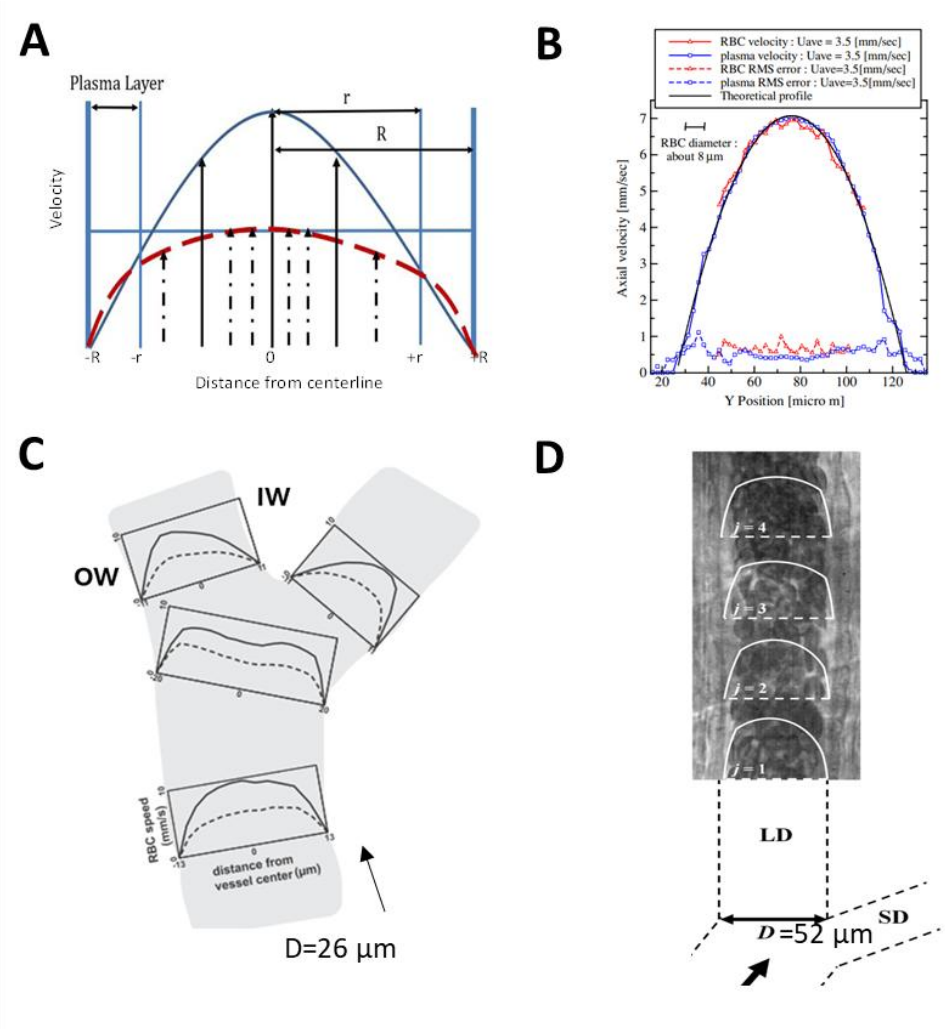

Figure 1.9: Parabolic and blunt flow velocity profiles. (A) Blunt velocity profile influenced by the presence of CFL [85]. (B) Time-averaged axial velocity profiles under conditions of 21% haematocrit and high wall shear rate [84]. (C) Velocity profiles in the cortical bifurcated arteriole in mice [89]. (D) Velocity development along the downstream vessel in rat [90].

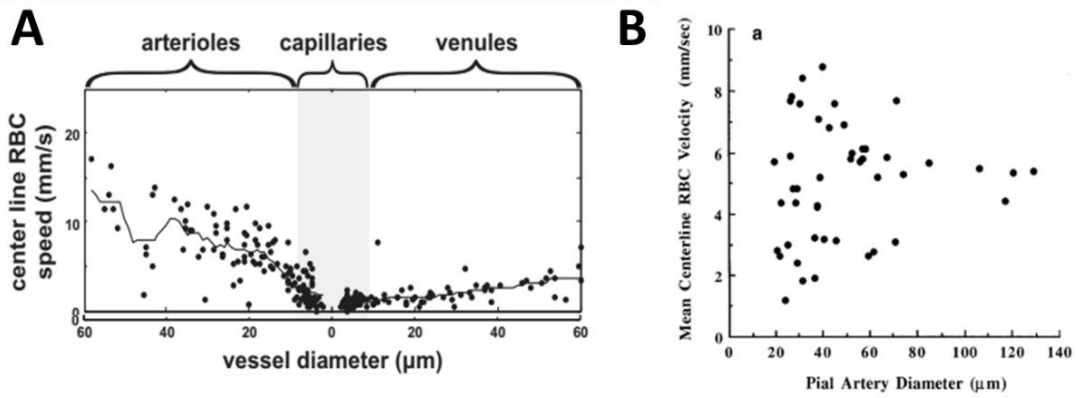

Figure 1.10: Microvascular velocity as a function of vessel diameter and location. (A, B) Centreline velocity in the cortical vessels, measured via fluorescence microscopy [89], and in rat pial arteries, measured using high-speed video [91].

1.4.1.10 Wall shear stress

In steady pressure-driven blood flow through a cylindrical tube, the velocity gradient at the wall generates a shear stress (τ) that balances the pressure gradient. The specific shear stress at the wall is termed wall shear stress (WSS), which for a Newtonian fluid is calculated as the product of the local viscosity and the wall shear rate (Fig. 1.11A and Eq. 1.21) [92, 93].

$$\tau_w = \mu \left(\frac{\partial u}{\partial y}\right)_{y=0} \tag{1.21}$$

The wall shear rate is directly proportional to the magnitude of the velocity in the near-wall region. A higher near-wall velocity corresponds to a higher wall shear rate. Calculating WSS for non-Newtonian fluid such as blood is complex because viscosity is not constant but depends on shear rate [94]. Using the simple Poiseuille law, which assumes a constant viscosity, leads to a significant underestimation of the true WSS by as much as 60-65% [95]. The proposed solution is to adjust this standard formula with a correction factor that incorporates the effects of haematocrit and the fluid's shear-thinning nature. As shown in Fig. 1.11B, the non-uniform distribution of WSS across the microvasculature, evidenced by significantly lower levels in venules compared to arterioles or capillaries, points to the fundamental role of non-Newtonian fluid dynamics in shear exposure for the endothelium [50, 67]. The average WSS in

rabbit mesenteric arterioles is approximately 1.82 Pa, with values ranging from 0.51 to 5.0 Pa [96]. In cats, WSS averages 4.71 ± 2.34 Pa, while in rats, arterioles exceeding 15 μm in diameter exhibit levels close to 5 Pa [97]. In the rat cremaster muscle, WSS averages 3 ± 0.5 Pa proximally and 2.1 ± 0.5 Pa distally [98].

WSS regulates vessel diameter by acting on endothelial cells to modify their production of vasoactive mediators, such as nitric oxide and prostaglandins [99]. The release of these substances causes the artery to either dilate or constrict, allowing it to adapt to changes in flow or viscosity. This process, which helps maintain WSS within a normal range, also has the secondary benefit of preventing platelet aggregation.

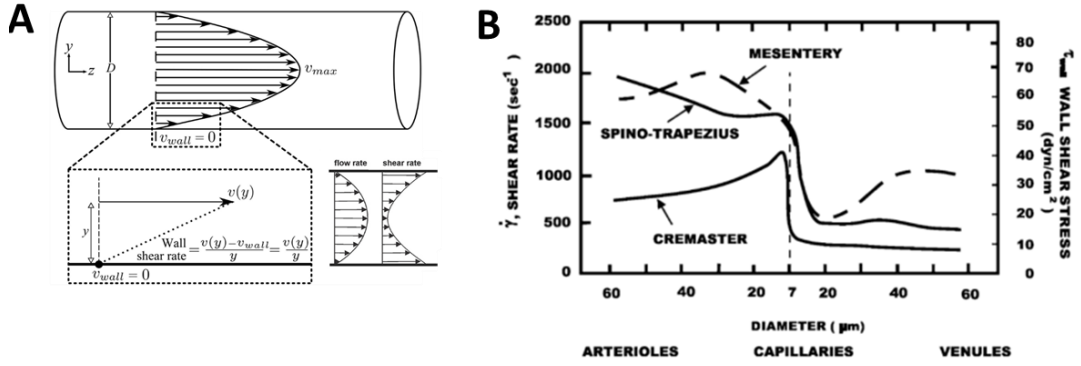

Figure 1.11: WSS development. (A) Schematic diagram of shear rate and shear stress in a long, cylindrical three-dimensional (3D) vessel with constant diameter, with incompressible, Newtonian, laminar fluid. Shear rate, which is the gradient of flow [93]. (B) WSS distribution in microvascular geometry [50].

1.4.2 Physiological blood flow behaviour

1.4.2.1 Cell-free layer (CFL)

In microfluidic blood flow, RBCs tend to concentrate at the centre of the vessel, leaving a plasma-rich region near the channel walls known as the cell-free layer (CFL) [100]. The formation of CFL is clearly visualised in the image of Fig. 1.12A, which depicts labelled RBCs flowing along the CFL's boundary. A diameter-dependent trend is observed, with CFL thickness ranging from 0.8 to 2.9 μm in cat arterioles having

inner diameters between 10 and 50 μm [101]. A comparable trend is observed in vessels 10–40 μm in diameter, where CFL widths ranged from ~1 to ~4 μm [102].

Beyond the vessel diameter, the CFL thickness is also a function of several parameters, including haematocrit, RBCs aggregation, flow rate and vessel diameter [103, 104]. With increasing haematocrit, the thickness of the CFL tends to be reduced, as depicted in Fig. 1.12B, which shows an overall reduction in CFL thickness as the haematocrit increases. CFL development results from local shear rate variations. Low shear promotes RBC aggregation and migration, enhancing the CFL formation and increasing the blood viscosity. Conversely, high shear can deform or even damage RBCs.

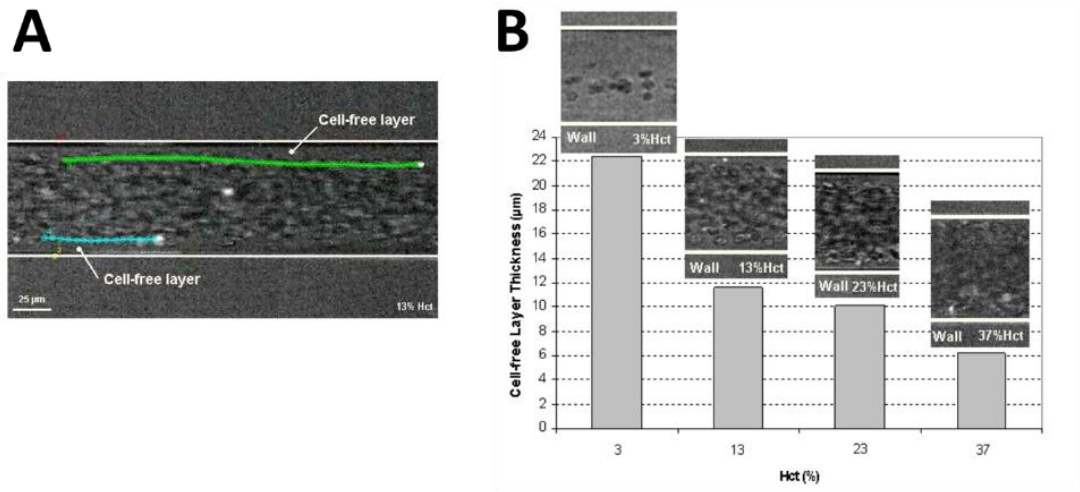

Figure 1.12: Cell-free layer (CFL) formation. (A) Labelled RBCs flowing around the boundary region of the CFL [82]. (B) CFL thickness in different percentages (%) of hematocrit in a 75-μm circular ploydimethysiloxane (PDMS) microchannel [79].

This near-wall plasma layer has a lower viscosity than the RBC-rich core. Consequently, a thicker CFL results in a lower apparent viscosity of the blood [105-108] and WSS [109, 110]. Moreover, the CFL reduces both oxygen diffusion to tissues [111] and the scavenging of nitric oxide (NO), a key vasodilator [112]. Therefore, the CFL acts as a barrier between RBCs and the endothelium [113]. It limits NO movement from the vessel wall to the RBCs [64, 74] and makes gas exchange between RBCs and tissues less efficient [29, 74]. However, when the CFL is thinner, oxygen reaches tissues more easily due to the shorter diffusion distance [112].

1.4.2.2 Phase separation

Microcirculatory networks involve numerous diverging and converging bifurcations, affecting RBCs movement during circulation. At a diverging bifurcation, common in arterioles, RBCs and plasma often split unequally between two daughters, a phenomenon known as phase separation. This effect has been studied in artificial systems [114, 115], in the microcirculation (Fig. 1.13A&B) [116] and using modelling approaches [117, 118]. The most relevant variables are the distribution of volumetric flow rate, the diameter ratio of tube to particle, the average haematocrit and the haematocrit profile in the feeding (parent) vessel.

Pries et al. (1989, 2005) [57, 80] describe phase separation in microvessels as a function of fractional flow and vessel size. These models relate the fraction of RBCs entering the daughter branch (FQ_E) and the fraction of the bulk in the same branch (FQ_B), [56], as illustrated in Fig. 1.13C. FQ_E is the daughter-to-parent RBC flux ratio, while where FQ_B is the daughter-to-parent bulk flux ratio. In an idealised condition without phase separation (e.g., equal flow distribution to two daughters in a symmetric bifurcation), FQ_E perfectly matches FQ_B, creating a direct linear relationship, depicted by the dashed diagonal line. However, actual physiological conditions demonstrate a non-linear, sigmoidal relationship, indicating that $FQ_E \neq FQ_B$. High-flow branches ($FQ_B > 0.5$) exhibit RBC enrichment ($FQ_E / FQ_B > 1$), while low-flow branches ($FQ_B < 0.5$) experience plasma skimming ($FQ_E / FQ_B < 1$). The presence of the CFL causes peripheral plasma-rich layers to enter low-flow branches, reducing the haematocrit in those branches and elevating it in the higher-flow pathways [56].

In the capillary scale bifurcation (Fig. 1.13B&D, parent vessel ~7 μm), a dividing streamline directs individual RBCs to each daughter vessel. Local fluid forces at the branch point (stagnation point) determine whether a cell enters the left or the right branch [56]. For larger vessels (~30 μm, Fig. 1.13E), RBCs have a non-uniform distribution across the vessel radius due to their size, deformability and the presence of near-wall CFL. This creates a radial haematocrit profile, where RBCs are concentrated in the centre and are sparse near the edges. At a bifurcation, the dividing streamline then effectively splits the flow with differing upstream haematocrits.

Consequently, the smaller daughter branch draws blood from the lower-haematocrit regions of the near-wall CFL [56].

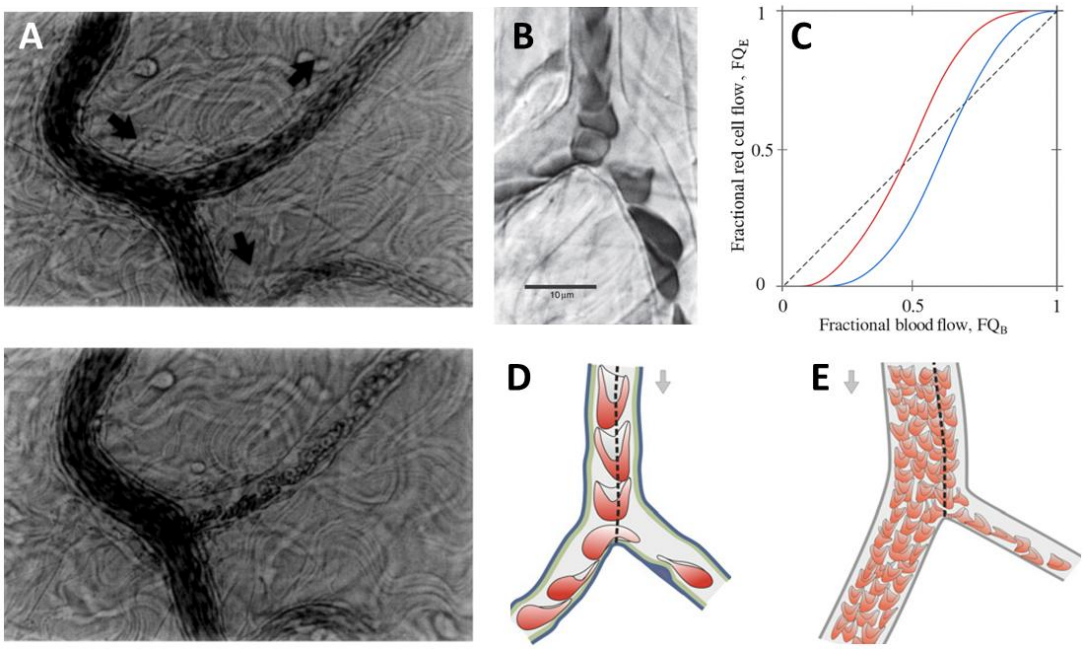

Figure 1.13: Phase separation in a diverging bifurcation. (A) The arteriolar bifurcation in the rat mesentery, highlighting different flow rates in the daughter branches [116]. (B) RBCs flow in a rat microvessel [39]. (C) Schematic depiction of the relationship between $\boldsymbol{FQ_B}$ and $\boldsymbol{FQ_E}$. The diagonal dashed line represents no separation, while the red and blue sigmoidal curves indicate actual phase separation (unequal flow split) in the daughter branches. (D, E) The graphic descriptions of how the dividing streamline (dashed) separates flow at the capillary level and a larger vessels, respectively [56].

1.4.2.3 Lateral migration of individual particles

In fluid dynamics, the Stokes regime, also called creeping flow, refers to conditions where the particle Reynolds number ($Re_p << 1$) and viscous forces dominate over inertial forces [119]. This Stokes regime commonly appears in microfluidics and capillary blood flow, where suspended particles such as RBCs move smoothly along streamlines without significant deviation [120]. Because inertia is negligible, the flow is reversible and predictable; however, cell deformability and wall interactions can still induce subtle lateral migration.

Drag forces are the resistive force opposing particle motion through fluid, as shown in Fig. 1.14A. Under Stokes conditions, the drag force is linearly proportional to the velocity, following Stokes' law ($F_D = 3\pi\mu d_p u$, where d_p is the particle diameter) [121]. In blood, the drag force governs the primary transport of RBCs, platelets and other particulates [120]. However, the unique biconcave and deformable geometry of the RBCs introduces complexities not captured by rigid-sphere models. For low Re conditions, correlations for the drag coefficient and the lift coefficient for non-spherical particles provide accurate predictions and serve as validation for computational models [119].

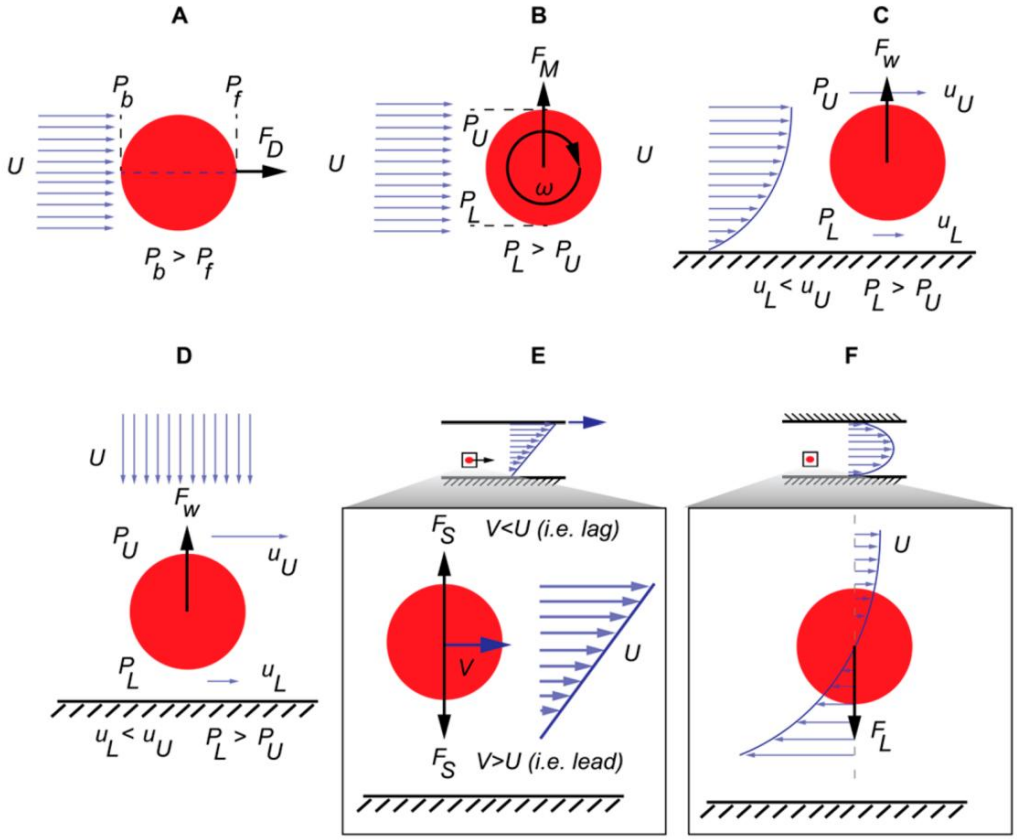

Figure 1.14: Hydrodynamic effects on suspended particles. (A) Drag force (F_D) acting in the direction of the flow. (B) Magnus forces (F_M), caused by particle rotation. (C, D) Wall forces (F_W) for a particle moving parallel (C) or perpendicular to the wall (D), respectively. (E) Saffman forces (F_S) push particles toward faster-moving regions. (F) Shear-induced lift force (F_L), caused by a parabolic flow profile, tends to drive particles toward the walls. P_b and P_f are the pressures at the back and front of the particle, respectively, the difference of which creates drag forces. P_L and P_U is the pressure on the lower and upper sides of the particle, the difference of which creates lift forces. V is the velocity of the particle, which can be less than (lag) or greater than (lead) the mean fluid velocity U [122].

Lift forces act perpendicular to the flow direction and are generally minimal in pure Stokes flow, becoming significant when inertia increases or particle symmetry is broken [120]. In microchannels and blood vessels, lift arises from multiple components: shear-gradient lift, wall-induced lift, Saffman lift due to shear-slip interactions, and Magnus lift induced by particle rotation (Fig. 1.14B). A shear-gradient lift (F_L) pushes particles toward the channel walls (Fig. 1.14F), while a wall-induced lift (F_W) pushes them away (Fig. 1.14C&D).

The Saffman lift force arises in shear flows when particles move at a velocity different from the fluid, known as slip velocity [123, 124]. This velocity difference generates pressure imbalances around the particle due to fluid shear. With a large slip velocity (Fig. 1.15A), particles are pushed away from the wall toward the channel centreline, while at a small slip velocity (Fig. 1.15B), they are pushed toward the wall. Unlike other lift forces, the Saffman lift changes direction depending on slip conditions (Fig. 1.14.E & 1.15C).

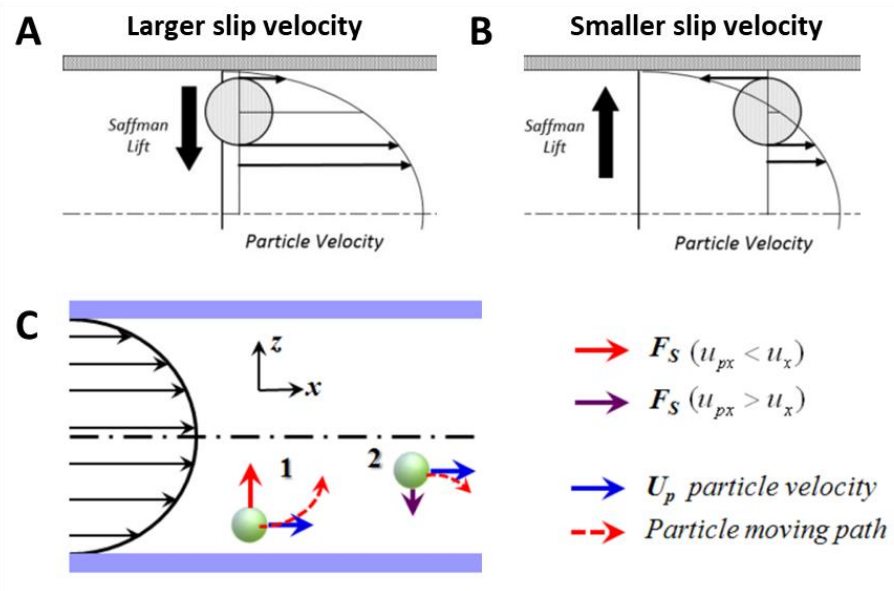

Figure 1.15: Relationship between Saffman lift and slip velocity. (A) Larger slip velocity. (B) Smaller slip velocity [123]. (C) Particle moving path influenced by the Saffman lift force [124].

In blood, these lift forces contribute to cell margination and radial alignment, which are essential for biological processes such as platelet localisation and for engineered systems including inertial microfluidics [125]. RBC lift forces, particularly wall-induced lift, drive cells away from vessel walls and are the primary mechanism behind the formation and maintenance of the CFL. When the lift is weakened, the CFL becomes thinner or disrupted [126]. The interplay of drag and lift enables precise focusing, ordering and separation of cells, which serves as the basis of modern microfluidic diagnostics and cell-sorting devices.

1.4.2.3 Radial dispersion of multiple RBCs

While cell deformability governs lateral migration in dilute solutions, particle-particle interactions become the dominant factor in concentrated suspensions such as blood when the volume fraction exceeds 6% [44, 127]. RBCs form flexible stacks called rouleaux, which are highly deformable and migrate more effectively than individual cells [128]. At low shear rates, these rouleaux make up the core of the blood flow. As shear rates increase (8.8 to 123 s^{-1}), these stacks are disrupted, leading to a thinner CFL near the vessel wall. However, at even higher shear rates (240-1200 s^{-1}), RBCs migrate laterally, which broadens the CFL [129]. This dynamic, non-uniform distribution of RBCs explains the Fåhræus-Lindqvist effect, where blood's apparent viscosity changes with vessel diameter.

According to Lima et al. (2008) [82], the transverse, random-like motion of RBCs, referred to as erratic movement, in flowing blood is influenced by the haematocrit and the vessel diameter. Figure 1.8A&B shows that in dilute suspensions with 2–3% haematocrit, RBCs in the central region move more freely, though the overall radial dispersion is low and mainly driven by shear rather than interactions. At a higher haematocrit, collisions dominate, increasing radial spread. Within the RBC-core region (0–0.4R), cells are too packed to move freely, while the mid-peripheral region (0.4–0.8R) shows the most erratic motion from frequent collisions. Closer to the wall (0.8–1R), RBC density and irregular movement are low. Overall, the erratic RBC motion is governed by both haematocrit and radial position, with the maximum randomness occurring in the mid-peripheral regions due to frequent collisions.

1.5 Computational Fluid Dynamics

Computational Fluid Dynamics is a numerical tool that is used widely in a broad range of fields, such as aerospace, chemical engineering, and bioengineering [130]. CFD methods provide a non-invasive simulation approach to examine the flow development in blood vessels and are therefore increasingly used to support clinical diagnosis, treatment and surgery planning [131, 132] and to understand blood perfusion dynamics at the microscale [133, 134].

1.5.1 Basic principles of fluid mechanics

This section outlines the theoretical framework for the haemodynamic modelling techniques utilised throughout this research. The mathematical expressions included are sourced from the STAR-CCM+ User Guide v18.02.010 (Siemens Industries Digital Software).

Although blood flow in microvessels typically exhibits non-Newtonian features [79, 86], its behaviour approaches Newtonian under conditions of high shear or low haematocrit [79]. For computational purposes, the governing blood behaviour is described using the incompressible Newtonian Navier-Stokes equations, consisting of three governing equations [135, 136].

The conservation of mass (continuity equation) ensures that fluid mass is neither created nor lost, which is key to predicting the velocity and density of a fluid. For an incompressible fluid, where density is constant, continuity equation simplifies to:

$$\oint_A \boldsymbol{v} \cdot d\boldsymbol{a} = 0 \tag{1.22}$$

where $\boldsymbol{v}$ is the continuum velocity vector, A is control surface and $\boldsymbol{a}$ is outward normal vector.

The Navier-Stokes momentum equation describes the relation between the velocity, pressure, and viscosity, over space and time. This equation is crucial for predicting fluid motion, shear stress and pressure fields. For an incompressible Newtonian fluid, it is expressed as [136]:

$$\rho\left[\frac{\partial}{\partial t}\int_{\mathrm{V}} \boldsymbol{v}d\mathrm{V} + \int_{A} \boldsymbol{v}\otimes\boldsymbol{v}\cdot d\boldsymbol{a}\right] = -\oint_{A} p\mathbf{I}\cdot d\boldsymbol{a} + \oint_{A} p\mathbf{T}\cdot d\boldsymbol{a} \tag{1.23}$$

here V is control volume, p is the pressure, **I** is identity tensor, and **T** is the viscous stress tensor.

1.5.2 Numerical methods

Blood flow modelling operates within a hierarchy of scales (Fig. 1.16), from molecular to continuum [137]. Fluid dynamics is governed by spectrum of length and time scales, ranging from molecular collisions to bulk fluid motion, with mesoscale approaches bridging these regimes by tracking particle distribution. As the Lattice Boltzmann Method (LBM) is a mesoscale technique derived from kinetic theory, it provides a highly appropriate computational approach for microvascular blood flow where RBC and vessel dimensions are comparable.

While LBM provides high physical accuracy, its computational cost and geometric constraints make it less practical for large-scale simulations. Our work employs a macroscopic multi-phase, multi-component continuum-based model as a valid simplification where RBC components are average into a continuous phase. The multi-phase, multi-component model captures interphase between RBC and plasma phase, allowing to calculate haematocrit and investigate physiological behaviour in microvessels, such as phase separation and CFL formation, without resolving the dynamics of every individual RBCs with greater computational efficiency than a true mesoscale model. The particular simulation on microvasculature is provided in the later section.

In CFD, numerical techniques such as the Finite Difference (FDM), Finite Element (FEM) and Finite Volume (FVM) methods are used to solve the partial differential equations (PDEs) that govern fluid flow by discretising the domain [135]. These approaches differ in their strengths. FDM is computationally efficient for simple, structured grids but handles curved, unstructured boundaries poorly. FEM is highly flexible for complex geometries but can be compromised by mesh distortion in high-deformation scenarios, such as red blood cell aggregation.

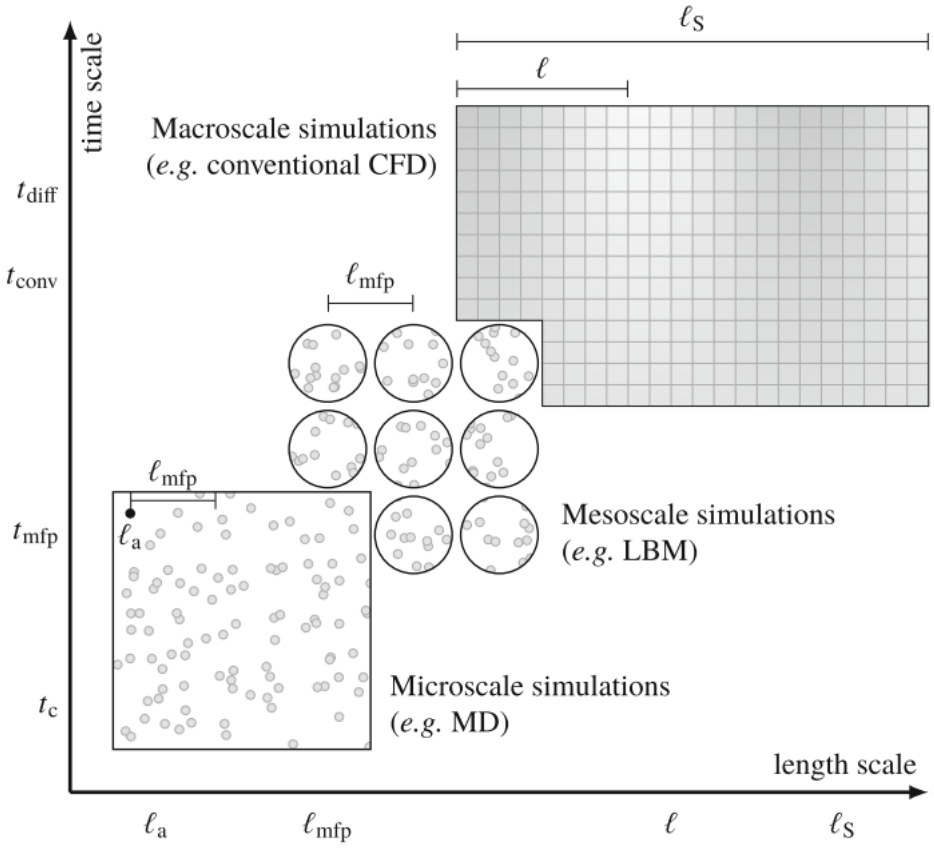

Figure 1.16: Spectrum of length and time scales to standard CFD problems [137].

Among the numerical methods, FVM is particularly effective for simulating blood flow due to its strong conservation properties and adaptability to complex geometries. FVM discretises the domain into small control volumes and applies conservation laws directly to each volume. The use of the divergence theorem transforms volume integrals into surface integrals, making FVM highly effective for solving mass, momentum and energy conservation equations. Due to its conservative nature and compatibility with complex geometries, FVM is widely used in commercial and open-source CFD software, including Simcenter STAR-CCM+ by Siemens, ANSYS Fluent or OpenFOAM.

The FVM is a numerical technique for solving PDEs through a series of steps. First, the continuous fluid domain is discretised into a finite number of control volumes (meshing). Next, the governing equations for mass, momentum and energy are integrated over each volume. A crucial step involves approximating the fluxes of these

quantities across the cell faces, often using upwind or central difference schemes, and treating any source terms. These discrete equations are then assembled into a large system of algebraic equations for variables including velocity and pressure. Finally, this system is solved using appropriate linear or nonlinear numerical solvers to determine the flow field.

1.5.3 Mesh generation

A mesh is a discretised geometric model formed by dividing the domain into subdomains where the governing conservation equations are numerically solved. Using the FVM, values are computed at the centre of these cells (Fig. 1.17A) to analyse the physical region. The cell, defined as either an area (2D) or volume (3D), is bound by points (vertices) connected through lines (edges) that form faces (Fig. 1.17A).

Simcenter STAR-CCM+ by Siemens employs a structed meshing process starting with geometry preparation, wrapping for complex surfaces, and defining part contacts to ensure mesh conformity. Initially, a closed surface is generated from the provided geometry; this is subsequently remeshed to enhance triangulation quality and facilitate the creation of prism layers. Volume meshing employs polyhedral, tetrahedral or timed, with optional prism layers for boundary layer resolution. Tetrahedral meshes are fastest but require higher cell counts for accuracy. Polyhedral meshes, generated via dualization from tetrahedral cores, deliver improved accuracy and efficiency. This process provides a flexible, repeatable pipeline independent of physics, suitable for complex geometries.

1.5.4 Wall treatment

For viscous flows, a structured mesh layer such as a prismatic layer, known as the boundary layer, is generated near wall surfaces after surface meshing to accurately capture viscous effects [136]. Prism layers not only enhance mesh density near wall boundaries but also enable the use of high-aspect-ratio cells, thereby improving cross-stream resolution without necessitating excessive refinement in the streamwise

direction. They also reduce numerical diffusion, a discretisation artefact that blurs steep gradients.

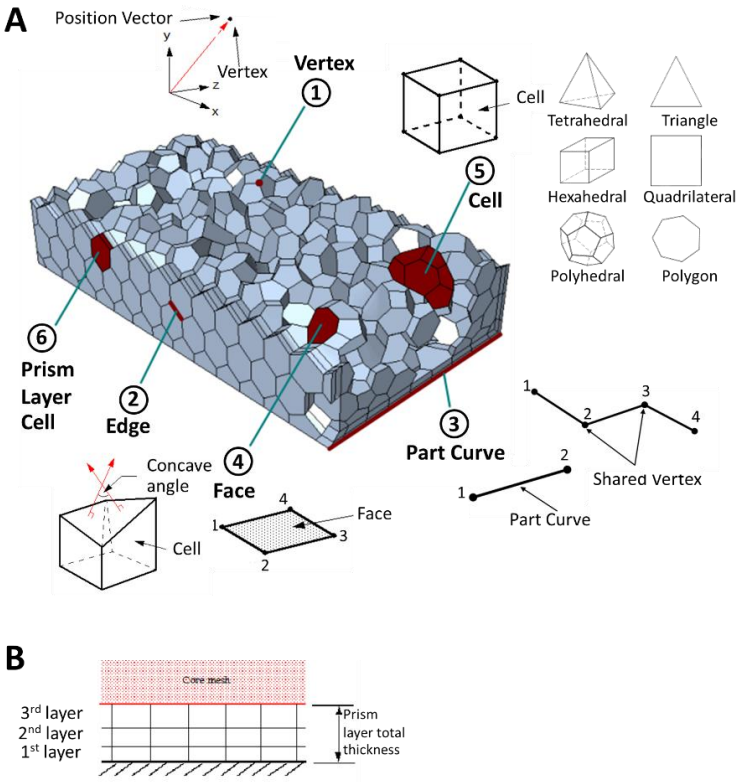

Figure 1.17: Mesh topology components and boundary definitions using in Simcenter STAR-CCM+ by Siemens [138]. (A) Key mesh elements including vertex, edge, part curve, face, cell, and prism layer cell, within a polyhedral volume mesh. (B) The prism layer total thickness controls the total overall thickness of the prism layers, here shown for 3 layers.

After the surface is meshed, a layer of orthogonal prismatic cells is created the viscous boundary layer near the wall boundaries. The layer is generated by extruding faces from the core volume mesh back to the original surface, based on a defined total thickness. To generate multiple boundary layers, the mesh starts with a small initial layer thickness adjacent to the wall, and subsequent layers increase in size according to a specified growth factor rate until the desired thickness is reached (Fig. 1.17B)

To characterise the quality of the near-wall mesh, the non-dimensional distance, known as the y+ value, can be used to determine the physical height of the first layer Δy_1 [139]:

$$\Delta y_1 = \frac{\mu y^+}{\rho U_T} \tag{1.24}$$

$$U_T = \sqrt{wss/\rho} \tag{1.25}$$

where the y^+ is satisfying the value of U^+ for low Reynolds numbers in microvessel flows. The $U^+$is the dimensionless velocity, which calculated from U/U_T [140, 141], where U_T is the friction velocity. Walls are a source of vorticity in most flow problems of practical importance. Therefore, an accurate prediction of flow and turbulence parameters across the wall boundary layer is essential.

1.5.5 CFD approaches in microvessels

At the microscale, fluid behaviour is governed by surface-related forces such as viscosity and surface tension. This shift is caused by a high surface-area-to-volume ratio, which results in low Reynolds numbers (typically <1) and predominantly laminar flow [135]. The Reynolds number ($Re = \rho UD/\mu$) is a dimensionless quantity comparing a fluid's inertial forces (ρU^2) to its viscous forces ($\mu U/D$). In physiological conditions, blood flow is considered incompressible and can be categorised as either laminar, transitional or turbulent.

Due to the complex physiology of the arterial system [142], physics-based models are a valuable tool for simulating physiological behaviour of the arteries. These models are commonly classified into reduced-order (0D, 1D) and high-dimensional (2D and 3D models) approaches (Fig. 1.18), each suited to different research aims. Reduced-order models, using simplified inputs including vessel geometry and basic mechanical properties, efficiently represent haemodynamics across extended lengths of the arterial system. In contrast, three-dimensional (3D) models provide detailed local flow information, but require significantly greater computational resources [143].

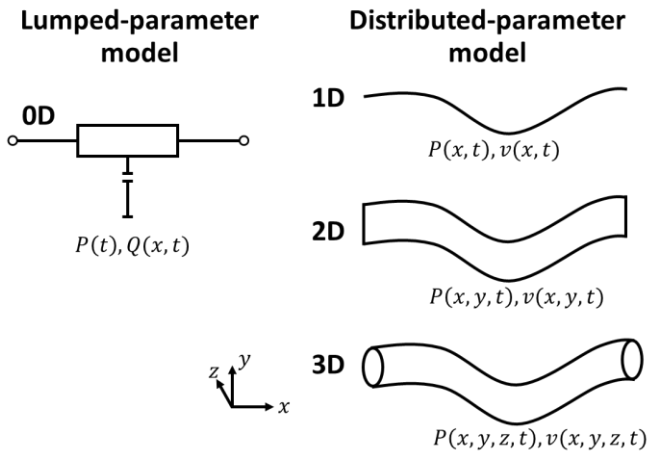

Figure 1.18: Physics-based models (modified from [143]).

0D models (lumped parameter models) treat each vascular compartment (e.g., cerebral haemodynamics) as a single compartment with no spatial variation, assuming uniform flow, pressure and other variables at any given time [142, 143]. Governed by ordinary differential equations, they are time-dependent only and computationally efficient, making them ideal for simulating the global cardiovascular dynamics and estimating boundary conditions in larger systems. For example, Loganathan et al. (2024) [144] developed a 0D model to analyse how occlusions reduce cerebral blood pressure and flow regardless of site. Similarly, Frash et al. (1996) [145] utilised a lumped Windkessel-based model to represent pulsatile pressure-flow dynamics in a microcirculatory bed. However, their lack of spatial resolution limits their application in microscale phenomena such as branching, local flow separation or cell-scale dynamics.

In the distributed parameter models, 1D models extend the 0D framework by incorporating spatial variation along vessel length. They solve simplified Navier-Stokes equations, enabling analysis of axial pressure and velocity gradients, flow resistance or phase separation effects (e.g., plasma skimming and Fahraeus effect) in vascular networks [146]. Building on this, 2D models simulate flow within planar or axisymmetric geometries. Ng et al. (2015) and Yin et al. (2013) both used 2D models to analyse blood flow in microvessels, with the former focusing on transient spatiotemporal variations in the CFL in arterioles, and the latter using the Lattice

Boltzmann method to investigate RBC separation at a simplified Y-shaped bifurcation. Extending further, 3D models provide the most detailed representation of blood flow. While Safaeian and David (2013) [147] simulated oxygen transport across a 3D cerebral capillary network using a continuum-based method, Fedosov et al. (2020) [148] utilised the dissipative particle dynamics method to resolve the motion and deformation of individual biconcave-shaped RBCs within a 3D microtube.

1.6.6 CFD approaches to the CFL

The presence of CFL decreases the apparent blood viscosity through the Fahraeus-Lindqvist effect, improving the flow efficiency, facilitating mass transport between blood and surrounding tissues, and critically influencing RBC distribution at a bifurcation [56]. Capturing these effects is crucial for accurate microvascular haemodynamic simulations, and many simulations incorporate the CFL for this reason. Blood flow modelling methods can be classified into continuum-based, particle-based and hybrid approaches. Continuum approaches rely on a mesh to solve bulk fluid, whereas particle-based methods are suitable for resolving discrete cellular dynamics, and hybrid models couple both frameworks. Each modelling level involves an inverse correlation between computational efficiency and spatial resolution, with the choice depending on the study's aims and required level of detail.

Computationally efficient single-phase models treat blood as a homogeneous fluid, implicitly accounting for the CFL rather than simulating it directly. The CFL is either represented through parameterising the known haemodynamic consequences of the CFL such as plasma skimming [149], or by representing its mechanical effect as a wall-slip boundary condition [150]. The methodologies developed to account for the summarises in Table 1.2. A key limitation of these methods is their inability to simulate the 3D dynamic formation of the CFL itself.

To introduce heterogeneity in single-phase frameworks, a two-phase layer model from previous studies have been proposed which assuming an RBC-rich core is surrounded by a near-wall CFL (Fig. 1.19). The CFL thickness is treated as predefined input parameter to investigate its influence on flow dynamics [151]. Alternatively, the CFL

width is predicted as a calculated output to elucidate phenomena such as the Fahraeus and Fahraeus-Lindqvist effects [152-154]. A detailed summary of these modelling approaches and their principal findings is presented in Table 1.2. However, these models lack explicit modelling of RBC-plasma interactions, limiting their ability to simulate 3D dynamic phase behaviour.

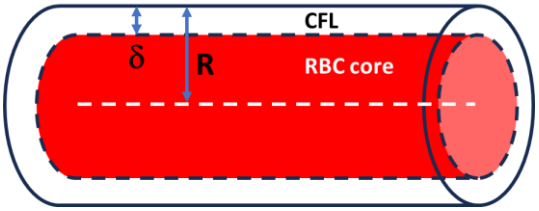

Figure 1.19: Schematic diagram of a two-phase flow layer. An RBC-rich core is surrounded by plasma-rich CFL layer. δ and R represent the CFL thickness and vessel radius, respectively [151-154].

More accurate two-phase flow models (Table 1.2) use multiphase methods that treat RBCs and plasma as separate, interpenetrating continua. These approaches solve the conservation equations for each phase and include terms to represent interfacial interactions. Achab and Iachacheene (2025) [155] employed the Volume of Fluid (VOF) method to track the interface between the RBC core and plasma. To improve accuracy, they applied a Piecewise Linear Interface Construction (PLIC) and calculated the surface tension using the continuous Surface Force model [156], integrating it as a source term in the momentum equation. This setup allowed initial CFL thickness ($R-R_0$) to be set at 7 μm for a vessel radius of 27.1 μm (Fig. 1.20A).

In another VOF study, Yadav et al. (2024) [157] modelled blood as a suspension of RBC particles dispersed in plasma by assigning a fixed haematocrit value and incorporating drag and lift forces to represent phase interactions. Their simulations showed a CFL formation in the centre of a confluence microchannel (Fig. 1.20B), an effect caused by the high shear rate near the apex which forces RBC to migrate away from this central region. Likewise, Valtchanov et al. (2025) [158] and Jafari et al. (2008) [159] used VOF modelling to treat plasma and cytoplasm as separate phases, integrating membrane force and deformation tensors in the momentum equation to

capture RBC deformation (Fig. 1.20C). Furthermore, Mendygarin et al. (2017) [160] simulated RBCs and platelets as dispersed particulate phases in plasma, with granular temperature driving migration away from the wall and creating a near-wall plasma region with nearly zero RBC volume fraction at one side, with the use of a three-phase EMP approach.

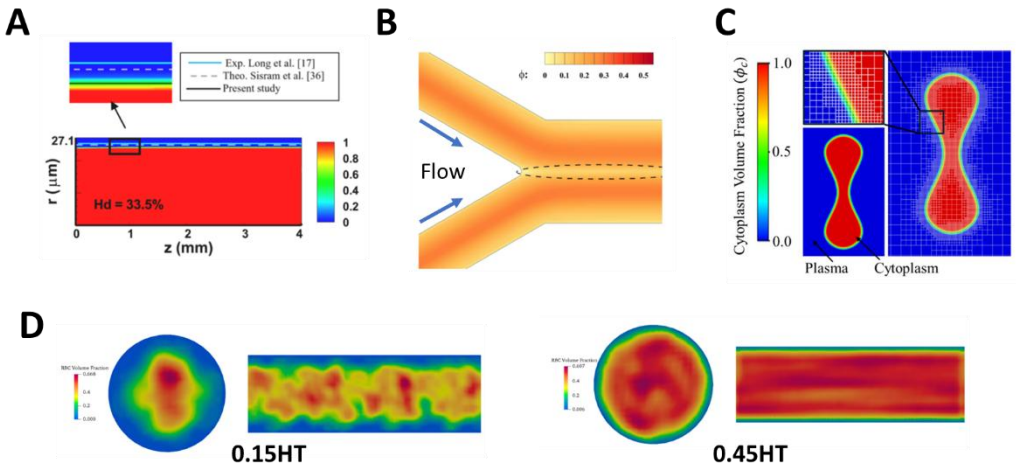

Figure 1.20: Examples of RBC-plasma interface simulations using the VOF method (A-C) and CFD-DEM model (D). (A) Achab and Iachacheene (2025) [155], (B) Yadav et al. (2024) [157], (C) Valtchanov et al. (2025) [158], and (D) Balachandran Nair et al. (2022) [83].

Hybrid methods are well-suited for simulating cellular-level dynamics by treating RBCs and plasma discretely. A Fluid-Structure Interaction (FSI) algorithm often combines the Lattice Boltzmann Method (LBM) for the plasma fluid and the Immersed Boundary Method (IBM) for the deformable structures. The RBCs elasticity is represented using models such as the Neo-Hookean model [161, 162], and oxygen transport can also be included [5]. The CFL, a key feature, is defined as the near-wall space with few RBCs, quantified by specific flux [5] or volume [161] thresholds (Table 1.3).

As provided in Table 1.4, Dissipative Particle Dynamics (DPD) is a fully particle-based mesoscopic method where particles represent atom clusters [163]. The models reveal that the CFL is a direct result of RBCs migrating across streamlines away from the vessel wall. This migration is driven by haemodynamic forces, specifically

repulsive cell-wall interactions and dispersive cell-cell interactions, as shown by Fedosov et al. (2010) [148] and Lykov et al. (2015) [164]. The thickness of the CFL is influenced by the feed haematocrit, the RBC deformability and the RBC aggregability. Higher haematocrit can promote the formation of compact rouleaux, which enhances the phase separation that creates the CFL. The DPD combined with LD-RBC (Linked-Disc RBC) model from Li et al. (2012) [165] demonstrates that CFL thickness depends on the haematocrit and cell properties. Furthermore, the SDPD-IBM (Smooth Dissipative Particle Dynamics-IBM) model from Ye et al. (2019) [4] links CFL formation to RBC migration driven by deformability and aggregation. Balachandran Nair et al. (2022) [83] used a resolved CFD-DEM (Discrete Phase Model) model with a reduced-order, deformable RBC to successfully simulate the formation of a CFL, finding its thickness depends on both the tube diameter and haematocrit, as visualised in Fig. 1.20D.

1.6.7 CFD approaches to the symmetric CFL formation

LBM–IBM simulations show that CFL development in straight microchannels occurs through RBC migration and subsequent reorganisation [3]. The characteristic recovery length required to achieve near-symmetric CFL typically spans 8–15D (150–300 μm) [3]. This recovery is strongly influenced by cellular properties: reduced deformability slightly shortens the distance, whereas lower haematocrit or increased aggregation significantly prolong it.

In contrast to straight channels, bifurcations and confluences introduce significant local disturbances to CFL structure. Downstream of a bifurcation, LBM–IBM simulations consistently show the development of an asymmetric CFL in daughter branches, becoming thinner near the inner wall and wider near the outer wall [5, 6, 166]. The inner wall is defined as the concave side of the bifurcation, situated within the branching angle between the daughter vessels, whereas the outer wall corresponds to the convex side, forming the outer curvature of the bifurcation. This asymmetry can persist for considerable distances, often greater than 8–10D and potentially exceeding 25D before symmetry is fully recovered, influenced by local haematocrit and flow rate [5, 6] (Table 1.5). Conversely, confluences induce a distinct central CFL just

downstream of the merging point, which is remarkably stable, persisting for up to 100 μm [166]. Notably, this central region accumulates microparticles or platelets, leading to an antimargination effect not observed at bifurcations.

Table 1.2: Continuum-based approaches for CFL studies.

Method & *Geometry*	**CFL treatment**	**Key findings**
Single-phase *Asymmetric network* [149]	**Input:** implicitly set via plasma skimming **Output:** CFL-related phenomena (haematocrit)	Accurately models haematocrit distribution using CFL-dependent plasma skimming.
Single-phase *10-75 μm tube* [150]	**Input:** implicitly set via wall-slip condition **Output:** CFL-related phenomena (WSS)	The lubricating effect of the CFL represented by a wall-slip condition in a single-phase model.
Two-phase layer (Newtonian core & CFL) *20–300 μm tube* [152]	**Input:** treated as unknown to within the viscosity and haematocrit **Output:** CFL thickness	Effective viscosity in the CFL is higher than pure plasma due to interface energy dissipation.
Two-phase layer (Power-law core + plasma CFL) *30–100 μm tube* [153]	**Input:** treated as unknown to within the viscosity data **Output:** CFL thickness	RBC aggregation increases the CFL thickness, especially at low shear rate.
Two-phase layer (Krieger-Dougherty core + plasma CFL) *5-75 μm tube* [154]	**Input:** treated as unknown by calibrating against empirical data **Output:** CFL thickness	A non-uniform haematocrit profile withing the core region is crucial for predict the CFL thickness.
Three-phase layer (Herschel-Bulkley core + CFL + porous wall) *Axisymmetric tube* [151]	**Input:** explicitly set as a fixed CFL thickness; **Output:** CFL-related phenomena (flow rate, resistance, etc.)	Modelling the vessel wall as a porous layer (glycocalyx) outside the CFL significantly increases the overall flow
VOF *Y-bifurcation* [159]	**Not an input** **Output:** CFL-related phenomena (qualitative visualisation of cell distribution)	VOF can simulate individual RBC.

VOF *25-330 µm tubes* [157]	**Not an input** (an emergent property from shear-lift force) **Output:** CFL thickness	Geometric constrictions can cause a fivefold enhancement of the CFL thickness downstream.
VOF (Herchel-Bulkley core + plasma) *27.1 µm tube* [155]	**Input:** explicitly set as CFL thickness **Output:** dynamic CFL thickness	An increase in haematocrit or blood yield stress causes the CFL thickness to decrease.
EMP for RBC, plasma, platelets phases *217 µm tube* [160]	**Not an input** (an emergent property of the multiphase simulation) **Output:** CFL formation (spatial distribution)	The model can predict the CFL formation and the platelets margination to the near-wall region.

Table 1.3: Hybrid approaches for CFL studies.

Method & *Geometry*	**CFL treatment**	**Key findings**
Hybrid		
FSI with VOF *20 µm RBC Couette* [158]	**Not an input** (an emergent property from cell collisions) **Output:** not focus on CFL	Intercellular collisions, the underlying cause of the CFL, are a dominant mechanism for RBC membrane damage.
IB-LBM *96 µm vascular network* [73]	**Not an input** (an emergent property from shear induced migration) **Output:** CFL thickness	CFL asymmetry develops after a bifurcation.
IB–LBM *Straight channel* [162]	**Not an input** (an emergent property of the simulation) **Output:** qualitative visualisation of CFL formation	RBC aggregation enhances CFL formation, while rigid (less deformable) cells do not form a clear CFL.
IB–LBM *9.97 µm Straight & bifurcation* [161]	**Not an input** (an emergent property from hydrodynamic forces) **Output:** CFL thickness	A thicker CFL in the parent vessel leads to more pronounced phase separation.
LBM-FEM-IBM *Tumour network* [5]	**Not an input** (asymmetric recovery after bifurcation) **Output:** CFL thickness	Abnormally short vessels in tumours prevent CFL symmetry, causing biased haematocrit splitting.

Table 1.4: Particle-based approaches for CFL studies.

Method & *Geometry*	**CFL treatment**	**Key findings**
DPD with a multi-scale RBC model *10–40 μm tubes* [148]	**Not an input** (an emergent property from the simulation) **Output:** CFL thickness	The model's CFL predictions agree well with *in vitro* data.
DPD with a multi-scale RBC model *10 μm Y-bifurcation* [164]	**Input:** a pre-formed CFL **Output:** CFL-related Phenomena (plasma skimming and cell recovery)	A new open boundary condition successfully generates a flow with a pre-formed CFL, enabling accurate simulation of plasma skimming.
DPD with a low-dimensional RBC model *40 μm Y-bifurcation* [165]	**Not an input** (an emergent property arising the simulation) **Output:** CFL thickness	A thicker CFL, resulting from a lower feed haematocrit, leads to more efficient plasma skimming.
SDPD-IBM *10 μm multi-bifurcation network* [4]	**Not an input** (an emergent property of the simulation) **Output:** CFL related phenomena (RBC flux distribution)	Lower cell deformability and stronger aggregation both enhance phase separation by altering the cell distribution that forms the CFL.
CFD-DEM *Straight & constricted tubes* [83]	**Not an input** (an emergent property of the simulation) **Output:** CFL thickness	The model accurately simulates the enhancement of CFL thickness downstream of a geometric constriction

Table 1.5: Computational approaches for CFL symmetry.

Method & *Geometry*	**CFL thickness**	**Key findings**
2D IB-LBM *20-24 μm straight* [3]	Nominal CFL thickness based on 10% cumulative frequency of wall-membrane distance	CFL symmetry recovery at 150-300 μm (8-15D)
2D IB-LBM *10 μm bifurcation* [161]	<2.5% RBC volume threshold from lower wall and >97.5% from upper wall	CFL thickness depends on phase separation,
LBM-FEM-IBM *33 μm network* [5]	Haematocrit threshold near vessel walls	CFL symmetry recovery at 25D
2D LBM-IBM *15 μm bifurcation* [6]	Distance from wall to cell-plasma interface (from simulation grid)	CFL symmetry recovery at >8D
3D LBM-IBM *32 μm bifurcation* *32 μm confluence* [166]	CFL zone (zero or low RBC density) near the wall	CFL remains asymmetric within simulation domain (50 μm) in bifurcation, while CFL symmetry recovers ~ 100 μm in confluence

1.5.7 Eulerian Multiphase Method (EMP)

The Eulerian Multiphase Method is part of a family of multiphase modelling approaches used in CFD to simulate flows involving multiple interacting phases (e.g. liquid-solid, gas-liquid, etc.). EMP and its related models fall under the broader Eulerian-Eulerian framework, where each phase is treated as a continuous field. A key characteristic of multiphase flows is that they consist of phases and interfaces. A phase is a distinct physical state, such as gas, liquid, or solid, defined by properties such as density, size or composition, and can coexist with other phases within the same domain. The interface is the boundary between distinct phases where fluid properties change abruptly and mass, momentum, and heat are exchanged, making simulations more complex.

1.5.7.1 Fundamental numerical equations in EMP

The EMP model, as utilised in Simcenter STAR-CCM+, treats each phase as an interpenetrating continuum and governed by its own set of conservation equations, solved simultaneously within a fixed spatial grid, also known as the Eulerian frame. While all phases are coupled through a common pressure field, the Eulerian averaging [167-169] of the transport equations introduces further interactions that consequently require closure models for phenomena such as drag, lift force an interphase heat transfer. Rather than tracking individual particles or interfaces, the flow is observed at fixed spatial locations. Each phase is represented using a volume fraction α_i, which denotes the share of the control volume occupied by the phase i. The total volume *Vi* of a phase is given by:

$$V_i = \int_V \ \alpha_i dV \tag{1.26}$$

where V represents volume. To ensure physical consistency, the sum of volume fractions across all n phases must satisfy:

$$\sum_{i=1}^{n} \alpha_i = 1 \tag{1.27}$$

The conservation of mass for a given phase i accounts for convective transport. In compressible condition, this is described by the continuity equation [170]:

$$\rho_i \left(\frac{\partial}{\partial t} \int_V \ \alpha_i \, dV + \oint_A \ \alpha_i \boldsymbol{v}_i \cdot d\boldsymbol{a} \right) = 0 \tag{1.28}$$

Here, ρ_i and $\boldsymbol{v}_i$ are the density and the velocity of phase i. Similarly, the momentum conservation equation for each phase in incompressible includes contributions from pressure gradients [170]:

$$\rho_i \left(\frac{\partial}{\partial t} \int_V \ \alpha_i \boldsymbol{v}_i \, dV + \oint_A \ \alpha_i \boldsymbol{v}_i \otimes \boldsymbol{v}_i \cdot d\boldsymbol{a} \right) = \int_V \ \alpha_i \nabla p \, dV + \oint_A \ \alpha_i \mathbf{T}_i d\boldsymbol{a} + \int_V \ M_i \, dV \tag{1.29}$$

In this expression, ∇p is the pressure graidient (assumed equal for all phases), $\mathbf{T}_i$ is viscous stress tensor and $\boldsymbol{M}_i$ is the interphase momentum transfer per unit volume of phase i. In laminar EMP models, the solid phase is treated as a fluid-like continuum. The pseudo-solid viscosity is a non-physical constant that serves as the laminar viscosity for this continuous solid phase, enabling the calculation of the viscous stress term in the momentum equation. This represents an effective laminar property rather

than a true molecular rather than a true molecular viscosity or granular model [171].

1.5.7.2 Phase Interaction Topology

EMP is capable of modelling both dispersed-continuous and continuous-continuous phase interactions. Dispersed-continuous flow models include a dispersed phase (such as bubbles or particles) distributed within a continuous phase, in contrast to continuous-continuous flow, where two phases are modelled as distinct, continuous bodies separated by a clear interface. In this study, the dispersed-continuous flow model is employed to represent blood as RBC particles suspended in the plasma, and thus it is presented here in more detail.

In the dispersed–continuous model, the interaction area density (A_{cd}) between the continuous and dispersed phases quantifies the interfacial area available for momentum, heat and mass transfer per unit volume. Since the EMP methods do not explicitly track interfaces, the A_{cd} is introduced as a closure term to represent total particle surface area available for these transfer processes. As shown in Fig. 1.21, the total surface area for N spherical particle is $n\pi d^2$, or equivalently $6\alpha_d V_{total}$ /d, giving an interface area density of $A_{cd} = 6\alpha_d/d$, where α_d is the dispersed-phase volume fraction and d is the particle diameter. However, this spherical model incorrectly predicts maximum interaction at $\alpha_d = 1$, when no continuous phase exists. To correct this, the Symmetric Interaction Area model includes the continuous-phase volume fraction α_c, yielding $A_{cd} = 6\alpha_d\alpha_c/d$, which accurately predicts zero interaction when either phase is absent.

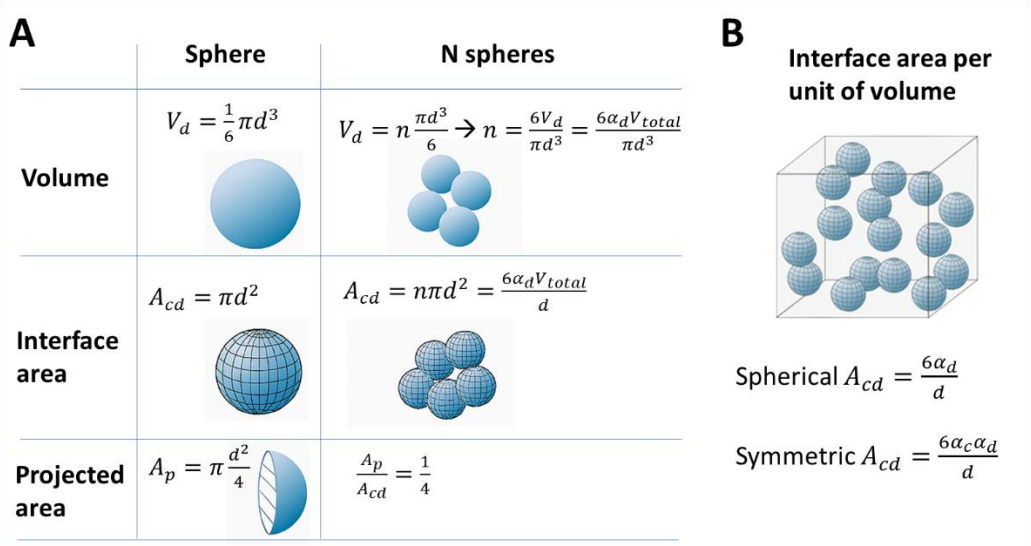

Figure 1.21: Fundamental geometrical equations used in the EMP method [170]. (A) Volume (V_d), interface area (A_s), and projected area (A_p) of sphere(s) and (B) interface area per unit of volume. d is the diameter of the spherical particle, *n* is the number of spheres, V_{total} is the total volume of spheres, and A_{cd} is the interaction area density, which representing interface area per unit of volume.

1.5.7.3 Momentum transfer

The momentum transfer is a crucial term in the EMP formulation that accounts for how phases exert forces on each other. These forces are modelled using various sub-models, with drag, virtual mass, lift, turbulent dispersion and wall lubrication forces.

Drag force (F_D) is the resistance a particle experiences as it moves through a fluid. For a single spherical particle, it is a function of the drag coefficient (C_D), the fluid density (ρ_c), the projected area (A_p), and the relative velocity ($\boldsymbol{u}_r = \boldsymbol{u}_i - \boldsymbol{u}_j$), where u_i, u_j the velocity of the i, j phase.

For an EMP simulation, the force on a single particle is scaled up to a 'total drag force per unit volume'. This is the drag force term that is added to the momentum equations in the solver. This is achieved by replacing the projected area with the spherical $A_{cd} = 6\alpha_d/d$. From Eq. 1.30, this is then expanded using the definition of A_{cd} to:

$$F_D = \frac{1}{8} C_D \rho_c \left(\frac{6\alpha_d}{d}\right) |\boldsymbol{u}_r| \boldsymbol{u}_r \tag{1.30}$$

This simplified equation [172] is the core model for drag on multiple particles in a dispersed flow. The drag coefficient is not a constant. It is a function of the particle Reynolds number (Re_d). In the very slow, viscous flows (Re_d<0.2), the drag coefficient is given by $C_D=24/Re_d$ [121].

The lift force (F_L) is a force that acts perpendicular to the relative motion between the phases. While drag force pushes a particle in the direction of the flow, the lift force pushes it sideways, enforcing movement perpendicular to the relative velocity [172].

$$F_L = C_L \alpha_d \rho_c [\boldsymbol{u}_r \times (\nabla \times \boldsymbol{u}_c)] \tag{1.31}$$

where C_L and $\nabla \times \boldsymbol{u}_c$ are the lift coefficient (a constant) and the vorticity of the continuous phase velocity, respectively. The lift force is particularly important in non-uniform or rotational flow fields with a strong velocity gradient, such as in flow through small diameters. It becomes especially significant near walls, where the velocity gradient is highest, and is proportional to the continuous phase density.

Virtual mass force (F_{VM}) is an additional resistance experienced by a dispersed particle when it accelerates or decelerates relative to the continuous phase. It is a force that arises from the need to accelerate the surrounding fluid.

$$F_{VM} = C_{VM} \alpha_d \rho_c (\boldsymbol{a}_c - \boldsymbol{a}_d) \tag{1.32}$$

where C_{VM} and $\boldsymbol{a}_c$, $\boldsymbol{a}_d$ are the virtual mass coefficient and the acceleration of continuous, dispersed phases, respectively [172].

1.5.8 SIMPLE algorithm

The SIMPLE (Semi-Implicit Method for Pressure-Linked Equations) algorithm is an iterative method used to solve the Navier–Stokes equations, where pressure and velocity are strongly coupled. Since there is no explicit pressure equation, SIMPLE uses a pressure correction strategy to enforce the continuity equation. The solver begins by guessing a pressure field, solving the momentum equations to estimate velocity, and then generating a pressure correction equation. This correction updates both the pressure and the velocity fields until convergence is achieved. The process repeats until the flow field satisfies the mass and momentum conservation throughout

the domain, making SIMPLE one of the standard approaches in many CFD solvers for steady-state incompressible flows [173].

1.5.9 Boundary conditions

1.5.9.1 Pressure outlet

A pressure outlet boundary condition specifies the static pressure of the environment into which the fluid exits, such as atmospheric pressure. As implemented in Simcenter STAR-CCM+, velocity and other scalar quantities are extrapolated from the interior of the solution domain,, while the static pressure is maintained at the specified working pressure [174]. This condition naturally allows for backflow if the interior pressure drops below the set outlet pressure. Pressure outlets are ideal when external pressure is known, making them suitable for vents, open-ended pipes, or exhaust. However, if the specified pressure does not reflect real conditions, it may lead to inaccuracies, especially in complex or compressible flows [174].

1.5.9.2 Flow split outlet

A split or mass-flow outlet specifies the mass flow rate or fraction of the total flow leaving the domain through each outlet. Unlike a pressure outlet, the solver adjusts the outlet pressure to achieve the specified mass flow distribution, while velocities are corrected to match the target flow rate. This boundary condition is useful when the flow division is known but downstream pressures are unknown, such as in manifolds or distribution networks. It assumes no backflow, and if backflow occurs, it indicates setup issues or non-physical flow conditions. While it offers precise control over outlet distribution, unrealistic split ratios can produce unstable or non-physical pressure fields [174].

1.5.9.3 Velocity inlet

A velocity inlet boundary sets the magnitude and direction of the fluid velocity entering the domain, marking the mass flow rate at the inlet. The pressure at the inlet is not fixed; instead, the solver calculates it as part of the solution to balance the specified inflow with internal flow and outlet conditions. Velocity inlets are widely used for internal flows and allow for detailed control of the inlet profiles, such as uniform, parabolic, or user-defined velocity distributions. They are often coupled with pressure outlets or flow split outlets to establish clear flow-driving conditions.

When a velocity inlet is paired with a pressure outlet, the simulation specifies the inflow speed and environmental outlet pressure. The solver computes the interior pressure field so that the continuity and momentum equations are satisfied, with the outlet velocity adjusting naturally based on the pressure differences and internal losses. Conversely, when a velocity inlet is coupled with a flow split or mass-flow outlet, the inflow is fixed, and the solver modifies the outlet pressures to achieve the specified flow distribution across the exits. This setup offers precise control of flow splits but requires careful configuration, as unrealistic split ratios can lead to excessive pressure adjustments or numerical instability [174].

1.6 Thesis aim and overview

1.6.1 Research questions and aims

A cornerstone of this research is the development of a novel multi-phase, multi-component continuum-based model using the Eulerian Multiphase (EMP) method, which treats blood as a suspension of RBCs in plasma. The primary aims and guiding research questions are outlined as follows:

- **Model development.** This objective is to answer three key questions. Firstly, can a continuum-based computational model be developed to sufficiently capture the disruption of the cell-free layer and its recovery downstream of a vessel bifurcation with high accuracy? Secondly, do the simulation results align with experimental observations? Thirdly, what are the specific

haemodynamic forces and mechanisms that explain the re-establishment of CFL? (This is addressed in Chapter 2).

- **Assessment of rheological behaviour.** The aim is to assess the multi-phase, multi-component flow model by comparing its predicted rheological behaviour with established findings. This addresses the question of whether the model can successfully capture the fundamental non-Newtonian, shear-thinning nature and its non-linear viscosity-haematocrit relationship (Chapter 2).

- **Parametric investigation.** This objective aims to test the model's robustness by assessing its ability to predict established microhaemodynamic phenomena under various simulated conditions. Specifically, the research explores how key physiological factors, such as the feeding haematocrit, inflow rate, biased outflow, and complex geometries including asymmetric or successive bifurcations, affect CFL dynamics and haematocrit partitioning (such as the Zweifach-Fung effect) (Chapter 3).

- **Application to realistic geometries**. This objective is to bridge the gap between idealised and physiological geometries. It involves investigating the haemodynamics in anatomically accurate vessel reconstructions for 20-µm testicular bifurcations to understand how phenomena such as the CFL formation and plasma skimming manifest in realistic, non-planar and tortuous microvessels (Chapter 4).

- **Network-Scale Analysis.** This investigation aims to answer: how do morphological differences in control (89 µm) versus atrophic testicular arterial networks (48 µm) translate into functional deficits in perfusion and resistance? Due to meshing strategy for the two-phase model limitations in the complex control, and a single-phase model was used to obtain preliminary haemodynamic comparisons. (Chapter 5)

- **Blood flow in the pulmonary arteries.** This study aims to establish a comprehensive haemodynamic baseline for blood flow in macro-scale pulmonary bifurcations. This work addresses how analysing this large-scale system provides the foundational data for future studies to bridge the gap

between the distinct haemodynamic principles governing the macro- and microcirculation (Chapter 6).

1.6.2 Overview

This thesis began in Chapter 1 by establishing the clinical motivation for studying microvascular haemodynamics and introducing the relevant computational tools, providing a conceptual basis for particulate blood behaviour. Although not included in the multi-phase multi-component model, cell behaviours, including aggregation and deformation, were provided in Chapter 1 to provide the background context of blood flow as a particulate flow. The central work and a key novelty of this thesis, detailed in Chapter 2, is the development of a multi-phase, multi-component continuum model to investigate the crucial phenomenon of CFL recovery downstream of a 20-μm bifurcation. A fundamental rheological assessment of the model is also provided in Chapter 2. This section details the quantitative validation using CFL and haematocrit data, the qualitative characterisation of the model's non-Newtonian behaviour and the dependency of viscosity on haematocrit. Chapters 3 and 4 present a series of model applications: parametric studies in 20-μm idealised and multi-phase, multi-component flow simulations in realistic testicular microvessels with diameter of 20 μm. Chapter 5 presents an analysis of a large, complex arterial networks in testis control (89 μm) and atrophy (48 μm) using a single-phase model to obtain preliminary haemodynamic comparisons due mesh limitation on the control network. Chapter 6 extends the analysis to the pulmonary arteries bifurcation (approximately 2 cm in diameter), establishing the characteristic haemodynamics of arterial flow in larger vessels. Chapter 7 collects the findings from all preceding chapters, providing an integrated conclusion on the importance of CFL and links the microvascular modelling with the large-scale arterial analyses.

Chapter 2

Multi-phase, multi-component flow model of the cell-free layer dynamics in arteriolar microvessels

2.1 Introduction

Pathological changes in the microvasculature reduce blood and oxygen delivery, resulting in ischemia and potentially critical organ damage. Understanding microvascular haemodynamics is therefore critical for identifying the underlying mechanisms of disease progression and improving therapeutic strategies. A key determinant of flow behaviour at the microscale is the heterogeneous distribution of red blood cells (RBCs) or haematocrit, influenced by the branching architecture of microvascular networks and the cell-free layer (CFL) [10, 43, 104]. This heterogeneity is the result of unequal partitioning of the CFL and RBCs through the network, that is through successive microvascular bifurcations, where phase separation (plasma skimming [175, 176], or the Zweifach-Fung effect [177, 178]) is known to take place (detailed in section 1.4.2.2). Under extreme conditions, a daughter branch with very low fractional flow may receive only plasma and no cells from the parent vessel's CFL [73, 176], whereas all the RBCs are diverted to higher-flow branches.

RBCs tend to migrate towards the centre of the vessel, thereby increasing the central accumulation of RBCs while allowing the development of a CFL between the lateral migration of RBC-rich core and the vessel walls [100, 179, 180]. The CFL is important as it governs the radial distribution of RBCs, which in turn dictates the local haematocrit within microvessels, consequently, the apparent viscosity of blood. Due to a velocity disparity between the CFL and the RBC-rich core layer, the discharge haematocrit (HD), that is, the concentration of RBCs in a bulk blood sample, is typically higher than the tube haematocrit (HT), which represents the average concentration of individual RBCs within the vessel volume [39] (described in section 1.4.1.8). Moreover, the lower viscosity in the CFL in comparison with the RBC-rich

core acts as a lubrication layer, reducing the resistance of blood flow and modulating wall shear stress (WSS) by lowering the near-wall viscosity [109, 181].

At the apex of a bifurcation, the RBC-rich core is disturbed due to the impinging flow on the wall (stagnation point), leading to flow split and the local disappearance of the CFL adjacent to the inner wall (the concave side of the branching angle) [10, 182]. The outer wall, by comparison, is the convex side on the outside of the bifurcation. This cell-depleted layer is expected to be progressively re-established at a long distance downstream of the bifurcation [3, 6, 90]. Although successive bifurcations in physiological networks prevent full CFL recovery due to short inter-branch distances, examining its re-establishment downstream of a single bifurcation remains essential for understanding local haemodynamics and their implications for microvascular function and disease.

Computational particle-based and hybrid methods have suggested that bifurcations disturb the RBC core, causing asymmetric CFL and transient haematocrit profiles [73, 161, 166]. Studies using the immersed boundary lattice Boltzmann method show that the CFL gradually reforms further downstream from the bifurcation and returns to a symmetric pattern at a long distance (>8-25D) [3, 5, 6], as detailed in Table 1.5 (section 1.6.7). *In vivo* studies reveal that asymmetry persisting for at least 6D (diameter from entrance) in ~50 μm arterioles with estimating full recovery at ~8-11D [90]. When the distance between successive bifurcations is short, these asymmetries may persist without a full CFL recovery [5, 182]. While particle-based methods, such as those tracking individual RBCs, can capture these effects with high fidelity, they are computationally expensive and time-consuming. This raises the argument that a continuum-based numerical method could be utilised instead, at a reasonable computational cost. In this study, we develop a novel multiphase flow model that captures the three-dimensional haemodynamics in arteriolar bifurcations, providing a mechanistic explanation for the CFL development and downstream recovery. To accomplish this, we developed a multi-phase, multi-component continuum-based model using the Eulerian Multiphase (EMP) method, which treats RBCs as a dispersed particulate phase suspended in a plasma fluid phase (hereinafter referred to as BRC-rich core), while the cell-depleted layer of plasma is referred to as CFL. The multi-

phase, multi-component flow model was validated through both quantitative and qualitative criteria to confirm its ability to accurately describe the blood behaviour in arteriolar microvessels.

2.2 Materials and methods

2.2.1 Arteriolar bifurcation model

A microvessel with a diameter (d0) of 20 μm (0^{th} generation parent vessel, i=0), which represents a typical diameter for studying blood flow in arterioles [91, 183, 184], was designed to bifurcate symmetrically in a Y-junction into two daughter vessels (d1, d2) with equal diameters of 15.9 μm (1^{st} generation, i=1), according to an extension of Murray's law [185], used in model to generate microvascular geometry [138].

$$\mathrm{d0} = \mathrm{d1}^3 + \mathrm{d2}^3 \tag{2.1}$$

For such a bifurcation, the angle was determined by the relation between the vessel diameters [149, 186], shown in Eq. 2.2.

$$\cos\psi_1 = \frac{d_0^4+d_1^4-d_2^4}{2d_0^2d_1^2}, \quad \cos\psi_2 = \frac{d_0^4+d_2^4-d_2^4}{2d_0^2d_2^2} \tag{2.2}$$

where ψ_1 and ψ_2 are the angles between the parent vessel's central axis and each respective daughter branch [149]. For the symmetric case, the Eq. 2.2 yields $\psi_1 = \psi_2 \approx$ 37.5°; thus, the angle between the two daughter branches is 75°.

The length for d0 and d1 was in a range of 100 and 380, which are within the physiological length [187-189]. This geometry represents the features of arteriolar architecture relevant to flow regulation, as demonstrated in networking-level haemodynamics [91, 183, 184, 187-189].

2.2.2 Mesh analysis

For the mesh, a hybrid mesh strategy [190, 191] was followed, combining polyhedral cells in the centre and a large total thickness of prismatic layers to resolve the steep near-wall gradients in velocity and the volume fraction within the viscous sublayer, especially in a curved geometry such as the bifurcation [192]. This discretisation (Fig. 2.1A) was generated using Star-ccm+ (Siemens). In order to capture the viscous effects, the height of the first prismatic layer (Δy_1) was specified at a distance of ~0.005d0 away from the wall, determined by the relation $\Delta y_1 = \mu y^+ / \left(\sqrt{wss}/\rho\right)$, where ρ, wss and μ assumed as 1.050 g/cm^3, 17 dyn/cm^2 and 4.0 mPa-s [193], respectively. The dimensionless value $y^+$is defined by the friction velocity ($U_T = \sqrt{wss/\rho,}$), where $wss = \frac{1}{2} C_f \rho {u_{bulk}}^2$ with $u_{bulk} = 1\ mm/s$ the mean velocity and

$$C_f = 2 * \left[\left(\frac{8}{Re}\right)^{12} + \left(\left(2.457 \ln\left(\left(\frac{Re}{7}\right)^{0.9}\right)\right)^{16} + \left(\frac{37530}{Re}\right)^{16} \right)^{-1.5} \right]^{1/12}$$

the skin friction coefficient, characterising the thickness of the viscous sublayer due to low Re of the flow [140, 141]. The prismatic boundary layer mesh was generated using with 20 layers a number which resulted from specifying the $\Delta y_1$and the prismatic layer total thickness. To ensure reproducibility, these two constraints were linked using an optimised growth ratio selected from the 1.1 to 1.3 range validated by our mesh independence study (Appendix A.1).

To enable an initial annulus symmetric CFL formation in the parent vessel, the total thickness of the prismatic layer was designed to exceed the assumed initial CFL (δ_{CFL}) thickness by about two thirds (Fig. 2.1B), as the numerical solution of the final CFL thickness was influenced by the inlet velocity and the haematocrit and cannot be precisely predicted. A series of simulations in this thesis were performed with a fixed prismatic layer thickness of 5 μm. According to a grid independence analysis, based on the maximum velocity upstream of the bifurcation, a mesh of around 0.5 million elements for the symmetric Y-junction was found to be sufficient for the flow regimes (Appendix A.1).

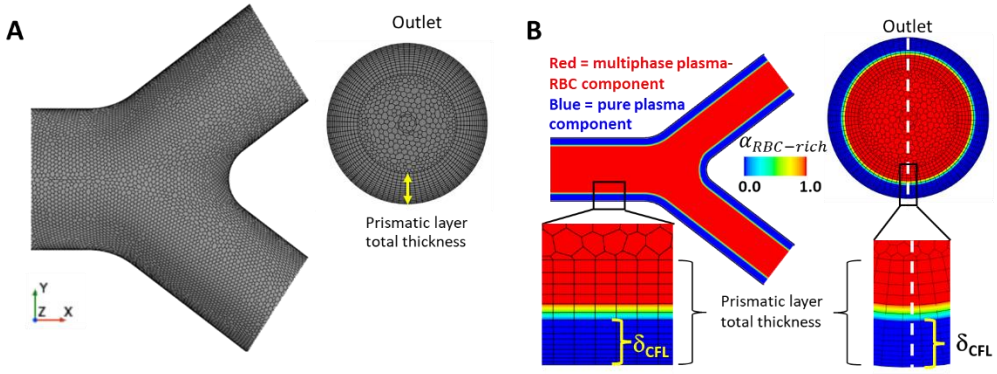

Figure 2.1: (A) The polyhedral and prismatic mesh at the junction and the outlet. (B) The initialisation of the multi-phase, multi-component model, consisting of the RBC-plasma (red) and pure plasma (blue) components. The CFL thickness (δ_{CFL}) is determined on the reference line (dash white) with volume fraction of plasma-RBC component ($\alpha_{RBC-rich}$) <0.05.

2.2.3 Eulerian Multiphase Approach

The EMP approach in the STAR-CCM+ software was employed to model a particulate RBC-rich core phase dispersed in a fluidic plasma phase. The progressive reduction in pulsatility index from proximal to distal cerebral arteries suggests that arterioles are subjected to significantly attenuated pulsatile forces [194]. With low Reynolds (Re ≈ 0.001), the flow is dominated by viscous forces, indicating a highly laminar and stable regime with negligible pulsatile nature. The conservation of mass and momentum equations for the multiphase plasma-RBC component and pure plasma component were solved separately. Under laminar and incompressible conditions, each component (α_i) shared the same pressure and was governed by:

$$\frac{\partial}{\partial t}\alpha_i\rho_i + \nabla\cdot(\alpha_i\rho_i\boldsymbol{u}_i) = 0 \tag{2.3}$$

$$\frac{\partial}{\partial t}\alpha_i\rho_i u_i + \nabla\cdot(\alpha_i\rho_i u_i\boldsymbol{u}_i) = -\alpha_i\nabla p + M_k \tag{2.4}$$

where M is the interphase momentum transfer, consisting of drag, lift and virtual mass forces.

The plasma phase was modelled as a Newtonian fluid with a viscosity of 1.3 mPa-s [195] and a density of 1.025 g/cm^3 [196], as shown in Table 2.1. Meanwhile, the pseudo-viscosity (section 1.5.7.1) and density of the multiphase plasma-RBC component were assumed as 3.45 mPa-s [197] and 1.125 g/cm^3 [196], respectively, in which solid RBCs with a diameter of 8 μm [198] are dispersed in plasma, with the Symmetric Interaction Area model (Section 1.5.7.2).

Table 2.1: Physical properties and boundary conditions for RBC-rich and plasma phases**.**

Conditions	Abbreviation	Unit	Value
RBC-rich phase			
Inlet velocity	$u_{RBC-rich}$	mm/s	1.2
Viscosity	$\mu_{RBC-rich}$	mPa-s	3.45
Density	$\rho_{RBC-rich}$	g/cm^3	1.125
Size of RBC phase		μm	8
Volume fraction	$\alpha_{RBC-rich}$		Eq. 2.5
Plasma phase			
Inlet velocity	u_{plasma}	mm/s	0.8
Viscosity	μ_{plasma}	mPa-s	1.3
Density	ρ_{plasma}	g/cm^3	1.025
Volume fraction	α_{plasma}		Eq. 2.6
Outlet pressure		mmHg	50
initial CFL thickness	initial δ_{CFL}	μm	1.8

For numerical initialisation, the multiphase configuration was assumed having a central multiphase plasma-RBC component surrounded by a pure plasma component, forming an annulus (Fig. 2.1B), throughout the bifurcation. This initialisation ensures that the upstream flow is nearly fully developed, enabling smooth progression through the bifurcation and downstream regions while avoiding the computational cost of generating phase separation from a completely mixed starting condition. As shown in Fig. 2.1B, the initial CFL thickness δ_{CFL} was defined by the wall distance function, which represents the distance from a cell centroid to the nearest wall face with a non-slip boundary condition. To achieve ~45% discharge haematocrit for diameter of 20 μm, the initial δ_{CFL} was assumed 1.8 μm, which is within physiological ranges [199].

The initial volume fraction of the multiphase plasma-RBC component and the pure plasma component were then computed as follows:

$$\alpha_{plasma} = \begin{cases} 1, & \text{if wall}_{\text{distance}} \leq \text{initial } \delta_{\text{CFL}} \\ 0, & \text{otherwise} \end{cases} \quad (2.5)$$

$$\alpha_{RBC-rich} = 1 - \alpha_{plasma} \quad (2.6)$$

where α_{plasma} is volume fraction of plasma phase and $\alpha_{RBC-rich}$ is volume fraction of RBC-rich core phase

This component-separated profile was prescribed in the global initial conditions and at the inlet and outlet boundaries to ensure consistency phase distribution across the computational domain. The initial velocities of the RBC-rich ($u_{RBC-rich}$) and plasma (u_{plasma}) phases were established using mixture velocity relation:

$$u_{bulk} = \alpha_{RBC-rich} u_{RBC-rich} + \alpha_{plasma} u_{plasma} \quad (2.7)$$

The velocity of RBC-rich and plasma phases were therefore assigned ~1.2 mm/s and then calculated ~0.8 mm/s, respectively, resulting in a blood velocity (u_{bulk}) of 1 mm/s, as it aligns with values reported for arterioles of 20 μm diameter in previous studies [22, 91, 183, 184]. This approach is essential for numerical stability because the interphase force is highly sensitive to velocity difference (relative velocity) between two components (Eq. 2.8 & 2.10). Introducing a small, non-zero slip avoids the instability of zero-slip conditions and the unphysical drag spikes caused by large velocity differences [200].

The initial velocity was specified as components of [$u_{RBC-rich}$, 0, 0] and [u_{plasma}, 0, 0]. The initial pressure and outlet pressure boundaries were assumed 50 mmHg (6666 Pa), according to physiological values in arterioles [51]. These initial and boundary condition setups were part of the new multi-phase, multi-component model proposed here to allow capturing the development of the CFL in a bifurcating arteriolar microvessel.

The inter-phase drag force F_D acting on the dispersed RBC-rich core due to the drag

of the plasma was implemented as:

$$F_D = \frac{1}{2} C_D \rho_{plasma} A_p |u_r| u_r \tag{2.8}$$

$$A_p = \pi \frac{d_{RBC}^2}{4} \; ; \quad C_D = \frac{24}{Re_d} \; ; Re_d = \frac{\rho_{plasma} \cdot |u_r| \cdot d_{RBC}}{\mu_{plasma}} \tag{2.9}$$

where C_D is the drag coefficient in Stokes flow regime (Re <<1) [201], A_p is the projected area of the RBC particles, u_r is the slip velocity ($u_{RBC-rich} - u_{plasma}$), and Re_d is the RBC particle Reynold number. The drag force was scaled with a volume fraction exponent of -9.3 and a maximum packing at 0.66 [202], following the Richardson and Zaki correlation. This correction account for the increased drag caused by particle hindering, where densely packed particles increase resistance to flow. As fluid volume decreases, the drag force rises sharply, simulating the effect of particles becoming tightly packed [200]. When the velocity of the continuous plasma phase varies spatially, the lift force acts perpendicular to the RBC-rich core motion relative to the fluid plasma:

$$F_L = C_{L,eff} \alpha_{RBC-rich} \rho_{plasma} \left[u_r \times \left(\nabla \times u_{plasma} \right) \right] \tag{2.10}$$

where $\nabla \times u_{plasma}$ represents the vorticity of the continuous plasma component. The effective lift coefficient $C_{L,eff}$ is calculated from $C_{L,1} \alpha_{plasma} f_l$, where $C_{L,1}$is -100 and f_l is lift correction. The f_l serves as dimensionless scaling coefficient and is approximated from wall induced lift force [203]:

$$C_{L,2} \cdot \rho_{RBC} \cdot |u_r|^2 \cdot \frac{d_{RBC}^4}{D^2}, \text{where } \mathrm{C_{L,2}} \text{ is } 0.25 \tag{2.11}$$

The virtual mass force, resulting from the relative acceleration between phases ($\boldsymbol{a_j} - \boldsymbol{a_i}$), is incorporated using spherical particle method [204] to model interphase dynamic effectively. This force described by:

$$F_{ij}^{VM} = C_{VM} \rho_{plasma} \alpha_{RBC-rich} \left(\boldsymbol{a_j} - \boldsymbol{a_i} \right) \tag{2.12}$$

$$C_{VM} = \left[\left(C_{VM,sphere} \right)^{-2} + C_{VM,max} \left(\alpha_{plasma}, \gamma_{min} \right)^{-2} \right]^{-1/2} \tag{2.13}$$

starting from the inviscid value $C_{VM,sphere}$=0.5 [205] and using a free stream minimum fraction (γ_{min}) of 0.45. The choice of 0.45 emerged through preliminary sensitivity analyses during the initial stage of the model development, ensuring numerical stability.

To ensure numerical stability and prevent non-physical oscillations, first-order convection schemes for velocity and volume fraction in the EMP model, and the implicit unsteady solver were prescribed. This computationally diffusive approach is essential to handle the highly non-linear and stiff equation sets governing the multiphase flow, such as interphase drag and volume fraction [206]. It can prevent the solver from crashing due to the non-physical overshoots that higher-order, unbounded schemes would produce at sharp phase boundaries. The segregated EMP was used with the phase coupled velocity and pressure with the implicit under-relaxation factor of 0.5 and explicit factor of 0.2. These low under-relaxation factors were applied to stabilise the iterative process and maintain convergence reliability in multiphase flows with strong pressure–velocity coupling [207]. For initialisation, the pseudo transient strategy was applied, with both the time step (Δt) and the total physical time set to 0.1 sec and a total of 20,000 iterations to drive the unsteady form of the governing equations (Eq. 2.3 & 2.4) towards a steady-state solution. This choice reflets the equivalence between pseudo-time marching and under-relaxation, where a suitably large step size acts as an implicit stabilisation mechanism for nonlinear multiphase flow [207, 208]. Once the fluid flow was fully developed, the simulation was continued with a time step of $5x10^{-4}$ seconds with three inner iterations for a total physical time of 1.1 seconds, to ensure the Courant number ($u(r)\Delta t/\Delta x$, where Δx is the cell length) remained below 0.5.

2.2.4 CFL, Haematocrit, viscosity, and WSS calculations

For this study, an RBC-rich region was defined in areas where the volume fraction of the multiphase plasma-RBC component $\alpha_{RBC-rich}$ exceeded 0.5, while the near-wall

regions with a $\alpha_{RBC-rich}$ value of below 0.05 were designated as the CFL region, as illustrated in Appendix A.2 (Fig. A.2), Fig.2.2 and Table 2.2.

The tube haematocrit HT on a cross-sectional plane was modified from the area-weighted average [76, 78], of local volume fraction of the RBC-rich core:

$$\mathrm{HT} = \frac{\alpha_{RBC-rich,ave} * A_{RBC-rich}}{A_{total}} \tag{2.14}$$

$$A_{RBC-rich} = \sum_{\alpha_{RBC-rich}=0.5}^{\alpha_{RBC-rich}=1} a_i \tag{2.15}$$

$$A_{total} = \sum_{\alpha_{RBC-rich}=0}^{\alpha_{RBC-rich}=1} a_i \tag{2.16}$$

Where $A_{RBC-rich}$ is RBC-rich core region, A_{total} is total area, $\alpha_{RBC-rich,ave}$ is the average volume fraction of the RBC-rich region on a cross-sectional plane, and a_i is the area of the meshed elements.

The feeding haematocrit (HF) was estimated from the discharge haematocrit (HD), which is calculated from the Fåhraeus effect describing the reduction of the average red blood cells concentration with decreasing vessel diameter [46, 47], as following [10]:

$$\mathrm{HF} = \mathrm{HD} = \mathrm{HT} * u_{RBC-rich}/u_{bulk} \tag{2.17}$$

The apparent or effective viscosity of the mixture was calculated as a volume-fraction-weighted sum of the individual viscosities of the RBC-rich and plasma regions:

$$\mu_{app} = \mu_{RBC-rich}\alpha_{RBC-rich} + \mu_{plasma}\alpha_{plasma} \tag{2.18}$$

WSS was calculated as:

$$\mathrm{WSS} = \mu_{dynamic}\left\{[(\nabla \boldsymbol{v}_{tan})_C + (\nabla \boldsymbol{v}_{tan})_C^T] - \frac{2}{3}(\nabla \cdot \boldsymbol{v}_{tan})_C \mathbf{I}\right\}\mathbf{n} \tag{2.19}$$

$$\boldsymbol{v}_{tan} = (\boldsymbol{v}_C) - [(\boldsymbol{v}_C) \cdot \mathbf{n}]\mathbf{n} \tag{2.20}$$

where $\mu_{dynamic}$ is the dynamic viscosity, *C* indicates a value at the centroid of the near-wall cell, **I** is the identity tensor, **n** is the wall-normal unity vector, $\boldsymbol{v}_{tan}$ is the

tangential velocity, and $\boldsymbol{v}_C$ is the velocity at the centroid of the near-wall cell, respectively.

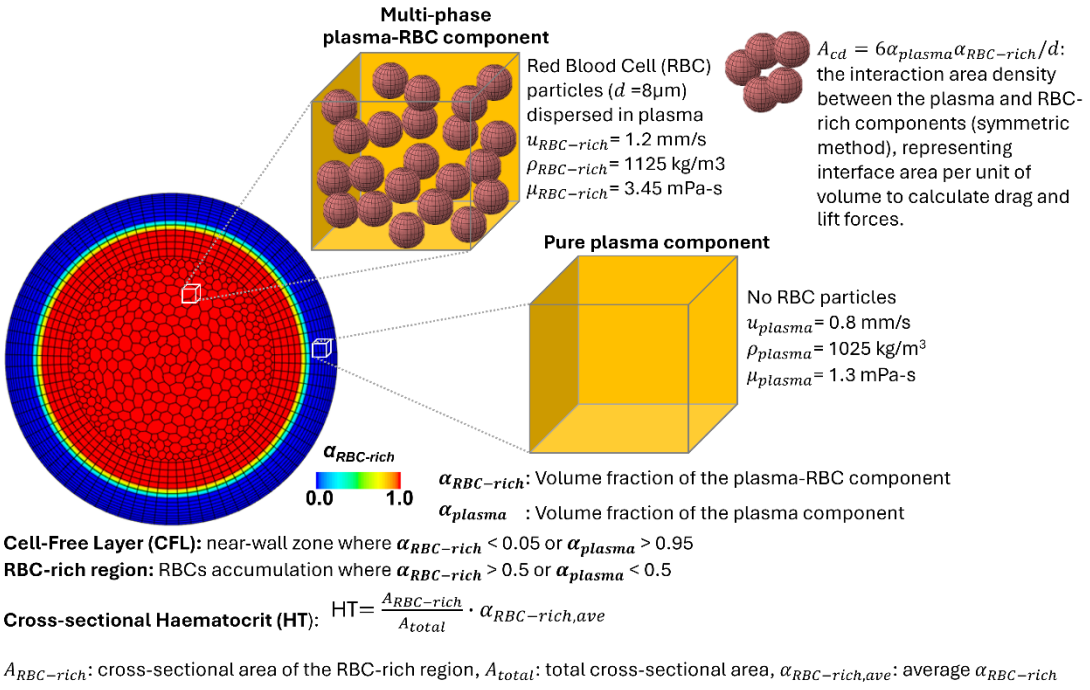

Figure 2.2: Description of the multi-phase, multi-component flow model.

Table 2.2: Terminology and definitions used in this study.

Terminology	Description	Figure
Multiphase plasma-RBC component ($\alpha_{RBC-rich}$)	RBC particles dispersed in plasma in unit of volume	Fig. 2.2
Pure plasma component (α_{plasma})	No RBCs in unit of volume	Fig. 2.2
RBC-rich region ($A_{RBC-rich}$)	$\sum_{\alpha_{RBC-rich}=0.5}^{\alpha_{RBC-rich}=1} a_i$ Total area of mesh elements (a_i) where $\alpha_{RBC-rich}$ lies between 0.5 and 1	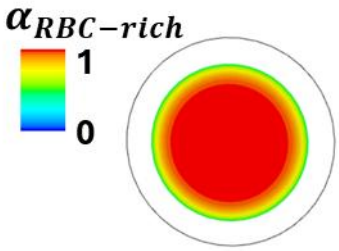
CFL region (CFL)	$\sum_{\alpha_{RBC-rich}=0}^{\alpha_{RBC-rich}=0.05} a_i$ Total area of mesh elements (a_i) where $\alpha_{RBC-rich}$ lies between 0 and 0.05	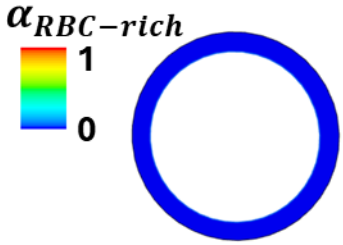
Tube haematocrit (HT)	Area-weighed haematocrit scaled by average of $\alpha_{RBC-rich}$ over the cross-sectional area	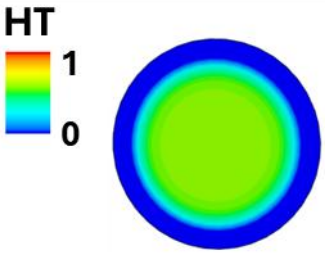
Discharge haematocrit (HD)	Flow-weighed haematocrit scaled by average of $\alpha_{RBC-rich}$ over the cross-sectional area	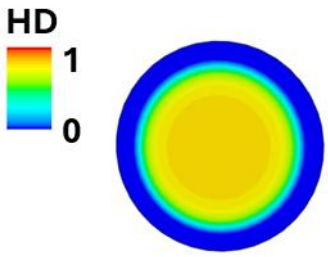

2.3 Validation

We performed a validation study of the presented multi-phase, multi-component model for the parent vessel, by generating four straight arteriolar segments of diameters 15, 20, 25, and 30 μm (Fig. 2.3A). For each vessel diameter, a numerical simulation was conducted by prescribing an initial CFL thickness (δ_{CFL}) and subsequently determining both the final δ_{CFL} and the discharge haematocrit (HD). This produced a set of predicted (δ_{CFL} and HD) data pairs (filled markers) which were then compared to literature values (open markers) at 30±2% and 43±1% haematocrit [72, 199] for validation. Because local HD depends on feeding haematocrit and flow rate, the two haematocrit conditions were implemented using different initial CFL thickness and flow rate consistent with the reference studies. Our model calculated local HD, whereas experimental studies measure haematocrit at systemic level (section 1.4.1.8). These metrics were assumed interchangeable, as both quantify RBC proportion and are reported as near-equivalent in several studies[67, 69, 71, 73]. Predicted haematocrit of approximately 30±2% (Fig. 2.3A) and 43±1% (Fig. 2.3B), obtained for different δ_{CFL} values, fell within the experimental data reported from same-diameter microvessels at 30% haematocrit [72] and animal studies at 41±2% haematocrit [199], respectively. This confirms the model's ability to predict pairs of δ_{CFL} and HD values across varied vessel diameters and haematocrit levels.

In addition, the velocity of the pure plasma component was used to represent the bulk velocity (u_{bulk}, defined as the averaged velocity), as it demonstrated close corelation with the multiphase plasma-RBC component velocity within the RBC-rich region, as shown in Appendix A.2 (Fig. A.2D), consistent with literature (Fig. 1.9B) [84]. The predicted velocity profiles for a 34-μm-diameter straight vessel were further compared with those reported in a same-size arteriole during systole (u_{bulk}=9.56 mm/s; u_{bulk} is mean velocity) and diastole (u_{bulk}=6.33 mm/s). Fig. 2.3C&D showed a good agreement between the present model's prediction and the *in vivo* experiment [89], with a percentage difference for the integral of the velocity profiles at 6.8% and 9.9%, for systole and diastole, respectively.

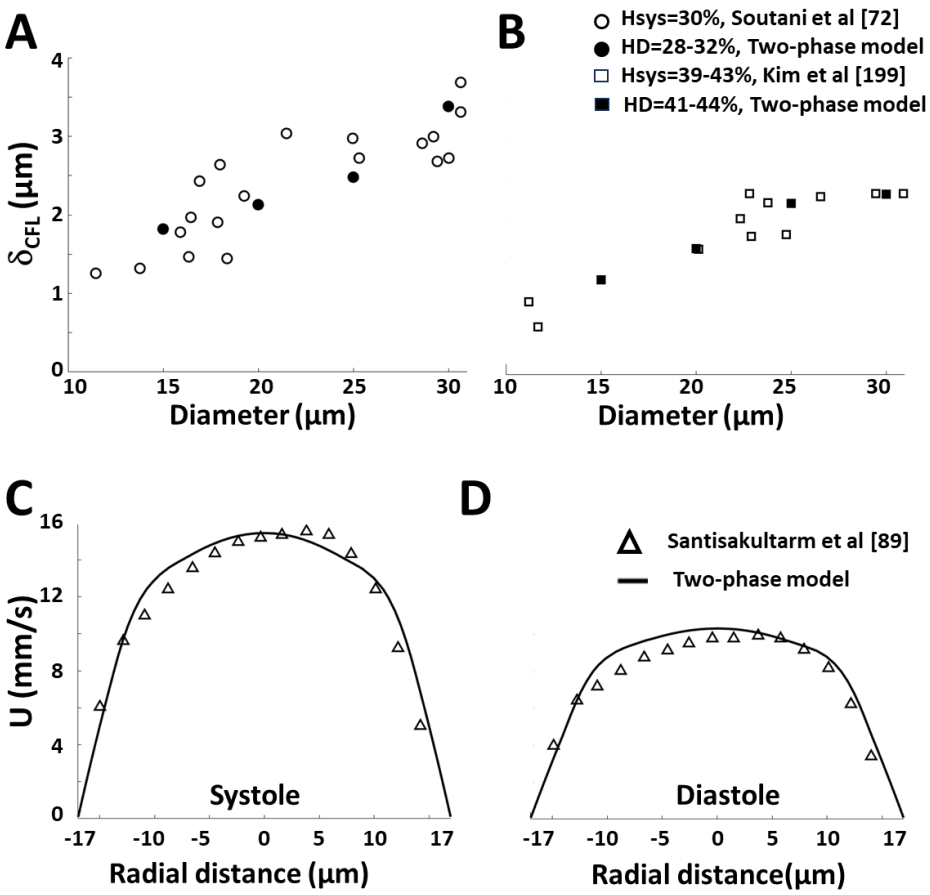

Figure 2.3: Validation of the multi-phase, multi-component continuum-based model with experimental measurements. (A, B) The haematocrit validation with the literature at 30% and 39-43% Hsys, respectively [72, 199]. (C, D) The predicted velocity profile was validated with experimental data at systole and diastole, respectively [89].

2.4 Results

2.4.1 Model Sensitivity

2.4.1.1 Comparison with a single-phase flow model in a 20µm arteriole vessel

To access the efficacy of the multi-phase, multi-component continuum model for bifurcated arteriolar microvessels over the conventional single-phase (Newtonian) approach, the velocity profile was comparatively analysed under controlled inlet velocity and initial viscosity conditions in a symmetrically bifurcated vessel of diameter 20 µm (Appendix A.3). As shown in Fig. 2.4A, despite similar inlet shear rates, the multi-phase, multi-component model exhibited a more blunt velocity profile

with a lower maximum velocity at the pre-junction vessel for a 20 µm arteriole. At the entrance of the daughter vessel, peak velocity shifted towards the outer wall (OW), consistent with the literature [89, 209], contrasting with the central peak in the single-phase model. As shown in Fig. 2.5A, the multi-phase, multi-component model highlighted a spatially varying WSS distribution further downstream from the junction. Conversely, the single-phase model showed a more uniform WSS pattern immediately after the junction.

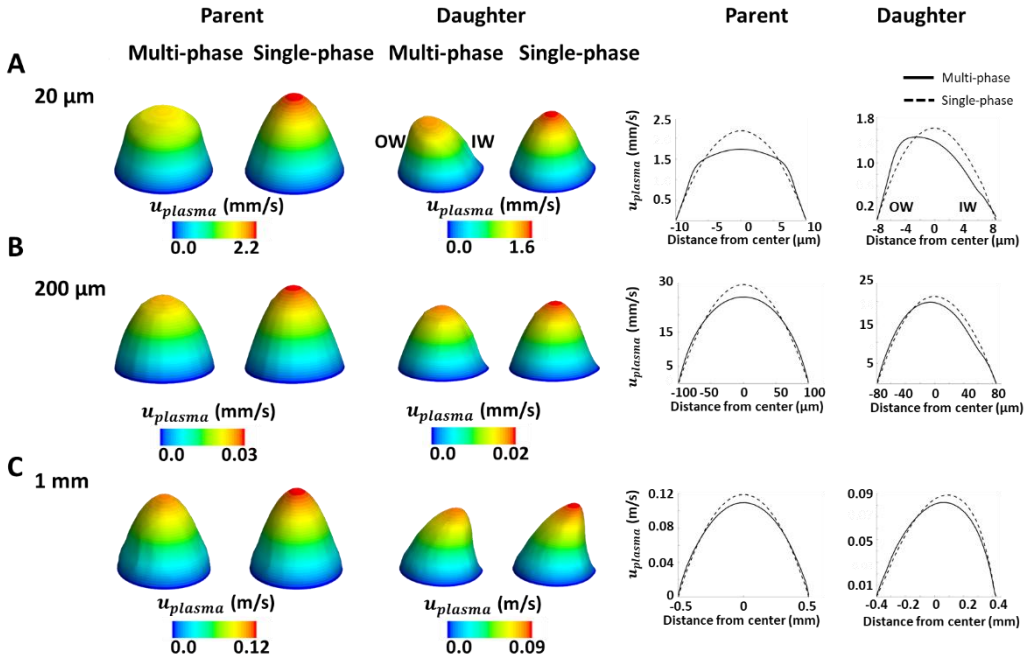

Figure 2.4: Sensitivity tests between the proposed multi-phase, multi-component model and the conventional single-phase continuum-based model for bifurcated vessels. (A-C), The three- and two-dimensional distribution of velocity profiles for the symmetric bifurcations with diameters of 20µm, 200µm, and 1mm. The velocities were analysed at cross sections 1P and 0D (see Fig. 2.6C) in the parent and daughter branches, respectively.

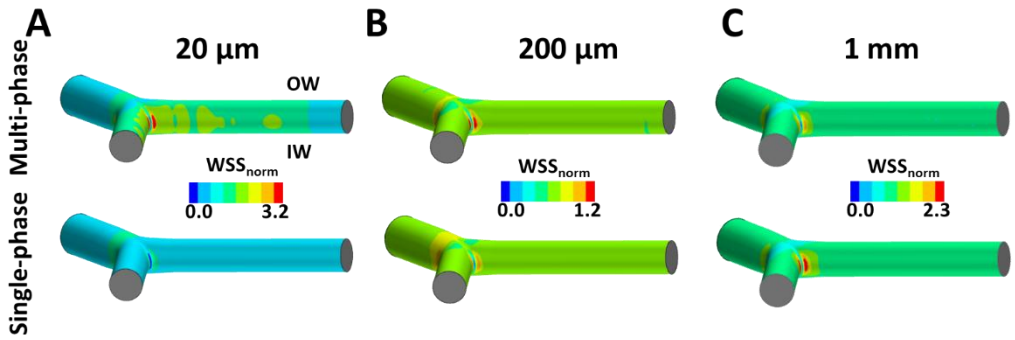

Figure 2.5: Wall shear stress distribution for the symmetric bifurcation in various scales. (A–C) Distributions are shown for diameters of 20, 200 and 1000 µm. The normalised WSS (WSS_{norm}) distribution is normalised by the WSS at the inlet.

2.4.1.2 Testing the model at different scales

The scalability of the multi-phase, multi-component model was assessed in larger bifurcated vessels (200 µm and 1mm) by maintaining comparable pseudo shear rates (PSR = U/D) (Appendix A.3). In smaller bifurcations (20 and 200 µm), the peak velocity in the multi-phase model shifted towards the outer wall (OW) of the junction, contrasting with the central peak in the single-phase models (Fig. 2.4A&B). However, at larger scales, both models produced similar velocity profiles with peak velocities near the IW (Fig. 2.4C&D). At 0D, velocity profile differences between the models were 9.2%, 5.3% and 3.8%, ranging from arteriole- to artery-sized vessels, respectively. Additionally, the multi-phase, multi-component model better captured the higher WSS at junctions in smaller bifurcations compared to the singe-phase model, with more uniform downstream WSS in the 200-µm and 1-mm sizes (Fig. 2.5). Therefore, the multi-phase, multi-component model proves to be a valuable and valid tool for microvessel simulations, whereas in larger vessels, the effects of the cell-free layer are negligible.

2.4.1.3 Viscosity as a function of shear rate

To examine whether the model captured key non-Newtonian features of blood, the relationship between viscosity and pseudo-shear rate was analysed. Simulations were conducted in a 20 μm tube, varying both the PSR (5 to 380 s^{-1}) and the feeding haematocrit (HF) (1% to 55%) for two different intrinsic RBC pseudo-solid viscosities ($\mu_{RBC\text{-}rich}$ = 3.4 and 6.5 mPa·s), as detailed in Appendix A.4. The resultant shear-thinning response was then quantified by fitting the data to the Power-law [210], Casson [211] and Carreau-Yasuda [211] rheological models, with R^2 values of 0.82 or higher across all conditions (Appendix A.5; Table A.5). The curves in Appendix A.5 (Fig. A.5) demonstrated two clear trends: (i) viscosity decreased with increasing PSR, and (ii) viscosity levels shifted downward as haematocrit decreased. The investigation confirms the model accurately captures blood's essential non-Newtonian properties, specifically shear-thinning, allowing its simulation results to be interpreted as physically accurate.

2.4.1.4 Viscosity as a function of haematocrit

Appendix A.5 (Fig. A.6A) showed a strong positive correlation between discharge haematocrit (HD) and effective viscosity (μ_{eff}) for both pseudo-solid viscosities ($\mu_{RBC-rich}$ = 3.45 and 6.50 mPa·s) in a 20 μm tube. The polynomial models provided excellent fits ($R^2 \approx 0.9957$ and 0.9955) with the equations $\mu_{eff} = -0.001927HD^2 + 0.004461HD + 0.000362$ and $\mu_{eff} = -0.003484HD^2 + 0.008373HD + 0.00068$, respectively. While the relationship was nearly linear below 30% haematocrit, the viscosity increased curved non-linear above physiological levels (~45%), particularly when $\mu_{RBC-rich}$ = 6.50 mPa·s. The polynomial fit suggested slight non-linearity at high haematocrit due to increased cell interactions. As shown in Appendix A.5 (Fig. A.6B), the inverse relationship between HD and CFL thickness provided a clear mechanical explanation for the non-linear viscosity curves. At low HD, a thick CFL created a lubricating effect, which kept the viscosity low. As HD increased to ~40%, the CFL diminished, causing greater cell-wall interaction and a steep increase in viscosity. The study proves that the polynomial viscosity equations are physically

correct, as they link high haematocrit to a diminished CFL and a corresponding, sharp increase in flow resistance.

2.4.2 Haemodynamic evaluation in the symmetric 20-μm arteriole bifurcation

In the parent vessel of the 20μm arteriole bifurcation, blood flow was approximated with the developed multi-phase, multi-component model, characterised by a central RBC-rich core and a peripheral CFL region in an annulus, symmetric formation. Assuming steady inlet flow rate of 1 mm/s and pressure outlets of 50 mmHg. The symmetric flow was defined by the location where the CFL thickness, δ_{CFL}, at both the inner IW ($\delta_{CFL,IW}$) and outer OW ($\delta_{CFL,OW}$) walls become identical, here termed the symmetric δ_{CFL} ($\delta_{CFL,SYM}$). This configuration was demonstrated by the relative haematocrit (HT*) distribution along the bifurcation plane (Fig. 2.6C, 1P) and the local HT on the cross-sectional plane at 1P (where P = parent vessel diameter d0), as illustrated in Fig. 2.6A.

At the entrance of the daughter vessel, (i.e., 0D, where D = diameter of daughter vessels d1 or d2), the RBC-rich region was shifted towards the IW, while the CFL region was enlarged near the OW. Downstream of the bifurcation, the RBC-rich zone underwent lateral migration, forcing the RBC-rich region to move away from the IW. Reattachment of the CFL along the IW was observed at a distance of approximately 2D. As the flow progressed downstream, the inner-wall CFL thickness $\delta_{CFL,IW}$ continued to progressively increase, whereas the outer-wall CFL thickness $\delta_{CFL,OW}$ experienced fluctuations in size. The flow eventually recovered a concentric annular symmetric shape at a distance 16D downstream of the junction (Fig. 2.6A&C, at position16D).

The velocity profile was influenced by the CFL downstream asymmetry. As shown in Fig. 2.6B, at concentric CFL locations (e.g. at the cross-sections 1P and 16D), the peak velocity appeared at the centre of the vessel, while in cross sections with eccentric CFL regions (0D-15D) the peak velocity was laterally shifted towards the enlarged CFL, along the OW. As illustrated in Fig. 2.6C, the boundary-layer development in the

daughter vessel resulted in a fully symmetric flow profile further downstream of the junction. The CFL eccentricity also impacted the spatial variation of the WSS distribution, which exhibited a complex pattern governed by shear rate and viscosity (Fig. 2.6D and Appendix A.6).

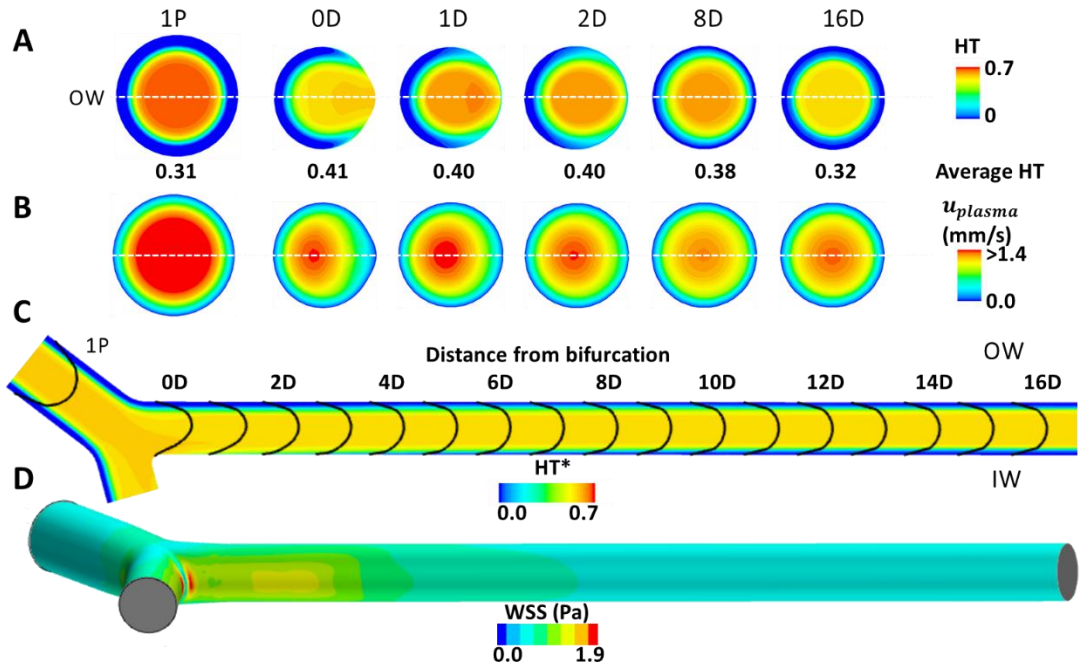

Figure 2.6: Haemodynamics in the symmetric 20-µm bifurcation in baseline conditions ($2.5x10^{-13}$ m^3/s). (A, B) The cross-sectional planes in the parent (1P) and daughter (0D-16D) vessels showing the distribution of the RBC-rich core and CFL regions with localised cross-sectional haematocrit (HT), and velocity magnitude, respectively. The HT is calculated using the local cross-sectional area ratio. (C) The development of the boundary layer from an asymmetric to a symmetric profile is visualised on the mid-plane of the bifurcation, where the background colour map indicates the relative haematocrit (HT*) derived from a reference area ratio at the 1P location ($\alpha_{RBC-rich} * A_{RBC-rich,at\ 1P}/A_{total,at\ 1P}$). (D) WSS distribution.

Appendix A.6 illustrated how CFL eccentricity generated regions of uneven shear rate and viscosity. At the entrance of the daughter vessel, RBC-rich zone (high haematocrit) aligned along the near wall, the CFL nearly zero, increasing cell-wall interactions and resulting elevated viscosity and low shear gradient. Further downstream, with the lateral RBC-rich region (low haematocrit), a thicker CFL developed, reducing resistance and promoting shear-thinning behaviour. This

haematocrit-driven and shear-dependent non-Newtonian behaviour directly caused the velocity profile shifted toward enlarged CFL regions and created complex WSS distribution.

2.4.2.1 Underlying mechanism response

To understand the downstream reestablishment of a symmetric CFL, we examined the haemodynamic forces driving the lateral migration of the RBC-rich region. The slip or relative velocity ($u_r = u_{RBC-rich}$ - u_{plasma}) refers to the velocity difference between the RBC-rich and plasma phases. in Fig. 2.7A-C the $u_{RBC-rich}$ (red line) was greater than u_{plasma} (blue line) from the vessel wall to the RBC-rich boundary, producing a gradient-slip profile (black line), while both velocities become identical within the RBC-rich region, forming a flattened profile inward. Fig. 2.7D&E illustrated that the width of the gradient-slip indicates the radial distance of strong shear interaction between plasma and RBC-rich region, whereas its height reflects the magnitude velocity difference, signifying the strong interfacial decoupling. The magnitude of the gradient-slip was around 0.100-0.101 mm/s, while the minimal slip velocity (<0.001 mm/s) in the RBC-rich region (Fig. 2.8A&E) reflected a strong coupling between the multiphase plasma-RBC and the pure-plasma components, implying that their relative motions closely aligned.

As illustrated in Fig. 2.7A-C and Eq. 2.10, $\alpha_{RBC-rich}$, u_r and plasma vorticity (ω_{plasma}) were used to calculate the lift force at the interaction area density (A_{cd}; interfacial area between the two components). The u_r peaked away from the maximum A_{cd} (Fig. 2.7B), indicating that the slip velocity did not dominantly govern the lift magnitude but influenced its direction, as lift vectors point from high-slip to low-slip region (Fig. 2.7H). The peak lift force (Fig. 2.7C, F-I) occurred at the RBC–plasma interface (Fig. 2.7C), where vorticity and interaction area density were greatest, not at the slip velocity peak. The lift force exceeding 1 pN, compared to drag forces below 0.001 pN, highlighting the dominant role of interfacial shear and rotational flow in RBC lateral migration.

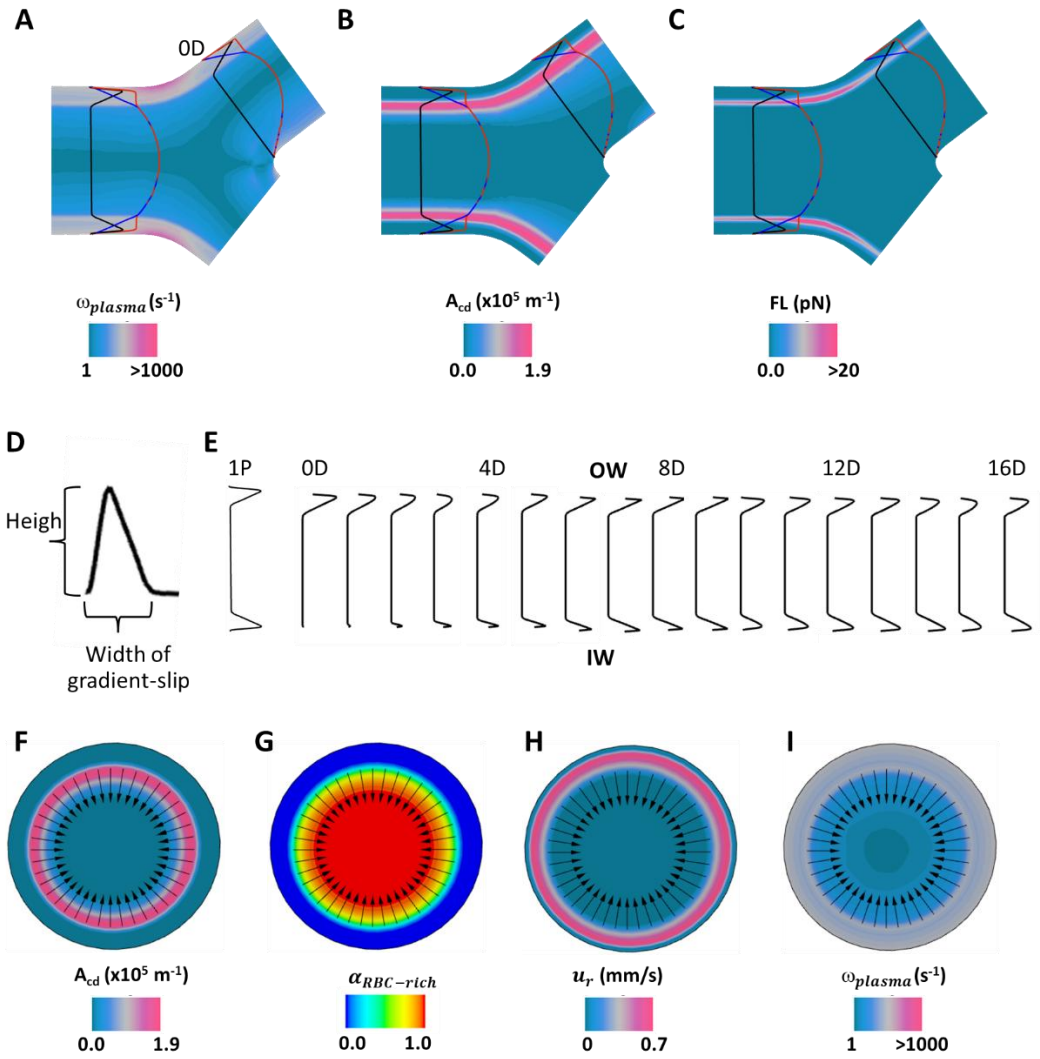

Figure 2.7: Slip velocity profile at the mid-plane of the bifurcation and maximum lift force at the 1P cross-sectional plane. (A–C) The slip velocity (black line) is the difference between the RBC-rich velocity (red profile) and the plasma velocity (blue profile), demonstrating on the plasma vorticity, interaction area density, and lift force, respectively. The RBC-plasma interface was characterised as the maximum interaction area density. (D) The characteristics of gradient-slip. (E) The boundary development of a balanced slip profile (F-G) The maximum lift vector on the interaction area density, volume fraction of multiphase plasma-RBC component, slip velocity, and plasma vorticity, respectively.

At the upstream location 1P (Fig. 2.8A&E), the flow was symmetric, and the slip velocity vector was primarily parallel to the vessel axis. The vorticity (Fig. 2.8B&F) formed a symmetric, ring-shaped pattern indicative of stable, laminar flow. The lift force (Fig. 2.8C&G) acted radially inward to the RBC-rich core towards the centre. In contrast, the drag force (Fig. 2.8D&H), driven by axial slip, was weaker in magnitude.

As the blood flow approached the bifurcation, both the near-wall vorticity and the slip velocity intensified at the vessel outer curvature (Fig. 2.8A&B). Along the midplane, the slip velocity vector formed into two counter-rotating streamwise vortices (as indicated by the red arrow in Fig. 2.8A). This vortex was confirmed to arise from phase coupling, rather than bulk rotation flow, as the absence of such vortex characteristics in the individual plasma or RBC velocity fields, which display white vector parallel to the axis (Appendix A.2; Fig. A.3). A stronger lift force emerged where this vortex slip formed (Fig. 2.8A&C), suggesting that the RBC-rich region was shifted towards the centre, creating a dense haematocrit at the apex (Fig. 2.6C). Simultaneously, the gradient interaction area density spatially at OW expanded (Fig. 2.7B), indicating enhanced dispersion or a freely moving state of the RBC-rich phase.

At the entrance of the daughter vessels (0D), the enlarged CFL at the OW exhibited a gradient-slip (Fig. 2.7A-E and Fig. 2.8A-D), while it was zero at the IW. The low-vorticity core (Fig. 2.8F, 0D) was skewed towards the high slip OW region (Fig. 2.8E, 0D) but became more central at 2D, where its value increased near the IW. At 2D, a smaller-vertex slip (highlighted by the blue arrow in Fig. 2.8A) emerged along the IW, alongside the onset of increased slip and lift forces. Further downstream, the slip-gradient at the OW became narrower and its maximum intensity decreased (Fig. 2.7E). Meanwhile, the slip-gradient at the IW progressively increased in both width and magnitude. Eventually, the values of the slip-gradient velocity became equal along both walls, resulting in a balanced slip velocity profile, consistent with the reformation of symmetric CFL.

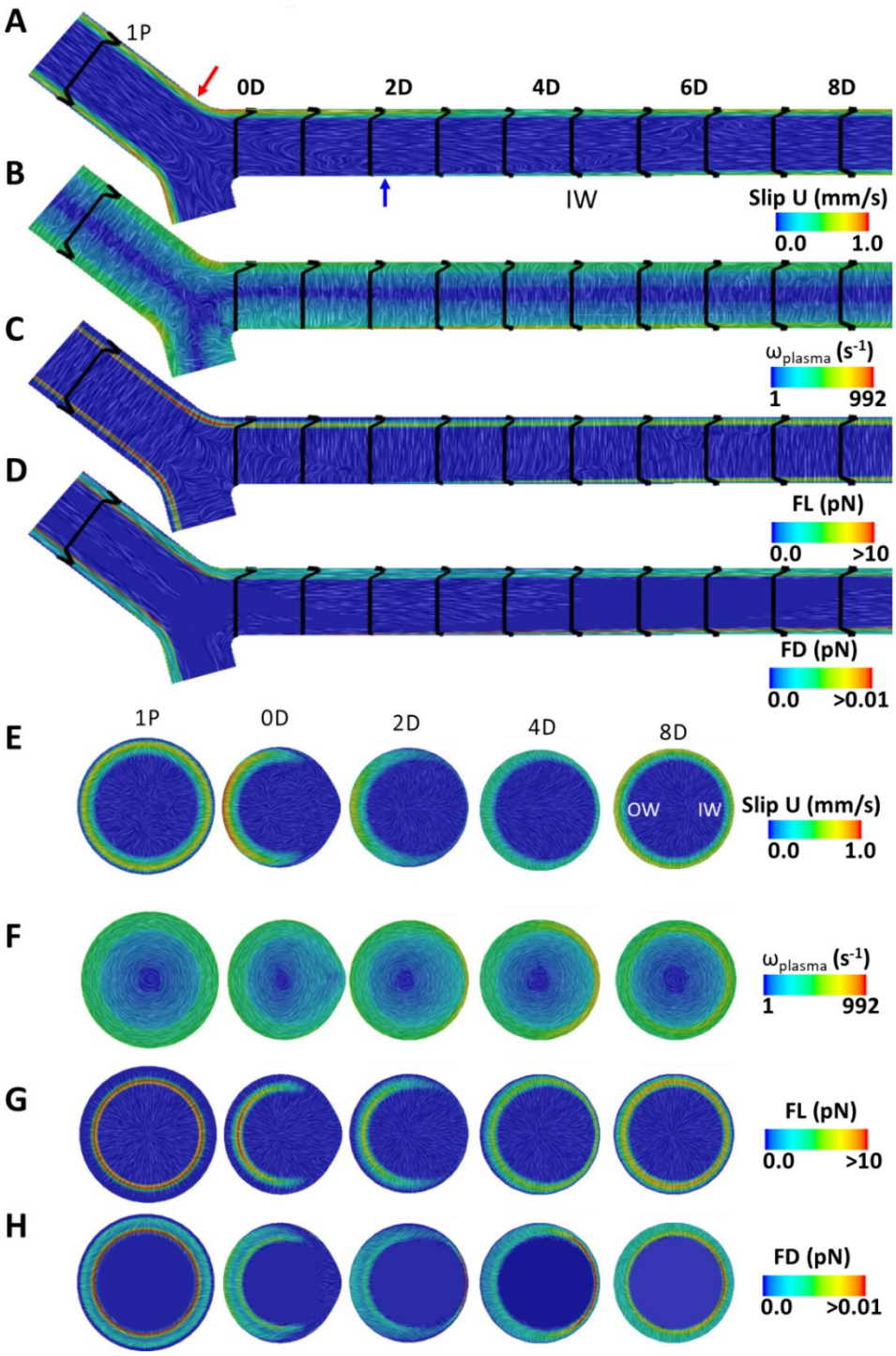

Figure 2.8: Interface interaction metrics in the symmetric 20-µm bifurcation for the baseline boundary conditions (Fig. 2.6). (A–D) Longitudinal views show slip velocity, vorticity of plasma phase, lift and drag forces, with slip velocity profiles. Red and blue arrows mark a vortex-like pattern. (E-H) Cross-sectional views at multiple axial locations.

2.5 Discussion

The goal of this chapter was to outline a novel multi-phase, multi-component model for describing the blood flow in a bifurcating arteriole microvessel, incorporating RBCs as dispersed particles in plasma and a cell-free layer. The model was validated against literature data and successfully captured the recovery of symmetric CFL downstream of the bifurcation, enabling a detailed investigation of the 3D haemodynamics in branching flows and providing a mechanistic explanation of the downstream CFL formation. Additionally, this study demonstrates the haematocrit distribution along the vessels, thereby establishing a link between numerical predictions and microvessel haemodynamic measurements. Despite the EMP's limitation in visualising discrete RBC trajectories, it offers computationally efficient, stable simulations that capture averaged flow features and key interface mechanisms, such as slip velocity, lift force and drag force distribution.

2.5.1 Novelty and contribution to knowledge

To the author's knowledge, this is the first study to apply the EMP method to investigate blood flow in arterioles and the downstream development of symmetric CFL. While multiphase flow methods such as the EMP and the volume of fluid (VOF) have been applied to study the effects of CFL blood behaviour in microvessels [155-157], the flow dynamics that result in the downstream formation of the near-wall CFL have not been observed before. The novelty in this chapter lies, therefore, on the new methodology within the EMP framework, alongside new observations of the three-dimensional haemodynamics and a mechanistic explanation for downstream CFL formation.

In developing our methodology, we introduced three key steps: (1) designing a bespoke mesh specifically for near-wall CFL development, (2) assigning an initial volume fraction for the RBC-rich region (corresponding to 44% haematocrit) and the initial CFL thickness, and (3) setting the EMP parameters to ensure numerical stability.

2.5.2 Comparison of the CFL development with previous works

Previous publications by other research groups have used the Lattice Boltzmann method (LBM) coupled with an Immersed Boundary Method (IBM) to observe the development of the CFL [14, 157,152]. Table 2.3 provides a comparative overview of our findings against such prior studies, illustrating how variations in geometry, haematocrit, flow conditions, and numerical settings influence the distance of downstream CFL recovery. According to Oulaid and Zhang (2015) [3], the CFL symmetric establishment in straight vessels with diameter D between 20 and 24 μm occurred within 8-15D, with the CFL thickness defined as the distance δ where the cumulative frequency of all instantaneous wall-to-membrane distance measurements reaches 10%. Ye et al. (2016) [6] reported that a minimum distance between successive generations of asymmetric T-bifurcations (inter-bifurcation distance) of over 8D is required for the CFL to symmetrically recover downstream of a 15 μm-diameter daughter vessel. Meanwhile, Bernabeu et al. (2020) [5] identified a longer recovery distance of 25D downstream of an extended double-T bifurcation with an approximately 33 μm-diameter parent vessel with inlet velocity of 0.6mm/s. In the present study, the CFL achieved symmetric recovery at 16D downstream of the 16 μm daughter branch under 44%HF and 53 s^{-1}.

Although the definition of CFL thickness differs among studies due to variations in modelling techniques and measurement methods, the approach to assessing the symmetry of the CFL uses a similar framework. In Ye et al.'s study [6], the CFL thickness was defined as the distance between the RBCs and the vessel wall. Bernabeu et al. (2020) [5] defined the CFL width as the distance through which 1% of the average RBC density flux occurs, with the symmetry similarly interpreted as the statistical equivalence between opposing walls. In our study, the CFL thickness was determined as the region where the volume fraction of the plasma-RBC component ($\alpha_{RBC-rich}$) was below 0.05. Across all studies, the symmetric CFL is consistently defined as the condition in which the CFL thickness is uniformly distributed adjacent to the wall across a cross section, reflecting balanced cross-sectional flow conditions.

Table 2.3: Comparison of the distance required for symmetric CFL.

	Oulaid & Zhang (2015) [3]	**Ye et al. (2016) [6]**	**Bernabeu et al. (2020) [5]**	**Our study**
Geometry	Straight channel	Asymmetric diameter T-bifurcation	Extended double-T bifurcation	Symmetric Y-bifurcation (75°)
Recovery distance	8D – 15D	>8D	25D	8D-16D
D* (μm)	20 - 24	15	33	16
U inlet (mm/s)	1	NM	0.6	0.2-3
HD	37%	62%	20%	18-66%
HT	31%	55%	NM	11-55%
PSR (s^{-1})	42 - 50	60.3	18	50
Time step (s)	$3.99x10^{-8}$	$1x10^{-7}$	NM	$5x10^{-4}$

D* is the diameter of the vessel which is used to measure the CFL thickness; PSR = U/D; NM = not mentioned.

2.5.3 Haemodynamics of the downstream asymmetric CFL

The model presented in this study examined the relationship between the eccentric CFL development and the 3D distribution of the velocity and WSS downstream of a symmetric bifurcation. One key observation was that due to the asymmetric CFL at the daughter vessels' entrance, the maximum velocity skewed towards the enlarged CFL at the outer wall (OW). This asymmetric velocity profile has been previously detected in flows with very low Reynold numbers (<1), reported in rat bifurcated arterioles [89, 90] and bifurcated microchannels [209]. Moreover, the haematocrit shifted in the opposite direction of the velocity profile, i.e. towards the IW. This inverse relationship between velocity and haematocrit is in agreement with previous observations in animal microvessels [212] and microfluidic studies [213]. Further downstream of the junction, the haematocrit profile became progressively more concentric with increasing distance; in other words, the asymmetry reduced, consistent with findings in the literature [6, 64]. This study revealed three-dimensional spatial disparities of the WSS distribution, which was governed by the eccentric pattern of the CFL due to the bifurcation. As the CFL re-formed downstream of the bifurcation, variations in the near-wall viscosity and shear rate led to WSS fluctuations that

gradually reached uniformity once a critical CFL thickness was established. Notably, greater WSS variation was associated with a narrower CFL width, an observation which has been previously reported in a two-dimensional numerical bifurcation model [6].

2.5.4 Mechanism response

The combined action of the wall-induced lift force and shear-gradient-induced lift force enable the lateral migration of the RBCs towards the low-shear central region of the daughter vessels, displacing the pure plasma outward and allowing the formation of a near-wall CFL. A wall-induced lift correction was implemented in the model to account for repulsive forces. This refers to a force that develops as particles move close to a wall, where a pressure buildup drives them away from the boundary [214, 215].

The shear-gradient lift force (Eq. 2.10) acts as the interplay between the volume fraction of the RBC-rich component, the slip velocity and the plasma vorticity. A high slip velocity was observed between the RBC-plasma interface and the vessel wall, while the slip velocity was nearly zero toward the centreline, generating lift forces that act upon the RBCs in an inward radial direction (Fig. 2.7H and 2.8C&G). This lift is explained by the Saffman force, a shear-induced force emerging due to the pressure difference generated by the non-uniform velocity field of the fluid and directs particles towards either the wall or the centreline in microchannels, depending on their local velocity gradients and slip velocity [203, 216]. Our study revealed that the near-wall slip velocity contributes significantly to the CFL formation. This aligns with other studies [150] that also highlight the importance of slip, although they employ a different approach by prescribing slip as a boundary condition in monophasic models to approximate CFL haemodynamics.

The plasma vorticity, generated by strong near-wall shear gradients [203, 214], also plays a key role in the downstream CFL formation. At the bifurcation point, elevated lift forces are observed, driven by high plasma vorticity and steep slip gradients within the CFL. The vortex likely governs the RBC migration at the bifurcation, contributing

to the asymmetric CFL at the daughter branch entrance. Furthermore, just beyond a distance of two diameters (2D) downstream of the junction, along the IW, a vortex-like structure appears in the slip velocity in a region of locally intensified plasma vorticity, triggering noticeable lift and initiating the CFL formation further along the flow path (Fig. 2.8). This unexpected pattern emergence, even at extremely low magnitude (<0.001 mm/s), highlights significant phase coupling and the influence of micro-scale interfacial dynamics on lift and lateral migration of the RBCs. This underscores why high-resolution slip velocity analysis is essential to detect hidden flow structures and non-obvious force mechanisms that drive phenomena such as the CFL formation. Overall, this study shows that lift-driven motion facilitates the downstream CFL reformation, consistent with prior reports highlighting lift as a primary factor in maintaining CFL stability [73, 203, 217].

2.5.5 Physiological relevance

Whilst the volume fraction of the RBC-rich region ($\alpha_{RBC-rich}$) from the multi-phase, multi-component model shares a conceptual basis with tube and discharge haematocrit, it differs fundamentally in scale. HT represents a microscale average based on individual cells in flow and naturally exhibits a centralised RBC core with a near-wall CFL. By contrast, in this study, $\alpha_{RBC-rich}$ represents a mesoscopic, grid-level fraction that visually reproduces the RBC-rich core–CFL pattern. Its gradient arises from numerical mixing and meshed cell averaging rather particle resolution.

Generally, HT is computed as the ratio of the RBC core area to the total blood area [76, 77]. Within the framework of the presented model, the HT was calculated as $A_{RBC-rich}/A_{total}$, where A is area, multiplied by $\alpha_{RBC-rich,ave}$ (Eq. 2.14), and then converted to HD via Eq. 2.17, thereby demonstrating the Fåhræus effect, which describes that the RBCs concentration in the blood (haematocrit) is reduced as the blood passes through small vessels, like arterioles [46, 47]. The resulting HD showed good agreement with systemic *in vivo* values, reproducing comparable CFL thickness values at specified diameters, including cases near 30% and 43% systemic haematocrit, as demonstrated in the validation section (Section 2.3). These findings

suggest that $\alpha_{RBC-rich,ave}$ can serve as a practical correction factor for physical HT. A similar approach was taken by Yazdan et al. (2022) [78], who also used a validated correction to convert a simple two-dimensional area fraction into an accurate three-dimensional tube haematocrit.

2.5.6 Characterisation of Non-Newtonian Blood Rheology

The Power-law model represented the shear-thinning behaviour of blood in a 20-μm diameter vessel simulated with an EMP approach, producing a flow index of n≈0.9. This increased value of n reflects the Newtonian tendency of blood in microvessels, driven by elevated shear rates (>200 s^{-1}) and the lubricating effect of the CFL, which together attenuate non-Newtonian characteristics. This result is corroborated by the work of Salame & Fenech (2025) [218], whose *in vitro* study found the Power-Law model produces indices between 0.931 and 0.950. However, they offer a critical insight that this near-Newtonian characteristic is also a reflection of the model's limitations. They argue that the Power-Law model, being a single-phase approximation, cannot resolve the distinct dynamics of the RBC-rich core and the plasma-rich CFL. In contrast, our findings differ from the lower n values of 0.51–0.61 in bulk arterial flows (Cho & Kensey, 1991) [197] and 0.35–0.68 in microchannels (Mehri et al., 2018) [219]. The flow behaviour index n approaches unity, indicating more Newtonian behaviour, under conditions of high shear or low haematocrit [220].

Applying the Casson model to the 20 μm multi-phase, multi-component simulations highlights important micro-rheological behaviour. At 44% haematocrit, the predicted yield stress (τ_0 = 0.38–0.58 mPa) and plastic viscosity (μ_p= 1.58–3.08 mPa·s) differ markedly from the bulk blood measurements at similar values of haematocrit (τ_0 ≈ 5.0–6.8 mPa; μ_p≈ 3.5 mPa·s) [197, 221]. The close agreement of the predicted plastic viscosity with bulk values confirms the model's validity under high shear conditions (>200 s^{-1}). The lower yield stress reflects microvascular physics rather than model error, as geometric confinement and near-wall CFL formation in a 20 μm vessel inhibit large-scale RBC aggregation responsible for higher bulk yield stress [65]. Since yield

stress quantifies aggregation, reduced values correctly indicate weaker aggregation in microvessels.

The Carreau–Yasuda analysis of the 20-μm EMP simulation showed a monotonic decrease in μ_0 and μ_∞ with decreasing haematocrit, consistent with the 25-50 μm and the ~100 μm in *in vitro* experiments by Salame & Fenech (2025) [218] and Mehri et al. (2018) [219], respectively. Our μ_0 values (1.59–2.98 mPa·s under 18% HF) and relaxation times (λ=0.02–0.09 s) are far lower than those reported by Mehri's (~26.9–118.6 mPa·s; ~3.3 s at 15% HF). It reflects smaller-diameter haemodynamics with a pronounced CFL and enhanced radial RBC migration that reduces wall viscosity. This finding is corroborated by Salame & Fenech [218], whose experiments in similarly sized 25 μm and 50 μm channels also yield zero-shear viscosity values (7.27–13.2 mPa·s), significantly lower than those reported for larger conduits.

Our Carreau-Yasuda model also offers a clinically interpretable framework for modelling pathological haemodynamics. Our calibration (Appendix A.5 Table A.5) shows μ_0 rising from 1.58 mPa·s at 1% HF to 4.84 at 55% HF, reflecting the transition from anaemia (low μ_0, reduced resistance) and polycythaemia (high μ_0, hyperviscosity). This trend parallels Behir et al. (2024), who reported μ_0 increasing from 17.8 mPa·s in anemia (25% haematocrit) to 859.2 mPa·s in hyperviscosity (65% haematocrit) [222], indicating marked shear-thinning resistance. Similarly, Mehri et al. (2018) demonstrated that μ_0 correlates with RBC aggregation, where diminished aggregation at 5% haematocrit lowers viscosity, while larger clusters at 10-15% haematocrit under low shear drive hyperviscosity [219]. Méndez-Mora et al. (2021) further confirmed that viscosity falls significantly as haematocrit decreases from 50% to 35% [223], and Cabrales et al. (2006) observed reductions to 21 mPa·s at Hct 11% during extreme haemodilution [224]. These observations underscore that μ_0 serves as an indicator to replicate pathological haemodynamics, including impaired perfusion in anaemia and thrombosis risk in polycythaemia.

2.5.7 Viscosity as a function of haematocrit

The relationship between viscosity and discharge haematocrit in the multi-phase, multi-component model clearly showed a non-linear rise in viscosity with increasing HD (Appendix A.5 Fig. A.6), consistent with previous experimental and computational findings. At low haematocrits (<30%), viscosity increased gradually, reflecting a dilute suspension behaviour, similar to what is reported by Wells and Merrill (1962) [225] and Pries et al. (1992) [58] in bulk and microtube flows, respectively.

The non-linear rise in viscosity with HD can be explained by changes in the CFL. At low HD, a thick CFL lubricated the vessel, minimising friction and maintaining low viscosity. As HD increased (especially >40%), this layer became thinner, causing more direct interaction between the RBC-rich core and the vessel wall. This structural shift is in agreement with microtube findings by Pries et al. (1992) [58] and Reinke et al. (1986) [108], showing that compressed CFL heightens viscosity.

2.5.8 Applicability and breakdown regimes

The continuum representation of the plasma–RBC component, surrounded by a near-wall plasma layer, has been validated against experimental data for vessel diameters between 15 and 30 μm at haematocrits of 30% and 40%, with CFL thickness at 15 μm predicted as 1.8 μm and 1.4 μm (Fig. 2.3B). Experimental data show that at diameters below 15 μm and 40% haematocrit, CFL thickness falls below 1 μm, which cannot be represented under the current implicit tree method due to its minimum wall distance constraint. Future work may extend to capillary-scale diameters (8μm) by implementing the PDE wall distance method in place of the implicit tree approach. This alternative method offers adjustable under-relaxation factors and iterative control, which may enable CFL thickness values below 1 μm.

Furthermore, the relationship between CFL thickness and feeding haematocrit determines the model's performance in dilute regimes. While 30-40% haematocrits are experimentally validated (section 2.3), the model successfully simulates the

transition to 1% feeding haematocrit, where the CFL thickness expands to 5 μm (Appendix A.5; Fig. A.5). Such low-viscosity, near-Newtonian behaviour signifies a regime of minimal RBC interaction, which aligns with the physical reality of highly dilute blood [63, 66]. This confirms that the model captures physical tendencies even at extreme dilutions (1% haematocrit), while remaining most robust within the validated 30–40 % range.

Beyond the validated diameter and haematocrit ranges, a further limitation of the continuum EMP formulation arises in aggregation-dominated flow regimes. In the present framework, RBC transport and CFL structure are represented through phase distributions rather than discrete cell morphology or intercellular adhesion. As a result, microscale processes such as rouleaux formation [8, 9] and deformation-mediated interactions [10, 11], which become significant in pathological states and low-shear environments, cannot be directly captured. The volume-averaging inherent to the RBC–plasma interface prevents explicit resolution of clustered cell structures or dynamic shape changes, marking a fundamental boundary of model validity. Future extensions targeting strongly aggregating regimes would require aggregation-aware rheological modelling or hybrid particle–continuum approaches to achieve greater physical fidelity.

2.5.9 Limitation and Future work

The multi-phase, multi-component model effectively captures key haemodynamic observed in microvessels, including asymmetric flow and CFL development. However, its reliance on volume fractions introduces a smoothed interface, contrasting with the sharp RBC–plasma boundaries observed in real blood [39, 79]. This smoothing, a result of numerical grid-based averaging [211, 212], may lead to confusion, especially for readers unfamiliar with continuum-based approaches, as the visual output may not reflect the distinct particle-based nature of blood.

To address the visual smoothing inherent in the Eulerian multi-phase model, a Lagrangian–Eulerian approach [226] offers a more physically intuitive alternative. By

treating RBCs as discrete particles, this method captures the sharp transitions between RBC-rich and plasma-rich zones [227]. Although this approach demands greater computational resources, it yields more detailed insights into microvascular dynamics. Using the Lagrangian–Eulerian model alongside EMP under the same conditions would clarify how discrete particle behaviours correspond to the smoothed fields in EMP. If similar trends are observed, the Lagrangian results can serve as a visual reference, helping readers interpret the EMP's diffuse interfaces as representations of underlying particle dynamics, rather than physical blending.

Our model captures essential haemodynamic trends, such as CFL formation and haematocrit distribution. However, it simplifies RBC behaviour by excluding deformability and aggregation, which are critical for microscale accuracy. These properties affect local viscosity and CFL thickness, particularly in low-shear or narrow vessels [11, 64, 65]. Incorporating them, via source terms in the RBC transport equation, would improve physiological fidelity, especially in pathological contexts where reduced deformability and increased aggregation impair microvascular flow.

Advancing the model to include oxygen and nitric oxide (NO) transport is vital for linking haemodynamics to vascular function. Oxygen delivery depends on haematocrit and CFL thickness [228-230], while NO produced in response to wall shear stress [231], regulates vascular tone [232] and is preserved by the CFL through reduced RBC scavenging [233]. Incorporating these species would enable the model to simulate biochemical responses, offering insights into pathologies including hypertension and atherosclerosis. Modelling oxygen and nitric oxide transport will extend our work from flow analysis to predicting key biochemical responses in vascular health and disease. This is crucial for studying tissue oxygenation and NO-related dysfunction in conditions such as hypertension and atherosclerosis.

Chapter 3

Multi-phase, multi-component model investigation under various conditions

3.1 Introduction

In microvascular flow, the CFL plays a critical role in regulating the hemodynamic behaviour and facilitating gas exchange [43]. Previous research suggests that this layer may lubricate blood flow, decrease flow resistance [108, 234] and mitigate wall shear stress [235], thereby reducing the production of vasodilators such as nitric oxide (NO) and prostaglandins in the endothelium [236]. A thicker CFL would enhance these effects. The layer also helps protect NO produced by the endothelium from being scavenged by the blood lumen [236]. To fully understand the physiological impact of these changes on tissue function, it is vital to study the behaviour of CFL formation within the arteriolar network, which is influenced by blood flow partitioning at bifurcations.

The CFL thickness arises from RBCs migration toward the vessel centre, driven by haemodynamic forces such as cell-wall repulsion and cell-cell interactions [148, 164]. The thickness depends on the feeding haematocrit, the RBCs deformability and aggregation [4, 165]. Higher haematocrit and stronger aggregation reduce the CFL, while deformability enhances RBC lateral migration and CFL expansion. Increased shear flow contributes to the stabilisation of the CFL by reducing both its thickness and temporal fluctuations [199]. Moreover, the biased outflow [73], upstream RBC distribution [118], and diameter asymmetric bifurcation [56] influence the unequal distribution of the RBCs and plasma at diverging bifurcations. The underlying mechanism is plasma skimming, where the CFL is preferentially diverted into the smaller or low-flow branch. The outcome of this process is the Zweifach-Fung effect [177, 178], which leads to a drop in haematocrit in the branch with lower flow. This happens because RBCs tend to follow the faster stream at a bifurcation, causing the

slower branch to receive mostly plasma with fewer cells. Since little information is available on the downstream CFL formation in arteriolar networks, this study aims to provide a computational analysis that will help in better understanding its physiological implications.

Chapter 2 demonstrated that our novel multi-phase, multi-component model can be a valuable tool for investigating the haemodynamics in symmetric arteriole bifurcations and the CFL development, offering a mechanistic explanation for the downstream recovery of a symmetric CFL. However, the simulations in Chapter 2 were conducted on a symmetric bifurcation under the boundary conditions of a constant inlet velocity and identical daughter pressure outlets. It demonstrated ideal separation, with the RBC-rich flux being equally distributed to the two daughter vessels. In reality, blood flow is characterised by a heterogeneous haematocrit throughout the network, with varied flows, resulting in phase separation.

This study aims to investigate how key haemodynamic factors, such as the feeding haematocrit, the upstream flow rate, uneven flow split between the daughter branches, and different diameters and distances between successive bifurcations affect the CFL formation and downstream recovery of symmetric flow. Using the multi-phase, multi-component model, we examined how these factors influence the downstream CFL thickness, the tube haematocrit, the viscosity and the WSS. Special attention was given to the role of the slip velocity and its vortex structures in modulating local lift forces and RBC distribution. By integrating these complex interactions, this study provides a deeper mechanistic insight into how the local slip velocity patterns and the CFL dynamics are influences by vascular and flow conditions, offering an understanding of microvascular impairments such as ischaemia.

3.2 Material and methods

3.2.1 Construction of idealised bifurcations

Microvascular networks *in vivo* are composed of asymmetric bifurcations with variable lengths of the vessel segments between successive branching points, known

as inter-bifurcation distance (λ). This natural complexity is crucial for their function in enabling efficient RBCs migration, which ensures for delivering oxygen and nutrients to tissues, and possibly results in flow patterns that differ from those of a symmetric bifurcation. To investigate the effect of diameter asymmetry, two Y-junction geometries were created and later compared against the symmetric configuration defined in Chapter 2. In these two asymmetric geometries, one branch diameter was held constant at d1 = 16 μm, while the d2 branch was set to either 19 μm or 11 μm. These specific diameter values for d2 were derived from Eq. 3.1 for a physiologically representative asymmetric bifurcation (d0 = 20 μm and η_d = 0.56 [149]). This design allows systematic evaluation of diameter asymmetry while controlling for angular effects, thereby improving interpretability of the results.

$$d_x = \sqrt[3]{\mathrm{d0}^3/(1+\eta_d^3)}, \quad d_y = \sqrt[3]{\mathrm{d0}^3 - d_x^3} \tag{3.1}$$

where d_x is diameter of the smaller daughter branch and d_y is the diameter of the larger daughter branch.

The final two geometries represented microvascular networks composed of three generations (considering the parent vessel as the 0th generation) and three symmetric bifurcations. In reference to the symmetric bifurcation, the 2nd generation (i=2) was divided from the 1st generation, where d1 bifurcated into d3 and d4, and d2 into d5 and d6, resulting in four daughter branches. The diameter of the 2nd generation was 13 μm and the length was 320 μm. The length of the 1st generation, or inter-bifurcation distance (λ), was varied at 4D and 8D, with D denoting the diameter of d1, so the distance varied with vessel size. These specific distances were chosen based on findings from the Chapter 2, which showed that under baseline condition (44% HF and 1 mm/s), the CFL becomes concentric at the distance of 16D. Figure 3.1 illustrated the full set of geometries examined throughout this chapter.

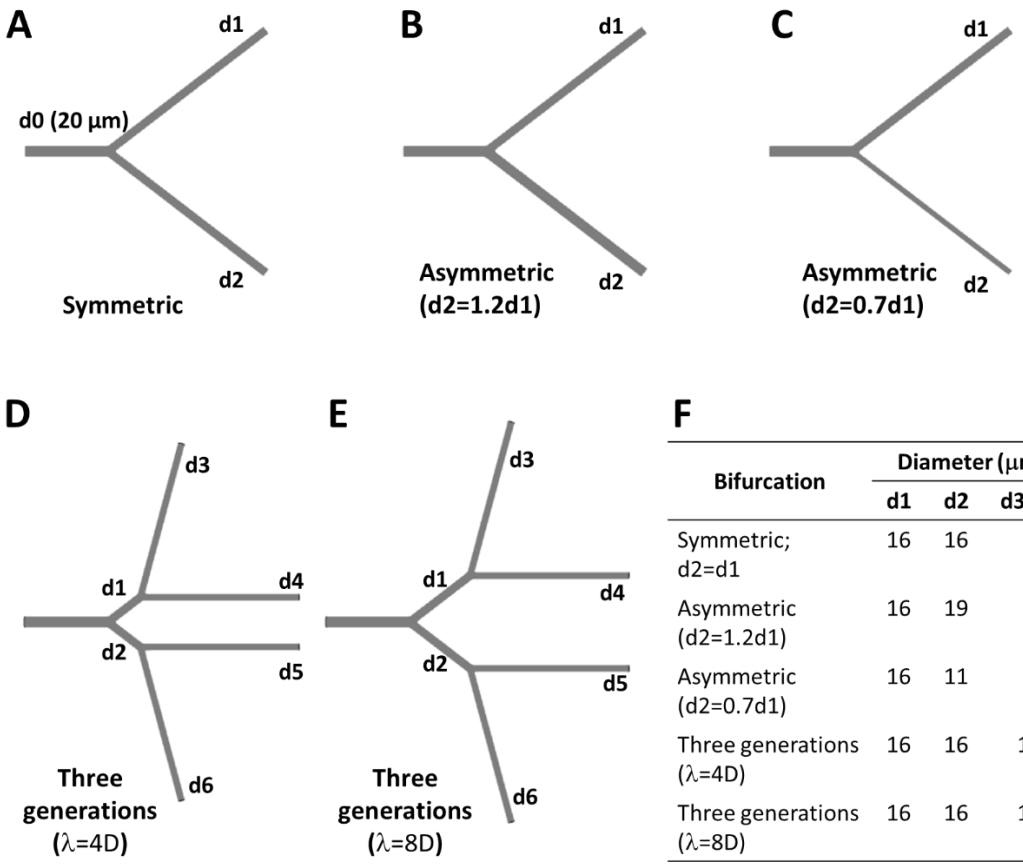

F

Bifurcation	Diameter (μm)		
	d1	d2	d3-d6
Symmetric; d2=d1	16	16	-
Asymmetric (d2=1.2d1)	16	19	-
Asymmetric (d2=0.7d1)	16	11	-
Three generations (λ=4D)	16	16	13
Three generations (λ=8D)	16	16	13

Figure 3.1: Idealised bifurcation studied in this chapter. (A) Symmetric bifurcation. (B&C) Asymmetric bifurcation with daughter vessel d2 larger and smaller than d1, respectively. (D&E) Three-generation bifurcation with inter-bifurcation distance of 4D and 8D, respectively. (F) Daughter vessel diameters prescribed for all idealised bifurcation.

3.2.2 Meshing

Chapter 3 extended the study from Chapter 2 by varying the feeding HF between 18% and 66%, which corresponded to initial CFL thicknesses δ_{CFL}ranging from 3.3 μm to 1.0 μm. To ensure the CFL region was adequately captured in all cases, the prismatic layer total thickness (PLTT) was set to 5 μm, this value was chosen to exceed the maximum CFL thickness (3.3 μm) by approximately two-thirds. This mesh configuration had originally been applied in Chapter 2 for the baseline simulation at 44% HF and was retained in Chapter 3 to maintain consistency across all simulations

within the 20 μm Y-junction bifurcation geometry. This approach allowed the impact of haemodynamic variations on CFL formation to be isolated and accurately assessed.

3.2.3 EMP

The EMP parameters were largely consistent with those described in Chapter 2, except for the initial δ_{CFL} and boundary conditions, which were modified to examine the influence of the feeding haematocrit, inflow and biased outflow to the downstream CFL formation. HF was varied between 18–66% (anaemic to polycythaemic), including normal (~44%) [215], with initial δ_{CFL} estimated from literature [72, 199] for these haematocrit values. Flow rates of $0.2Q_0$, Q_0, and $3Q_0$ ($Q_0 = 2.5 \times 10^{-13}$ m³/s) were applied, representing velocities of 0.2–3 mm/s in 20 μm arterioles [22, 91, 183, 184]. These values were used to approximate $u_{RBC-rich}$ and $u_{RBC-plasma}$, while u_{bulk} was calculated using Eq. 2.17 to ensure consistency with the target velocity range. For outflow bias, d1 was fixed at 50 mmHg (6666 mmHg) [51] and d2 adjusted to achieve Q_2:Q_1 ratios of 0.4 and 0.2 (Table 3.1).

Table 3.1: Boundary conditions and initial values in variation of feeding haematocrit, inflow, biased outflow, and asymmetric bifurcation.

Condition	δ_{CFL} (μm)	PSR (s^{-1})	u_{bulk} (mm/s)	$u_{RBC-rich}$ (mm/s)	u_{plasma} (mm/s)	d2 Outlet (Pa)
44% HF	1.8	53	1.06	1.2	0.8	6666
66% HF	1.0	56	1.12	1.2	0.8	6666
55% HF	1.4	55	1.1	1.2	0.8	6666
18% HF	3.3	49	0.97	1.2	0.8	6666
0.2Q	1.8	13	0.27	0.3	0.2	6666
3Q	1.8	153	3.06	3.2	2.8	6666
Q_2:Q_1=0.4	1.8	53	1.06	1.2	0.8	6767
Q_2:Q_1=0.2	1.8	53	1.06	1.2	0.8	6733
Asym.bif.	1.8	56	1.06	1.2	0.8	6666

Asym.bif. stands for asymmetric diameter bifurcations; PSR is pseudo shear rate (U/D).

The fraction of RBC-rich region entering the daughter branch (FQ_E) and the fraction of the bulk in the same branch (FQ_B), [56], was calculated to present phase separation following:

$$FQ_{E,di} = Q_{RBC-rich,region,di}/Q_{RBC-rich,region,d0} \quad (3.1)$$

$$FQ_{B,di} = Q_{blood,di}/Q_{blood,d0} \quad (3.2)$$

where d0 is parent, di is daughter d1 or d2, $Q_{RBC-rich,region}$ is flow rate of the RBC-rich region, Q_{bulk} is flow rate of blood.

3.3 Result

3.3.1 Influence of the feeding haematocrit

To access the influence of varying RBC concentration on downstream flow characteristics, HF was set at 18%, 55%, and 66%, with CFL thicknesses of 3.3–1.0 μm, while 44% (physiological norm) was included to represent the physiological norm and maintain continuity. This range represented anaemic to polycythaemic conditions haemotological disorders [237]. With a consistent inlet velocity of 1.06 ± 0.058 mm/s across all four cases, the observed differences in downstream hemodynamic characteristics can be attributed to the influence of the HF. HF is applied here to represent the haematocrit entering the inlet, as this parameter directly governs downstream flow behaviour, whereas HT denotes local haematocrit within the tube and is presented as a result along the vessel length (section 1.4.1.8).

In Fig. 3.2A&C, increasing the feeding haematocrit resulted in a thinner outer-wall CFL thickness ($\delta_{CFL,OW}$) at 0D, with the thickness of 0.5 μm for 66% HF, 1.1 μm for 55% HF, 1.5 μm for 44% HF and 2.8 μm for 18% HF. As the flow progressed downstream, higher HF promoted faster development of a symmetric CFL, observed at 8D, 15D and 16D with $\delta_{CFL,SYM}$ values of 0.4, 0.8 and 0.9 μm, for 66%, 55% and 44% HF, respectively. At the lowest 18% HF, however, symmetry in the CFL was not clearly established. As expected, higher HF led to a higher local HT and increased effective viscosity in the daughter branch, respectively (Fig. 3.2B). Consequently, higher HF resulted in more pronounced spatial fluctuation of HT throughout the

bifurcation, as shown in Fig. 3.2C&E-F, and variations in magnitude of WSS (Fig. 3.2D), primarily due to the thinner CFL and increased apparent viscosity. Fig. 3.2E showed that reducing HF increased CFL thickness, which decreased the maximum velocity in both the parent (1P) and daughter (0D) branches. Meanwhile, Fig. 3.2F indicated that lower HF enhanced bluntness in the parent's symmetric velocity profile, while in the daughter branch, the peak velocity shifted toward the enlarged CFL, most prominently at the lowest HF.

The haematocrit level directly influences the haemodynamic forces. High HF was characterised by a thinner CFL, which resulted in high near-wall vorticity (Fig. B.1B), creating a strong lift force at RBC-plasma interface (Fig. B.1C). This induced a vortex-like motion of the slip velocity in the RBC-rich region (Fig. B.1A). In contrast, lower HF caused a thicker CFL, which resulted in low vorticity and a weaker lift force. The high HF condition also promoted a quicker development of symmetric slip velocity, as the slip gradient at 0D at the OW was smaller and balanced out over a shorter distance (Fig. B.1A).

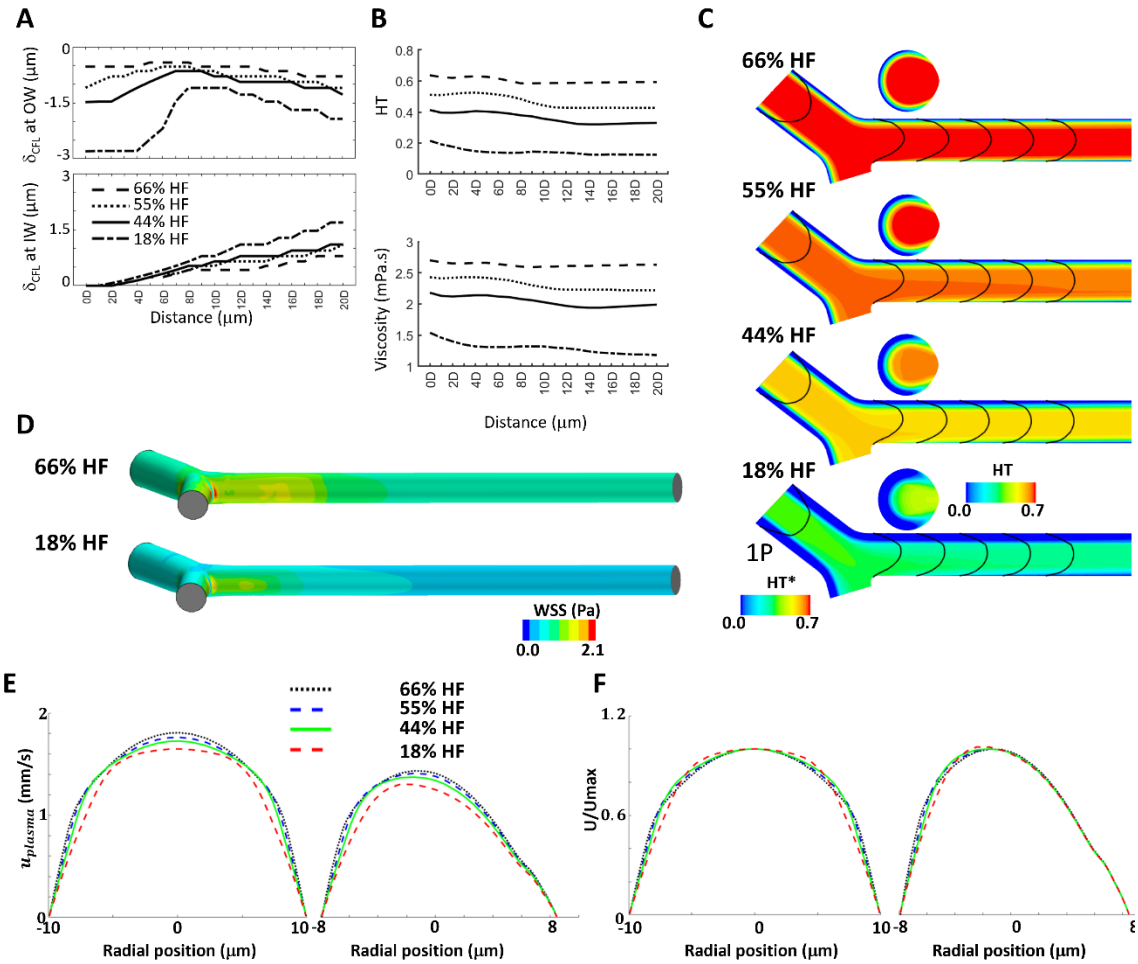

Figure 3.2: Haemodynamic variations in the symmetric bifurcation with varying feeding discharge haematocrit. (A) CFL thickness $\delta_{CFL,OW}$ and $\delta_{CFL,IW}$ along the inner and outer walls of the daughter. (B) Variation of the HT and apparent viscosity. (C) Tube haematocrit distribution, where the mid-plane value is derived from a reference area ratio at the 1P location (HT*), while the daughter entrance (0D position) is calculated using the local cross-sectional area ratio. The black lines represent a velocity profile. (D) WSS distribution. (E, F) Actual velocity and normalised velocity (U/Umax), respectively, at 1P and 0D positions. Lower HF increased bluntness and the daughter's peak velocity shifted toward the enlarged CFL.

3.3.2 Effects of altering the inflow conditions

To examine the effect of upstream flow on CFL dynamics, the simulation from Chapter 2 (Q_0 = 2.5×10^{-13} m^3/s, ~1 mm/s) was extended to include $0.2Q_0$ and $3Q_0$, corresponding to velocities of ~0.2 and ~3 mm/s, which fall within the range observed in 20 μm arterioles [22, 91, 183, 184] [89, 91]. Under identical feeding 44% HF,

increasing the flow rate caused a thinner $\delta_{CFL,SYM}$, measuring 1.9, 1.9, 2.0 μm at the 1P position of the parent vessel, resulting in 41%, 31%, and 26% HT for $0.2Q_0$, Q_0, and $3Q_0$, respectively. This influence of flow rate on haematocrit was further confirmed by the HD, an analogue of HF, which changed to 55%, 43%, and 36%, respectively.

As shown in Fig. 3.3A&C, at the entrance of the daughter vessels (at 0D position), the increased flow rates were associated with thicker CFL thicknesses at the OW, with $\delta_{CFL,OW}$ of 1.7, 1.5 and 1.3 μm for $3Q_0$, Q_0 and $0.2Q_0$, respectively. By a distance of 8D downstream of the junction, this pattern reversed, with the thinnest CFL corresponding to the highest inlet flow rate. Along the IW, longer distances were required for the emergence of measurable cell-free layer ($\delta_{CFL,IW}$) at 1D, 3D and 5D downstream of the bifurcation, as flow increased from $0.2Q_0$ to Q_0 to $3Q_0$, respectively. Beyond these points, symmetric CFL ($\delta_{CFL,SYM}$) was detected at 8D, 16D and 16D distance, respectively for the low, medium, and high flow rates, with corresponding $\delta_{CFL,SYM}$ values of 1.5, 0.9 and 0.4 μm. At 0D, the HT was observed to decrease with increasing flow rate and continued to decline further downstream until approximately 14D downstream of the junction. After this location, the $0.2Q_0$ and Q_0 cases achieved similar haematocrits (27-34% HT), demonstrated in Fig. 3.3B.

While the overall HT appeared similar for the $0.2Q_0$ and Q_0 cases (~34%), the distribution of the RBC-rich and pure plasma components differed significantly, as shown in Fig. 3.3C (16D). This outcome reflected the interplay between the RBC-rich region size and density rather than uniform distribution. As shown in Fig. 3.3C (16D), at $0.2Q_0$, the near-wall CFL was thicker, and the RBC-rich region was more densely packed, occupying 41.2% of the lumen. In contrast, Q_0 exhibited a thinner CFL and a broader RBC-rich region (57.28%) with lower local RBC-rich density. Similarly, the $3Q_0$ case showed an RBC-rich coverage of 54.73%, but its density was markedly reduced due to stronger lift forces at higher flow rates (Fig. B.2B).

A high inflow rate resulted in a thick $\delta_{CFL,OW}$ with high vorticity (Fig. B.2B), which generated a strong lift force (Fig. B.2C). This led to a large disparity in the slip velocity profiles between the OW and IW of the daughter vessel. As a result, a long distance of

17D was required to achieve a balanced slip velocity profile but restore symmetric CFL at 16D. Additionally, the RBC-rich region in all cases exhibited vortex-like and non-axial slip velocity patterns.

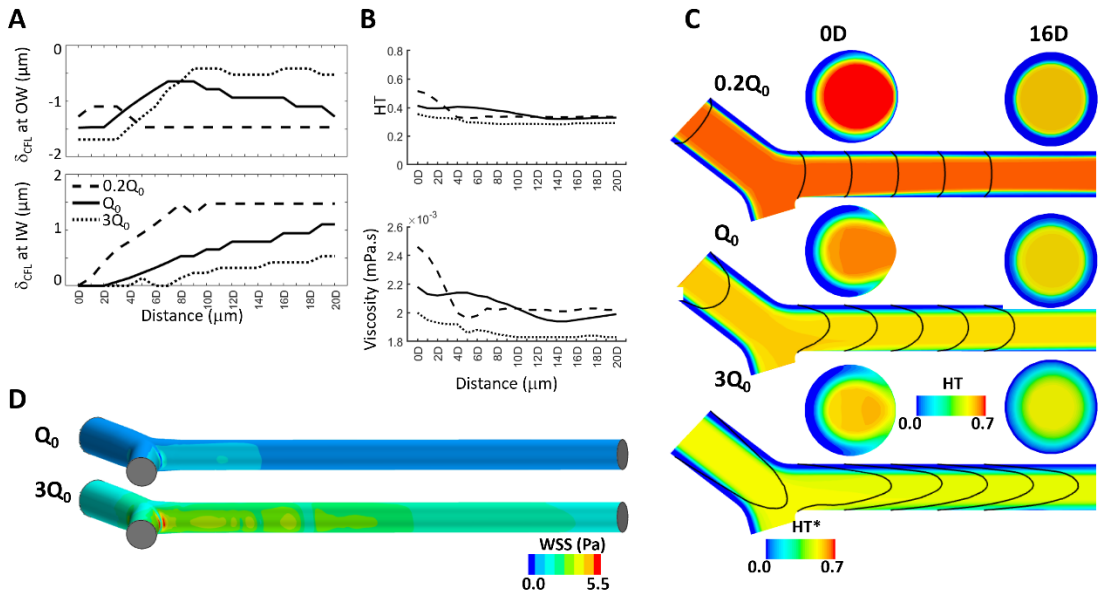

Figure 3.3: Haemodynamic variations in the symmetric bifurcation with varying inflow flow rates. (A) CFL thickness $\delta_{CFL,OW}$ and $\delta_{CFL,IW}$ along the inner and outer walls of the daughter vessels. (B) Variation of HT and apparent viscosity. (C) Tube haematocrit distribution, where the mid-plane value is derived from a reference area ratio at the 1P location (HT*), while the daughter entrance (0D position) is calculated using the local cross-sectional area ratio. The black lines represent a velocity profile. (D) WSS distribution.

3.3.3 Effects of unbalanced outflow conditions

To investigate the impact of different flow splits between the two daughter vessels, the flow rate ratio between the daughter branches (Q_2:Q_1) was modulated by increasing the outlet pressure at the d2 branch by 0.5 and 0.75 mmHg, resulting in Q_2:Q_1 ratios of approximately 0.4 and 0.2, respectively (Fig. 3.4). In the 0.4 ratio, Q_1 and Q_2 were 2.32×10^{-13} and 0.96×10^{-13} m^3/s; in the 0.2 ratio, they were 2.74×10^{-13} and 0.54×10^{-13} m^3/s, respectively.

The lowest flow split ratio (Q_2:Q_1=0.2) exhibited the most pronounced asymmetry in OW CFL thickness $\delta_{CFL,OW}$ (Fig. 3.4B) and pronounced flow development, which was indicated by the difference in haematocrit distribution between the daughter vessels d1 and d2 (as shown in Fig. 3.4A). This was confirmed by the ratio of the fraction of RBC-rich region flux to the total flow flux (FQ_E: FQ_B; Eq. 3.1-3.2; section 1.4.2.2), which was 1.04 in the high-flow branch d1 and 0.78 in the low-flow branch d2. For comparison, under the Q_2:Q_1=0.4 condition, the FQ_E: FQ_B ratio was 1.03 for d1 and 0.90 for d2. A ratio greater than 1 indicates RBC-rich enrichment in the high-flow branch, while a ratio less than 1 reflects plasma enrichment in the low-flow branch (plasma skimming). The WSS distribution further highlighted this effect, with the Q_2:Q_1=0.2 case showing the greatest disparity between the two branches (Fig. 3.4D).

The study identified a non-linear and intricate interplay between biased flow, haematocrit and effective viscosity. In branch d1, the decreased flow ratio cases (Q_2:Q_1 = 0.4 and Q_2:Q_1 = 0.2) produced a marked increase in effective viscosity (Fig. 3.4A; 4th row), while haematocrit (Fig. 3.4A; 3rd row) showed only a slight rise compared to the baseline (Q_2:Q_1 = 1). This observation underscores the exponential relationship between haematocrit and viscosity. Appendix A.5 (Fig. A.5A) reinforces this interpretation, demonstrating that even small changes in haematocrit can lead to substantial viscosity increases, as illustrated by the PSR values: 81.25 s^{-1} (54%HD, 44%HT) for Q_2:Q_1 = 0.2 versus 48.75 s^{-1} (50%HD, 41%HT) for the baseline. These results for a 16 μm diameter vessel can be compared with the 20 μm diameter case at 44% HF shown in Appendix A.5 (Fig. A.5A).

Branch d2 acts as the outlet for low-flow conditions when the flow ratio decreases. As shown in the third row of Fig. 3.4B, haematocrit levels are notably lower than the baseline: 38%HD (32%HT) at a Q_2:Q_1 ratio of 0.4, and 27%HD (22%HT) at a ratio of 0.2. The PSR values also drop dramatically, from 48.75 s^{-1} in the baseline to just 0.03 s^{-1} and 0.018 s^{-1}, respectively. Despite lower haematocrit, viscosity peaks under these conditions (Fig. 3.4B, 4th row), highlighting blood's shear-thinning nature, viscosity

increases sharply at low shear rates due to RBC aggregation [65, 72]. Appendix A.5 confirms this, showing exponential viscosity rise near-zero shear.

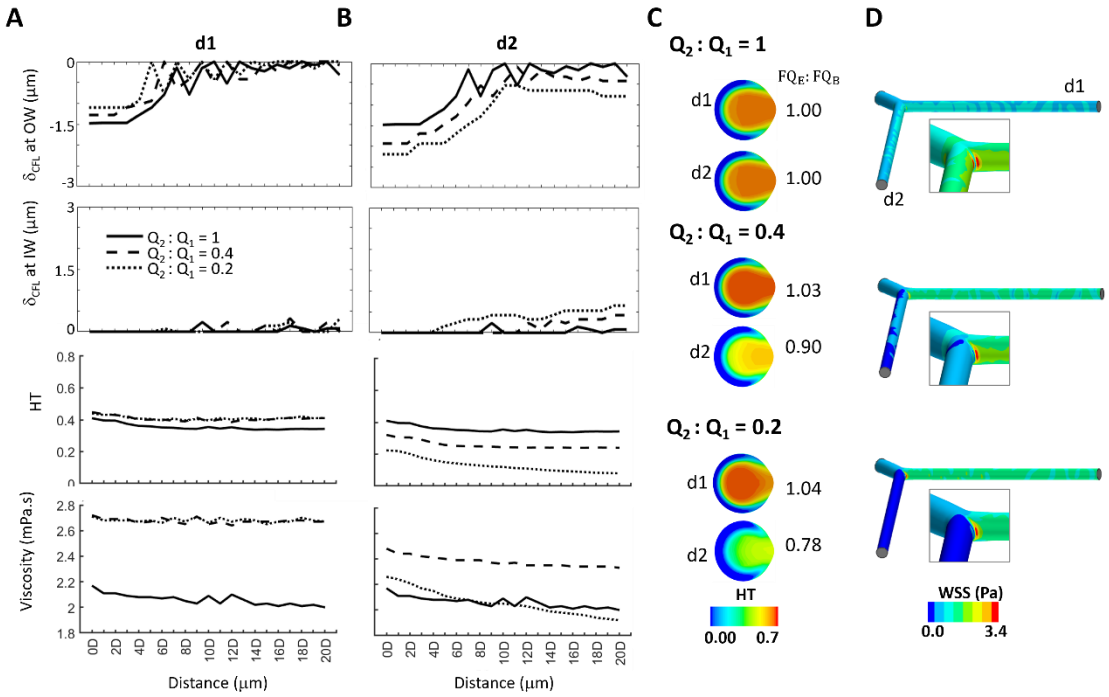

Figure 3.4: Haemodynamics variations in the symmetric bifurcation with varying outflows on two daughters (d1 and d2). (A) CFL thickness $\delta_{CFL,OW}$ and $\delta_{CFL,IW}$. (B) HT and apparent viscosity. (C) HT on the cross-sectional 0D planes and WSS distribution, with the inset highlighting elevated WSS at the apex.

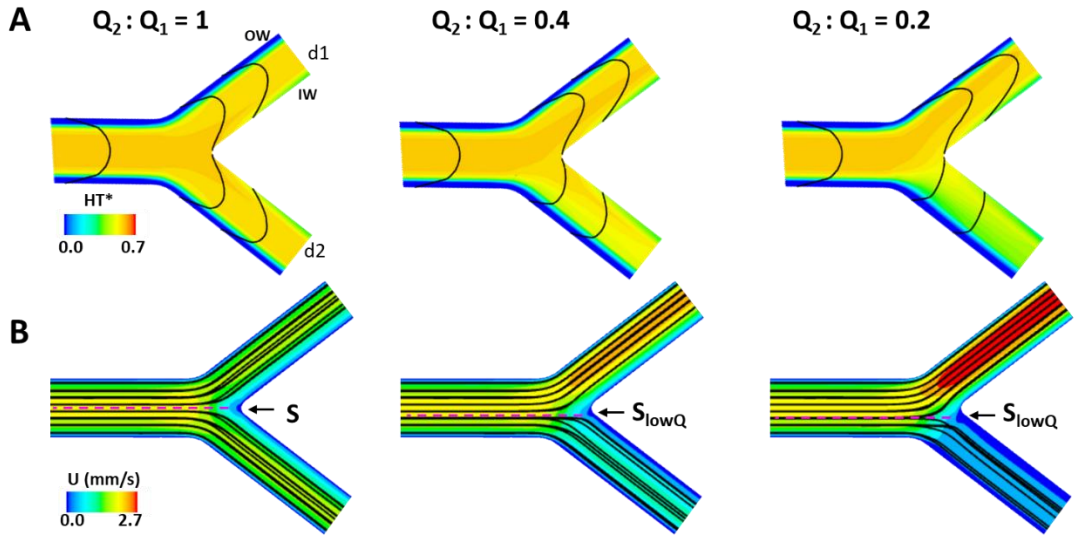

Figure 3.5: RBC phase separation under varying outflows. (A) Phase separation with RBC-core and CFL regions, represented by is represented by the relative tube haematocrit based on reference area ratio at 1P. The black lines represented the velocity profile. (B) The velocity contour with the velocity streamline. The dividing streamline (dashed pink) moved away from the apex and closer to the lower-flowrate branch d2. The stagnation shifted towards the lower-flower branch (S_{lowQ}). See Appendix B.3 for a detailed explanation of the dividing streamline**.**

In Fig. 3.5B, the dividing streamline of the flow being directed to each of the daughter branches and the stagnation point shifted towards the lower-flow rate d2 branch. This adjustment resulted in enhancing the RBC-rich region transport into the higher-flow branch d1, while the branch d2 received more plasma, as illustrated in Fig. 3.5A. The increased diversion of the RBC-rich region into branch d1 was likely due to the higher resistance in branch d2, with the pressure ratio between d1 and d2 (P_1/P_2) of 99.1% and 98.6% under the Q_1:Q_2 = 0.4 and Q_1:Q_2 =0.2, respectively.

When the flow rate ratio was reduced, the vortex-like feature in the slip velocity field near the upstream wall moved towards the entrance of the high-flow daughter branch, while being deformed and moving away from the entrance of the low-flow branch (Fig. B.4). The slip velocity, vorticity and lift force increased in the high-flow d1 branch, consistent with the higher RBC-rich influx. In contrast, the low-flow d2 branch exhibited weaker forces due to a reduced entry of RBC-rich region.

3.3.4 Effect of different diameter of the d2 daughter

To investigate how variations in the diameter of the neighbouring d2 branch influence downstream haemodynamics, the d2 branch diameter was varied relative to a fixed d1 diameter of 16 μm, using ratios of 1.2d1 and 0.7d1, which were derived from Eq. 3.1 to represent a physiologically realistic asymmetric bifurcation [149]. As shown in Fig. 3.6A&B, the daughter diameter significantly affected the symmetric CFL recovery. In d1, the CFL symmetry was achieved at 14D, 16D and 16D, with $\delta_{CFL,SYM}$ of 0.6, 0.9 and 1.3 μm, while in d2, it occurred at 11D, 16D and 18Dat the $\delta_{CFL,SYM}$ of 0.4, 0.9 and 1.8 μm, for the 0.7d1, 1.0d1 and 1.2d1 cases, respectively. This variation arose from the difference in the hydraulic resistance. The narrower branch exhibited higher resistance and lower flow rate, as would also be predicted by the Poiseuille's law ($R=8\mu L/\pi r^4$; $Q=\pi r^4 \Delta P/8\mu L$), leading the RBC-rich region to preferentially entry the wider, lower-resistance branch. As highlighted in Fig. 3.6C & 3.7A, these flow conditions demonstrated plasma skimming. The wider daughter branches showed RBC enrichment (FQ_E/FQ_B = 1.91 and 1.03 at 1.2d1 and 0.7d1, respectively), while the narrower branches presented RBC depletion and richer in plasma (FQ_E/FQ_B = 0.97 and 0.86, respectively).

In a single bifurcation, the smaller daughter branch consistently exhibited lower haematocrit and viscosity than the larger one (Fig. 3.6A&B). For the 0.7d1 case, the wider d1 branch showed higher WSS (Fig. 3.6C) due to lower CFL thickness (Fig. 3.6A, 1st and 2nd rows), higher haematocrit (Fig. 3.6A, 3rd row), and higher viscosity (Fig. 3.6A, 4th row), in comparison to the narrower d2 branch (Fig. 3.6B). When comparing the d1 branch across three cases, differences in HT at the 0D position (Fig. 3.6A&C) reduced and became equal at approximately 20D. However, the d1 branch under the 0.7d1 condition had a thinner CFL thickness, resulting in higher viscosity and WSS, when compared to the remaining cases. Interestingly, both d1 and d2 branches in diameter-asymmetric bifurcations exhibited higher viscosity than in the symmetric geometry with equal daughter diameters. For example, the increased viscosity of d2 branch under 0.7d1 condition was due to reduced CFL thickness, despite lower haematocrit in comparison to the symmetric bifurcation. This suggests that the distribution of the RBC-rich region near the wall, as governed by the height of

the CFL thickness, is a crucial factor in determining viscosity, not just the overall haematocrit.

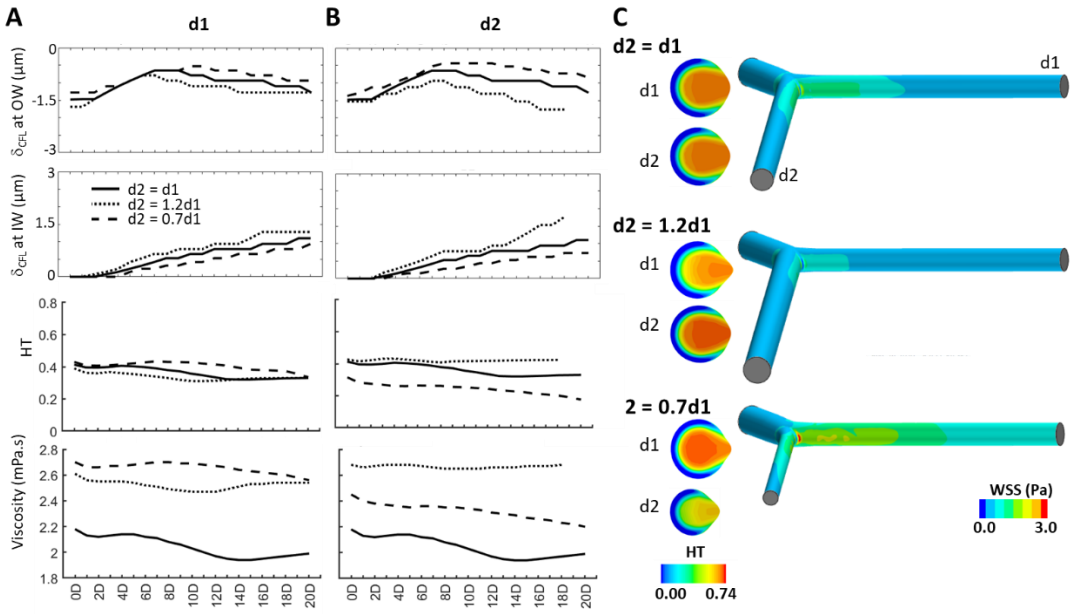

Figure 3.6: Haemodynamic variations in the diameter-asymmetric bifurcations on two daughters (d1 and d2). (A, B) CFL thickness $\delta_{CFL,OW}$ and $\delta_{CFL,IW}$ (top two rows), HT (third row) and apparent viscosity (fourth row), for branches d1 (A) and d2 (B). (C) HT on the cross-sectional 0D planes and WSS distribution.

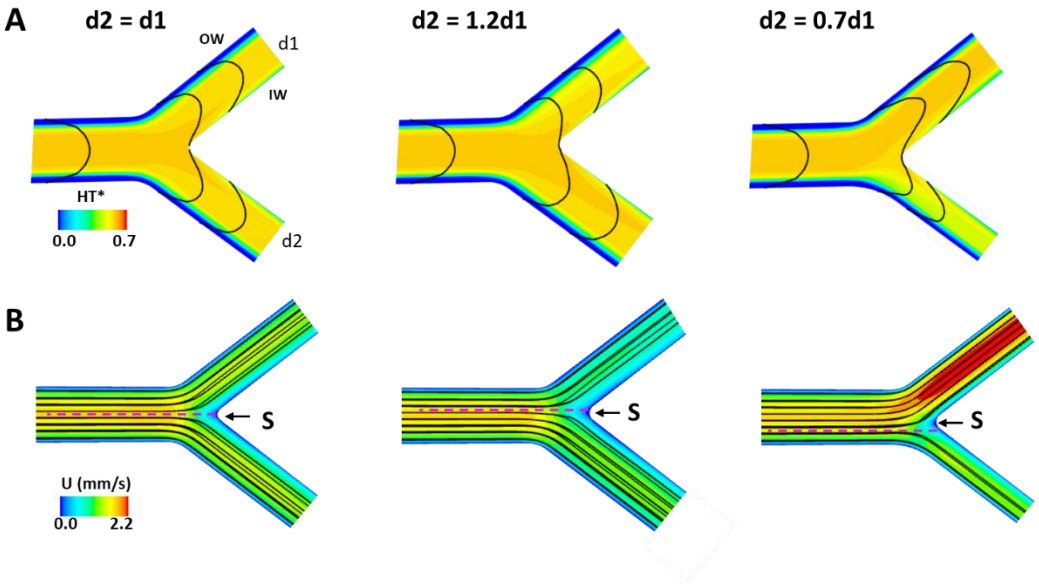

Figure 3.7: Flow development in diameter-asymmetric bifurcations. (A) Flow distribution of the RBC-rich and CFL regions on the midplane of the tubular vessels, represented by the normalised haematocrit (HT*), derived from a reference area ratio at the 1P location. The black lines represented the velocity profile. (B) The velocity contour on the midplane overlaid by 3D velocity streamlines. The dividing streamline (dashed pink) shifted towards the narrower (lower-flow) branch, with a central stagnation point. See Appendix B.3 for a detailed explanation of the dividing streamline**.**

As demonstrated above, the flow development was governed by differences in the daughter vessel diameters. Despite similar pressure and a central stagnation (Fig. 3.8B), the dividing streamline tended to shift towards the narrower branch, directing more RBC-rich flow into the wider branch (Fig. 3.8A). Fig. B.5 in Appendix B.5 revealed that high vorticity was detected on the bifurcation outer-wall curve towards the wider branch, accompanied by a vortex-like slip velocity pattern near the daughter entrance. In contrast, the bifurcation curve towards the narrower branch exhibited low vorticity and weak lift force, with the vortex-like slip velocity pattern appearing to be cancelled out and located further from the daughter entrance. The results suggest that the asymmetric distribution of forces, specifically high vorticity and lift on the curved outer-wall connected to the wider daughter branch, is the direct physical mechanism responsible for directing the RBC-rich flow into the wider diameter bran. Meanwhile, the narrower branch received less RBC-rich flow due to the absence of these forces.

3.3.5 Effect of inter-bifurcation distance

To evaluate how inter-bifurcation distance (λ) influenced the downstream CFL recovery, the 1st-generation branch length was varied between 4D and 8D, based on findings in Chapter 2 that a concentric CFL typically forms at 16D under baseline condition (0.44 HF, 1 mm/s). It is consistent with studies of 'tumour-inspired' networks that use a 4D distance to demonstrate CFL recovery failure, a condition found in vessels with diameters in the 20-40 μm range [5]. As expected, (Fig. 3.8A&C), a shorter λ=4D was insufficient for full concentric CFL in the region upstream of the 1st-generation branches (d1 and d2, Fig. 3.8B). This upstream asymmetry in the flow enhanced plasma skimming, leading to more RBC-rich flow entering the d4 branch, which was connected to the IW region of d1 where the CFL was thinner. In contrast, the OW of the d3 branch was a continuation of the OW of the d1 branch, where the CFL was thicker, and thus received less RBC-rich flow. As a result, the d4 branch exhibited a higher RBC-rich influx and a higher flow rate, with a Q_3:Q_4 flow ratio of 0.76. Extending λ to 8D promoted a more symmetric CFL recovery and more balanced RBC-rich flow distribution. At the 0D cross-sectional plane, the d3 and d4 branches showed tube haematocrits of 38% and 50% (λ=8D) compared to 31% and 61% (λ=4D) (Fig.3.8A), respectively, despite the similar HT (39%-40%) at the region upstream of the 2nd generation bifurcation and nearly identical Q_3:Q_4 flow ratios (~0.77). This suggests that the uneven distribution of the RBC-rich region stemmed from the upstream CFL configuration rather than the flow split differences, for the same diameter daughter vessels under the same outlet pressure conditions.

In Fig. 3.8D, despite the central stagnation point, the dividing streamline was shifted towards the lower-flow d3 branch. Consequently, more of the RBC-rich region was directed towards branch d4, reinforcing the plasma skimming effect. Slip velocity profiles further support this interpretation (Fig. B.6). At the end of the d1 branch, the λ=4D condition exhibited a greater upstream unbalanced force than the λ=8D condition. This was evident with the thinner CFL, which showed higher vorticity and lift along the IW of d1 compared to OW.

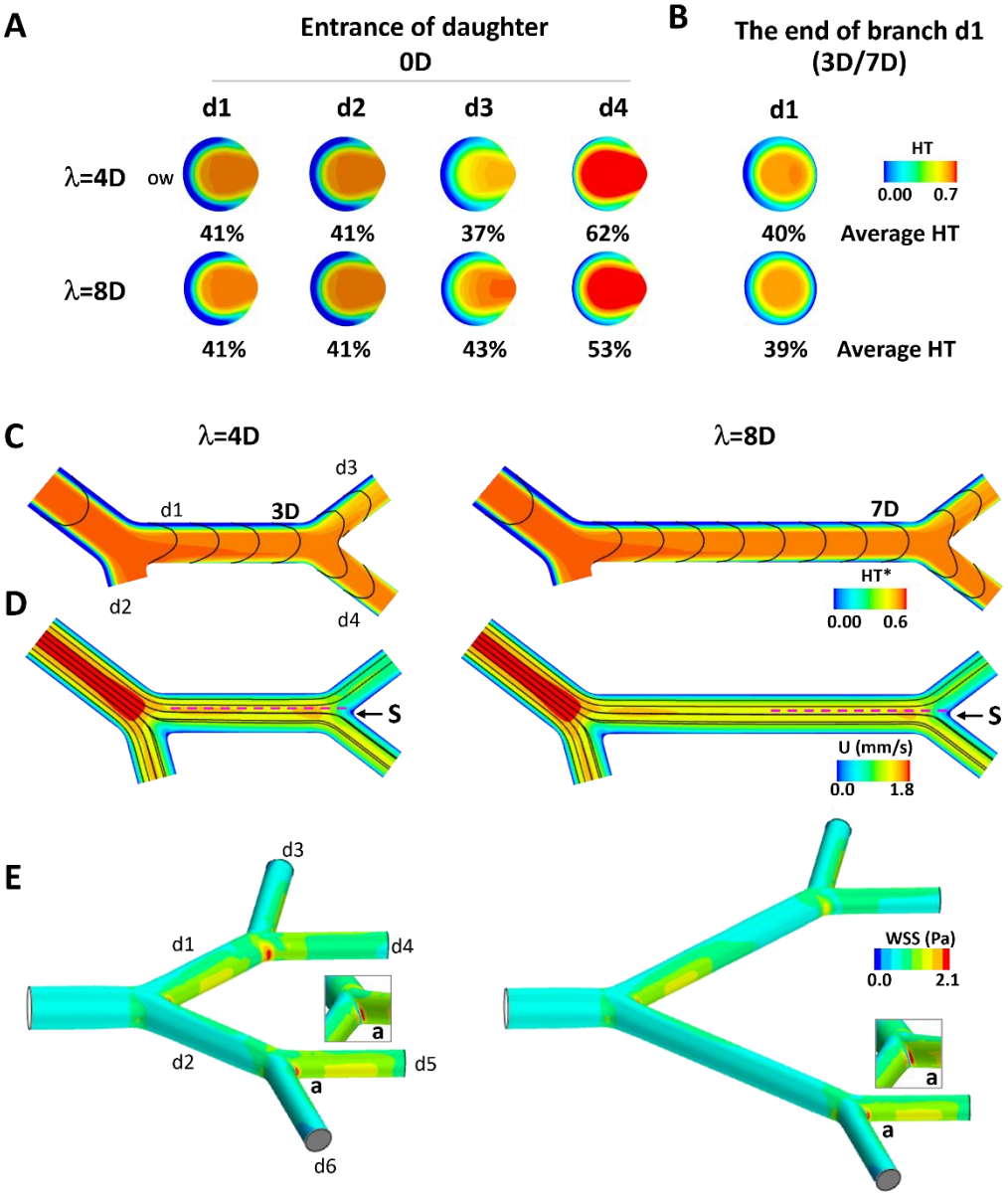

Figure 3.8: Haemodynamics in arteriole networks with different inter-bifurcation distance. (A) The HT on cross-sections at the daughter entrance (position 0D) for branches d1-d4 and at the region upstream of d1 at 4D and 8D cross-sections for λ=4D and λ=8D, respectively. The HT with the area-weight at specific cross-sections. (B) The mid-plane of the planar tubular network coloured by HT*, which is derived from a reference area ratio at the location 1P of the parent (d0) branch. (C) The velocity contour on the mid-plane, overlaid by velocity streamlines. The dividing streamline (dashed pink line) was shifted towards the d3 branch despite the central stagnation. (D) WSS distribution, with insets comparing WSS at apex of the second bifurcation. See Appendix B.3 for a detailed explanation of the dividing streamline.

Interestingly, this asymmetric partitioning also influenced the WSS. The shorter inter-bifurcation distance led to a non-uniform WSS profile along the IW of d1, with higher WSS observed at the apex between the d1 and d4 compared to that between d1 and d3 (Fig. 3.8E). Simultaneously, the asymmetry was observed at the apex of the second bifurcation, where the entrance to d3 experienced higher peak WSS than d4, as highlighted in the inset. Since the branch d2 bifurcated into the d5 and d6 branches in a symmetric way as the d1-d3-d4 bifurcation, the mirrored results were observed, i.e. the inner, d5 branch exhibited the same RBC-rich flow distribution as d4, while the outer d6 branched had the mirror flow of d3.

3.3.6 Dominant and secondary determinants of CFL formation

Feeding haematocrit and inflow constituted the dominant determinants of CFL behaviours because they established the fundamental physical environment within which RBC-rich phase organised. The inflow rate defined the shear forces and velocity gradients that generated lift forces, which drove RBC-rich phase away from the vessel wall and initiated CFL formation. Haematocrit, in contrast, governed the extent of cell–cell interactions: higher concentrations increased collisions and repulsion, thereby restricted the expansion of the CFL, while lower haematocrit permitted greater radial migration. As summarised in Table 3.2, these two independent variables combined established the initial apparent viscosity, CFL thickness and the primary distribution of RBC-rich and plasma phases before the flow encountered any geometric irregularities or bifurcations.

By comparison, vessel geometry, biased outflow, and inter-bifurcation distance were considered secondary factors because they did not generate the CFL but instead modified the pattern established upstream. As outlined in Table 3.3, diameter asymmetry and outflow imbalance influenced how the RBC-rich core divided between daughter branches, producing different degrees of plasma skimming, yet these effects depended entirely on the RBC distribution already shaped by haematocrit and inflow. Similarly, the inter-bifurcation distance determined whether upstream asymmetry was retained or was dissipated: a short distance restricted the ability of lift and shear forces

to restore symmetry, while a longer distance allowed full recovery. These variables acted as modulators that adjusted or preserved pre-existing flow characteristics rather than creating new haemodynamic conditions.

Relative sensitivity was assessed by calculating the proportional change in tube haematocrit and apparent viscosity along the d1 branch under each parameter variation, using the standard baseline (44% HF with symmetric bifurcation and balanced outflow) as the point of reference (Fig. 3.9). Across all perturbations, HF and inflow generated the highest relative deviations, whereas biased outflow and diameter asymmetry induced low-magnitude, slowly varying responses. This quantitative ranking corroborates the conceptual distinction between dominant and secondary parameters.

Table 3.2: Influence of Feeding Haematocrit and Inflow on CFL Formation and Apparent Viscosity

Parameter	Condition	Impact on		Primary Regulators
		CFL	**Viscosity**	
HF	**High** (66% HF)	Thinner; Faster symmetric recovery	Higher	Determines fundamental fluid properties
	Low (18% HF)	Thicker; Symmetry not established	Lower	
Inflow	**High** ($3Q_0$)	Thinner; Delayed recovery	Lower	Drives lift forces and RBC phase migration
	Low ($0.2Q_0$)	Thicker; Faster recovery	Higher	

Table 3.3: Effects of Geometric and Flow Asymmetries on Phase Separation and CFL Recovery

Parameter	Condition	Impact on		Primary Regulators
		Phase separation	**Symmetric recovery**	
Biased Outflow	Unbalanced (Q_2=0.2Q_1)	Significant plasma skimming at the low-flow branch (d2)	Not determined	Shifts dividing streamlines and stagnation points
Diameter asymmetry	Wider d2 (d2=1.2d1)	RBC phase enriches in d2	Delayed symmetry in d2	Dictated by hydraulic resistance
	Narrower d2 (d2=0.7d1)	Plasma skimming in d2	Earlier symmetry in d2	
Inter-bifurcation distance	Short (λ=4D)	Enhance plasma skimming into the 2nd generation	Failure of CFL recovery at the 1st generation	Dictates spatial partitioning based on inherited upstream radial distribution
	Long (λ=8D)	More balance RBC distribution	Promote symmetric recovery	

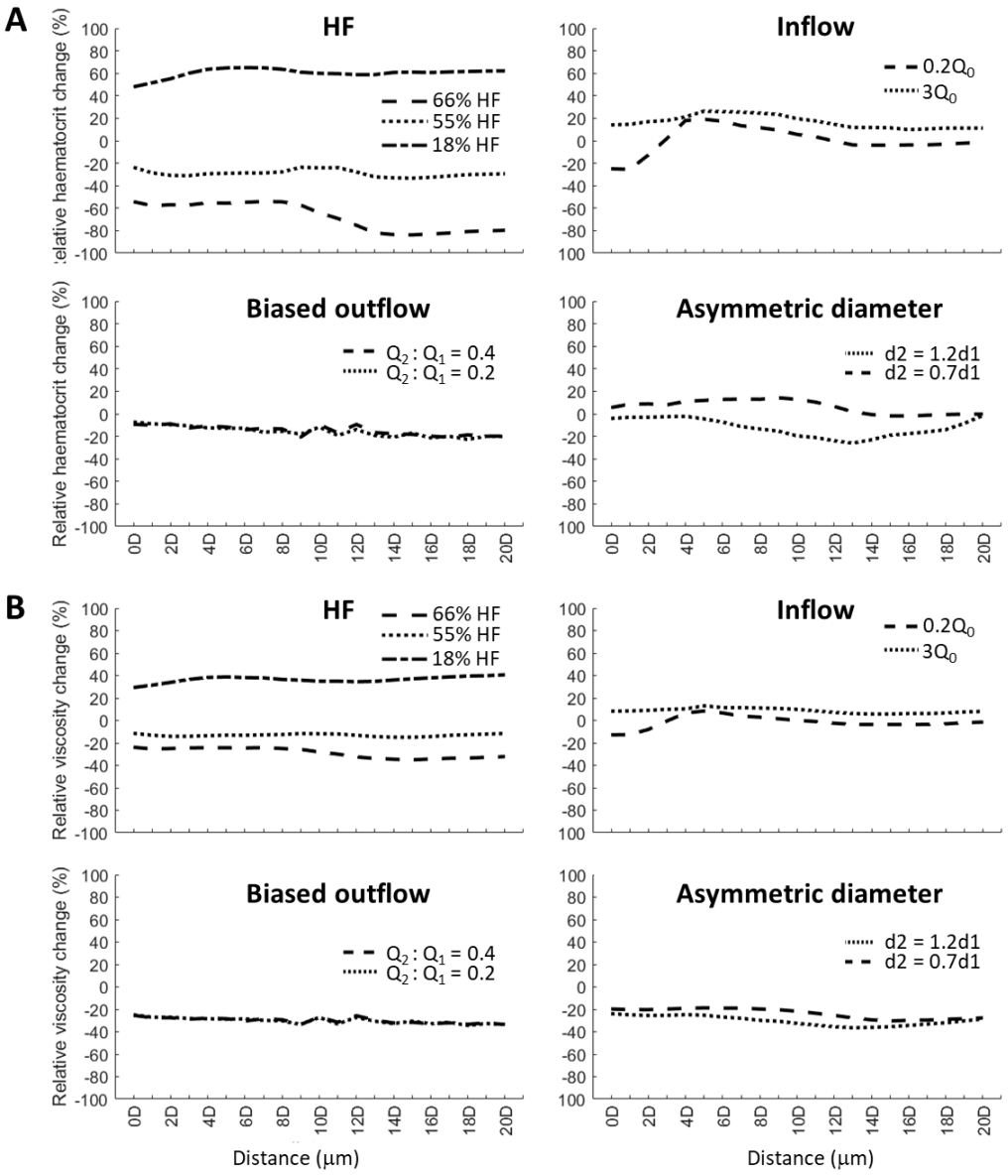

Figure 3.9: Relative change in (A) tube haematocrit and (B) apparent viscosity along the d1 branch under variations in feeding haematocrit, inflow rate, biased outflow, and diameter asymmetry, normalised by the baseline condition (44 % HF with symmetric bifurcation and balanced outflow)**.**

3.4 Discussion

3.4.1 Downstream recovery of symmetric CFL

Symmetric CFL recovery in the 16 μm daughter vessel occurred between 8D and 16D, depending on feeding haematocrit (18%–66% at 53 s^{-1}), inflow (13–153 s^{-1} at 44%HF) and bifurcation geometry (at 44%HF and 53 s^{-1}). Lower haematocrit reduced the blood viscosity, delaying the CFL symmetric recovery, while producing thicker CFL layers. Under stronger inflow rates, the CFL recovery was delayed, and it became thinner due to intensified shear forces. In diameter-asymmetric bifurcations, the recovery distance in d1 was influenced by the d2 diameter. Wider d2 branches (1.2d1), exhibited a higher flow rate and delayed CFL recovery to 16D, while narrower ones (0.7d1) allowed earlier CFL recovery at 14D. These findings highlight the complex interplay between haematocrit, flow rate, flow resistance and geometry in shaping CFL dynamics. The comparison with other works is discussed in Chapter 2.

3.4.2 Influence of feeding haematocrit and inflow

Our simulations demonstrated that low feeding haematocrit produced a pronounced CFL, associated with low vorticity and thus weaker lift forces. In contrast, high haematocrit resulted in the CFL recovering symmetry over a shorter downstream distance, high vorticity and stronger lift forces, indicating greater RBC–wall interactions. This strong lift induced a vortex-like slip velocity motion in the RBC-rich core region, and the high haematocrit condition also promoted a quicker development of symmetric slip velocity. This behaviour reflects the influence of RBCs concentration on haemodynamic forces: fewer cells mean reduced wall collisions, leaving a broader CFL. Salame and Fenech (2025) [7] reported similar findings in 25–50 μm microchannels, where a low haematocrit promoted CFL expansion due to reduced cell-cell interactions and enhanced lateral migration.

Under comparable haematocrit, increasing inlet flow rate significantly reduced the CFL thickness in our simulations. Higher flow rate amplified the shear and lift forces, accelerating the RBC-rich migration towards the core and displacing the plasma

towards the wall. Salame and Fenech (2025) [7] inferred the role of lift forces from shear rate gradients, suggesting that at low shear gradients, rouleaux formation impairs lift and limits the CFL development; at higher gradients, disaggregation restores RBC deformability, facilitating lift-induced CFL thickening. Our direct lift force measurements validate this interpretation, confirming that higher flow rates, and thus higher shear gradients, produce stronger lift forces and thicker CFLs.

Both haematocrit and flow rate influence the CFL development through hydrodynamic lift, but via distinct pathways (shear vs concentration). At low haematocrit, reduced cell-cell interaction (aggregation) and fewer collisions allow RBCs to deform and migrate freely, whereas at high flow, shear gradients dominate, overcoming aggregation and enhancing lift. These complementary mechanisms explain why thick CFLs occur under both conditions, reinforcing previous reports that CFL thickness depends on haematocrit [83, 238] and shear forces [239]. Furthermore, RBC partitioning at bifurcations also depends on the upstream haematocrit distribution [240-242].

3.4.3 Influence of biased outflow

At the lowest flow ratio, the simulations showed pronounced asymmetry in the downstream CFL and a high degree of plasma skimming, leading to a significant haematocrit difference between the daughter vessels, an outcome consistent with the Zweifach-Fung effect [177, 178]. The unequal outflows shifted the dividing streamlines and stagnation points towards the low-flow branch. As a result, the RBC-rich central flow was directed into the high-flow branch, while the low-flow branch received plasma-rich peripheral fluid. The disproportionality of flow rate between the two daughter branches affected the eccentric position of the dividing streamline [243] and protrusion cap [73], resulting in unequal stream paths for the RBC-rich region. The protrusion cap refers to a curved zone near the bifurcation apex where red blood cells initially follow streamlines into the lower-flow branch but are subsequently diverted into the higher-flow branch due to streamline separation [73]. This

observation aligns with previous studies reporting that the separating streamline of the flow tends to attach towards the low flow rate daughter vessel [240, 244].

In the high-flow daughter branch (d1), a greater influx of RBC-rich regions correlated with increased slip velocity, vorticity and lift force. The strong forces on the bifurcation curve generated a stronger lift force, driving the RBC-rich region more towards the centre and reinforcing the high RBC-rich concentration in d1. Within d1, the elevated RBC-rich concentration intensified interactions with the surrounding plasma, producing sharper shear gradients and higher vorticity, which further increased the lift force. In contrast, the low-flow branch (d2) experienced weaker forces, reflecting reduced RBC-rich entry (RBC-depleted regions) and a less haemodynamic variation. This is confirmed by the vortex-like slip velocity in the RBC-rich core, where the upstream vortex shifted towards the entrance of the d1 branch and was detected more frequently in this branch. Conversely, the upstream vortex was eliminated and moved further from the d2 entrance, which predominantly exhibited axial slip velocity rather than vortex formation.

3.4.4 Influence of diameter-asymmetric bifurcations

This study demonstrated the underlying mechanism of how the diameter of the daughter branches influences the downstream recovery of symmetric CFL due to differences in hydraulic resistance, with narrower branches having higher resistance and lower flow. The simulations showed the occurrence of plasma skimming, where wider branches preferentially received the RBC-rich regions, while narrower branches received a plasma-rich flow. Evidence of increased flow rate in the wider daughter branch resulting in higher haematocrit is reported in studies on micro-occlusion in animal microvessels [177] and simulations using a diffusive flux model [245].

The central stagnation point in the diameter-asymmetric bifurcations suggests that flow development is primarily governed by an asymmetric distribution of hydrodynamic forces. The dividing streamline shifts towards the narrower branch, directing the RBC-rich flow into the wider branch. This occurs because the curved

bifurcation along the OW connecting to the wider branch exhibited high vorticity and lift force, while the one leading to the narrower branch has low vorticity and lift force. As with biased outflow, a vortex-like slip velocity moves towards the daughter's entrance with high vorticity, whereas the vortex was disrupted and located further away from the entrance of the low-vorticity branch. This is consistent with the finding that a greater bending angle of the branching curvature along the OW in the narrower side branch is associated with more pronounced attenuation of CFL width in the parent vessel [182].

The high vorticity and lift force within the wider branch (exhibiting higher flow) are a result of a greater concentration of RBCs in the RBC-rich region and more intense interactions with the plasma. In contrast, the lower haemodynamic forces in the narrow branch reflect a reduced RBCs concentration and weaker interactions. Therefore, the higher flow rate in the wider branch arises as a consequence of the RBCs enrichment, rather than being driven by an independent external force.

3.4.5 Influence of inter-bifurcation distance

In the short inter-bifurcation distance (λ=4D), the asymmetric CFL observed at the region upstream of the 1st-generation branches (i.e., within d1) enhances plasma skimming at the subsequent bifurcation, directing a greater proportion of the RBC-rich region in the 2nd-generation branch d4, which was in continuation of the thinner CFL region in d1 (i.e., d4). Consequently, the trajectory of the RBC-rich component from the upstream to the downstream vessels is governed by its initial radial position within the region of the upstream branch. This is directly supported by Pskowski et al. (2022) [246], who demonstrate that after an initial bifurcation, RBCs remain skewed toward the inner wall and enter the next bifurcation with a positional bias that leads to preferential flow into the adjacent daughter channel. Quantitative evidence shows that CFL asymmetry at short inter-bifurcation distance causes uneven haematocrit split [5], and that asymmetric CFL in the upstream vessel influences RBC separation [247, 248]. Hyakutake et al. (2022) [249] report that RBC distribution in the parent channel significantly influences partitioning in the daughter channels.

3.4.6 Physiological relevant

Our main observation is that CFL is acutely sensitive to both systemic factors (such as haematocrit) and local conditions (including flow rate and geometry), providing a unified, physics-based framework that explains key phenomena in both physiological regulation and pathological states such as ischaemia. The simulation offers a compelling haemodynamic explanation for the microvascular dysfunction observed during upstream occlusions (sections 3.3.1 and 3.3.2). In the low-flow, low-pressure environment characteristics of ischaemia, our model shows that altered CFL dynamics lead to an increase in apparent viscosity at the daughter entrance (Fig. 3.3). This provides a precise physical basis for experimental findings, such as those of Yalcin et al. (2015) [193], which attributed the increased vascular resistance post-occlusion to changes in blood properties. This is consistent with clinical data from Allport et al. (2005) [2] and Harrison et al. (1981) [21], where high haematocrit was linked to poorer stroke outcomes. Our model provides a physics-based framework for investigating perfusion deficits as we show that haematocrit is determinant of CFL dynamic and effective viscosity (as Fig. 3.2). These factors govern perfusion: high apparent viscosity (at high HF) directly increases flow resistance, while the altered CFL thickness provides a direct mechanism to study future impacts on both oxygen diffusion distance [111, 112] and the WSS-mediated release of vasodilators such as NO [236].

This study explains the complex microvascular response to a downstream occlusion (Fig. 3.4). Research by McGahren et al. (1997) [250] and Frisbee et al. (2000) [251] used a parallel occlusion model to investigate flow-induced dilation, occluding one daughter branch to augment flow through the unoccluded branch. Our findings indicate that the unoccluded branch receives a greater flux of the RBC-rich region and an increased flow rate, producing a thinner CFL and higher WSS. This elevated shear stress is the presumed a stimulus for the release of vasodilators from the endothelium, which is the focus of those papers [238, 239].

The potential applications of this study can extend from ischaemic conditions to stroke modelling and broader vascular pathology. The findings may be integrated into advanced computational models to more accurately predict infarct size using patient-specific haematocrit and occlusion data, thereby potentially supporting personalised ischaemic or stroke management. The work also can provide a promising rationale for haemodilution therapy, offering a framework through which reductions in haematocrit might be quantitatively linked to improvements in viscosity and flow, thus guiding future therapeutic targets [2]. Beyond ischaemia and stroke, the simulation platform could serve as a valuable preclinical tool for screening novel agents that alter RBCs behaviour and may also help to illuminate microvascular impairment in conditions such as sepsis, diabetes and dementia.

3.4.7 Limitation and Future work

A primary limitation of the current study is the lack of direct experimental validation. While our simulations show tendencies in blood behaviour consistent with other studies, a direct comparison with microfluidic or *in vivo* data under identical conditions is necessary to fully confirm the model's accuracy. We have successfully reproduced similar blood behaviours to previous experimental and computational findings, such as (1) the influence of shear rate and haematocrit on the CFL thickness, (2) the dependence of RBC-rich distribution on upstream haematocrit patterns, and (3) the effect of unequal outflows on dividing streamlines and stagnation points. However, the absence of a one-to-one validation of our specific parameter combinations and geometric setups with physical experiments means our findings primarily serve as a theoretical exploration of these hemodynamic principles. Another limitation was the assumption of planar geometries. Despite the simplification, this facilitated the interpretation of the underlying mechanisms of the CFL development.

Future work should expand the scope of the model to include additional rheological parameters and more complex flow conditions. In particular, incorporating the effects of RBC aggregation and deformability is crucial, as these factors are known to significantly influence the CFL dynamics and the overall haemodynamics in the

microcirculation. The current simulations focus on flow regimes where these effects are less prominent, but their inclusion would enhance the physiological relevance and applicability to a wider range of clinical conditions. A more detailed discussion of these parameters can be found in Chapter 2.

Another area for future development involves refining the initial conditions of the simulations. This study simplifies the upstream blood flow by assuming a symmetric CFL. Moving forward, it would be beneficial to conduct simulations with asymmetric CFLs or a non-uniform radial haematocrit distribution in the parent vessel. Such conditions offer a deeper insight into how pre-existing asymmetries affect the downstream CFL recovery and partitioning behaviour. Since the path an RBC takes is determined by its initial radial position, starting with an asymmetric haematocrit distribution would allow for a more accurate investigation into how heterogeneous flow conditions propagate through a network and contribute to specific pathological states such as ischaemia. This is especially relevant given that asymmetric upstream conditions have been shown to influence RBC separation and downstream partitioning.

Chapter 4

Multi-phase, multi-component blood flow model on anatomically-realistic testicular bifurcations

4.1 Introduction

The cardiovascular system relies on a combination of rapid convective transport and slow-localised diffusion to efficiently deliver oxygen to every cell [252]. This process is complicated by the unique architecture of the microvasculature, where the branching of vessels can cause red blood cells to distribution. Under low-flow conditions, red cell aggregation and sequestration at bifurcations can increase haemodynamic resistance, leading to non-linear pressure–flow relationships that deviate from Poiseuille's law [50] To manage this and ensure proper oxygen and nutrients' exchange, the body uses capillary recruitment, a mechanism regulated by arteriolar resistance. The size of this regional exchange area is determined by the number of perfused capillaries [253].

While small arteries (~300 μm) contribute some resistance, arterioles serve as the primary regulators of regional blood flow. These vessels also exhibit mechanical autoregulation, which is a key characteristic of the microvasculature that helps maintain constant blood flow. First described by Bayliss [254], autoregulation ensures that an increase in arteriolar pressure causes the vascular smooth muscle to contract, thereby stabilising blood flow to vital organs such as the brain and heart over a wide range of pressures. This mechanism is crucial for regulating flow in response to high metabolic activity and tissue hypoxia, which prompt the dilation of local arteriolar vessels to increase the microcirculatory exchange area [255].

The testes are vital for producing sperm production and steroid hormone secretion [256], with spermatogenesis occurring in the seminiferous tubules. These vessels, which include arterioles, venules, or thick capillaries, are found situated within the

columns of tissue surrounding the tubules [23, 24]. Larger blood vessels are generally found within these intertubular columns. Arterioles create two types of capillaries: a mesh-like network of peritubular capillaries and a complex intertubular branching pattern (Fig. 4.1A-C). Intertubular capillaries either connect to the peritubular mesh or drain into an intertubular venule, called arterio-venous anastomoses, which bypass capillary beds, help regulate blood flow and pressure and facilitate heat exchange. Additionally, arterioles can form arterio-arterial anastomoses (Fig. 4.1C) creating a redundant vascular network that maintains the blood flow supply and prevents ischaemia during localised disruptions. A common feature is a thicker intertubular capillary (≥15 μm) that forms a direct connection from an arteriole to a venule within the same column, forming an intertubular arteriolo-venular capillary channel [23]. At the branch points of these intertubular vessels, undifferentiated spermatogonia are clustered within a specialised microenvironment of the basal compartment, as shown in Fig. 4.1D [257], as shown in Fig. 4.1D.

The primary objective of this work was to evaluate whether a multi-phase, multi-component model can be applied to subject-specific anatomically-realistic 3D microvascular bifurcations that incorporate non-planar geometry and angles, curvature and tortuosity, as well as vessel tapering, features that idealised models cannot capture. Using this framework, we investigated how subject-specific vessel geometry influences key flow characteristics, including the CFL formation and plasma skimming. Ultimately, this approach aims to enhance our understanding of haemodynamic regulation within the rat testicular vasculature, where complex bifurcation geometry plays a critical role in microcirculatory resistance and flow distribution. To achieve this, the model was applied to testicular arterioles branching into small distal arterioles or thick capillaries with a diameter of approximately 20 μm, reflecting physiologically relevant vessel dimensions.

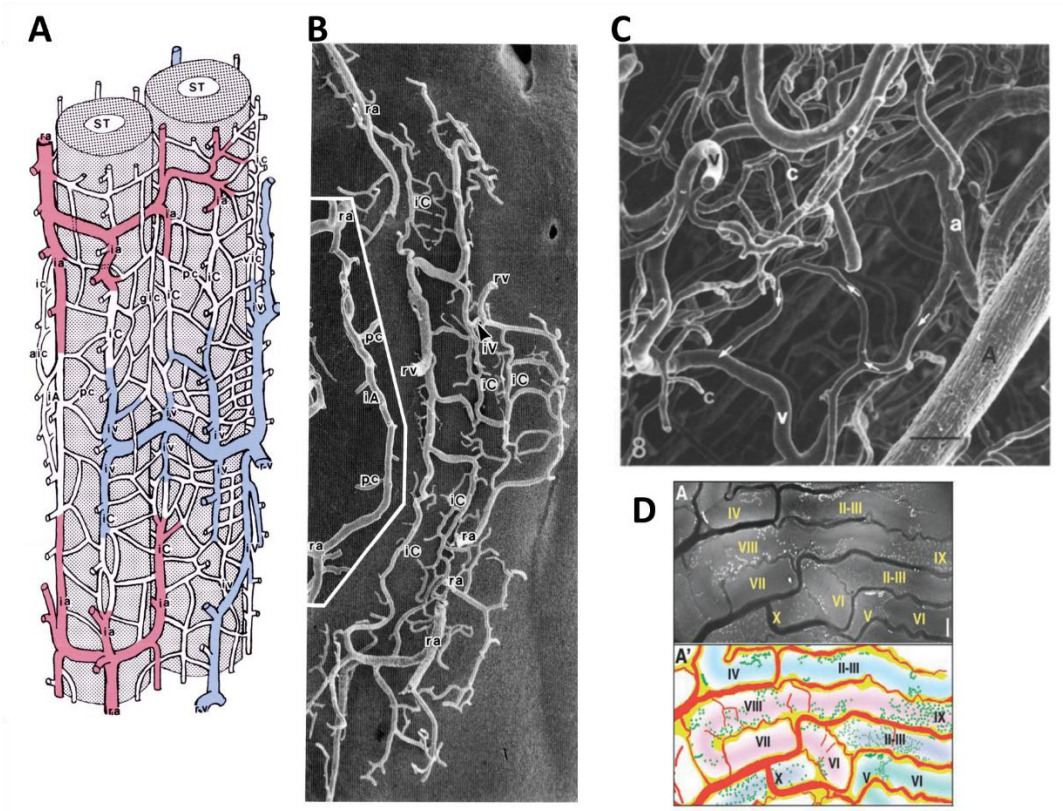

Figure 4.1: Testicular microvascular networks. (A) Diagram showing the distribution pattern of intertubular arterioles (ia, red-coloured vessels), capillaries (ic, white), and venules (iv, blue), and peritubular capillary (pc, white) around the seminiferous tubules (ST) [24]. (B) A scanning electron microscopic study of the network [24]. Note that the terminal branches of radiate artery (ra) and radiate vein (rv) are distributed at a different level of the networks. (C) Micrograph of arterio-arterial anastomoses (arrows) [23]. (D) Seminiferous epithelial, spermatogonia (dot green) with intertubular arterioles and venules [257].

4.2 Material and methods

4.2.1 Reconstruction of testicular network

From optical projection tomography (OPT) images of a healthy rat testis, provided by Dr. Junxi Wu (University of Strathclyde, following all animal ethical protocols), three distinct vascular bifurcations were chosen for reconstruction into subject-specific anatomically-realistic three-dimensional models using SimVascular [258] (Fig. 4.2). These geometries, labelled ‘A’, ‘B’, and ‘C’, were selected from different regions within the testis. The reconstruction process began with establishing centreline paths

by manually placing control points along the lumen. Lumen boundaries were segmented with a circular tool on various two-dimensional slices, which were then lofted to create a three-dimensional solid model. After refining the model with the PolyData method, it was smoothed to eliminate artefacts. Finally, the vessel boundaries were extended by 10D using VMTK [259] to minimize boundary effects. The hydraulic diameters of the original vessels were approximately 24 μm, 23 μm, and 20 μm, for bifurcations 'A', 'B', 'C', respectively. For consistency, all inlets were standardised to a uniform circular diameter of 20 μm.

The total vessel length (S) is calculated by discretely summing the Euclidean distance between consecutive 3D coordinates (x_1, y_1, z_1) and (x_2, y_2, z_2) along the centreline, following Eq. 4.1.

$$\mathrm{S} = \sqrt{(x_2 - x_1)^2 + (y_2 - y_1)^2 + (z_2 - z_1)^2} \tag{4.1}$$

The tortuosity index (TI) is calculate from [260]:

$$\mathrm{TI} = \frac{S}{L} \tag{4.2}$$

where L is line distance between the two ends (Fig. 4.2D).

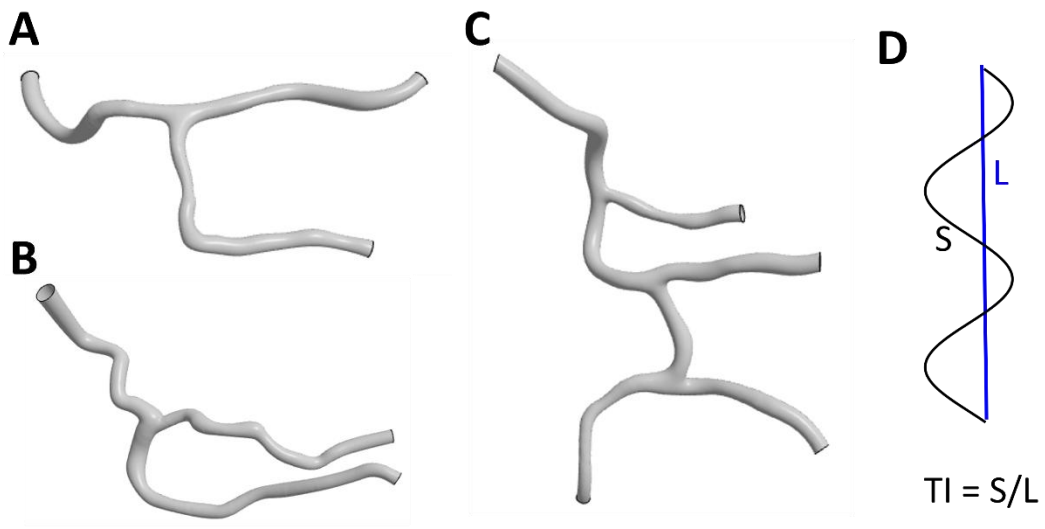

Figure 4.2: Three-dimensional reconstructions of healthy testicular bifurcations. (A-C) The bifurcations are labelled 'A', 'B', 'C', respectively. (D) Schematic illustrating tortuosity index (TI) measurement.

4.2.2 Meshing and EMP model application

The meshing and EMP setup followed the procedure described in Chapter 2. A hybrid meshing strategy was employed, combining polyhedral elements in the core with a substantial prismatic boundary-layer region to resolve the sharp near-wall gradients in velocity and volume fraction characteristic of curved bifurcating vessels. The mesh was generated in STAR-CCM+. The first prismatic layer height (Δy_1) was set to approximately 0.005d0, calculated using the standard y+ formulation, with density, wall shear stress and viscosity values of 1.050 g/cm³, 17 dyn/cm² and 4.0 mPa·s [193], respectively. The dimensionless wall distance y+ was defined using the friction velocity, derived from the skin-friction coefficient applicable to low-Reynolds-number flow [140, 141]. Thirty prismatic layers were used, determined by the specified first-layer height and total boundary-layer thickness, with the mesh base size of a base size of 8.5×10^{-7} m. The resulting meshes for bifurcation geometries 'A', 'B', and 'C' were around 0.8, 0.9, and 1.1 million cells, respectively. The mesh independence study for bifurcation 'B' was detailed in Appendix C.1, Fig. C.1.

Across the three anatomically realistic bifurcations, the computational requirements were comparable despite increasing geometric complexity. Real-world wall-clock

runtimes ranged from 4.2 to 10.8 hours, with corresponding CPU workloads of 168–401 CPU-hours. Memory consumption was consistently low at 0.28–0.32 GB, and solver convergence required approximately 25,000–56,000 iterations, depending on geometric complexity. Bifurcation 'B' converged most rapidly due to its lower tortuosity, whereas the multi-branching morphology of bifurcation 'C' resulted in the highest computational cost. These values demonstrate that the computational cost remains moderate and scalable for larger or multi-subject vascular datasets.

In this work, two pressure outlet strategies were implemented: (i) identical pressure outlets consistent with the methodology in Chapter 2, applying a fixed outlet pressure of 50 mmHg across all bifurcations, and (ii) a diameter-based pressure outlet configuration designed to reflect physiological variations in vessel diameter for bifurcation 'C'. Moreover, to enhance physiological relevance, two inlet velocities were applied. These inlets were assigned identical mean velocities (~1 mm/s) and shared the same pressure outlet conditions.

Diameter-based pressure outlet modelling was implemented through a preliminary single-phase simulation to determine appropriate outlet boundary conditions for the multi-phase, multi-component model. This simulation applied pressure outlet boundaries with flow fractions derived from Murray's law and an initial domain pressure of 50 mmHg. The flow was assumed to be steady, laminar, and incompressible, governed by the Navier–Stokes equations. To ensure consistency, the inlet mean velocity was adjusted using Equation 2.7 to match the conditions of the multi-phase simulation.

Flow distribution was calculated using Murray's law [185], which estimates branching flow rates according to vessel diameters. The split ratio for each branch was defined as:

$$Q_i/Q_t = \frac{D_i^3}{\sum_i D_i^3} \tag{4.1}$$

where i represents the branch index and Q_t the total flow rate.

4.3 Results

4.3.1 3D reconstruction of testicular bifurcations

Three non-planar bifurcation geometries were found to be consistent with an intertubular arteriole connecting to capillaries (Fig. 4.1) [23, 24, 257]. Their paths were curvilinear, with gentle bends and turns that allowed them to navigate around the seminiferous tubules. The branching points were characterised by splits of various shapes at acute angles. The distal capillaries that connected to these arterioles were represented as thicker vessels, consistent with a scanning electron microscopy study that reported their diameters to be at least 15 μm [23].

Bifurcations 'A' and 'B' consisted of a parent (0^{th}-generation) and two daughter branches (1^{st}-generation), as shown in Fig. 4.2. In both cases, the junction included a left (in the direction of upstream flow, or upper) branch that was relatively in the same direction to the parent vessel, and a right (lower) branch emanating almost in the perpendicular direction from the junction before bending sharply to run almost in parallel to the first daughter branch. The splitting angle α and the curved angle β of the bifurcation 'A' were both sharper compared to those of the bifurcation 'B'. The vessels in the bifurcation 'B' were slightly more tortuous than those of 'A', with the average tortuosity indices of approximately 1.254 vs 1.216, respectively. The degree of planarity was illustrated in Fig. 4.3 and Table 4.1. As illustrated in Fig. 4.2C, the network 'C' was composed of four generations and three junctions. Its 0^{th}-genearation curved parent vessel split into the 1^{st}-generation consisting of a left branch and a right branch, emanating perpendicularly before bending sharply to run in parallel with the first branch. The right bent branch then immediately bifurcated into two 3^{rd} generation daughter vessels, with also one left branch being aligned and the other, right branch splitting perpendicularly. The latter further split into two 4^{th}-generation branches, creating a T-shaped junction. The vessels in the bifurcation 'C' were less tortuous (average TI of 1.153) than those in 'A' and 'B', as the values listed in Table 4.1.

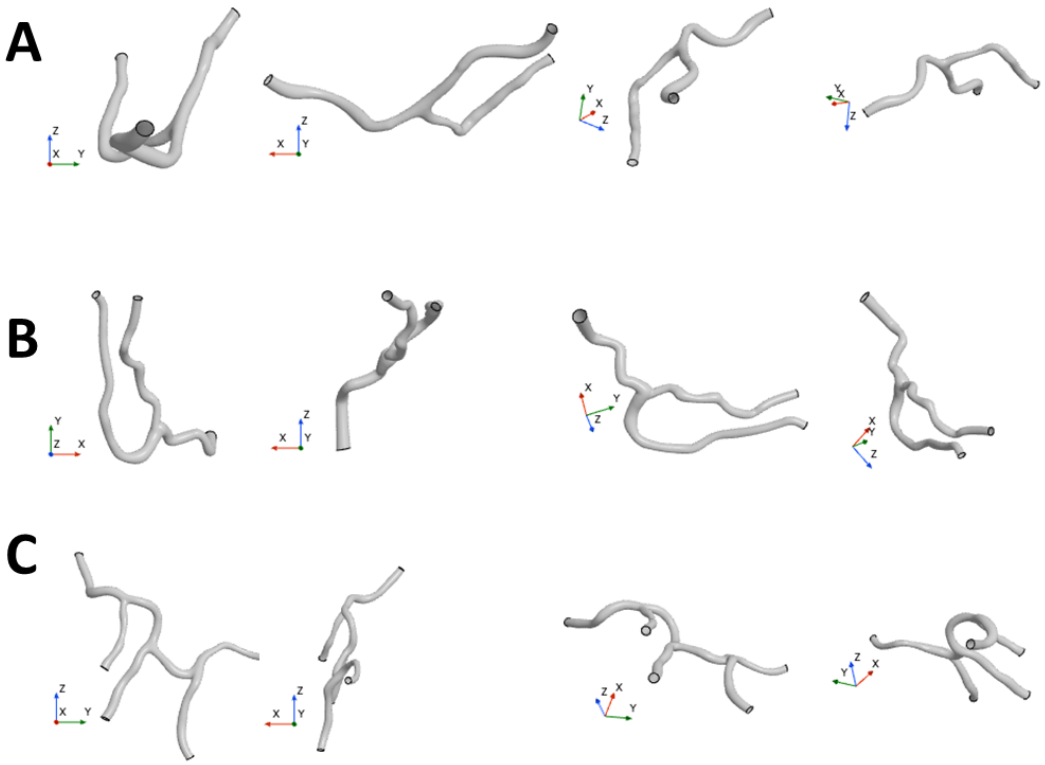

Figure 4.3: Multiple viewing perspectives of the three reconstructed testicular bifurcations, illustrating their three-dimensional spatial geometry. (A, B, C) Bifurcations 'A', 'B', and 'C', respectively.

Table 4.1: Tortuosity index (TI) of the three testicular bifurcations

	A	B	C
0^{th}-generation	1.177	1.225	1.213
Left 1^{st}	1.079	1.120	1.058
Right 1^{st}	1.393	1.418	1.340
Left 2^{nd}			1.014
Right 2^{nd}			1.101
Left 3^{rd}			1.083
Right 3^{rd}			1.259
Mean	1.2163	1.2543	1.1526
STD	0.1312	0.1234	0.1107

4.3.2 Haemodynamics in the three bifurcations

4.3.2.1 RBC-rich region distribution

The multi-phase, multi-component model was successful in capturing the dynamic near-wall CFL in non-planar, realistic bifurcated microvessels. Similar to findings in idealised bifurcations (Chapters 2 and 3), the RBC-rich region impinged on the apex of the junction and aligned with the inner wall before flowing centrally further downstream, allowing subsequent formation of the inner wall CFL regions (Fig. 4.4C, 4.5C&D and, 4.6A-C). An enlarged CFL was detected at the curved bifurcation and the entrance of the daughter branches. The perfectly symmetric CFL observed in the idealised bifurcations of Chapters 2 and 3 was not observed in these anatomically-realistic vessels due to their non-uniform, curved, short and constricted paths.

The vessel geometry, especially curvature and tortuosity, was the primary factor influencing the flow patterns and CFL development. In the 1st-generation left daughter vessel, greater tortuosity (TI=1.120) in geometry 'B' led to a more asymmetric CFL (Fig. 4.5C&D), whereas the straighter paths in 'A' (TI=1.079) (Fig. 4.4C) and 'C' (TI=1.058) (Fig. 4.6A) quickly achieved almost symmetric flow. In the right branch of the 1st-generation, the sharp angle β in bifurcation 'A' rapidly promoted an almost-symmetric CFL, whereas the wider angle β in case 'B' caused the RBC-rich region to migrate near the IW before becoming almost symmetrical over a longer distance. In the vascular network 'C', the wide angle β (Fig. 4.6H) also caused a shift in the RBC-rich region, but the flow became almost symmetrical before splitting into the 2nd-generation. These findings strongly suggest that geometry was the primary factor influencing these flow patterns and the development of almost symmetric flow.

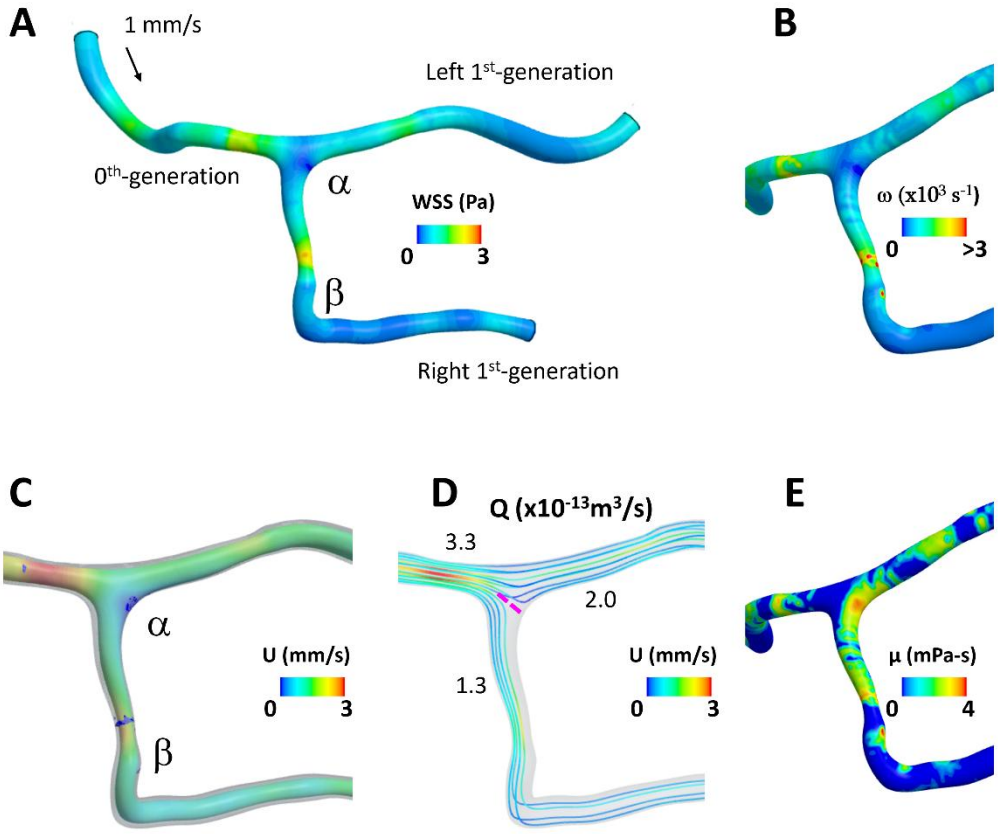

Figure 4.4: Haemodymics in bifurcation 'A'. (A, B, E) Visualisations of WSS, vorticity, and viscosity, respectively, on the wall. (C) RBC-rich region distribution represented by an iso-surface of 50% tube haematocrit coloured by velocity values. The gap in the grey surface was part of the CFL. (D) Velocity streamlines and flow rates for each branch. The dividing line (dash pink) shifted toward the low flow branch. The numerical values adjacent to each branch indicate the corresponding flow rate, reported in multiples of 10^{-13} m^3/s.

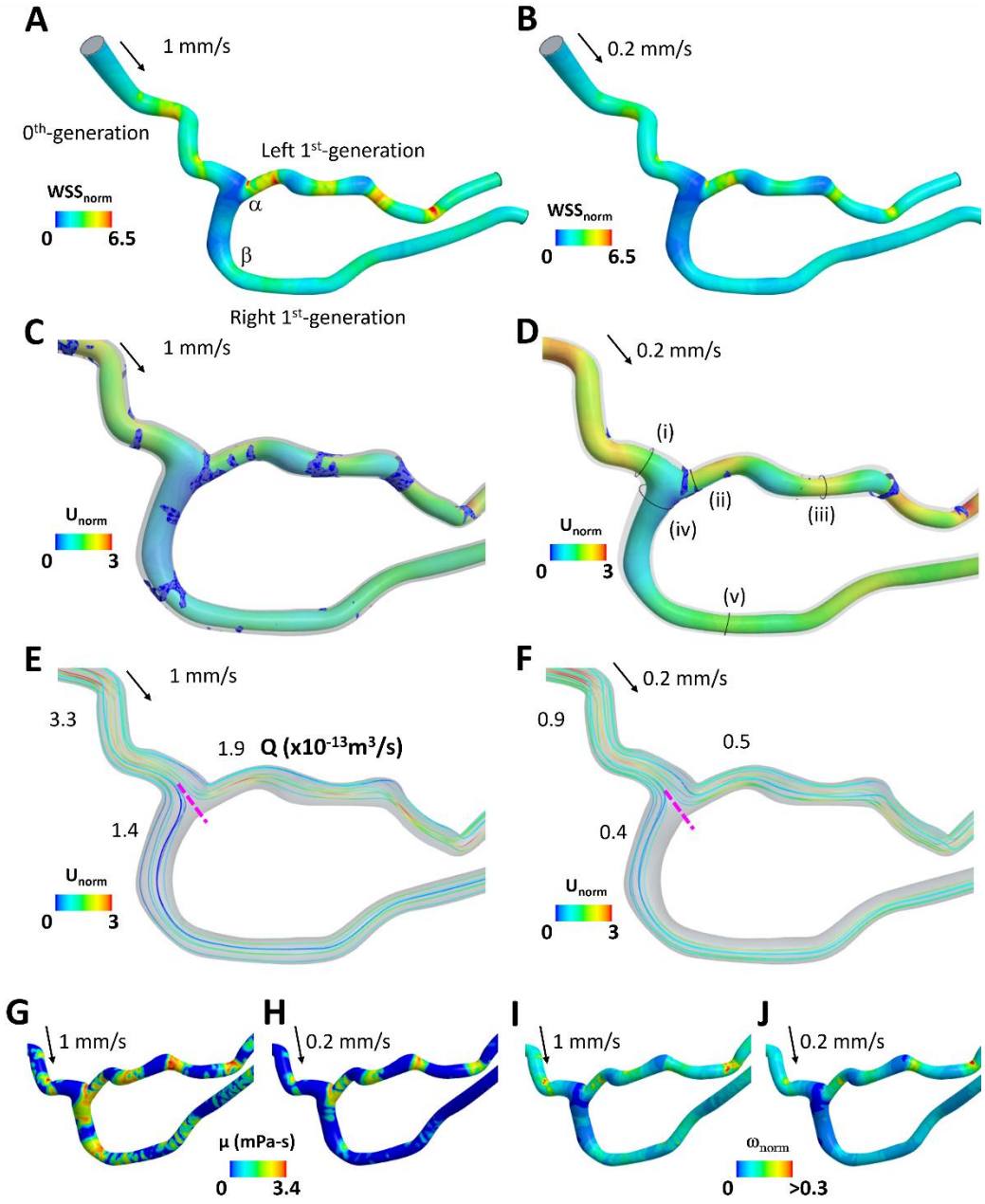

Figure 4.5: Haemodymics in bifurcation 'B' for inlet flow rate values of 1 and 0.2 mm/s. (A, B) WSS distribution on the vessel wall. (C, D) Iso-surface of 50% tube haematocrit with the normalised velocity, relative to the inlet. (E, F) Velocity streamlines with the dividing line (dashed pink) shifted towards the high flow branch. The numerical values adjacent to each branch indicate the corresponding flow rate, reported in multiples of 10^{-13} m^3/s. (G, H) Effective viscosity on the vessel wall. (I, J) Normalised vorticity, relative to the maximum value across the bifurcation on the vessel wall.

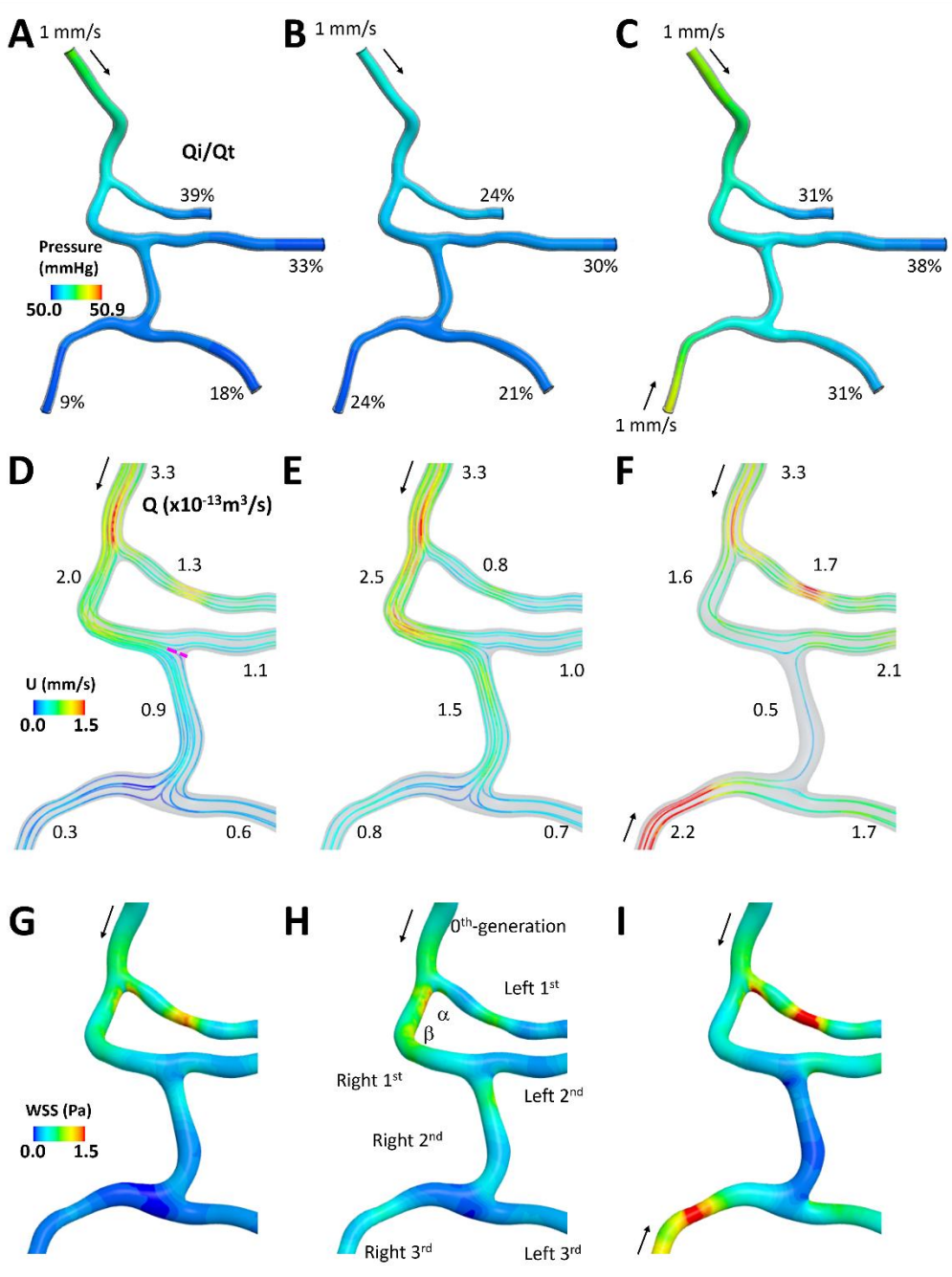

Figure 4.6: Haemodymics in bifurcation 'C' for three different boundary conditions. (A, D, G) Single inlet velocity and identical pressure outlets. (B, E, H) Single inlet velocity and diameter-based pressure outlets. (C, F, I) Two inlets and identical pressure outlets. (A, B, C) Iso-surface of 50% tube haematocrit coloured by the pressure distribution. The numerical values adjacent to each branch indicate the corresponding flow fraction. (D, E, F) Velocity streamlines. The numbers represent the volumetric flow rate in each branch, expressed in units of 10^{-13} m^3/s. (G, H, I) WSS distribution.

4.3.2.2 Resistance

To assess the influence of vessel geometrical properties, three bifurcations were analysed under identical inlet velocity and outlet pressure conditions. Consequently, the pressure drop (ΔP, outlet pressure minus inlet pressure) was uniform among the daughter branches within each bifurcation but varied across bifurcations. The pressure drops of bifurcations 'A', 'B', and 'C' were 0.97, 1.97 and 0.65 mmHg, respectively. The higher ΔP observed in bifurcation 'B' reflects its greater three-dimensionality and tortuosity (mean TI = 1.254), which increase energy dissipation. Conversely, the lower ΔP in bifurcation 'C' (mean TI = 1.1526) due to its four outlets distribution the flow among multiple branches, reducing the flow fraction per branch, and increase effective viscosity (μ_{eff} = 2.25 mPa·s) and thereby lowering the pressure drop compared with bifurcations 'A' (μ_{eff} = 2.14 mPa·s) and 'B' (μ_{eff} = 2.16 mPa·s), each of which has only two outlets.

Within bifurcation 'B', a comparison of the pressure drop per unit length (ΔP/L), an indicator of localised energy loss, revealed that the right (lower), longer and less smoother branch exhibited reduced ΔP/L (3.53 mmHg/mm) than the left branch (4.34 mmHg/mm). This finding suggests that the smoother path of the right (lower) branch facilitates more efficient flow. Therefore, three-dimensionality is a more dominant factor in determining localised energy loss than vessel length. In network 'C', which lacked highly complex branches, differences in ΔP/L were governed primarily by vessel length. The shortest branch (left/upper branch in the 1st-genaration) showed the highest ΔP/L (1.53 mmHg/mm), while the longest branches (3rd-genaration branches) exhibited the lowest ΔP/L (~0.84 mmHg/mm), as shown in Table 4.2.

Table 4.2: Pressure and RBC influx of distal branches.

Bif	generation	L (μm)	ΔP (mmHg)	ΔP/L (mmHg/mm)	FQ_B	FQ_E	FQ_E/FQ_B
A	Left 1st	544	0.97	1.78	0.606	0.624	1.03
	Right 1st	632	0.97	1.53	0.394	0.376	0.95
B.1	Left 1st	454	1.97	4.34	0.576	0.580	1.01
	Right 1st	559	1.97	3.53	0.424	0.420	0.99
B.2	Left 1st	454	0.41	0.91	0.541	0.561	1.04
	Right 1st	559	0.41	0.74	0.459	0.439	0.96
C.1	Left 1st	426	0.65	1.53	0.394	0.371	0.94
	Left 2nd	619	0.65	1.05	0.550	0.581	1.06
	Left 3rd	777	0.65	0.84	0.667	0.662	0.99
	Right 3rd	785	0.65	0.83	0.333	0.338	1.01
C.2	Left 1st	426	0.36	0.85	0.242	0.236	0.97
	Left 2nd	619	0.47	0.76	0.400	0.412	1.03
	Left 3rd	777	0.55	0.71	0.467	0.547	1.17
	Right 3rd	785	0.62	0.79	0.533	0.453	0.85
C.3	Left 1st	426	0.58	1.35	0.515	0.493	0.96
	Left 3rd	777	0.58	0.74	0.773	0.772	1.00

Noted: For bifurcation 'B', conditions B.1 and B.2 represent inlet velocities of 1 mm/s and 0.2 mm/s, respectively. For bifurcation 'C', the conditions are as follows: a single-inlet with an identical pressure outlet (C.1), a single-inlet with a diameter-based pressure outlet (C.2), and a double-inlet configuration (C.3). $\Delta P = P_{inlet} - P_{outlet}$. $FQ_B = Q_{bulk,dauther}/Q_{bulk,parent}$. $FQ_E = Q_{core,dauther}/Q_{core,parent}$.

4.3.2.3 Plasma skimming

The three bifurcations were simulated with identical inlet velocities and pressure outlets, ensuring that morphological variations were responsible for the haemodynamics. In bifurcations 'A' and 'B', the left (upper) branch exhibited a higher flow rate than the right (lower) branch, resulted in a greater RBC-rich region being drawn into it, with an RBC-rich influx (FQ_E) of 0.624 and 0.580, respectively (Table 4.2). Conversely, in bifurcation 'C', the left (upper) branch in the 1st-generation exhibited a lower flow rate compared to the right (lower) branch, leading to a reduced RBC-rich influx of 0.371. The higher flow rate in the right branch was due to its downstream split into a branching network. This biased RBC-rich partitioning into the

high-flow branch is a key feature of classic plasma skimming. The preferential RBC-rich partitioning into the daughter branches was visually confirmed by the position of the dividing streamline, which shifted towards the low-flow branch, consequently directing a greater volume of the central RBC-rich region to the high-flow branch (Fig. 4.4D, 4.5E and 4.6D).

4.3.2.4 Wall shear stress

WSS from the multi-phase, multi-component model was determined by the combined effect of near-wall viscosity and shear rate, both of which were influenced by CFL formation (as described in Chapters 2-3). In geometrically-complex regions, shear gradients became more pronounced, making shear effects more important than viscosity. For instance, in bifurcation 'A', the right (lower) branch at the constricted region had the highest WSS (Fig. 4.4A) with both high viscosity (Fig. 4.4E) and high shear (Fig. 4.4B), the latter of which was represented by vorticity. In contrast, the daughter entrances showed high viscosity but weak vorticity, resulting in low WSS. Similarly, in bifurcation 'B', the constricted regions on the left (upper) vessel exhibited high WSS (Fig. 4.5A), viscosity (Fig. 4.5G) and shear (Fig. 4.5I). Meanwhile, at the IW entrance of the right (lower) daughter branch's inner wall entrance, WSS was low since vorticity was minimal even though viscosity was high.

4.3.3. Different inflow in the bifurcation 'B'

4.3.3.1 RBC-rich region distribution

Under the low inflow condition of 0.2 mm/s, Fig. 4.5C&D demonstrated that the RBC-rich region rapidly regained a near-symmetrical profile, which was notably more symmetric than that observed under high inflow condition. In the upstream 0^{th}-generation, high inflow produced a more asymmetric radial haematocrit distribution (Fig. 4.7A(i)) with a smaller CFL region (4% vs. 16%) compared to the low inflow (Fig. 4.7B(i)). The maximum velocity positioned in the opposite direction of the

haematocrit peak. The low inflow also led to an enlarged CFL in both daughter vessels. At the branch entrances, low inflow increased the CFL, rising from 3% to 12% in the left (upper) branch and 6% to 22% in the right (lower) branch, as illustrated in positions (ii) and (iv) in Fig. 4.7 (tube haematocrit colour map). This pattern was also observed in the constricted areas at position (iii), where high inflow resulted in greater flow asymmetry and a nearly absent CFL (0.09% vs. 8.9%).

4.3.3.2 Resistance and plasma skimming

As shown in Table 4.2, reducing the inflow lowered the overall ΔP (0.41 mmHg), with the ΔP/L falling to 0.91 and 0.74 mmHg/mm for the left and right branches, respectively. The left branch maintained a higher flow rate than the right branch (0.5 $x10^{-13}$ vs. 0.4 $x10^{-13}$ m^3/s), pulling in a larger portion of the RBC-rich region, with an influx of 0.561 (compared to 0.439), as visually confirmed by Fig. 4.5E&F. The RBC-rich influx values at the high inflow were slightly different (FQ_E = 0.580 vs. 0.420). Plasma skimming was more pronounced under the low inflow case, with the FQ_E/FQ_B ratio for the right branch dropping from 0.99 under the high inflow to 0.96 under the low inflow.

By removing the influence of the inlet speed, the normalised velocity analysis directly revealed how each bifurcation's unique geometry dictated its distinct flow resistance. In the left (upper) branch, at the higher inflow of 1 mm/s, intensified vorticity accelerated flow, producing a higher normalised velocity (1.46 ± 0.3), whereas at the lower inflow, diminished vorticity led to lower acceleration and a decreased normalised velocity (1.39 ± 0.3). This indicates that flow resistance in the left (upper) tortuous branch was inflow dependent. In contrast, the right (lower) branch, with its smoother and more uniform curvature, exhibited minimal vorticity (Fig. 4.5I&J), and its normalised velocity remaining stable at ~1.0, regardless of the inflow condition. Noted that, the normalised velocity relative to the inlet was calculated as the average across ten cross-sectional planes along each vessel, with the resulting differences clearly illustrated in Fig. 4.5C-F.

A lower normalised WSS in both magnitude and spatial distribution (Fig. 4.5A&B), was detectable in the low inflow case. A high inflow, conversely, intensified and broadened the WSS due to the thinning of the CFL and the skewing of the RBC-rich region in curved and constricted vessels, which subsequently elevated both viscosity and vorticity near the vessel wall (Fig. 4.5G-J).

4.3.3.3 Haemodynamic forces

Using a realistic model revealed the complexity of haemodynamic forces. The localised lift force was determined by the volume fraction of the multiphase plasma-RBC component, the slip velocity and the plasma vorticity. A comparison was made between the entrance of the two daughter branches (Fig. 4.5D(ii)&(iv)), where RBC-rich phase skewed towards the inner wall, and a downstream region where the CFL recovered (Fig. 4.5D(iii)&(v)). The magnitude of the haemodynamic forces was greater under high inflow, a phenomenon attributable to a higher near-wall shear gradient. Nevertheless, both inflow conditions yielded similar characteristic distribution patterns. In Fig. 4.7A&B, under the low inflow condition, the distribution of these forces was more symmetrical, allowing for a clearer visual comparison.

At the entrance of the high-flow right branch (Fig. 4.7B (ii)), the maximum velocity was situated opposite the skewed RBC mass. This generated high near-wall slip velocity and vorticity, culminating in a substantial lift force at the enlarged CFL at the outer wall. A similar, but weaker, pattern of forces was observed at the entrance of the low-flow right (lower) branch (Fig. 4.7B(iv)), which received a lower RBC influx.

In the downstream, symmetric-like CFL (Fig. 4.7(iii)) located in a constricted area in the left (upper) branch exhibited high flow rate. The reduced cross-sectional area produced a higher velocity (0.42 mm/s) compared to the entrance of the same vessel (0.36 mm/s), resulting in stronger haemodynamic forces. The areas exhibiting high vorticity and lift occurred at the location where the velocity peak has shifted. In contrast, position (v), which was situated in a low-flow right (lower) branch, exhibited a more uniform and concentric CFL. The haemodynamic forces were symmetrically

distributed in a ring around the periphery, but their magnitude was weaker than at position (iii) due to the slower flow velocity (0.32 mm/s).

Overall, the results demonstrated that changes in vessel geometry, from the entrance to the downstream branches, created the localised lift force to shift the RBC-rich region towards the inner wall at the junction, before subsequently guiding it back towards the vessel centreline. Moreover, this recovery mechanism was directly modulated by plasma skimming. The greater intensity of haemodynamic forces in the high-flow branch reflected the preferential partitioning of RBCs into it, leaving the low-flow branch with weaker forces and a lower cell concentration.

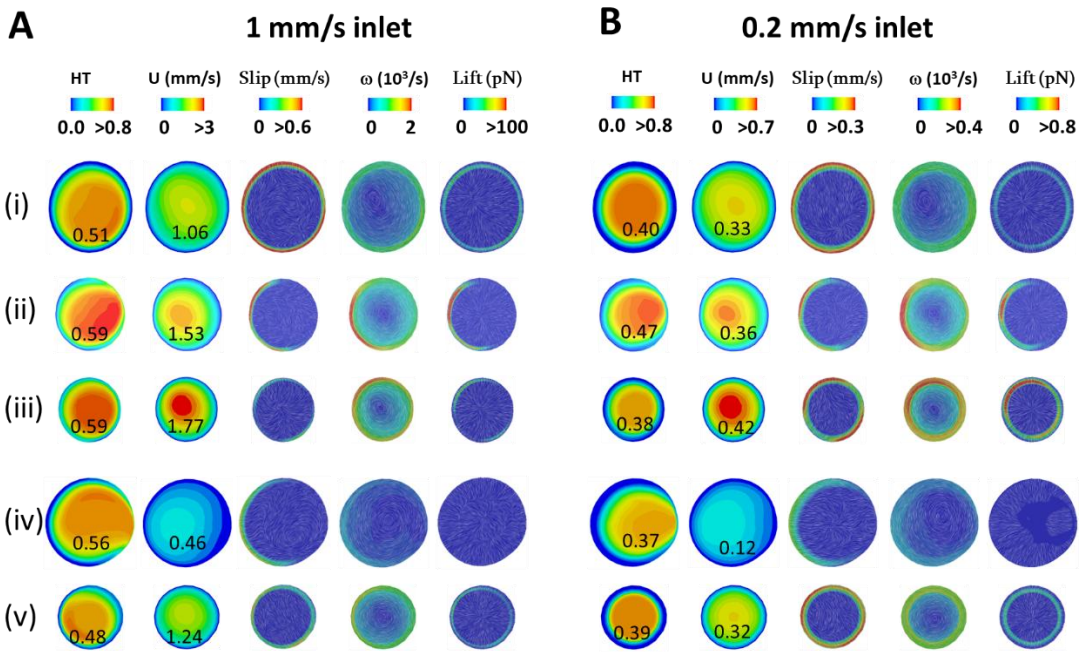

Figure 4.7: Haemodynamics in the bifurcation 'B' with high (A) and low (B) inflow. These cross-sectional regions are corresponding to positions in Fig. 4.5D, located at the upstream parent (i), entrance of the left (upper) branch (ii), constricted area on the left branch (iii), entrance of the right (lower) branch (iv), and the smoother area on the right branch. The averaged tube haematocrit and averaged velocity were shown inside the cross-sectional planes. The numbers inside the cross-sectional planes indicate the value of tube HT and velocity (mm/s).

4.3.4 Effect of boundary conditions in the network 'C'

While the identical pressure outlet simulation was used to isolate the effects of geometry, it may lack physiological accuracy because arterial branch pressures were not uniform *in vivo* [261]. An alternative approach, the diameter-based pressure outlet condition, derived from Murray's Law [185], provides a more realistic flow distribution, based on the principle of optimal energy use in healthy circulatory systems. Furthermore, to achieve greater physiological realism, the simulation was performed with two distinct inlet velocities to model the effects of a collateral blood supply.

The prescribed boundary conditions significantly altered the flow distribution among the network's outlets. Under the identical pressure outlet condition (Fig. 4.4A&D), flow was unevenly distributed. The proximal branches (1st- and 2nd- generation) received the largest flow fractions (0.39 and 0.33), while distal branches (3rd-generation) were poorly perfused with fractions of only 0.18 and 0.09. This corresponded to flow rates of 1.3 x10^{-13} and 1.1 x10^{-13} m^3/s in the proximal branches, while the poorly perfused distal branches received significantly less flow, with rates of only 0.6 x10^{-13} and 0.3 x10^{-13} m^3/s. In contrast, applying a diameter-based pressure outlet (Fig. 4.4B&E) resulted in a more balanced and physiological distribution, with corresponding flow fractions from 0.21 to 0.30, leading to comparable flow rates that ranged from 0.7 x10^{-13} to 1.0 x10^{-13} m^3/s. These findings indicate that realistic boundary conditions are critical for predicting physiological flow, providing the basis to examine plasma skimming.

When comparing the diameter-based pressure outlet to the identical pressure outlet, significant differences in plasma skimming were observed. In the left 1st- and 2nd-generation branches, the diameter-based model exhibited lower flow rates, resulting in reduced RBC-rich influx (FQ_E = 0.236 and 0.412, respectively). This diminished the plasma skimming effect (the FQ_E/FQ_B ratio approached one), as the ratio increased from 0.94 to 0.97 in the 1st- generation and decreased from 1.06 to 1.03 in the 2nd-generation (Table 4.2). The most dramatic reversal occurred at the 3rd-generation branches. Under the identical pressure model, higher flow was directed to the left branch (0.6 x10^{-13} vs. 0.3 x10^{-13} m^3/s), whereas the diameter-based model favoured the

right branch (0.7 vs. 0.8 x10^{-13} m^3/s). This shift had a major impact on RBC-rich influx, transforming the left branch from a neutrally perfused vessel (FQ_E/FQ_B = 0.99) in the identical outlet model into one heavily affected by plasma skimming (FQ_E/FQ_B = 1.17) in the diameter-based outlet model, as shown in Table 4.2.

Furthermore, both ΔP and ΔP/L for four outlets were lower under the diameter-based pressure condition, ranging from 0.36–0.62 mmHg and 0.71–0.85 mmHg/mm, respectively (Table 4.2). In contrast, the identical pressure condition exhibited a higher overall pressure drop of 0.65 mmHg and a steeper pressure gradient, with ΔP/L values ranging from 0.83–1.53 mmHg/mm. These findings indicate that adhering to a physiological flow distribution (the diameter-based case) minimises the energy needed to perfuse the vascular network, a hallmark of an efficient circulatory system. In addition, WSS patterns differed significantly between the two conditions. The diameter-based pressure outlet model (Fig. 4.4H) exhibited more localised patterns of high WSS distributed throughout the branching network, whereas the identical pressure outlet model (Fig. 4.4G) primarily showed elevated WSS values concentrated in the proximal branches.

The two-inlet collateral supply model (Fig. 4.4C&F) produced another distinct pattern. The convergence of the two inlet streams resulted in a mixed, high-flow channel through the left 2nd-generation branch, which captured the largest flow fraction (0.38) and flow rate (2.1 x10^{-13} m^3/s). The remaining outer branches (1st- and 3rd-generation) did not experience this mixing, as each was perfused independently by a single inlet, resulting in equal, lower flow fractions (0.31) and flow rates (1.7 x10^{-13} m^3/s). The highest WSS was observed at the constricted regions on the 1st-generation branch (Fig. 4.4I).

4.3.5 Single-phase model

For bifurcation ‘C’, the multi-phase, multi-component and single-phase models produced similar flow rates (Fig. 4.4D-F and Fig. 4.6A-C, respectively), but their velocity and WSS calculations showed notable differences. The single-phase model

yielded average velocities of 0.509, 0.525, and 0.690 mm/s for ideal pressure outlet, diameter-based pressure outlet and double-inlet conditions, respectively (Fig. 4.6A-C), which were slightly different to the multi-phase, multi-component model (0.506, 0.527, and 0.663 mm/s; Fig. 4.4D-F). However, the maximum velocity in the single-phase model (1.02, 1.05, and 1.33 mm/s) was obviously higher than in the multi-phase, multi-component model (0.817, 0.850 and 1.07 mm/s, respectively). Similarly, the WSS values were higher in the single-phase model (0.43, 0.45 and 0.72 Pa; Fig. 4.6D-F) than in the multi-phase, multi-component model (0.31, 0.33 and 0.50 Pa; Fig. 4.4G-I). Noted that the averaged velocity and WSS was calculated from the entire geometries. In the single-phase, the WSS was enhanced at the high-curvature regions but reduced at the initial IW of the daughters' entrances. This reduction occurred because the single-phase model produced a symmetric flow, while the multi-phase, multi-component model generated an asymmetric CFL at the daughter entrance, which resulted in high near-wall viscosity and a high shear gradient, consequently high WSS.

Similarly, for bifurcation 'B', the single-phase model produced a slightly higher average velocity (0.321 mm/s) than the multi-phase, multi-component model (0.313 mm/s). The maximum velocity was also higher in the single-phase model (0.640 mm/s; Fig. 4.6G) compared to another model (0.507 mm/s). A significant difference was observed in WSS, with the single-phase model yielded a value of 0.62 Pa being more than double that of the multi-phase multi-component model (0.27 Pa), as demonstrated in Fig. 4.6H&I.

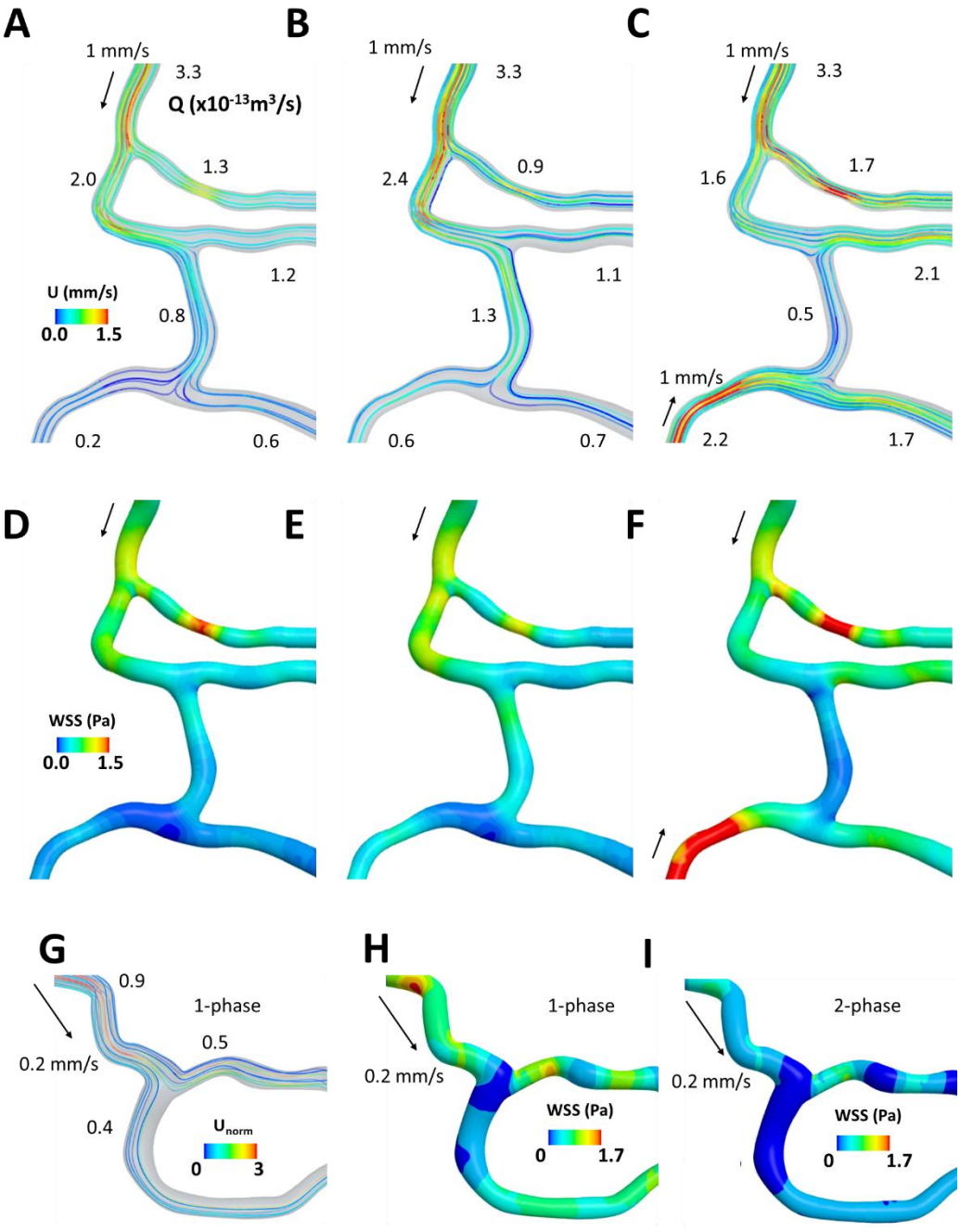

Figure 4.8: Single-phase simulations on bifurcations ‘C’ (A-F) and ‘B’ (G-I). (A-C, G) velocity streamlines. (D-F, H-I) WSS distribution.

4.4 Discussion

The aim of this chapter was to present the application of the multi-phase, multi-component model for simulating blood flow in subject-specific anatomically-realistic, highly-curved bifurcations of the mouse testis, overcoming the limitations of idealised designs. The model enables us to capture the detailed CFL dynamics in these complex structures and their influence on near-wall haemodynamics. Furthermore, the model's responsiveness to varying boundary conditions, such as identical pressure, diameter-based outlets, and collateral inlets, highlights its capability to replicate physiological flow regulation of collateral branching pattern of interbular vessel. This work establishes a clear link between geometry, vascular resistance, and haemodynamic forces, providing a reliable framework for microvascular research.

4.4.1 Testicular microvascular architecture

The bifurcations 'A', 'B', and 'C' in this work align with anatomical descriptions of testicular microvasculature. They form part of an interbular arteriole connected to capillaries and have curvilinear paths that navigate around the tubules [23, 24]. These bifurcations are characterized by gentle blends, turns and splits at acute angles. Such high-curvature is a key feature of testicular microvasculature, which is essential for functions such as temperature regulation [24]. The testicular artery and its branches are often coiled and convoluted, which serves to reduce blood flow velocity and dampen pressure fluctuations. Moreover, the bifurcations correspond to anatomical locations of a specialized microenvironment, which is the vascular branch points where undifferentiated spermatogonia preferentially cluster [257].

4.4.2 CFL formation

In this study, while perfectly symmetric flow was not achieved downstream of realistic bifurcations, the RBC-rich region showed a tendency to shift towards the vessel centre, producing a concentrated core surrounded by nearly equal CFL regions, referring to as

'symmetry-like'. Greater tortuosity in bifurcation 'B' resulted in a more asymmetric CFL compared to the straighter paths in bifurcations 'A' and 'C', which achieve symmetry-like flow more rapidly. Moreover, the angle β of the right (lower) daughter branches also played a role. A sharper angle β promoted a symmetric-like CFL, whereas a wider angle caused the RBC-rich region to migrate and skew towards the inner wall before becoming symmetrical over a longer distance. The observation that blood flow in curved microvessels is asymmetrical and skews towards the inner bend is supported by both the lattice Boltzmann method [262] and a study on cerebral microcirculation [263], which observed asymmetric velocity profiles *in vivo*.

The simulation provides specific quantitative evidence for the critical role of the CFL in haemodynamics. In bifurcation 'B', the CFL region was significantly larger under the low inflow condition (12%) compared to high inflow (3%). The finding that a larger CFL promotes flow symmetry is supported by observations in penetrating arterioles [264], where the plasma layer varies with vessel diameter and acts as a buffer, allowing the central RBC-rich region to remain stable and less unaffected by the vessel wall movements.

4.4.3 Resistance

The overall energy required to drive blood through a vascular network is represented by the global total pressure drop (ΔP), whereas local resistance is assessed by the pressure drop per unit length (ΔP/L). Bifurcations 'B' and 'C' exemplify two contrasting strategies for regulating flow. Bifurcation 'B' demonstrated a high ΔP/L due to its tortuosity, which acted as a local regulator by dissipating energy and slowing blood flow, a feature associated with precise control in regions such as the testis, where temperature regulation is critical [24, 265, 266]. Bifurcation 'B' maintained a high total ΔP, demonstrating that its geometry overwhelms the effect of its short length and this feature served for a specific, localised function of testis. Conversely, bifurcation 'C' exhibited low global resistance (i.e., low total ΔP) resulting from the parallel multi-branching path, a strategy that reduced total resistant. Its low ΔP/L indicated that this resistance was distributed more evenly, supporting its role in efficient global perfusion.

Pressures within biological systems are complex and dynamic, influenced by the cardiac cycle and local gradients, while arteriolar resistance modulates the exchange area [252]. Numerous studies have established the pressure drop as a key diagnostic tool for perfusion and oxygen delivery, with this metric being primarily shaped by local geometry [134, 267, 268]. Tortuosity diminishes the Fahraeus effect by reducing the average RBC speed, which could influence the rate of oxygen transport [269]. Hossain et al. (2024) [270] reported that significant increases in pressure drop can result from changes in vessel length and bifurcated angle, such as those found in hypertensive vessels, supports this view [271]. This is functionally demonstrated in the hamster testis, where wide variations in arterial pressure play a role in maintaining a consistently low mean capillary pressure.

4.4.3 Plasma skimming

Bifurcation morphology drives unequal flow between daughter branches, leading to disproportionate RBC separation into higher-flow pathways, a hallmark of plasma skimming. The identical pressure model of the present study proved non-physiological, creating a skewed distribution that overloaded proximal branches while starving distal ones, representing a fragile and inefficient system. Such fragility mirrors the risk of ischaemia when upstream supply is disrupted. In contrast, the diameter-based pressure model, which adheres to Murray's Law [185], represented an optimised and healthy physiologically-relevant case, ensuring efficient and equitable perfusion to all branches. The two-inlet collateral supply model demonstrated resilience and redundancy. It eliminated poor perfusion by ensuring all branches received adequate flow, highlighting the body's use of collateral pathways as a crucial safety net to protect against ischemia. Testicular arterioles exhibit this through arterio-arterial anastomoses, which maintain stable blood flow and prevent ischaemia when disruptions occur [23]. This comparison underscores the importance of boundary conditions in accurately modelling the spectrum of vascular haemodynamics, from ideal efficiency to robust survival.

These findings highlight that plasma skimming is not static but can be modulated by the flow dynamics of the surrounding network. This observation aligns with a study on dog testicular arteries, where blood flow parameters varied by region and stage [266]. Microfluidic experiments further show that biased flow distribution in bifurcated vessels is highly sensitive to downstream vascular resistance [271], and that high flow in smaller branches makes the CFL thinner, thereby increasing haematocrit to those branches [182].

4.4.5 Wall shear stress

This study presents a new perspective on WSS in curved and tortuous vessels, revealing that the shear gradient, visualised through vorticity, is a more dominant factor than near-wall viscosity. This challenges the findings of idealised models, which locate the highest WSS at the initial inner wall of the daughter entrance. In a realistic bifurcation such as bifurcation 'A', the highest WSS occurred at a downstream constriction, where high vorticity, driven by the constriction, and elevated near-wall viscosity, was influenced by an almost absent CFL, combined to produce high WSS. Conversely, at the entrance of the smoother right branch, low WSS was observed due to a low vorticity, despite the presence of high near-wall viscosity. These findings highlight that the dynamics of asymmetric CFL and the geometry of tortuous or constricted vessels are key determinants of WSS, as they modulate both viscosity and the shear gradient.

Several studies confirm that the high WSS in stenosed and bifurcated vessels is found in tortuous regions and at points of high curvature [269, 271]. These findings establish a direct link between tortuosity and WSS, demonstrating that tortuosity induces CFL asymmetries, which in turn lead to WSS asymmetry. However, these studies do not decompose WSS into its contributing component in the same manner as the present work.

WSS is a crucial regulatory signal in microcirculation. Computational modelling has shown that vessel constriction induces substantial and widespread WSS changes

across the network, suggesting a mechanism for remote vasoregulation [272]. Moreover, WSS acts as a key mechanical signal for endothelial cells, as their sensitivity to its gradients triggers gene activation essential for processes such as angiogenesis and vessel remodelling [273]. A sustained, optimal level of WSS also supports a healthy endothelium by promoting the production of vasodilators such as nitric oxide, which helps to prevent atherosclerosis [268, 274]. Therefore, the high WSS detected in tortuous areas of the vessels suggests that these could be key locations for WSS-mediated biological responses.

4.4.6 Limitation and Future work

This work is limited to a small number of subject-specific anatomically-correct geometries, with bifurcations 'A' and 'B' representing an arteriole splitting into smaller arterioles or thick capillaries. Bifurcation 'C' could represent a mesh-like network of peritubular capillaries or serve as an arterio-venous or arterio-arterial anastomosis connecting to capillaries. A limitation of this approach is that these few geometries may not be representative of the full testicular network. Future work could involve reconstructing a larger number of geometries (e.g., 10–20 bifurcations) and extending the upstream and downstream sections of the bifurcations to connect with venules, thereby representing a wider range of capillary types.

Our simulations, which use fixed-pressure outlets, were limited in that they could not replicate the physiological autoregulation of arterioles. This process, which goes beyond simple geometric effects, involves the myogenic (Bayliss) response [254], where rising pressure triggers vasoconstriction to stabilise flow. Conversely, local metabolic signals induce vasodilation to increase perfusion in areas of high demand. In future work, we will address this limitation by incorporating a dynamic component that adjusts vessel diameter in response to simulated haemodynamic parameters, mimicking the myogenic response and chemical signalling such as the release of nitric oxide in response to shear stress [252, 255].

Another limitation is that the multi-phase, multi-component model does not incorporate a temperature model, which may limit its physiological relevance in the context of testicular function. Testes regulate their temperature to support normal spermatogenesis through a specialised counter-current heat exchange system [24, 265, 266]. The convoluted and coiled testicular artery transfers heat to the cooler pampiniform plexus, and its unique path effectively slows blood flow velocity to enhance the cooling process. Future work will address this limitation by incorporating a temperature model into the simulation.

To advance translational impact, we will conduct systematic occlusion experiments, ranging from partial narrowing to complete blockage and branch removal, on high-fidelity, three-dimensional non-planar bifurcations, where geometric complexity drives CFL asymmetry, WSS localisation, and RBC flow biasing. Prior studies demonstrate that isolated occlusions elicit compensatory redistribution, while multi-site obstruction accelerates perfusion failure and tissue hypoxia [16, 275]. CFL-mediated WSS computed on the true 3D wall manifold will be converted to nitric oxide bioavailability and tone, while CFL-limited oxygen diffusion furnishes extraction predictions concentrated in arterioles and early capillaries [276, 277]. Incorporating Moeini et al.'s framework [278], we will compute CTH (Capillary Transit Time Heterogeneity) as a network-level vulnerability index and correlate it with redistribution patterns under progressive vessel loss. By integrating these haemodynamic and metabolic markers, the model will provide a clinically relevant platform for forecasting perfusion resilience and guiding interventions in microvascular disease.

Chapter 5

Single-phase phase haemodynamic comparison of control and atrophic testicular arterial networks and exploration of atrophy with the multi-phase, multi-component flow model

5.1 Introduction

The typical human adult testis is approximately 4-5 cm in length [28], although its size can vary. When smaller than the 50th percentile for age, it is considered abnormally small [28, 29]. This condition, known as testicular atrophy, is a major contributor to male infertility and results from several conditions that impair blood supply and cause tissue damage. For instance, testicular torsion directly interrupts blood flow [26, 30], while mumps orchitis causes swelling and pressure that destroys sperm-producing tubules [31, 32]. Inguinal hernias and hydroceles can compress blood vessels, reducing circulation [26]. Varicoceles are associated with venous reflux and increased testicular temperatures, a combination that impairs sperm production [26, 33] and is linked to a significant reduction in testicular arterial blood flow and poor microcirculation [27]. Lastly, scrotal trauma can increase internal pressure, causing tissue death and reabsorption [30].

Testes are located outside the body to maintain a cooler temperature (2–8 °C) necessary for sperm production, a function supported by a counter-current heat exchange system [279]. Hypertension can disrupt this system by causing vascular abnormalities and reduced blood flow to the testes [23]. Even a moderate reduction in blood supply can trigger germ cell death (necrosis and apoptosis) and inflammation, while a more severe reduction can cause widespread tissue necrosis [280]. Therefore, testes are sensitive to even minor blood flow disruptions, which can lead to impaired spermatogenesis and male infertility. This highlights the critical need to characterise

testicular haemodynamics, particularly to map differences between abnormal flow in small, diseased testes and healthy controls. Analysing these flow changes provides a direct perspective into the state of the underlying microvasculature, linking structural vascular alteration to the resulting functional impairment.

Investigating these haemodynamics relies upon specific imaging technologies. Current non-invasive methods, such as Doppler ultrasound and Ultrasound Localization Microscopy (ULM), are commonly used to assess testicular blood flow. However, these methods are limited in their ability to fully map the entire three-dimensional testicular network. Doppler ultrasound is restricted to measuring flow in large vessels on the surface of the testis [265, 266, 281, 282]. While ULM provides super-resolution imaging of microvessels, it is constricted to a two-dimensional perspective [261]. This limitation hinders the ability of clinical and *in vivo* studies to establish a definitive link between microvascular 2D imaging and three-dimensional haemodynamic behaviour. Computational modelling can bridge this gap by exploring how vessel geometry influences blood flow distribution, pressure and resistance, which are difficult to measure directly *in vivo*.

The testicular artery originates from the abdominal aorta, follows a winding route through the pampiniform plexus, and then pierces the tunica albuginea, the outer capsule of the testis [24, 25]. A capsule artery then runs along the surface, branching into centripetal arteries that extend inward towards the centre (Fig. 5.1). These arteries then branch into radiating arteries, which supply both superficial and deep layers, ensuring consistent blood flow throughout the entire testicular vascular network. The system also includes arterio-arterial anastomoses [23, 24], which provide a fail-safe blood supply, and arterio-venous anastomoses that regulate blood flow, heat exchange and hormone transport. Overall, the testicular artery serves as the main blood supply to the testis. Its branches, the intratesticular arteries, deliver blood to the inner testis, while intertubular arterioles supply the capillaries located between the seminiferous tubules. These capillaries are responsible for the vital exchange of gases and nutrients.

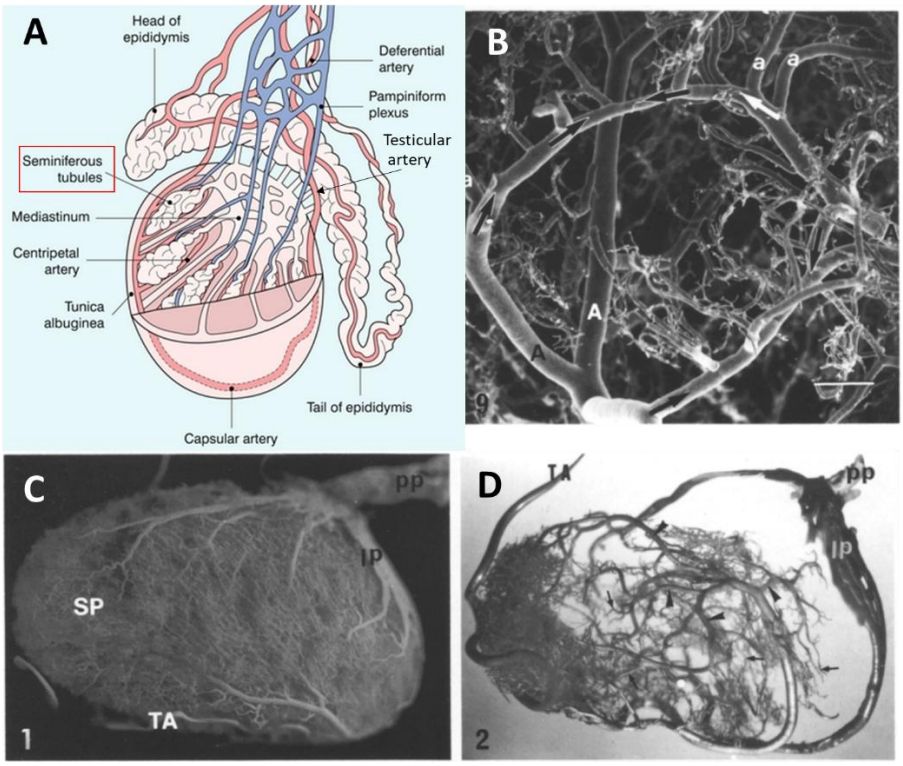

Figure 5.1: Testicular vasculature. (A), Diagram showing testis and vasculature (https://radiologykey.com/doppler-imaging-of-the-scrotum/). (B), arterio-arterial anastomoses (arrow) from micrograph of micro-dissected cast. (C), whole vascular cast of the rat testis. (D), Branching arterial pattern by partially filled cast, arrowheads representing major arterial branches [23].

We conducted a computational fluid dynamics (CFD) analysis to quantify the haemodynamic difference between healthy control and atrophic mouse testicular arterial networks. This investigation aims to clarify how morphological differences (89 µm parent vessel diameter in control, 48 µm in atrophic) translate into functional deficits in flow distribution and resistance. The multi-phase, multi-component model effectively captured flow of the atrophy but extending this approach to the control was constrained by meshing complexity, requiring further optimisation work. Therefore, a single-phase continuum-based model was employed for an initial analysis of blood flow, comparing the control and the atrophic cases. This study demonstrated that the single-phase model enables efficient investigation of how anatomical variations impact flow distribution and pressure, revealing distinctive haemodynamics between the two networks. Furthermore, the multi-phase, multi-component model of the testis

atrophy revealed haemodynamic features that both aligned and differed from those predicted by the single-phase model. This alignment supports the use of the single-phase framework as a practical tool for identifying the haemodynamic differences between control and atrophic networks, however the multi-phase, multi-component model remains essential for capturing RBC-rich partitioning, CFL dynamics, and local viscosity change.

5.2 Material and methods

5.2.1 3D vascular reconstruction

The three-dimensional geometries of the whole mouse testes were first visualised using MATLAB's volshow function to identify arterial bifurcation networks. Based on established differences in vascular structure and function [283], vessels of smaller diameter were designated as arteries. A region of interest (a0–a1 in Fig. 5.2A&B was selected in the control testis based on branching hierarchy and tapering diameter; a matching region was chosen in the atrophic testis (a0–a1 in Fig. 5.2C&D) for direct comparison. The main vessel lengths a0–a1 were comparable: 2625 μm (control) and 2470 μm (atrophy). These regions were reconstructed into realistic three-dimensional vascular models using SimVascular [258], with centreline paths and lumen boundaries manually segmented. The networks were generated using the PolyData method and smoothed to reduce artefacts. To minimise boundary effects, the vessels were extended by 10D (where D is the local branch diameter) using VMTK [259]. Inlet diameters were ~89 μm (control) and ~48 μm (diseased), measured using MicroDicom. (https://www.microdicom.com/).

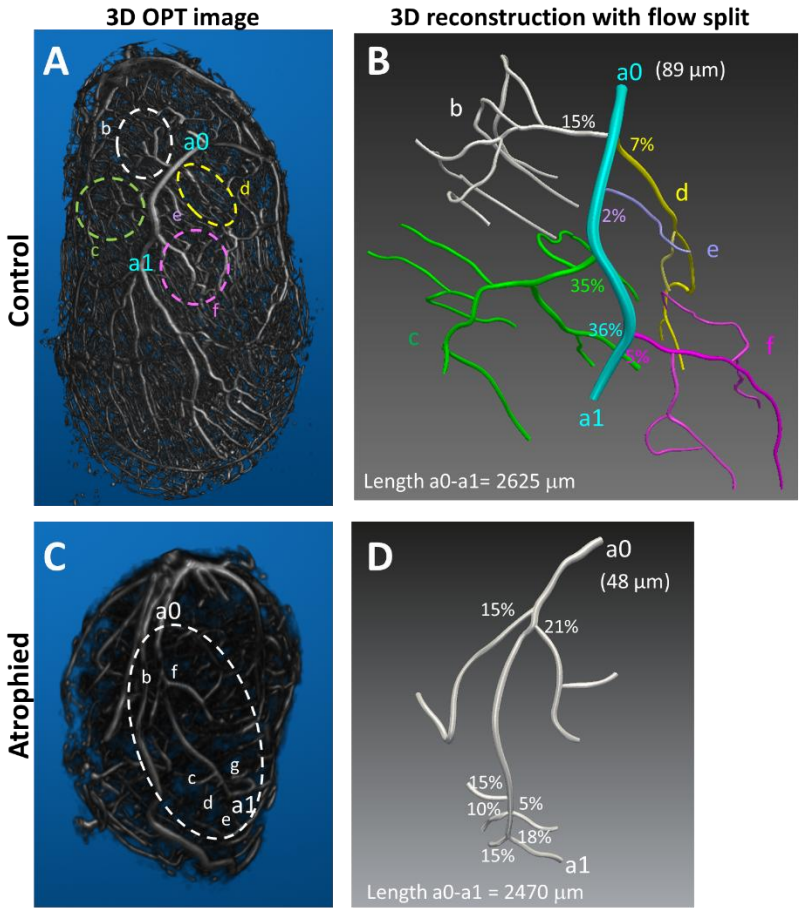

Figure 5.2: Testis control and atrophy. (A, B) Control testis. (C, D) Atrophied testis. (A, C) Whole testicular vasculature with the main arteries labelled (a0–a1) and colour-coded subtrees. (B, D) Reconstruction of arterial networks used in this study, with vessel diameter, length, and flow splits.

5.2.2 Single-phase CFD model

The computational meshes were discretised using polyhedral and prismatic elements in Simcenter STAR-CCM+ (Siemens). To capture the viscous effects, the first boundary layer was specified at a distance of ~0.004a0 away from the wall, where a0 was the diameter of the inlet of the network, with seven layers. The first layer was calculated based on a low y+ wall treatment using the formula $\rho(WSS/\rho)^{1/2}*y/\mu$, where ρ, WSS, y, and μ are the density (1060 kg/m^3), the wall shear stress (140 dyn/cm^3) [43], the target dimensionless wall distance, and the viscosity (0.00345 Pa-s). According to a grid independence analysis based on the maximum velocity upstream of the networks, meshes of around 3.7 and 1.9 million elements for the control and

diseased cases, respectively, were found to be sufficient for the flow regimes examined in this study. The mesh independence test was performed as detailed in Appendix D.1 (Fig. D.1 and D.2).

Blood flow in the testicular arterial networks was simulated in Siemens STAR-CCM+. The flow was assumed to be steady, laminar and incompressible, and governed by the Navier-Stokes equations:

$$\nabla \cdot u = 0 \tag{5.1}$$

$$\rho(u \cdot \nabla)u = -\nabla p + \mu \nabla^2 u \tag{5.2}$$

where u, p, ρ, μ is the blood velocity vector, the pressure, the density and dynamic viscosity, respectively. In the model, a steady, parabolic inlet velocity profile was assigned at the inlet, according to the equation:

$$U_{par}(x, y) = 2\mathrm{U} * (1 - \frac{4(x^2+y^2)}{D^2}) \tag{5.3}$$

with mean velocity U = 6 mm/s, an approximately physiological value for arterial diameter of ~89 μm [91]. To maintain the physiological flow by controlling the pseudo-shear rate (U/D) [9, 66], the mean velocity of 3.2 mm/s was used in the testis atrophy.

The outlet flow distribution was determined using the Murray's law [185], which predicts flow rates in branching vessels based on their respective diameters. The flow split ratio for each branch (Q_i/Q_t) could be expressed as:

$$Q_i/Q_t = \frac{D_i^3}{\sum_i D_i^3} \tag{5.4}$$

where *i* indexes each branch and Q_t the total flow rate. The resulting flow split for each branch is presented in Fig. 5.2B&D.

The non-Newtonian Generalized Carreau-Yasuda viscosity model ($\mu(\gamma) = \mu_\infty + (\mu_0 - \mu_\infty)[1 + (\lambda\gamma)^a]^{\frac{n-1}{a}}$) was prescribed with an infinite shear viscosity (μ_∞) of 0.00345 Pa-s, a zero shear viscosity (μ_0) of 0.056 Pa-s, a power constant (n) of 0.356,

an 'a' parameter of 2.0, and a relaxation time (λ) of 1.902 s [197]. The viscosity and density (1060 kg/m^3) were assumed identical for both control and atrophic cases. The segregated flow solver employing the SIMPLE algorithm was utilised. The mass flow rate ($\dot{m} = \sum_f \rho_f v_f \cdot a_f$) was calculated for each subtree, where ρ_f, v_f, a_f was the face density, the face velocity, and the face area vector, respectively.

5.2.3 Multi-phase, multi-component flow model

The meshing setup followed the procedure outlined in Chapter 2. A final mesh of 1.8 million cells was achieved for the atrophic geometry using a base size of 2.0x10^{-6} m, 20 prism layers, and prismatic layer total thickness of 6.0x10^{-6} m, while other parameters were fixed as provided in Appendix C.1. Consequently, the near-wall first layer thickness was 1.0x10^{-7} m, satisfying the criterion of being finer than the y$^+$-based first layer thickness of 1.7x10^{-7} m (derived from a 3.0 mm/s velocity).

The EMP model was implemented as detailed in Chapter 4, employing the diameter-based pressure outlet (section 4.2.2). The inlet velocity for the multiphase plasma-RBC and pure plasma components was prescribed at 3.2 and 2.8 mm/s, respectively, while the initial CFL thickness was specified as 3 μm [199]. For transient simulation (Δt = 5x10^{-4} s), the number of inner iterations was increased to 10, compared with the three iterations previously sufficient for the idealised bifurcations and the arteriolar bifurcations. This adjustment was necessary for the atrophied network to achieve adequate convergence of the pressure–velocity coupling and phase interaction equations at each time step.

5.3 Result

5.3.1 3D vascular reconstruction of control and atrophied testes

The arterial network of the control testis was characterised by capsular arteries on the surface and centripetal arteries radiating inward towards the mediastinum. In Fig. 5.2A&B, the capsular trunk (a0 to a1) branched into four capsular and one centripetal

vessel, representing the 1st-generation of five subtrees, denoted with ‘b’ (white), ‘c’ (green), ‘d’ (yellow), ‘e’ (purple), and ‘f’ (magenta), shown in different colours in Fig. 5.2A&B. For subtrees ‘b’, ‘c’ and ‘f’, most 2nd-generation branches traversed along the surface of the organ before turning inwards; only a few vessels remained superficial. Further branching led to small, convoluted arterioles. A hierarchical reduction in vessel diameter (tapering) was observed, with the trunk measuring 89 µm, the 1st-generation entrance averaging 37±9 µm, and the terminal distal branches measuring 26±6 µm (Fig. 5.3A).

In the atrophied case, most arterial branches remained superficial, without extending into the deeper parenchyma (Fig. 5.2C&D). The diameter at the a0 entrance, the entrance of the 1st-generation and the terminal distal branches were 48 µm, 28.1±1 µm and 29±3 µm, respectively (Fig. 5.3A). The averaged length from the entrance of the 1st-generations to the end of the most distal branches in the atrophic geometry was 599.8±434 µm, which was shorter than that of the control (2202.4±687 µm) (Fig. 5.3B).

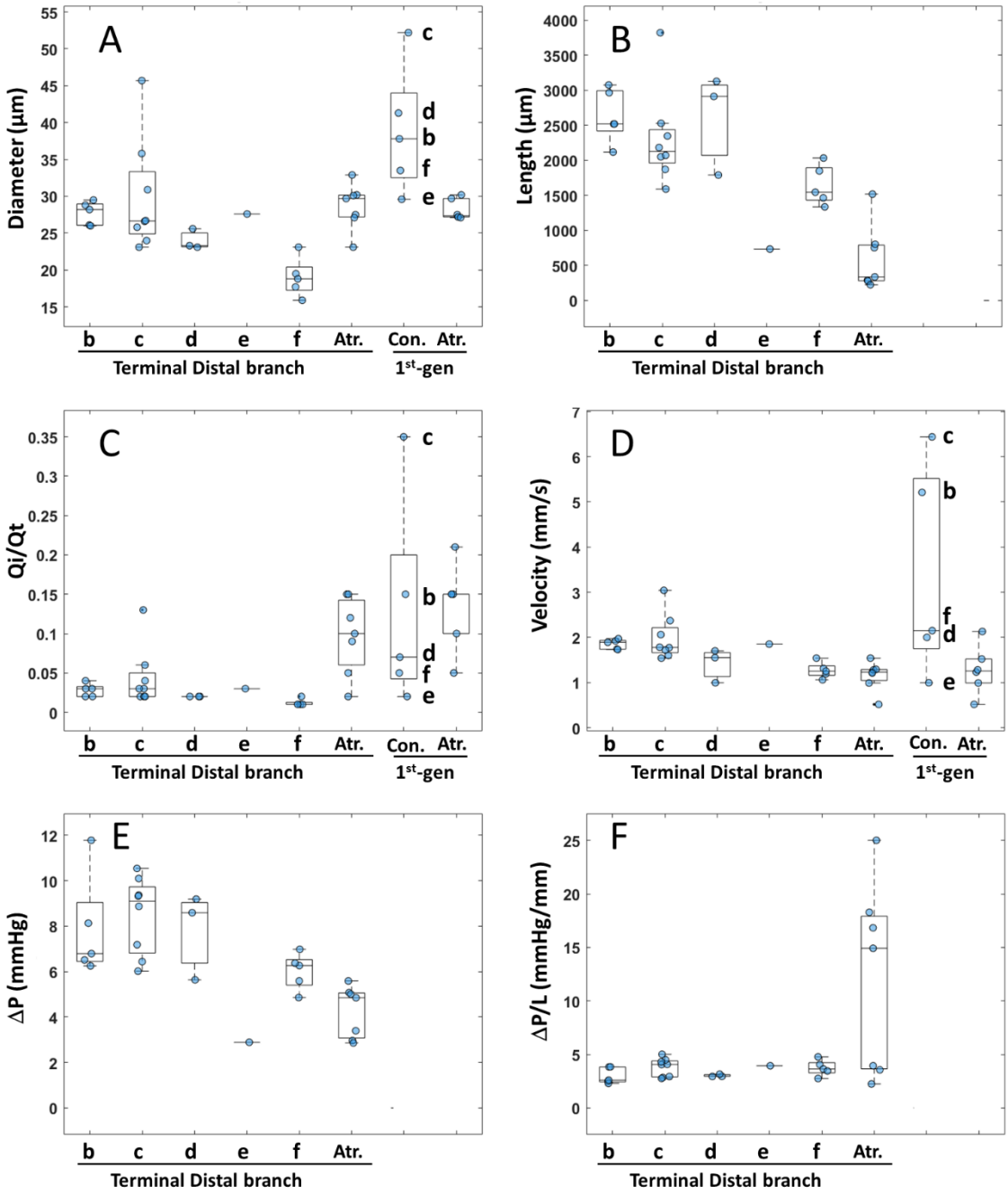

Figure 5.3: Geometry and haemodynamics of testis control and atrophy. (A) Diameter. (B) Length. (C) Flow fraction. (D) Velocity. (E) Pressure drop. (F) Pressure drop per length. Art., Con., 1st-gen stand for atrophy, control, and 1st-generation, respectively.

5.3.2 Haemodynamics in the control geometry

5.3.2.1 Branch flow split ratios

The single-phase simulation investigated arterial blood flow by assuming branch flow splits according to their relative outlet diameters (Murray's law), thereby reflecting a haemodynamically optimal perfusion. This approach ensured consistent velocities in the distal vessels, allowing sufficient blood pressure to reach the terminal branches to enable their function, such as supplying capillaries for oxygen exchange. The main branch (a0 to a1) tapered from 89 μm to 63.8 μm; however, the a1 outlet carried 36% of the total flow due to its role in supplying a major downstream region. Among the terminal distal branches, which had an average diameter of 24 to 30 μm (Fig. 5.3A), the subtree 'c' (8 branches) accounted for 35% of the total flow (Fig. 5.3C), the subtree 'b' (5 branches) for the 15% of the total flow and the subtree 'd' (3 branches) for 7%. With smaller distal diameters (~19 μm), subtree 'f' (5 branches) carried only 5% of the total flow, and branch 'e' only 2%. Fig. 5.3C showed that most distal branches exhibited, individually, a similar average flow fraction of 0.03±0.026 of the total flow. However, two specific branches in subtree 'c' were the exceptions: a 45-μm vessel with a flow fraction of $0.13Q_t$ and a 35-μm vessel with a flow fraction of $0.06Q_t$. These two branches supplied a downstream branching region comparable to that of a1, whereas the remaining branches connected to smaller arterioles or capillaries responsible for oxygen delivery. The large volume of the control testis accommodated more extensive branching and elongated centripetal arteries. The varied mass flow rates for subtrees 'c', 'b', 'd' and 'f' (18.5×10^{-9}, 7.6×10^{-9}, 3.8×10^{-9} and 3.4×10^{-9} kg/s, respectively) directly demonstrate that this branching pattern was structured to distribute blood flow in accordance with specific metabolic demands and physiological requirements.

5.3.2.2 Vascular resistance

The simulation demonstrated that pressure regulation in the arterial network was governed by two distinct parameters. The total pressure drop (ΔP) was a global parameter, showing that long distal branches in subtrees 'c', 'b' and 'd' at 1590-3822

μm (Fig. 5.3B) induced a significant ΔP of 8.2±1.8 mmHg (Fig. 5.3E and 5.4D). This pressure gradient was crucial for decelerating blood flow from high entrance velocities (6.4, 5.2 and 2.0 mm/s in the 'c', 'b' and 'd' subtrees, respectively) to slow terminal velocities (1.98±0.5, 1.85±0.1 and 1.41±0.1 mm/s among the distal end outlet vessels in the 'c', 'b' and 'd' subtrees, respectively) (Fig. 5.3D and 5.4A). The shorter length in subtree 'f' (1646±257 μm) exhibited a lower pressure drop of 6±0.7 mmHg. The resulting slow flow in the terminal distal branches before entering into the capillaries was essential for minimising mechanical stress and maximising the time available for efficient oxygen and nutrients exchange.

The pressure drop per length (ΔP/L), on the other hand, served as a local parameter indicative of the system's efficiency. The low and uniform ΔP/L of 3.5±0.8 mmHg/mm (Fig. 5.3F) across all subtrees demonstrated that pressure was declined at a constant and well-regulated rate. This controlled deceleration ensured the blood flow was optimally prepared for oxygen and nutrients exchange in the capillaries, highlighting the system's high efficiency and stability.

The main trunk, with a length of 2625 μm, was found to have the lowest ΔP (2.6 mmHg) and the lowest ΔP/L (1.0 mmHg/mm), as illustrated in Fig. 5.4D. This demonstrated its role as a low-resistance conduit. Its primary function was to transport a substantial volume of blood with minimal pressure loss, while preserving high upstream pressure to drive flow through the more resistive distal network (Fig. 5.5C). This contrasted with the smaller branches, which were structurally adapted to transform high-velocity, high-pressure flow into low-pressure conditions optimal for microcirculatory exchange.

5.3.2.3 WSS

The highest WSS was observed in a constricted, tortuous segment of the 2nd-generation of subtree 'c', labelled as region ζ (Fig.5.5A&C). This was attributed to a high flow rate (12.6 x10^{-12} m^3/s) passing through a narrow lumen, which significantly increased the near-wall shear gradient (Fig.5.5C). For region ε, located in the 1st-generation of

the same subtree, had a comparable flow rate (13.4×10−12 m³/s) but a wider and smoother geometry. This resulted in a low near-wall shear rate, and consequently a reduced WSS. In subtree 'b', region β also featured a constricted region with a diameter similar to that of region ζ, but the substantially lower flow rate (5.7 $x10^{-12}$ m^3/s) resulted in a diminished near-wall shear gradient and, subsequently, a lower WSS.

The main trunk at region δ exhibited the highest flow rate (28.9 $x10^{-12}$ m^3/s); however, due to the absent of constriction, the shear rate, and thus the WSS, was lower than in region ζ. Interestingly, the WSS at region δ was also influenced by near-wall viscosity, possibly because the velocity profile was blunt (Fig. 5.5C). In contrast, WSS in the other regions was primarily governed by the near-wall shear rate.

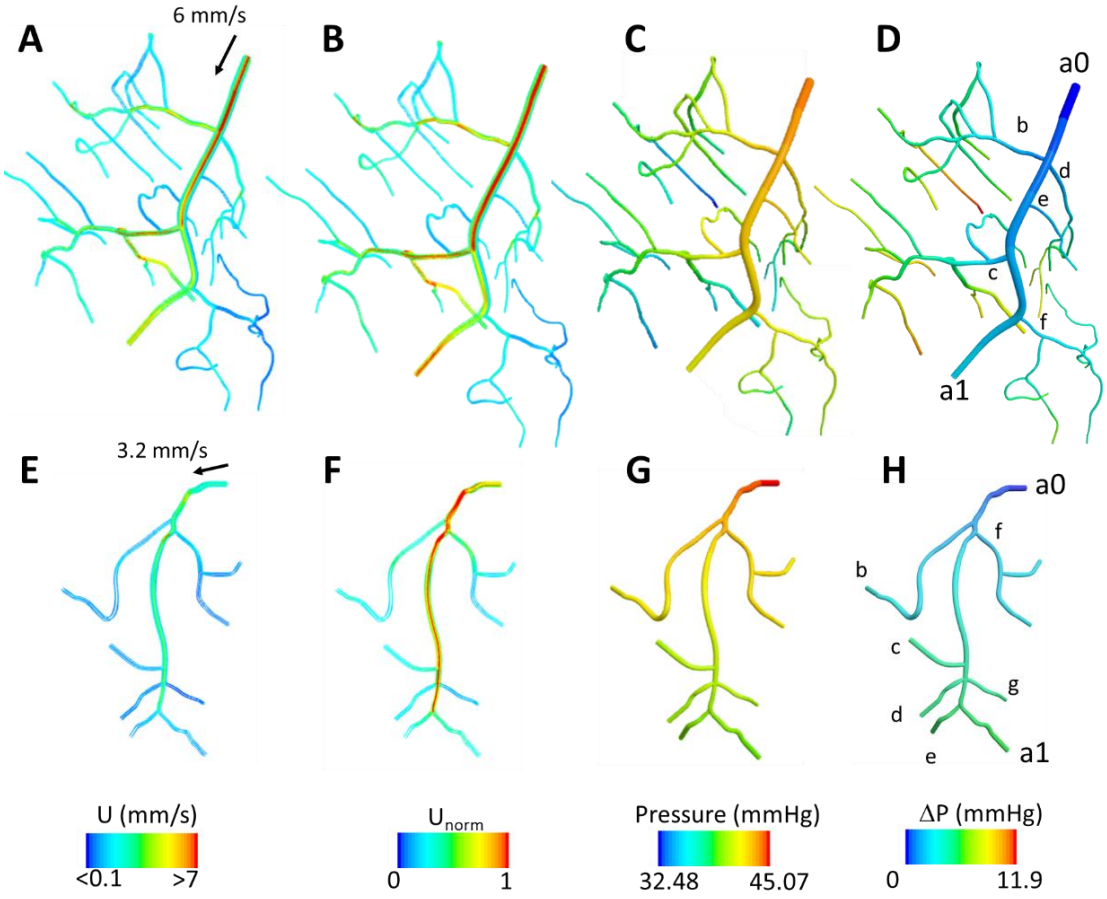

Figure 5.4: Haemodynamics in arterial testicular networks using a single-phase non-Newtonian flow model. (A-D) Control. (E-H) Atrophy. (A, E) Velocity. (B, F) Normalised velocity relative to the inlet. (C, G) Pressure. (D, H) Pressure difference.

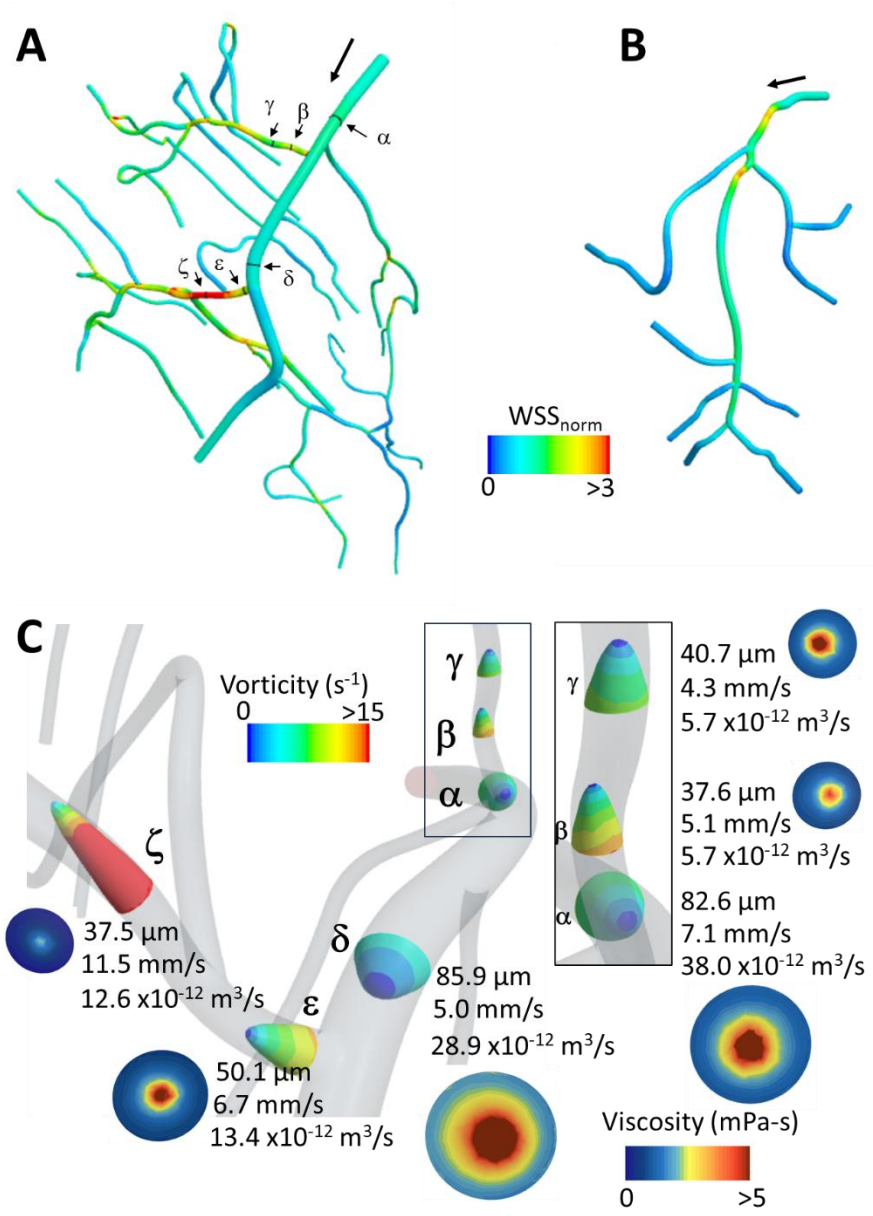

Figure 5.5: Wall shear stress in the testicular control and atrophy cases using a single-phase non-Newtonian flow model. (A, B) WSS of the control and atrophy vascular networks, respectively. (C) 3D velocity profiles coloured according to vorticity and viscosity on the cross-sectional area for specific areas on the main trunk (α, δ), subtree 'b' (β, γ) and subtree 'c' (ε, ζ). The diameter of these regions calculated from $\sqrt{4 * Area/\pi}$, where the Area was 5.35, 5.80, 1.11, 1.30, 2.01, and 1.10 x10^{-9} m^2, respectively. The shear rate or shear gradient was the slop of the velocity profile, which was equal to vorticity.

5.3.3 Blood perfusion in the control vs the atrophied vascular network

The atrophied testis exhibited a smaller diameter (48 μm), was modelled with a lower inlet velocity (3.2 mm/s) than the control case (6 m/s) to keep PSR (=U/D), as smaller arterioles are known to have reduced flow speeds [50, 91], which was consistent with the arterial flow reduction found in small testes [27]. Most distal branches in the atrophied testis resembled those of the control subtree 'e', being superficial and lacking further branching, whereas other control subtrees predominantly penetrated inwards. The averaged diameters of the atrophied distal branches (29 ± 3 μm) were comparable to those of the control (26 ± 6 μm), and the control subtree 'e' (27 μm), as shown in Fig. 5.3A. The atrophied vascular pathway was significantly shorter, averaging 599.8 ± 434 μm compared to 2202.4 ± 687 μm in the control network (Fig. 5.3B). However, its length was similar to that of the control subtree 'e' (734 μm).

Despite having similar distal diameters, the terminal velocities in the small, atrophied testis (1.2±0.3 mm/s) were lower than those in the control testis (1.7±0.4 mm/s), as demonstrated in Fig. 5.3D and 5.4A&E. This was due to a lower inlet velocity (3.2 vs 6 mm/s) and a higher flow split ratio (0.1±0.05 vs 0.03±0.03, as shown in Fig. 5.3C. The latter was a consequence of reduced branching in the atrophied vascular network. However, after normalising the velocity, both networks showed similar terminal velocities (0.31 for the atrophy network and 0.28 for the control), as depicted in Fig. 5.4B&F.

This performance was managed by the pressure. The shorter atrophied vascular network required a lower pressure drop (4.2 ± 1 mmHg) to reduce its entrance velocity, while the longer healthy control network required a greater pressure drop (7 ± 2 mmHg), as demonstrated in Fig. 5.3E and 5.4D&H. In Fig. 5.3F, the atrophic testis exhibited a significantly higher ΔP/L (12.11±8 mmHg/mm) compared to the control (3.51±0.8 mmHg/mm), indicating excessive pressure loss along the distal branches. This high resistance vessel caused the normalised velocity in the main trunk to increase, which in turn resulted in higher WSS (Fig. 5.5B).

In conclusion, the elevated resistance observed in the distal branch of the atrophied testis was a direct consequence of its less extensive branching and smaller overall size.

Fig. 5.4H showed a progressive pressure drop along the vascular network, including the main trunk. This haemodynamic profile is fundamentally different from the healthy control network (Fig. 5.4D), which functionally separated its low-resistance trunk from its high-resistance distal branches. In the atrophied model, the high resistance of the distal branches appeared to be reflected proximally, meaning the main trunk could not overcome the distal load and instead became an inefficient, high-resistance channel itself. Notably, the WSS patterns were reversed between the two networks. In the atrophy configuration (Fig. 5.5A&B), WSS was highest along the main trunk and decreased in the branching arterioles, whereas in the control, the opposite trend was observed, with WSS being predominantly higher within narrowed branching arterioles than in the trunk.

5.3.4 Multi-phase, multi-component flow model in the atrophy network

The multi-phase, multi-component model provided a more detailed characterisation of the RBC-rich flow and effectively captured the dynamic near-wall CFL at the network level in the atrophied testis. As illustrated in Fig. 5.6A&B, the RBC-rich region shifted towards the inner wall downstream of the first junction (a0-b), as observed in the main branch (inset of Fig. 5.6B showing the iso-surface of 50% volume fraction of the RBC-rich region in the arteriole segment ‘a-2’ and the distal branch ‘b’). This phenomenon is consistent with observations in idealised and testicular arteriolar bifurcations, as discussed in Chapters 2-4. A further characteristic was noted in the main branch segment ‘a-3’, where the RBC-rich region shifted towards the outer wall while the distal branch ‘f’ still exhibited a small RBC-rich region skewed towards the inner wall. This behaviour was attributed to two scenarios. Firstly, the short inter-bifurcation distance of the main branch ‘a-2’, preserving the asymmetric CFL before branching to the next bifurcation. Secondly, the higher flow rate in the main branch segment ‘a-3’ ($Q = 4.7x10^{-12}$ m^3/s), which pulled a greater volume fraction of the RBC-rich region, consequently enlarging the near-wall CFL at the bifurcation curve between the main branch ‘a-2’ and ‘f’, resulting in greater flux of near-wall CFL was drawn into the ‘f’ ($Q = 0.1x10^{-12}$ m^3/s). The multi-phase, multi-component model thus elucidated that the high resistance in the short distal branches promotes this strong plasma skimming

effect.

The asymmetric CFL strongly influenced haemodynamic outcomes, as demonstrated by comparison with the single-phase model under comparable boundary conditions. The multi-phase, multi-component simulation predicted lower WSS throughout the network (Fig. 5.6B), with a high WSS location in the main trunk and minimal WSS in distal branches. The pressure drop exhibited a similar trend, with the multi-phase, multi-component model showing a progressive decline along the vascular network, though less pronounced than in the single-phase case (Fig. 5.6C). Importantly, both models preserved the same overall spatial distribution of WSS and pressure drop. This supports the use of the single-phase model as a computationally efficient tool for comparative analysis of larger vascular networks. Although the multi-phase, multi-component model was not applied to the healthy control network, the agreement in spatial haemodynamic patterns with the single-phase model in the atrophied case supports the reliability of the single-phase data for evaluating haemodynamic differences between control and atrophy.

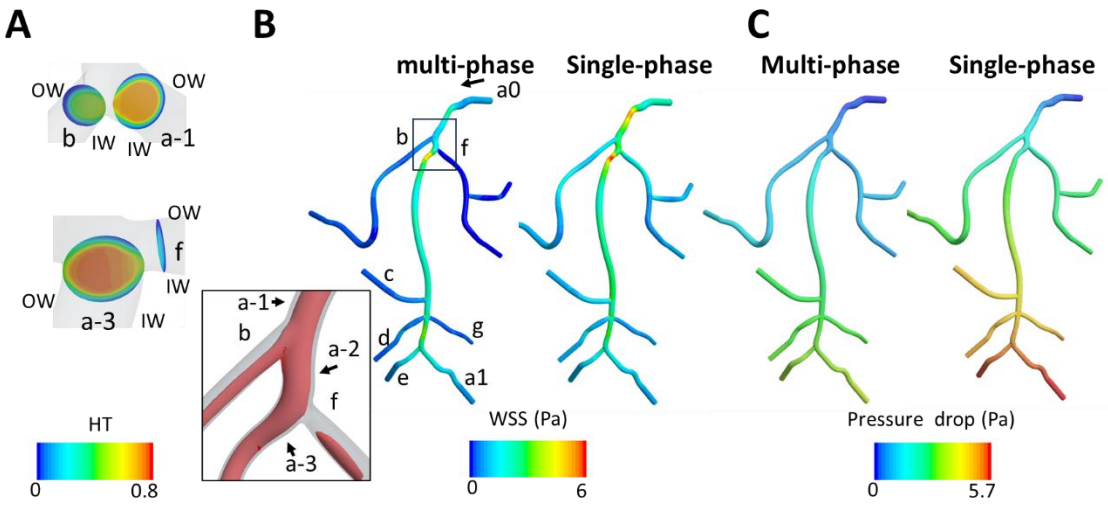

Figure 5.6: Haemodynamics in the atrophied testis using the multi-phase, multi-component flow model in comparison with the single-phase model. (A) Tube haematocrit profile on the cross-section planes of branches 'b', 'a-1', 'a-3' and 'f'. (B) WSS distribution with inset showing the RBC-rich region distribution represented by iso-surface of 50% volume fraction of the RBC-rich region. (C), Pressure drop distribution.

5.4 Discussion

This chapter aimed to distinguish the haemodynamic difference between the testicular atrophic and control mouse networks, with particular attention to the flow dynamics from the main trunk to the terminal distal branches. The novelty of this work lies in the use of a single-phase model to conduct the primary investigation, demonstrating how morphological variations translate into functional deficits. A further methodological contribution is the justification of this single-phase framework, by demonstrating its alignment with multi-phase multi-component model for the atrophy case.

5.4.1 Morphological differences between testis control and atrophy

The control network is a deeply penetrating, multi-branched system designed for volumetric perfusion, whereas the atrophic network is shorter, simpler, and confined to the surface. This structural contrast means the control network supplies the entire organ, while the atrophic network is limited to superficial regions. Despite this, both networks exhibit similar terminal vessel diameters (26 ± 6 μm vs. 29 ± 3 μm), suggesting that capillaries connected to distal branches may retain functional capacity, albeit at a smaller total cross-sectional area. These findings indicate that pathological changes in the vascular morphology primarily affect upstream architecture, length, depth, and branching, however a smaller number of terminal vessels mean a proportionally much smaller total cross-sectional area of peripheral tissue perfusion.

5.4.2 Haemodynamics in the arterial control testis

The use of fractional outlet boundary condition in this study reflects the physiological principle that blood flow is distributed according to tissue demand and vascular architecture. A direct correlation is observed between branching complexity and the percentage of flow received. For instance, the highly branched subtree ‘c’ (8 branches) receives 35% of the total flow, whereas the simpler subtree ‘d’ (3 branches) carries

only 7%. This demonstrates a precise, demand-based perfusion strategy. Furthermore, the functional role of these subtrees is not uniform. The high flow fractions (13% and 6%) in the two large-diameter distal vessels of subtree ‘c’ imply that this subtree does not merely supply local capillaries but serves as a critical conduit to major downstream multi-branching territories, indicating a sophisticated, multi-scale tissue perfusion system.

Testicular vascular morphology is key to haemodynamic function of the organ. The main trunk acts as a low-resistance conduit, evidenced by its minimal ΔP and ΔP/L relative to distal branches. This design facilitates high-volume blood transport with minimal pressure loss, thereby maintaining upstream pressure for perfusion of complex subtrees. Direct measurements in the hamster testis [270] revealed that the pressure in unbranched capsular artery is already less than 50% of the systemic pressure (41 vs 88 mmHg), demonstrating a considerable upstream pressure reduction and supporting its role as a low-resistance conduit. The trunk’s low resistance is therefore critical to preserve this remaining pressure, ensuring an adequate force mechanisms exist to overcome the cumulative resistance of the distal subtrees.

Unlike the main trunk, the distal branches are designed to dissipate pressure through increased length and branching, creating a marked pressure gradient across the network. This morphological arrangement ensures that blood flow decelerates sufficiently for effective capillary exchange of gases and nutrients [252]. This is supported by Doppler ultrasound measurements demonstrating a gradual reduction in flow parameters along the spermatic artery [265]. The slower flow also enhances thermal equilibration between arterial and venous blood, preserving the temperature required for spermatogenesis [252].

5.4.3 Blood perfusion in atrophied testis in comparison to control

The anatomical simplification of the atrophic network (being shorter, less coiled and less branched) suggests two key functional impairments. First, reduced arterial coiling likely disrupts countercurrent heat exchange with the pampiniform plexus,

compromising testicular thermoregulation [24]. Second, the atrophic network's reduced length and branching suggest impaired tissue perfusion capacity. Although our model assumed flow distribution proportional to the outlet diameters, implying optimised flow at the terminal vessels, the reduced number of terminal branches in the atrophic network inherently suggests different flow pattern and perfusion capability to the testis control. Studies in stallions confirm this link, showing that smaller, dysfunctional testes have significantly lower total arterial blood flow and higher vascular resistance [284]. Together, these structural changes possibly contribute to testicular dysfunction.

Our simulation reveals a crucial link between structural changes and pathological haemodynamics. Elevated $\Delta P/L$ and reversed WSS patterns indicate a compensatory shift in the main trunk in response to distal branch simplification. This distinct haemodynamic pattern provides a signature for the underlying structural deficiencies. Such deficits are observed in non-obstructive azoospermia (NOA) patients, whose low-density vasculature exhibits a 'relatively uneven' and 'non-uniform' pressure distribution, notably characterised by 'regions of low or absent pressure' [261]. The localised WSS patterns in the trunk of the atrophy are critical because WSS acts as a mechanical trigger for endothelial vasoregulatory feedback [272]. The contrasting localised WSS patterns in control and atrophied networks may reflect that this feedback mechanism is impaired in the atrophy.

5.4.4 Limitation and Future work

The current single-phase blood flow model successfully explains the haemodynamic differences between control and atrophied testes, providing crucial insights into convective transport and poor perfusion in the diseased state. The continuum approach is widely adopted in network level and has been applied to oxygen transport studies [285, 286]. The reliability of this continuum-based framework is supported by Rasmussen et al. (2017), who demonstrated that such models provide good global correspondence with experimental data and produce physiologically realistic haematocrit distributions even without discrete cell tracking [287]. However, a key

limitation is its tendency to overestimate parameters such as velocity and WSS, as confirmed by our multi-phase, multi-component simulations and previous studies. The simplification excludes multiphase phenomena such as CFL formation and plasma skimming, potentially lowering haematocrit in distal branches and exacerbating perfusion heterogeneity [288, 289]. These mechanisms could significantly alter oxygen availability in microvascular beds, especially under low-flow conditions associated with atrophy.

The absence of a formal uncertainty quantification framework in this study constrains the generalisability of testicular control results. Reliance on Murray's Law assumes an energetically optimal, passive system, whereas microvascular resistance is actively modulated by mural cells to regulate blood flow [290]. This active regulation introduces complexity that idealised partitioning fails to capture, particularly in systems including the retina where models must account for autoregulation to ensure accurate haemodynamic predictions [291]. Rasmussen (2025) demonstrates that boundary conditions at cut vessels heavily influence simulated results and represent a persistent challenge in microvascular modelling [292]. This suggests that deviations from Murray-type flow partitioning may significantly alter predicted haemodynamic metrics. Furthermore, extreme perfusion pressure changes can lead to a complete breakdown of autoregulatory control [35]. Without assessing how these active biological changes and boundary uncertainties interact, the precision of predicted WSS remains unknown.

The precision of the present model is constrained by the manual determination of segment radii, which introduces significant uncertainty due to the inverse fourth-power relationship (Poiseuille's law) between vessel radius and vascular resistance. Since vessel size and haematocrit vary inherently across patients and locations, results remain sensitive to input uncertainties. Rasmussen (2025) notes that diameter-related errors significantly influence the accuracy of microcirculatory simulations [292]. The static nature of the model ignores the active physiological responses described by Pappelis et al. (2020) and Milanovic et al. (2021), in which vessels adapt their calibre to metabolic stimuli [290, 291]. Diameter variations occurring at the time of imaging,

but not represented in the static geometry, therefore introduce additional uncertainty in the resulting pressure and wall shear stress predictions.

Material assumptions within the current modelling framework represent an additional source of uncertainty. Although the single-phase model provides a computationally efficient tool for large-scale network analysis, it lacks the discrete resolution required to capture RBC migration and interface dynamics. While a shear-thinning Carreau-Yasuda model is employed to capture non-Newtonian effects, the model does not account for the local viscosity fluctuations driven by discrete haematocrit partitioning at bifurcations.

Applying the multi-phase model to the control testis remains challenging due to its anatomical complexity, including tapering from 89 μm proximally to approximately 15 μm distally, pronounced tortuosity, and frequent constrictions. These features require a high mesh density. Specifically, the height of prismatic layer total thickness must exceed the thickness of the CFL, complicating the mesh generation. Consequently, the multi-phase, multi-component model was only feasible to implement in the atrophic model. Future work should focus on developing mesh optimisation strategies that reduce cell count while preserving the prismatic layer fidelity, enabling accurate modelling of the control testis.

Application of the multi-phase meshing strategy to the control network is restricted by the interplay between CFL resolution and prism-layer growth constraints. For large arterioles (~89 μm), CFL estimates of approximately 3.9 μm [199] provided the choice of a prismatic layer total thickness exceeding the CFL by roughly two-thirds (≈6.5 μm), ensuring stable phase separation across varying flow conditions. In contrast, the single-phase control model was discretised with ~3.7 million cells using seven prism layers, a stretching ratio of 1.3, and a total prismatic thickness of ~0.7 μm. Multi-phase simulations require a lower stretching ratio (1.1); in the atrophied network this already necessitated ~20 prism layers to reach 6 μm. Together, the increased total thickness and reduced stretching substantially increase layer count and mesh size, rendering full multi-phase discretisation impractical.

Chapter 6

Macroscale pulmonary artery bifurcation

6.1 Introduction

Turner syndrome (TS) is a chromosomal disorder characterised by partial or complete absence of the second X chromosome. Although uncommon, it is the most frequent chromosomal abnormality in females, affecting ~1 in 2,500 live births (Europe/East Asia/North America) [293-295]. Approximately half of women with Turner syndrome are born with a congenital cardiovascular defect, and this prevalence persists among children aged 2–19 years [296-298]. These congenital cardiovascular abnormalities predominantly involve the left heart and the aortic arch, notably an elongated transverse aortic arch, bicuspid aortic valve, aortic dilatation, coarctation, and aberrant right subclavian artery [299-303]. These anatomical defects, together with a predisposition to obesity and hypertension, contribute to increased cardiovascular risk and reduced life expectancy of this patient group [304]. These features, alongside metabolic and blood-pressure predispositions, underpin elevated cardiovascular risk in TS.

Direct structural defects of the pulmonary artery (PA) in TS are rare, with works largely limited to case reports of valve stenosis [305]. More significantly, functional PA changes are common due to related conditions such as Partial Anomalous Pulmonary Venous Return (PAPVR). With a prevalence of 13%-15.7%, PAPVR causes volume overload on the PA, demonstrating that abnormal flow can exist within a structurally normal vessel [301, 303]. Considering the systemic abnormality characteristic of Turner Syndrome, this study extends the investigation in bifurcating vessels to the pulmonary arteries. We aim to determine whether haemodynamic and geometric features, such as distributed flow patterns or secondary flow vortices, are also present at the PA bifurcation, which provides a clear rationale for this functional flow analysis.

The pulmonary arteries exhibit distinctive anatomy and biomechanics. Under physiological conditions, the bifurcation operates as a low-resistance, low-pressure and high-flow circuit [306]. Alterations in systemic or pulmonary pressures can modify the arterial wall compliance and thickness, affecting both the proximal and distal segments of the arterial tree [307, 308]. Because anatomical geometry strongly shapes haemodynamic behaviour in both normal and diseased states, this relationship remains an important target for further research [309-311].

Computational fluid dynamics (CFD) effectively analyses pulmonary haemodynamics. In tetralogy of Fallot (TOF), patient-specific models have demonstrated the influence of pulmonary bifurcation geometry (branch angles, curvature, tortuosity and planarity) on haemodynamic factors including wall-shear distributions, inter-branch pressure differences and flow splits [312-314]**.** Similarly, studies in pulmonary hypertension have demonstrated that flow disturbances are influenced by anatomical and functional changes within cardiopulmonary circulation rather than by pressure alone [315]. While CFD has illuminated the interplay between pulmonary artery and haemodynamics in those pathologies, to our knowledge, analogous patient-specific analyses of the pulmonary arteries in Turner syndrome have not been reported before. We therefore apply CFD methods to the PA in paediatric Turner syndrome patients to assess the presence of distinctive flow and shear characteristics.

6.2 Material and methods

6.2.1 Patients cohorts

This retrospective study analysed magnetic resonance imaging (MRI) scans obtained from a cohort of four girls (n=4; mean age 13±5 years) with karyotypically proven Turner syndrome, attending the paediatric TS clinic at the Royal Hospital for Children, Queen Elizabeth University Hospital (RHC, QEUH). It was noted that patient TS3 had undergone a coarctation repair during the neonatal period, whilst TS5 had a left congenital diaphragmatic hernia repaired at birth; both surgical interventions were

anatomically remote from the proximal pulmonary arteries, the region of interest. For patient TS5, an anomalous crisscross origin of the branch pulmonary arteries was identified, with the left pulmonary artery (LPA) arising superiorly to the right pulmonary artery (RPA) and appearing smaller in diameter. It is noted that the 'TS5' number designation is linked with the corresponding aortic geometry presented previously in Johnston et al. (2023) [316].

All cardiac data were acquired on a 1.5T Siemens MAGNETOM scanner (2015–2018) with full ECG and respiratory gating. Through-plane flow was quantified at the main pulmonary artery root using a 2D time-resolved phase-contrast MRI sequence. Key acquisition parameters included: VENC = 150–400 cm/s; TE = 2.66–3.33 ms; TR = 9.94 ms; slice thickness = 3.5–5 mm; FOV = 300 × 300 mm. This protocol resulted in an image matrix of 256 x 256 and a spatial resolution of 1.17 × 1.17 × 3.5–5 mm.

A healthy control group was established using data obtained from the Vascular Model Repository, comprising five age- and gender-matched girls (average age 13 ± 2 years) without any history of pulmonary disease. The control cohort (H1 [317], H2 [318], H3 [317], H4 [318] and H5 [318]) primarily consisted of anatomical datasets. A key limitation was that detailed hemodynamic flow information was present for only a single individual (H5). Although BMI was not explicitly provided, the repository's quality standards suggest it is reasonable to assume all individuals fell within a normal physiological range.

6.2.2 Flow information

To characterise the velocity profile at the main pulmonary artery (MPA) root, phase-contrast magnetic resonance imaging (PC-MRI) data were analysed using the Segment Research software [319]. For each of the four patient geometries, both phase-contrast and magnitude image stacks were acquired throughout the cardiac cycle (Fig. 6.1C&D). The luminal circumference of the MPA was delineated on every frame to determine the instantaneous velocity (Fig. 6.1E & Fig. 6.2). The time average mean velocity (TAMV) calculated as the integral of the velocity (time curve divided by the

total duration of measurement), providing a robust estimate of the MPA velocity (Table 6.1).

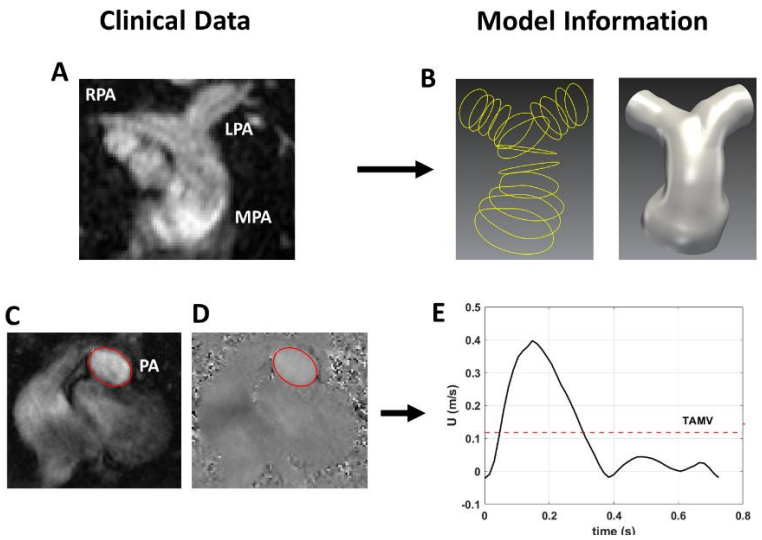

Figure 6.1: Overview of the MRI data processing workflow. (A) Anatomical magnetic resonance imaging of the pulmonary artery bifurcation, detailing the main (MPA), left (LPA), and right (RPA) arteries. (B) The resulting reconstructed patient-specific geometry (patient TS2). (C-E) The process of extracting blood flow data, where (C) magnitude and (D) phase-contrast (PC-MRI) images are used to isolate the MPA root (red circle) and calculate the (E) resulting velocity profile.

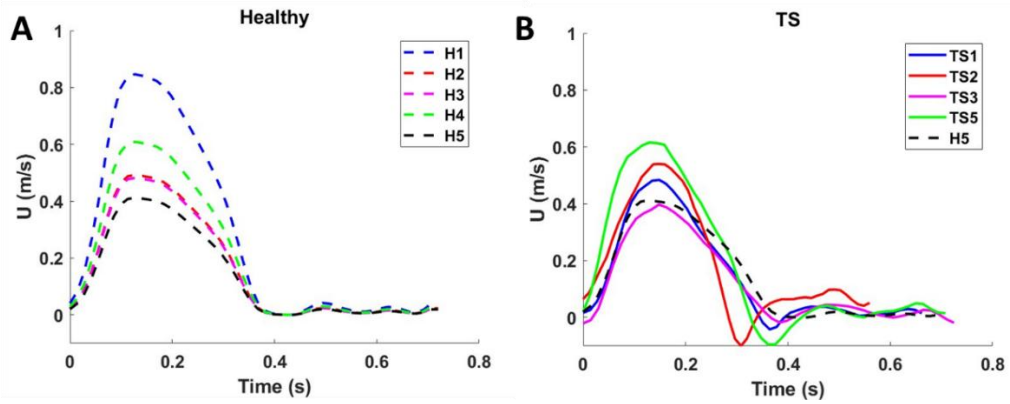

Figure 6.2: Inlet velocity waveforms for healthy and TS cohorts. (A) The inlet velocity profiles used for the five healthy subjects. As flow rate data was only available for one subject (H5), this single profile was scaled by the inlet area of each individual to generate their respective velocity profiles. (B) The patient-specific pulsatile inlet velocity profiles for the TS subjects, derived from their individual measurements.

Table 6.1: Pulmonary Artery Characteristics in Turner Syndrome and Healthy Control Cohorts.

	Age (y)	Diameter (mm)			Flow split %		Q (mL/s)	U (m/s)	Re_{MPA}
		MPA	RPA	LPA	RPA	LPA			
H1	11	19	10	11	0.43	0.57	83.5	0.29	1441
H2	8	26	15	16	0.45	0.55	83.5	0.17	1146
H3	11	25	13	12	0.56	0.44	83.5	0.16	1079
H4	13	23	15	14	0.55	0.45	83.5	0.21	1254
H5	22	28	17	20	0.38	0.62	83.5	0.14	1032
mean	13.0	24.2	14.0	14.6	0.5	0.5	83.5	0.2	1190.2
std.	4.8	3.1	2.4	3.2	0.1	0.1	0.0	0.1	145.8
TS1	14	19	12	12	0.5	0.5	70.9	0.15	755
TS2	10	22	15	14	0.55	0.45	117.6	0.19	1108
TS3	15	27	13	12	0.56	0.44	80.0	0.11	787
TS5	13	16	11	8	0.66	0.34	59.3	0.18	763
mean	13.0	21.0	12.8	11.5	0.6	0.4	81.9	0.2	853.3
std.	1.9	4.1	1.5	2.2	0.1	0.1	21.8	0.0	147.3

Note: ‘TS’ designation was previously linked with the aorta in a study by Johnston et al. (2023) [316].

6.2.3 3D vascular reconstruction

Patient-specific three-dimensional models of the pulmonary artery bifurcation were reconstructed from MRI data using the SimVascular software [320]. To capture the vessel anatomy with high fidelity, the vessels centrelines were segmented, by first segmenting the centreline of the main pulmonary artery (MPA) and extending it into the right pulmonary artery (RPA). A second, separate centreline was created to delineate the geometry of the left pulmonary artery (LPA).

Along each centreline, the vessel lumen was segmented on each image slice using a semi-automatic active contour tool, with manual refinement undertaken to ensure accuracy. The segmentation of the RPA and LPA was terminated prior to their first distal bifurcations. The two-dimensional contours from each path were then lofted into separate three-dimensional models, which were subsequently merged and smoothed to form a single, cohesive geometry. Finally, to mitigate the influence of boundary conditions on subsequent simulations, vessel extensions were performed. An extension

of 0.5 times the inlet diameter (D) was added to the MPA inlet [313], whilst extensions equivalent to 10 times the vessel diameter were added to the RPA and LPA outlets. The diameters of the MPA, RPA, and LPA vessels for each patient are shown in Table 6.1.

6.2.4 Computational fluid dynamics

CFD simulations were conducted in Siemens STAR-CCM+. The nine geometries were discretised with polyhedral elements, refined near the vessel wall using a seven-layer prismatic mesh to accurately capture near-wall viscous effects and velocity gradients. The first prismatic layer (Δy_1) was positioned at a distance of approximately 0.001–0.002D from the wall and ranged between 0.1 and 0.6 μm in thickness. They were closer to the wall than the distance calculated from the target dimensionless wall distance (y^+) via $\Delta y_1 = \mu y^+ / \left(\sqrt{wss}/\rho\right)$. This calculation utilised a density (ρ) of 1060 kg/m^3, viscosity of 4x10^{-3} Pa·s WSS of 4 dyn/cm^2 [321], and the dimensionless wall distance ($y^+ = u_{bulk}/\sqrt{wss/\rho}$, where u_{bulk} = 0.1 m/s). The total number of elements for the nine geometries was between 0.4 – 1.2 million cells.

The governing equations were the incompressible Navier–Stokes equations:

$$\nabla \cdot \boldsymbol{u} = 0 \tag{6.1}$$

$$\rho \frac{\partial \boldsymbol{u}}{\partial t} + \rho(\boldsymbol{u} \cdot \nabla)\boldsymbol{u} = -\nabla p + \mu \nabla^2 \boldsymbol{u} \tag{6.2}$$

where $\boldsymbol{u}$ is the mean velocity and p is the pressure. Blood was modelled as an incompressible non-Newtonian fluid using the Generalized Carreau-Yasuda viscosity law: ($\mu(\gamma) = \mu_\infty + (\mu_0 - \mu_\infty)[1 + (\lambda\gamma)^a]^{\frac{n-1}{a}}$) with an infinite shear viscosity (μ_∞) of 0.00345 Pa-s, a zero shear viscosity (μ_0) of 0.056 Pa-s, a power constant (n) of 0.356, an a parameter of 2.0, and a relaxation time (λ) of 1.902 s [197]. The SST k–ω turbulence model was applied to capture transitional and turbulent features of the flow [322]. Pressure–velocity coupling was handled via the pressure-implicit with splitting of operators (PISO) scheme under an unsteady segregated solver. Rigid, no-slip

boundary conditions were applied at the walls. Inlet conditions were defined from patient-specific pulsatile velocity waveforms (Fig. 6.2B), while physiological mean flow splits were applied at the RPA and LPA outlets based on diameter (Table 6.1). This physiological flow split was calculated using Murray's Law [185], a formula where the flow rate (Q) is proportional to the branch diameter (D) cubed (n=3). The expression for the LPA is given by:

$$Q_{LPA}/(Q_{LPA} + Q_{RPA}) = D_{LPA}^3/(D_{LPA}^3 + D_{RPA}^3) \quad (6.3)$$

The time-averaged wall shear stress (TAWSS) was calculated for each model by integrating the instantaneous wall shear stress over the period of a single cardiac cycle (T), according to the formula: $\text{TAWSS} = \frac{1}{T}\int_0^T wss\, dt$. For comparative purposes, the resulting TAWSS distribution was subsequently normalised by the TAWSS value computed at the inlet of each respective model.

6.3 Results

6.3.1 Morphological analysis

The healthy cohort demonstrated considerable morphological variability. While some models including H3 and H5 were fairly symmetric, others such as H1 and H2 displayed significant MPA curvature and non-planar branching (Fig. 6.3A). This suggested that a wide range of shapes were able to exist within a healthy population. The bifurcation angles appeared generally wide and open.

The TS cohort also showed variability but included the most extreme outlier. In line with the clinical notes, TS1 and TS2 appeared morphologically normal and were difficult to distinguish from the symmetric healthy cases (Fig. 6.3B). TS3 was subtly different due to its high branching point. However, TS5 was anatomically distinct from all other geometries. Its crisscross, non-planar origin and the size discrepancy between the LPA and RPA represented a clear congenital anomaly that would be expected to produce blood flow patterns that deviate from those of normal PA anatomy.

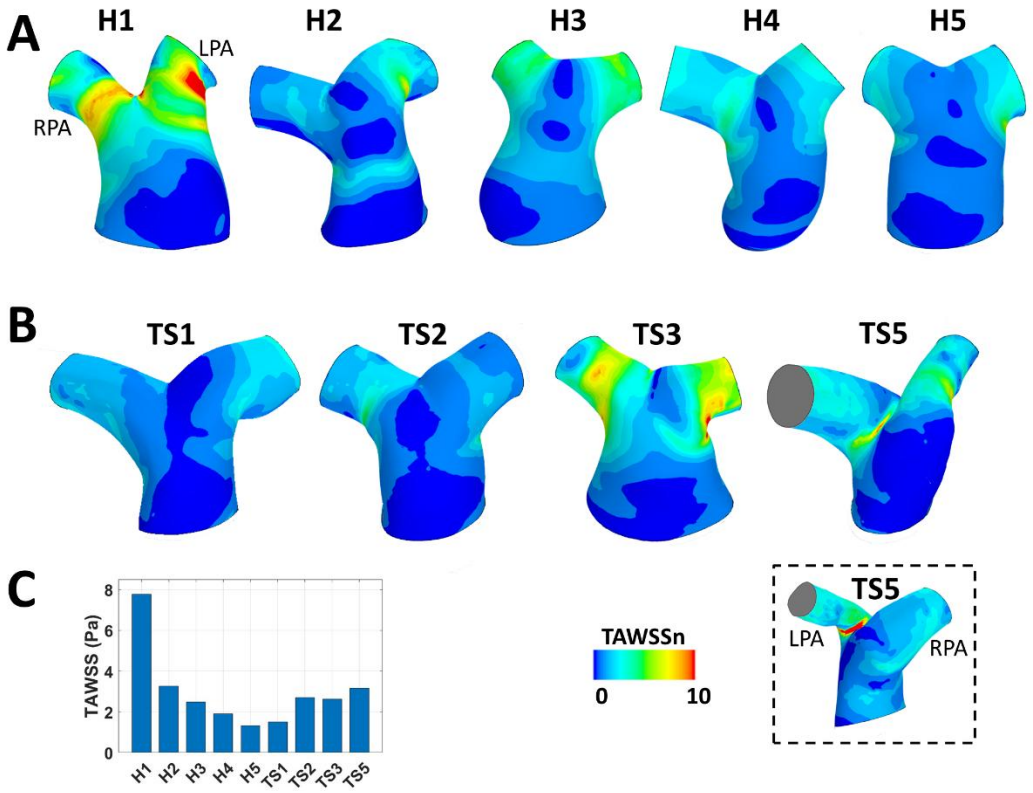

Figure 6.3: Wall shear stress distribution. (A, B) Non-dimensional time-average WSS (TAWSSn) in the healthy and TS patient-specific geometries, respectively. The inset provided a posterior view of the abnormal TS5 geometry. (C) TAWSS plot, calculated based on the whole geometry of PA.

6.3.2 Time-average Wall shear stress

The distribution of TAWSSn, normalised by the inlet value for each model and visualised in Fig. 6.3A&B, was found to be highly heterogeneous, reflecting the underlying vascular morphology. Across most geometries, TAWSSn was predominantly low, with distinct regions of elevated WSS consistently localised at the bifurcation apex, or flow divider, and the outer wall of the LPA entrance (H1, TS3). This concentration of high TAWSSn was an expected consequence of direct flow impingement at the point where the main pulmonary artery divides into its primary branches [314].

The results indicate that there is no clear distinction of TAWSSn patterns between the healthy with the TS patients. Two dominant TAWSSn patterns were observed across both the healthy and patient geometries, governed by subtle variations in arterial geometry such as the MPA curvature. The first pattern was characterised by localised elevated TAWSSn concentrated at the flow divider, as observed in models H1, H3 (Fig. 6.3A) and TS3, TS5 (Fig. 6.3B). The second pattern in the remaining cases involved elevated TAWSSn extending more diffusely along the outer walls of the RPA and LPA. It was suggested that these differences were driven by subtle variations in each patient's unique anatomy, including the curvature of the arteries.

The magnitude and pattern of TAWSS was primarily governed by the inlet velocity and 3D morphology. This velocity-dependence was clearly demonstrated in the healthy cohort, where a uniform pulsatile flow profile was applied to each patient's unique inlet area resulted in proportionally higher velocities in smaller diameter arteries. The extreme TAWSS in case H1 (almost 8.0 Pa across the entire geometry, as demonstrated in Fig. 6.3C) was a direct result of its high inlet velocity (~0.85 m/s peak velocity value, as depicted in Fig. 6.2A), which is a consequence of its relatively small MPA diameter. A decreasing trend in absolute TAWSS was observed from H2 down to H5, which correlated with an increase in their MPA diameters.

The haemodynamic of the TS cohort was more complex with distinct velocity profiles and generally moderate TAWSS values (1.5-3.2 Pa), as provided in Fig. 6.2B and 6.3C. TS5, whose anomalous 'crisscross' morphology, exhibited the highest velocity and TAWSS (~3.2 Pa) of the TS group. TS2 displayed a higher peak velocity than TS3, but their absolute TAWSS values were almost identical (~2.8 Pa and ~2.7 Pa).

6.3.3 Velocity distribution

6.3.3.1 Velocity streamlines

Analysis of the non-dimensional velocity streamlines in the healthy cohort consistently identified a three-phase haemodynamic sequence throughout the cardiac cycle including peak systole, mid-deceleration and mid-diastole. As demonstrated in Fig. 6.4, at peak systole (I), the flow in all healthy patients (H1-H5) was represented as a smooth, high-velocity laminar stream splitting efficiently at the pulmonary artery bifurcation. As the flow decelerated (II), this organised pattern was disturbed with the emergence of secondary flows, indicated by rotating streamline paths, particularly near the outer vessel walls. Finally, the cycle culminated in a low-flow diastolic phase (III) dominated by large, slow-moving vortical structures and flow recirculation within the MPA.

The evolution of blood flow in the TS patients revealed significant haemodynamic instabilities throughout the cardiac cycle. At peak systole (Fig. 6.5I), patient TS3 exhibited intense acceleration forming a high-velocity stream within the narrowed segment of the daughter branches, while TS5 presented different flow development, with a skewed flow and streamlines diverted predominately towards LPA branch, leaving the RPA branch poorly perfused due to anatomical anomalies. During systolic deceleration (II), this asymmetry in TS5 persisted and transformed into a secondary vortex and a strong skewness, similar to the behaviour observed in TS1. The cycle culminated in a chaotic mid-diastolic phase (III), characterised by complex, disorganised vortical structures, and in some cases, near-stagnant flow.

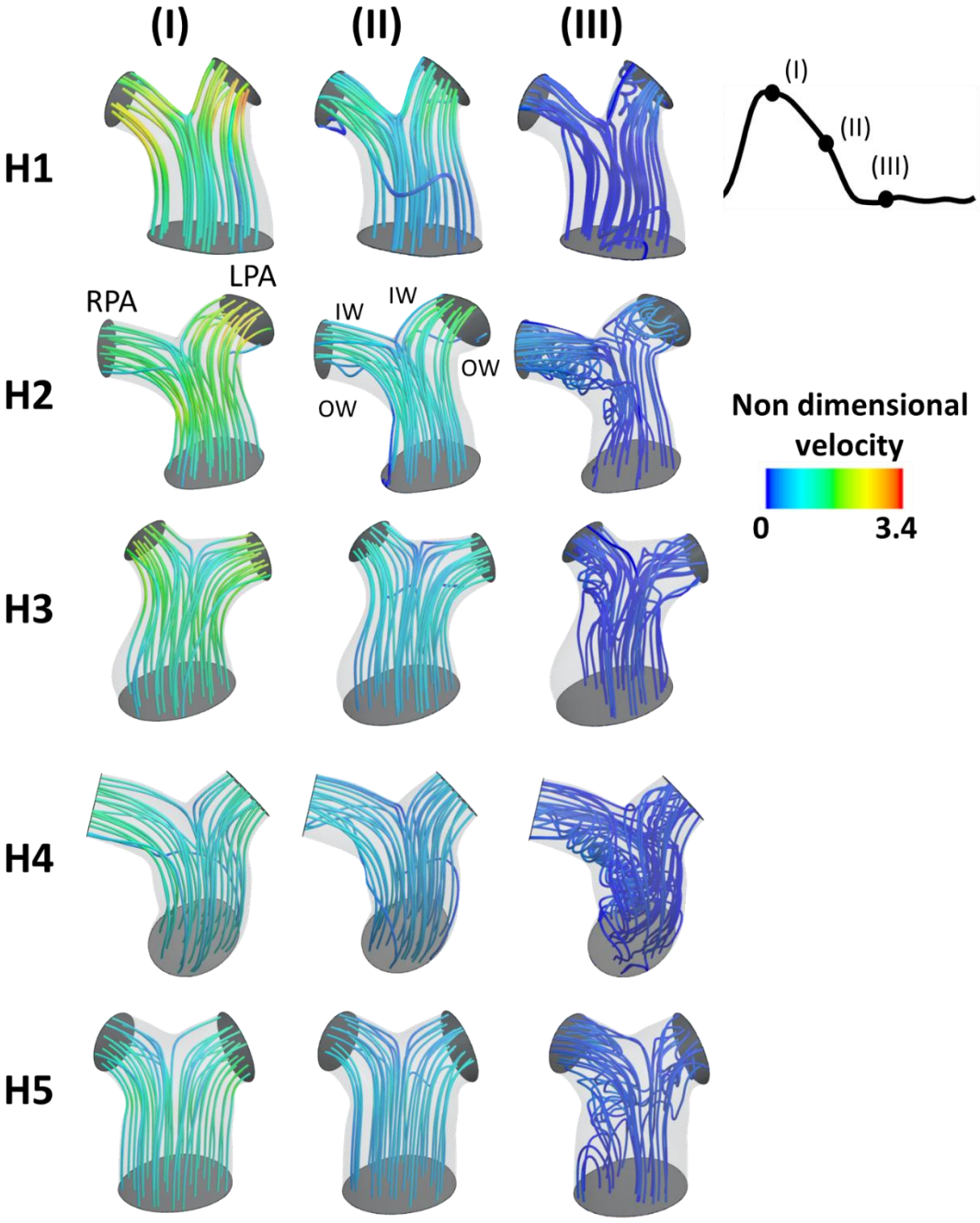

Figure 6.4: Velocity streamlines and associated flow waveforms within the healthy patients. Results were shown for three selected points of the cardiac cycle: peak (I), mid deceleration at systole (II), and mid diastole (III) for the healthy patients' inlet waveform. The streamlines were coloured according to the non-dimensionalised velocity magnitude, which was normalised based on the average inlet velocity.

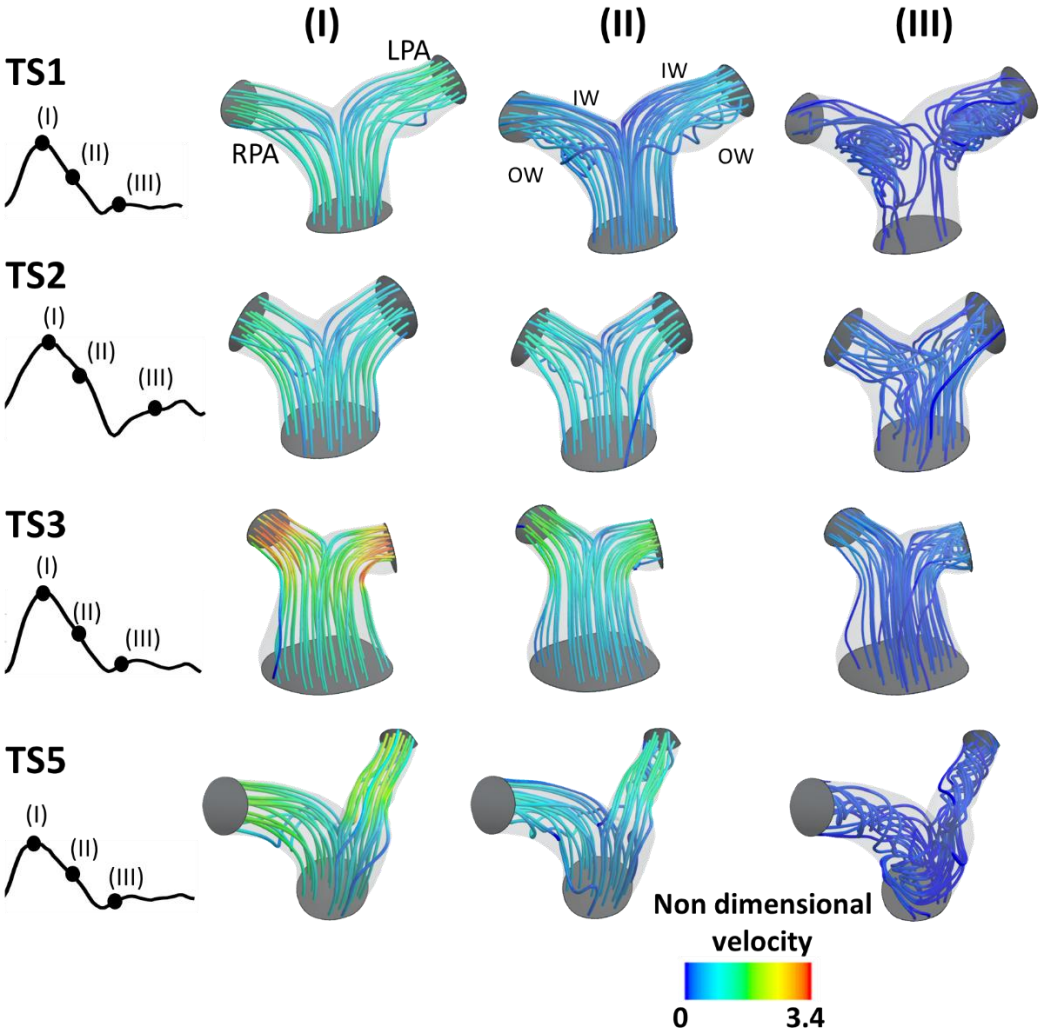

Figure 6.5: Velocity streamlines and associated flow waveforms within the TS cases. Results were shown for three selected points of the cardiac cycle: peak (I), mid deceleration at systole (II), and mid diastole (III) for the corresponding TS inlet waveform. The streamlines were coloured according to the non-dimensionalised velocity magnitude, which was normalised based on the average inlet velocity.

6.3.3.2 Secondary flow

The secondary flow within the healthy subjects was varied. At peak systole (Fig. 6.6 (I)), the flow was observed as a C-shaped accelerated flow adjacent to the outer wall (as in H1 and H2) and a more diffuse central high-velocity core (H3; LPA of H4 and H5). Patient H4 exhibited a single in-plane vortex at the posterior OW of the RPA. This flow pattern is in agreement with previous results for healthy volunteers [313]. During systolic deceleration (II), the initial high-velocity stream mostly transformed into a pair of counter-rotating Dean vortices, some cases showed a single vortex (RPA of H4, LPA in H1). However, the highly skewed velocity in H2's LPA created a distinctly asymmetric vortex pair. During mid-diastole (III), the flow followed two different pathways: most cases (H1, H2, H4) resolved into a complex, multi-vortex state, while in others (specifically the RPA of H4 and H5) the flow merged into a single, larger vortex.

Pathological haemodynamics can seemingly mimic healthy patterns, but subtle or specific variations often distinguish the two states. For example, the TS2 and H4 exhibited similar swirling flow patterns in the RPA and had slightly different patterns in the LPA. As shown in Fig. 6.6 (I), TS2 exhibited a distinct pair of vortices at peak systole, in contrast to the more diffuse and less defined swirling pattern observed in H4. Furthermore, instability within the patient cohort was also evident at peak systole, characterised by accelerated flow in TS3. In the case of TS5, the crisscross anatomy caused the blood flow to develop pairs of Dean vortices in both the RPA and LPA at the peak systole (I), which progressed into more asymmetric and then single enlarged vortices at time points (II) and (III), respectively.

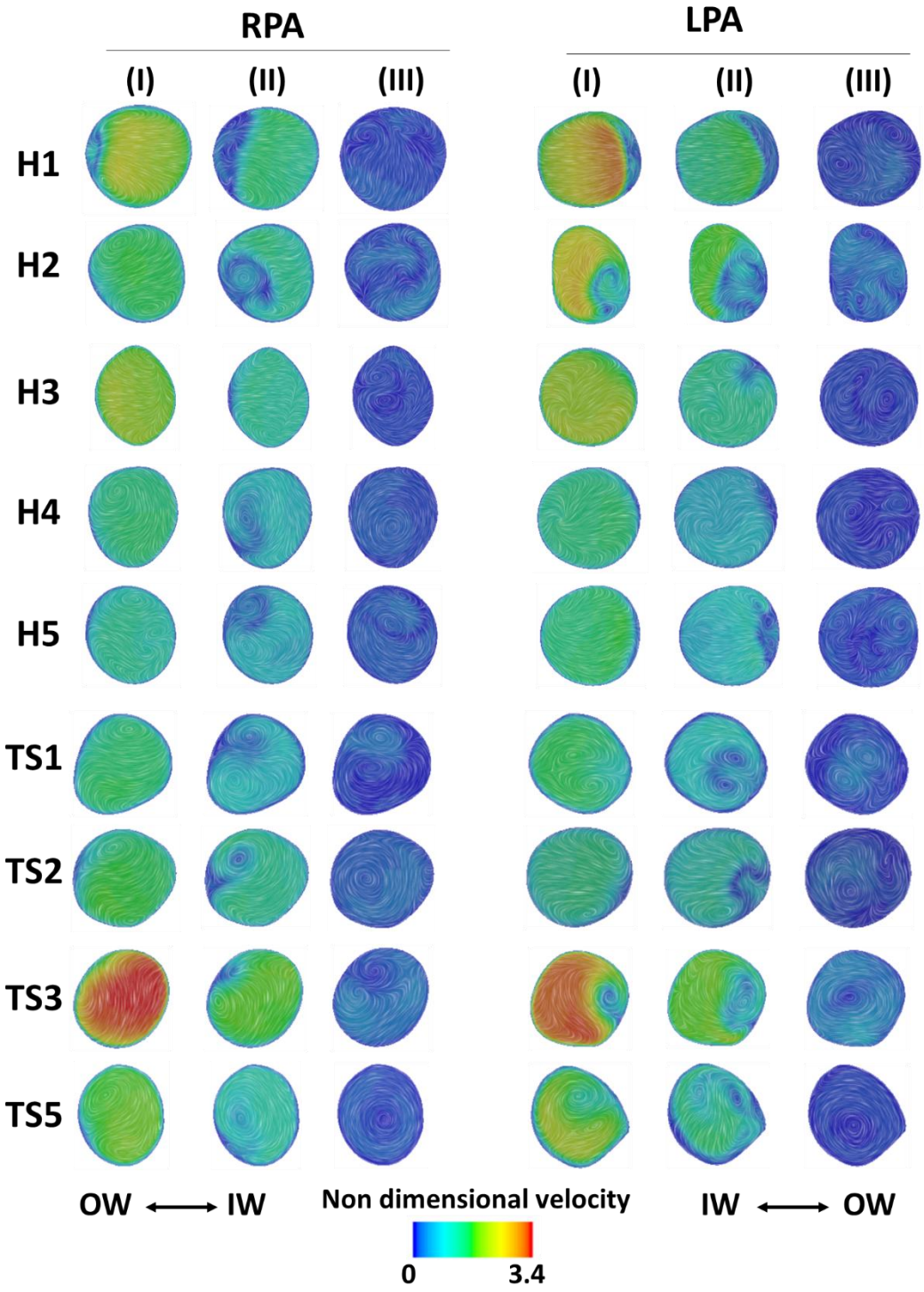

Figure 6.6: Secondary flow on cross-sectional planes (at the distal end of Fig. 6.4-6.5, prior to the first branching) in the RPA and LPA branches of healthy and TS patients. The flow was visualised using in-plane velocity vectors and contours of normalised velocity during peak (I), mid deceleration at systole (II) and mid diastole (III). The outer (OW) and inner (IW) walls are indicated for anatomical reference.

6.4 Discussion

To the best of our knowledge, this chapter presents the first haemodynamic study in the pulmonary arteries of paediatric Turner syndrome patients. Although the PA is not a primary locus of pathology in TS, it is susceptible to secondary hemodynamic effects from associated left-heart and aortic abnormalities. This work provides a novel characterisation of these sub-clinical flow disturbances and establishes a foundational hemodynamic baseline essential for future research and clinical assessment of this patient cohort.

6.3.1 Haemodynamics on variation morphology among healthy and TS

This study characterised the complex interplay between pulmonary artery morphology, velocity pattern and TAWSS in healthy subjects and a patient cohort The results indicate that the key distinctions between patient groups are primarily driven by anatomical differences. The healthy cohort, despite its morphological variability (including variations in MPA curvature or bifurcation angles), established a predictable flow characterised by laminar systolic acceleration and the consistent formation of symmetric, paired Dean vortices. The use of a uniform, pulsatile input velocity profile pattern for all five models may contribute to this observed consistency in flow characteristics. In contrast, TS patients universally exhibited flow instability (Fig. 6.5) as the flow deviates from being laminar, even in cases considered morphologically normal such as TS1, showing high skewness at time points II and III of the cardiac cycle. The flow instability that was evidently caused by morphological abnormality is demonstrated by asymmetric and skewed flow in TS5 (crisscross anatomy) or accelerated flow in TS3 (high branching point). The TAWSSn distribution was consequently affected. Extreme TAWSS values for H1 was driven by the inlet velocity. TS5 exhibited high TAWSSn predominantly at the bifurcation apex, whereas TS3 with lower inflow than TS5 showed accelerated flow and a more spatially extensive region. These observations confirm that although TAWSS is velocity-dependent, extreme anatomical irregularities can disrupt this principle.

6.3.2 Clinical relevance

The clinical relevance of the obtained results is multifaceted. Several notable haemodynamic similarities and differences were identified between healthy and TS patients. The TS1 patient geometry, despite being identified morphologically normal, demonstrated flow characteristics comparable to those of the H2 patient during peak systole, but transitioned to a more skewed configuration during deceleration and diastole (Fig. 6.4 and 6.5). This finding underscores that haemodynamic disturbances can occur even in anatomically normal pulmonary arteries, reinforcing the need for functional analysis in diagnostic practice. From a clinical perspective, TS1 therefore represents a case in which haemodynamic complexity is detectable without reaching established thresholds for intervention. In this case, the presence of hypertension, bicuspid aortic valve morphology, and aortic dilatation constitutes a recognised high-risk aortopathy phenotype, for which surveillance and intervention thresholds are determined by indexed aortic dimensions and growth rates rather than pulmonary flow behaviour [299, 323]. The haemodynamic observations presented here thus support exclusion of pulmonary vascular involvement while reinforcing the need for structured aortic monitoring in TS1.

In TS2, the clinical report identified that structurally normal pulmonary artery coexisted with a significant PAPVR shunt, resulting in a pulmonary circuit overload (Qp:Qs ratio of 1.37). The Qp:Qs ratio is a haemodynamic metric that quantifies the total blood flow returning to the lungs (Qp) relative to the blood flow distributed to the rest of the body (Qs), indicating the severity of the shunt. In contemporary congenital heart disease frameworks, Qp:Qs ratios below 1.5 are generally considered to represent mild haemodynamic disturbance when not accompanied by right ventricular dilatation or pulmonary hypertension [300, 304]. The haemodynamic characteristics of TS2 remained comparable to that of H2 (Fig. 6.6). This suggests that the elevated flow into the MPA may not substantially alter the overall haemodynamics. Nevertheless, the presence of an elongated transverse aortic arch in TS2 case constitutes a recognised anatomical risk factor for future aortopathy in Turner syndrome, necessitating careful longitudinal surveillance [299, 323]. In this context, CFD offers a potential tool to identify early haemodynamic transition points, such as the emergence of disorganised

flow patterns or elevations in WSS, that may precede irreversible structural remodelling and thereby inform earlier intervention [324].

The findings for patient TS3 are indicative of a latent functional anomaly. Although the pulmonary artery was morphologically normal, the CFD analysis revealed anomalous, high-velocity flow at the bifurcation (Fig. 6.5 and 6.6). In the absence of a stenosis, this observation strongly suggested a functional disturbance originating upstream, perhaps in the heart's pumping mechanism. In individuals with a history of coarctation repair, re-intervention is typically guided by haemodynamic criteria, particularly a systolic pressure gradient > 20 mmHg or signs of left-ventricular adaptation [325]. The CFD-derived flow abnormalities therefore provide functional evidence to interrogate whether a morphologically normal vessel masks a significant pressure drop. Despite normal pulmonary venous drainage, such accelerated flow has been associated with haemodynamic instability that may precede MRI-detectable structural changes, supporting the use of multimodality surveillance and potentially closer follow-up in post-repair patients with Turner syndrome [299, 323, 324].

In the case of TS5, the CFD analysis served to confirm and explain the functional consequences of a known clinical structural defect. The clinical report identified a significant crisscross congenital anomaly, and the CFD results demonstrated that this abnormal geometry was the direct cause of the observed chaotic, asymmetric and disorganised flow patterns. Importantly, crisscross pulmonary artery anatomy is recognised to induce disturbed flow and elevated WSS through acute branch angulation rather than fixed luminal obstruction, providing a mechanistic basis for abnormal haemodynamics in the absence of stenosis [326, 327]. In clinical practice, isolated criss-cross anatomy is typically haemodynamically benign, with intervention guided primarily by the development of airway compromise or secondary complications rather than Qp:Qs alone [328, 329]. Although TS5 maintains a near-physiological shunt ratio ($Qp:Qs = 1.16$), three-dimensional geometric assessment remains critical for identifying early functional changes. Consequently, the clinical decision point for TS5 is not immediate surgical repair but intensified multimodality surveillance. In this strategy, CFD analysis enhances traditional anatomical imaging by identifying high-risk haemodynamic transition points, such as

pathological WSS or pressure spikes, that may manifest before measurable structural progression.

6.3.3 Integrating micro- and macroscale

The separation between the microscale investigations presented in earlier chapters and the macroscale pulmonary analysis reflects differences in dominant physical mechanisms rather than a lack of haemodynamic continuity. Across all chapters, blood flow is governed by shared conservation principles and organised by vascular architecture, with pressure–flow relationships and WSS serving as central descriptors of haemodynamic behaviour. While the microscale analyses addressed low-Reynolds-number particulate flow dominated by RBC-core phase migration, plasma skimming and CFL formation, the macroscale pulmonary study examined inertial, pulsatile flow characterised by curvature-induced secondary structures and transient shear. Despite these differences, both regimes exhibit analogous haemodynamic outcomes: geometric complexity produces skewed velocity fields, and heterogeneous time-averaged WSS (TAWSS), highlighting architectural asymmetry as a unifying source of flow inefficiency across scales.

This architectural continuity provides a strong foundation for future simulations in which microscale and macroscale models are explicitly connected rather than sequentially interpreted. Building on the multiscale pulmonary strategies of Ebrahimi (2020) [330] and the structured-tree arterial–venous coupling developed by Colebank et al. (2021) [34], multi-phase microcirculatory solvers could be integrated downstream of a pulsatile pulmonary network, with both systems running concurrently and exchanging haemodynamic state variables. In such a framework, microscale bifurcation-induced plasma skimming and CFL formation would inform effective resistance and WSS distributions at the macroscale, while curvature-driven secondary flows would impose physiologically realistic loading on the microcirculation.

6.3.4 Limitation and future work

A limitation of this study is the sample size. Furthermore, the Turner syndrome group was notably heterogeneous. It included a clinically normal geometry (TS1), a subject with marked volume overload (TS2), a case exhibiting a functional accelerated flow (TS3), and an anatomy with a major congenital anomaly (TS5). Although this diversity yields valuable case-level insights, it restricts the generalisation of findings at the group level and limits the strength of any statistically robust conclusions regarding TS pulmonary haemodynamics overall. This limitation is clinically relevant, as structural defects of the pulmonary artery in TS are uncommon, while functional alterations are frequently driven by anomalies such as Partial Anomalous Pulmonary Venous Return (PAPVR) [301, 303]. With a prevalence of 13–15.7%, PAPVR imposes considerable volume loading on the pulmonary artery, illustrating that haemodynamic disturbance can arise even in the absence of intrinsic arterial malformation [303, 331]. To confirm these preliminary results, a larger, multi-site cohort is needed. Future studies should enrol more patients and stratify them into subgroups such as TS with- vs without-PAPVR, to isolate condition-specific effects on haemodynamics. Beyond this, the coexistence of pulmonary venous varices with PAPVR and typical lesions such as bicuspid aortic valve introduces a layered complexity, amplifying the challenge of accurate haemodynamic interpretation and risk stratification [331].

Another limitation concerns the input conditions for the healthy group, where a single velocity profile (from H5) represented the inflow for all subjects due to the absence of further individual measurements. This uniformity may obscure physiological variability and reduce the sensitivity of comparisons with patient data. In contrast, patient-specific simulations incorporate unique flow features, enabling more precise interpretation of pathological haemodynamics. Nevertheless, computational studies suggest representative pulsatile waveforms effectively recover dominant pulmonary haemodynamics [332]. The use of quasi-patient-specific, waveform-invariant conditions preserves systematic WSS trends across disease severity groups, indicating limited sensitivity to individual variability. An averaged inflow waveform from healthy 4D Flow MRI datasets was sufficient to reproduce the principal flow organisation and WSS distributions in both individual and averaged geometries [313,

314]. As healthy bifurcations are highly efficient, dominant flow structures remain consistent across subjects, primarily dictated by arterial geometry rather than specific inlet profiles [309].

Our PA simulations assumed rigid arterial walls, a common simplification in pulmonary CFD research. Other vascular artery study suggests that secondary-flow patterns change minimally when dynamic compliance is introduced. However, that same study establishes that those authors also found that full wall motion is required to accurately mimic *in vivo* flow, suggesting that rigid models may lack the precision necessary to capture nuanced heart-vessel interactions. Furthermore, Bazileves et al. (2009) demonstrated that even where wall displacements reach ~0.064 cm at rest, rigid assumptions fail to capture the energy-damping effect of arterial expansion in a patient-specific study[333]. This omission potentially leads to an over-prediction of both instantaneous flow speed and peak wall shear stress by as much as 17%. Although peripheral resistance was not explicitly modelled, physiologically relevant outlet splits were applied. The pulmonary valve was not represented, which may limit accuracy near the valve.

Chapter 7

Discussion and Future Work

7.1 Novelty

The primary novelty of this work lies in the development of a robust methodology for the implementation of the Eulerian multiphase (EMP) method and appropriate configuration of the EMP parameters to investigate the CFL formation downstream of 15-48 μm vascular bifurcations. This approach integrates a novel hybrid meshing strategy, multi-phase plasma-RBC and pure plasma initialisation, and optimised EMP settings to ensure numerical stability. Validation studies confirmed that the model accurately predicts the CFL thickness across a range of haematocrit values and reproduces the shear-thinning behaviour characteristic of non-Newtonian blood rheology. Operating at a macroscopic scale while capturing microscale phenomena, such as plasma skimming, this framework provides a mechanistic link between CFL geometry, lift forces, and WSS distribution, advancing continuum-based CFD modelling of microvascular haemodynamics.

Another novelty of this work is its ability to reveal the model's capacity to explain the interplay between the CFL formation and haemodynamic forces. For idealised bifurcations, the study demonstrates how CFL governed by shear-induced lift force influences the velocity profiles and WSS distribution, providing a mechanistic basis for RBC-rich partitioning and plasma skimming across varying inflow and network asymmetry. This connection between systemic flow and local forces offers a predictive framework for microvascular regulation.

Extending this approach to realistic testicular bifurcations introduces a further novelty. The approach captures geometry-dependent phenomena absent in idealised models, such as asymmetric CFL formation, tortuosity-driven resistance, and shear-gradient dominance in WSS regulation. By testing multiple boundary conditions, the study

reveals adaptive strategies for energy efficiency and perfusion stability, offering a physiologically-grounded framework for understanding blood flow regulation in reproductive microcirculation.

The single-phase model offers a practical and computationally efficient tool for comparative haemodynamic analysis between control and atrophied networks. Its ability to replicate the spatial WSS and pressure patterns of multi-phase, multi-component simulation validates its use for preliminary screening. Crucially, it revealed a reversal in WSS architecture in the atrophied network, characterised by elevated proximal resistance and inefficient trunk flow, offering a mechanistic insight into systemic vascular dysfunction.

This study provides a new perspective on the challenge of distinguishing TS from healthy individuals when morphological differences are minimal. Although most Turner Syndrome cases appeared morphologically similar to healthy controls, combined velocity and TAWSS analysis revealed subtle functional differences, demonstrating that haemodynamic assessment can uncover vascular abnormalities not evident from geometry alone.

7.2 Key findings

This thesis presents a series of key findings on the haemodynamics of vascular bifurcations using a novel multi-phase, multi-component model and single-phase continuum-based CFD approximations, building upon the research questions provided in Chapter 1.

- The new developed multi-phase, multi-component model successfully simulates the downstream recovery of a symmetric CFL, which occurs between 8D and 16D in a 16 μm daughter vessel, under varying feeding haematocrit values (18% – 66% at 53 s^{-1}), inflow conditions (13 – 153 s^{-1} at 44%HF), and asymmetric diameter bifurcations (at 44%HF and 53 s^{-1}), as summarised in Table 7.1. Lower haematocrit and stronger inflow conditions contribute to a

delayed CFL symmetric recovery due to reduced viscosity and intensified shear forces, respectively. Additionally, asymmetric bifurcations exhibit diameter-dependent recovery behaviour, where wider branches with higher flow rates extend the recovery distance. These results align closely with previous mesoscale computational studies, which report CFL recovery distances ranging from 8D to 25D for vessel diameters between 15 and 33 μm [3, 5, 6]. Overall, the results emphasise the intricate interdependence haematocrit, flow rate, vascular resistance, and vessel geometry in governing the behaviour of downstream CFL dynamics. (Chapters 2 & 3).

Table 7.1: CFL Recovery distances and thickness under varying haematocrit, Inflow, and bifurcation conditions

Scenario	parameter	CFL recovery distance		CFL thickness (μm)	
		d1	d2	d1	d2
Baseline	44% HF; $1Q_0$	16D	16D	0.9	0.9
High HF	55% HF	15D	15D	0.8	0.8
	66% HF	8D	8D	0.4	0.4
Low inflow	$0.2Q_0$	8D	8D	1.5	1.5
High inflow	$3Q_0$	16D	16D	0.4	0.4
Narrow diameter	d2=0.7d1	14D	11D	0.6	0.4
Wide diameter	d2=1.2d1	16D	18D	1.3	1.8

- The asymmetric CFL formation influences microvascular haemodynamics. At the bifurcation entrance, the velocity profile skews towards the outer wall [89, 90, 209], coinciding with the enlarged CFL, a phenomenon typical of low Reynolds number flows. RBC-rich distribution exhibits inverse skewness [212, 213], concentrating near the inner wall where CFL is minimal. This results in elevated local viscosity and reduced shear gradients due to increased cell-wall interactions. Downstream, the CFL thickens, causing the effective viscosity to drop and the shear rate to peak before gradually declining as the flow becomes

symmetric. These changes produce local WSS spatial variations that reflect shear-thinning behaviour. (Chapter 2).

- Hydrodynamic interactions are fundamental drivers of CFL development and plasma skimming. Wall-induced lift, driven by near-wall pressure gradients, is combined with shear-induced lift governed by plasma vorticity and slip velocity to reposition the RBC–plasma interface towards the vessel centre where low-shear regions exist, reflecting Saffman's model of velocity-gradient-driven particle motion [203, 216]. The RBC-rich lateral migration is promoted, while the pure plasma region migrates outwards, establishing the near-wall CFL. The plasma vorticity, generated by steep shear gradients, amplifies the lift forces. The slip velocity mapping reveals that strong gradient-slip zones at the RBC–plasma interface govern the direction of lift vectors, even when the slip velocity magnitude does not coincide with peak lift force. (Chapter 2)
- The model effectively bridges the conceptual gap between numerical volume fraction of the multi-phase plasma-RBC component ($\alpha_{RBC-rich}$) and physical tube haematocrit (HT) by translating grid-level data into physiologically meaningful metrics. While $\alpha_{RBC-rich}$ shares conceptual similarities with HT, it operates at a macroscopic scale, capturing the RBC–plasma interface through averaged mesh values rather than discrete particle resolution. By scaling $\alpha_{RBC-rich}$ with area-weighted influx and converting it to discharge haematocrit, the model achieves strong agreement with *in vivo* measurements [72, 199], validating its utility as a correction factor. (Chapter 2)
- The multi-phase multi-component simulation reveals that blood rheology in 20 μm-diameter microvessels with a distinct CFL diverges significantly from bulk and wider microvascular studies. Unlike bulk flow (blood outside microvessel), where aggregation and friction dominate, the presence of a lubricating CFL in our model attenuates non-Newtonian effects, yielding a higher Power-law index and lower Casson yield stress. These values contrast sharply with those reported in wider microchannels and bulk vessels, where CFL formation is less pronounced. The Carreau–Yasuda analysis further supports this distinction, with lower zero-shear viscosity and faster relaxation

times reflecting enhanced radial migration and reduced wall friction. Comparable studies in microvessels of similar scale have demonstrated analogous rheological patterns. The findings highlight the critical role of the CFL structure in modulating local viscosity, a factor often underrepresented in conventional rheological models. (Chapter 2)

- Our direct measurements confirm that a pronounced CFL can emerge through two distinct mechanisms: low haematocrit, which reduces cell-to-cell interactions and results in weak lift forces, or high flow rate, which intensifies shear gradients and generates strong, shear-driven lift that actively organises RBC-rich migration and CFL structure. These simulation results highlight the dual influence of the haematocrit and flow rate on the CFL dynamics, offering a mechanistic explanation for the observed variations in CFL thickness and symmetry. The CFL thickness has been shown to be a function of shear rate [239] and haematocrit [83, 238]. (Chapter 3)
- The new multi-phase, multi-component model captures plasma skimming through three distinct but interconnected mechanisms: biased outflow, diameter asymmetry, and short inter-bifurcation distance. In biased flow, the RBC-rich region follows the high-flow path due to streamline shifts, increasing the local lift and vorticity. Diameter-asymmetric geometries similarly favour the RBC-rich entry into the wider, low-resistance branch, enhancing haemodynamic forces. Additionally, short inter-bifurcation distances preserve the upstream CFL asymmetry, guiding RBCs into the downstream branch aligned with the thinner CFL region. These results demonstrate the model's ability to reproduce physiologically relevant RBC-rich partitioning driven by both structural and functional asymmetries. (Chapter 3)
- A multi-phase, multi-component model is applied to testicular bifurcated arterioles (20 μm) that diverge significantly from simplified vascular representations, which typically assume planar, symmetric branching with minimal curvature. In contrast, bifurcations 'A', 'B', and 'C' exhibit non-planar geometries, acute angles, and curvilinear paths. These features reflect the spatial constraints imposed by the seminiferous tubules and result in asymmetric flow paths. For instance, bifurcation 'A' shows sharper angles and

less convolution than ‘B’, while geometry ‘C’ presents a more hierarchical structure with reduced tortuosity. (Chapter 4)

- Anatomically-correct (non-planar, tortuous) vascular geometries alter the CFL formation, compared to simplified bifurcations, which nonetheless capture the main characteristics and are useful in understanding the underlying haemodynamic mechanism. While simplified bifurcations produce perfectly symmetric CFL regions, realistic vessels exhibit only “symmetry-like” patterns, where the RBC-rich core gradually migrates toward the centre but retains residual asymmetry. Greater tortuosity, as observed in bifurcation ‘B’, delays this transition and results in persistent skewing of the RBC-rich region towards the inner wall, whereas straighter paths in bifurcations ‘A’ and ‘C’ achieve symmetry-like flow more rapidly. Additionally, branch angle influences the CFL behaviour; sharper angles promote faster centralisation of the RBC-rich region, while wider angles prolong asymmetry. These findings confirm that vessel geometry, rather than boundary conditions, is the dominant factor governing CFL development and RBC-rich distribution in realistic microvascular networks. (Chapter 4)
- Reconstructed testicular tortuous bifurcations exhibit higher pressure drops and localised energy loss, with bifurcation ‘B’ showing the greatest $\Delta P/L$ due to its convoluted path. This structural complexity also intensifies the shear gradients, producing elevated WSS values at constricted regions where the vorticity is high. Such localised resistance is consistent with mechanisms for precise flow control in temperature-sensitive regions [24, 265, 266]. The plasma skimming follows classic principles, with the RBC-rich region preferentially entering high-flow branches, as observed in bifurcations ‘A’ and ‘B’. In contrast, bifurcation ‘C’ demonstrates that network connectivity can override this bias, directing RBC-rich flow into curved branches feeding downstream splits. These results highlight that morphological variations, rather than boundary conditions, dictate flow partitioning and near-wall dynamics. (Chapter 4)
- Under varying inflow conditions while maintaining the same pressure outlets in bifurcation ‘B’, similar to simplified bifurcations, it was found that high

inflow reduces the CFL thickness and increases asymmetry, whereas low inflow enlarges the CFL and restores near-symmetric RBC distribution. Plasma skimming remains a common mechanism, directing the RBC-rich region into the higher-flow branches; however, the degree of skewing and its persistence downstream are far greater in realistic bifurcations. These observations underscore that realistic bifurcations capture complex geometry-driven interactions, such as shear gradients and lift forces. (Chapters 3&4)

- Boundary conditions strongly influence the haemodynamics in bifurcation 'C'. The identical pressure outlet model, though non-physiological, is valuable for isolating geometric effects and establishing a baseline. However, it creates non-physiological patterns, with proximal branches dominating perfusion and distal branches under-supplied. This imbalance elevates WSS locally and exaggerates plasma skimming. Conversely, diameter-based outlets reduce ΔP and $\Delta P/L$, promote uniform flow, and distribute shear forces more evenly. The collateral inlet model further enhances robustness by introducing redundancy and mitigating perfusion deficits. These findings show that while identical pressure outlets aid controlled comparisons, realistic conditions are essential for capturing adaptive strategies such as energy optimisation and shear regulation. (Chapter 4)
- The non-planar, tortuous geometries of arteriolar bifurcations (20 μm) are representative of the small, convoluted arterioles that form the essential micro-scale components of the control testicular network. The control network (89 μm) is described as a long, deep, multi-branched system designed for volumetric perfusion, and its function is achieved by these micro-scale structures. Conversely, the atrophic network (48 μm) remains confined to the surface, with markedly shorter branches and reduced complexity. This structural complexity ensures efficient distribution of flow and oxygen delivery, supported by mechanisms such as plasma skimming and CFL formation. In contrast, the atrophic network exhibits markedly reduced branching depth and length, confining perfusion to superficial regions and limiting haemodynamic adaptability. Despite similar terminal diameters, the loss of hierarchical branching compromises vascular resistance regulation and

shear distribution, reinforcing the functional importance of upstream geometry in maintaining microvascular efficiency. (Chapter 4&5)

- The multi-phase, multi-component simulations of arteriolar bifurcations and the atrophied network reveal consistent haemodynamic behaviours, including RBC-rich skewing towards the inner walls and asymmetric CFL formation, as observed in simplified bifurcations. However, the atrophy reveals complex network-level phenomena, such as asymmetry being preserved over short inter-bifurcation distances or even reversing (skewing to the outer wall) due to a higher-flow dynamics. This asymmetric CFL reduced the WSS and pressure drop compared to the single-phase model. Despite these magnitude differences, both models predicted similar spatial patterns of WSS and ΔP. This spatial agreement is the key finding that supports the use of the computationally efficient single-phase model [267, 334] as a reliable tool for a preliminary comparative analysis, to distinguish the patterns of blood flow between the control and atrophy networks. (Chapter 4&5)
- The numerical single-phase model provides a mechanistic perspective for how the vascular architecture achieves its function, surpassing the limitations of conventional experimental studies that primarily on anatomical observation. The simulation's ability to resolve pressure drop locally versus globally is a key finding. High global ΔP in long distal branches to slow flow for capillary exchange, while maintaining a low local resistance (ΔP/L) to dissipate pressure at a constant, effective rate. This local-level insight is also pivotal for WSS. While *in vivo* methods might identify a WSS pattern, the CFD model explains why it exists. For example, the high WSS values in region 'ζ' identifies its cause (a high shear gradient driven by high flow through a constriction), while simultaneously explaining why other high-flow (region 'δ') or constricted (region 'β') areas do not experience peak WSS. (Chapter 5)
- Assuming a physiologically based diameter-dependent outlet flow in both networks, the single-phase CFD model reveals that the difference between control and atrophied testes is not simply a matter of scale but a fundamental divergence in haemodynamic architecture. The control system features a low-resistance trunk to supply high-resistance distal branches, resulting in low

trunk WSS and high distal WSS. Conversely, the atrophied network's high distal resistance (ΔP/L) is reflected proximally, creating an inefficient, high-resistance trunk. This causes a complete reversal of the WSS pattern, with high WSS in the trunk and low WSS in the distal branches. For biology, this provides a mechanistic insight into testicular atrophy as a systemic failure of flow regulation. For computational science, despite its simplicity, the single-phase model matched the spatial haemodynamic patterns of the multi-phase, multi-component simulation, confirming its reliability and efficiency for this comparative analysis. (Chapter 5)

- In this thesis, modelling vascular bifurcations at different scales requires distinct approaches. In the microvascular testicular network, low Reynolds numbers (Re ~0.143) justify steady-state, laminar, and particulate nature of blood. The multi-phase, multi-component model is essential to capture the CFL formation and plasma skimming. The single-phase model is proved to be a practical tool for comparative analysis between control and atrophy. Conversely, the macrovascular pulmonary artery bifurcation (Re ~1040), required an unsteady turbulence model and a pulsatile inlet waveform to simulate cardiac-driven flow. Here, the single-phase model was sufficient to resolve transient flow structures and quantify TAWSS or secondary flow. (Chapter 5&6)
- This study revealed that distinguishing Turner Syndrome (TS) from healthy patients based on morphology and TAWSS is challenging due to overlapping features. Healthy models varied from symmetric (H3, H5) to more complex geometries (H1, H2), while TS1–TS3 appeared morphologically typical. TS5 was the only case with a clear structural anomaly, characterised by a crisscross vessel origin and disproportionate branch sizes, which led to highly asymmetric flow and elevated TAWSS in the RPA. TAWSS distributions across both cohorts showed two dominant patterns, localised stress at the bifurcation and diffused stress along branch walls, driven by arterial curvature. For example, TS2 and H4 both exhibited diffused stress along the outer walls, highlighting how subtle anatomical differences can produce overlapping haemodynamic signatures.

- The velocity analysis revealed both convergence and divergence in flow behaviour between healthy and TS cohorts, complicating diagnostic clarity. Healthy subjects showed consistent laminar flow at peak systole and predictable vortex development during deceleration and diastole. TS5, however, demonstrated a clear pathological signature, with skewed and chaotic flow due to its crisscross anatomy. However, TS2 presented a diagnostic challenge, as its RPA flow closely mirrored that of the healthy model H4, with similar swirling patterns. Differences emerged only in the LPA, where TS2 exhibited more defined vortex pairs.

7.3 Limitations and future works

The primary limitation of this study is the lack of direct experimental validation, which is necessary to fully confirm the model's accuracy. Although our simulations reproduce hemodynamic trends consistent with previous findings, the absence of a one-to-one comparison with physical experiments means these results are primarily a theoretical exploration. Moreover, the current assessment of non-Newtonian properties is limited by its focus on a single 20 μm tube, which prevents a comprehensive analysis of diameter-dependent rheology. The current assessment of non-Newtonian properties is limited by its focus on a single 20 μm tube, which prevents a comprehensive analysis of diameter-dependent rheology.

A key limitation is its visual output, which shows a smooth, diffuse gradient between the RBC-rich core and the plasma due to grid-based averaging. This contrasts with the distinct, sharp separation seen in real red blood cells, but it does not undermine the robustness of the model's underlying haemodynamic predictions. Future work could employ a Lagrangian–Eulerian model to overcome the visual limitations of the current approach by simulating RBCs as discrete particles, thus capturing sharp, physically realistic interfaces [226, 227]. This approach allows for detailed tracking of cell migration and dispersion, offering a direct performance comparison to the current model. Despite these advantages, the existing Eulerian model remains attractive for its computational efficiency in large-scale applications.

The model's primary limitation is its neglect of RBCs deformability and aggregation, which are crucial for microscale accuracy despite its success in capturing the bulk flow phenomena. These features significantly impact the local viscosity and the CFL thickness, so future work should incorporate them to better simulate pathological conditions where these effects are pronounced [11, 64, 65].

Another limitation of the current study is its assumption of a symmetric CFL, so future work should incorporate more realistic asymmetric upstream conditions. Since an RBC's path is determined by its initial radial position, simulating a non-uniform haematocrit distribution would allow for a more accurate investigation of downstream partitioning. This would also clarify how heterogeneous flow conditions contribute to pathologies.

To advance the model from a fluid dynamics tool to a comprehensive physiological one, it is imperative to incorporate the transport of oxygen and nitric oxide (NO) [228-230]. Modelling these species is critical because their bioavailability, which is influenced by flow, haematocrit, and the CFL, directly links haemodynamics to cellular function. This enhancement will enable the study of key biochemical responses in health and disease, such as tissue oxygenation and vascular dysfunction.

To advance beyond the current model's fixed pressure outlets, future work will incorporate physiological autoregulation by dynamically adjusting vessel diameters. This will be based on simulated haemodynamic parameters to mimic both the pressure-induced myogenic response and local metabolic signalling [252, 254, 255].

For realistic bifurcated arterioles, this study is limited to a few specific geometries, which may not be representative of the full testicular network. Future work should therefore involve reconstructing a larger number of bifurcations (10–20). Extending these models to connect with venules would also allow for the representation of a wider range of capillary types. To more accurately reflect testicular function, the model must account for temperature regulation, a critical process for spermatogenesis [24, 265, 266]. Therefore, a key area of future work is to address this current limitation by incorporating a temperature model into the simulation.

For the large, complex testicular arterial network, a significant limitation of the single-phase model, confirmed by comparison with the multi-phase, multi-component simulations, is its overestimation of crucial haemodynamic parameters including velocity and WSS. To improve the single-phase model, a carefully validated wall slip could be added to simulate the near-wall slip velocity of the CFL. For the multi-phase model, future work requires improving the meshing to handle large, complex networks. This approach is difficult because the testicular arteries require a high mesh density to ensure the prismatic layer thickness is greater than the CFL.

Finally, in pulmonary studies, the primary limitations are the small and notably diverse patient sample, which limits generalisability despite yielding important individual case insights. The analysis also relied on necessary modelling assumptions, including rigid vessel walls and the absence of a pulmonary valve. To build upon this foundational work, future research will require larger, multi-site studies with stratified patient cohorts to confirm these results and better isolate the specific haemodynamic consequences of conditions like PAPVR in Turner Syndrome.

Appendix A

Supplementary material for Chapter 2

A.1 Mesh independence analysis.

A mesh independence study was performed on the 20-μm symmetric bifurcation. This analysis was conducted using a single-phase, Newtonian laminar flow model with an inlet velocity of 1.1 mm/s. The parameters including cell-based size, number of prism layers and PLTT (prism layer total thickness) were varied as listed in Table A.1. Other meshing parameters were constant, including a relative surface size of 200%, minimum surface size of 10%, surface growth rate of 1.2, prism layer stretching of 1.1, volume growth rate of 1.2 and maximum Tet size of 100%. Based on the results (Fig. A.1), an optimal mesh with a base size of $8x10^{-7}$ m and 20 prism layers was chosen for subsequent analysis.

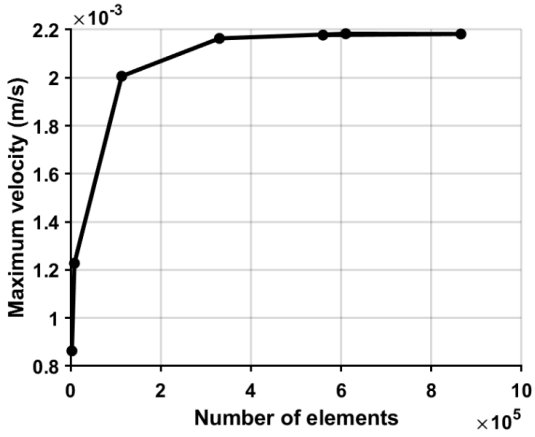

Figure A.1: Mesh independence based on maximum velocity.

Table A.1: Mesh parameter variation for a mesh independence analysis.

Based size (m)	No. PL	PLTT (m)	No. cell	Max. u_{bulk} (m/s)
$6x10^{-7}$	20	$5x10^{-6}$	865478	$2.18x10^{-3}$
$7x10^{-7}$	20	$5x10^{-6}$	610292	$2.18x10^{-3}$
$8x10^{-7}$	20	$5x10^{-6}$	559764	$2.18x10^{-3}$
$1x10^{-7}$	10	$2x10^{-6}$	330104	$2.16x10^{-3}$
$1x10^{-5}$	3	$1x10^{-6}$	113378	$2.01x10^{-3}$
$5x10^{-5}$	3	$1x10^{-6}$	8645	$1.23x10^{-3}$
$1x10^{-4}$	3	$1x10^{-6}$	3001	$8.63x10^{-4}$

A.2 Velocity distribution

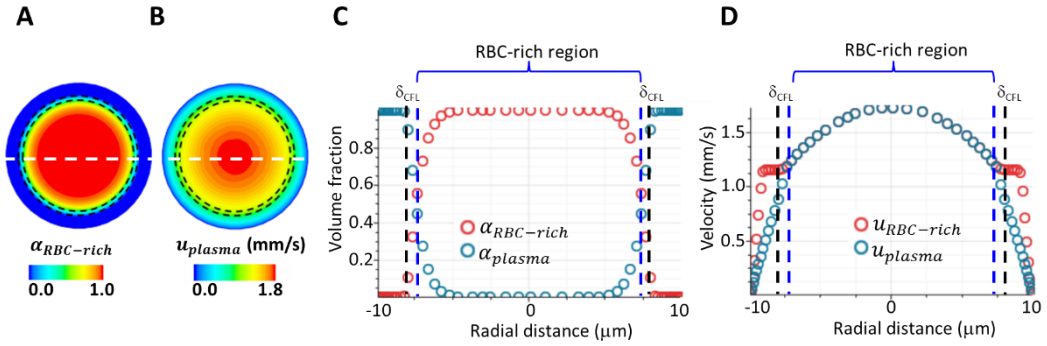

Figure A.2: Velocity profile of the RBC-rich and plasma phases at 1P of the parent vessel. (A) Volume fraction of the RBC-rich phase ($\boldsymbol{\alpha_{RBC-rich}}$) distribution on the cross-sectional plane. It is used to define the RBC-rich core region, where $\boldsymbol{\alpha_{RBC-rich}}$>0.5, and the CFL region, where $\boldsymbol{\alpha_{RBC-rich}}$ <0.05. The inner dashed circle delineates the boundary of the RBC-rich core region, and the CFL region is the area external to the outer dashed circle, extending to the vessel wall. (B) Velocity distribution of the plasma phase. (C, D) Volume fraction of the RBC-rich phase and velocity profile along the white dashed line in (A) and (B), respectively. The CFL thickness (δ_{CFL}) corresponds to the CFL region along the white line.

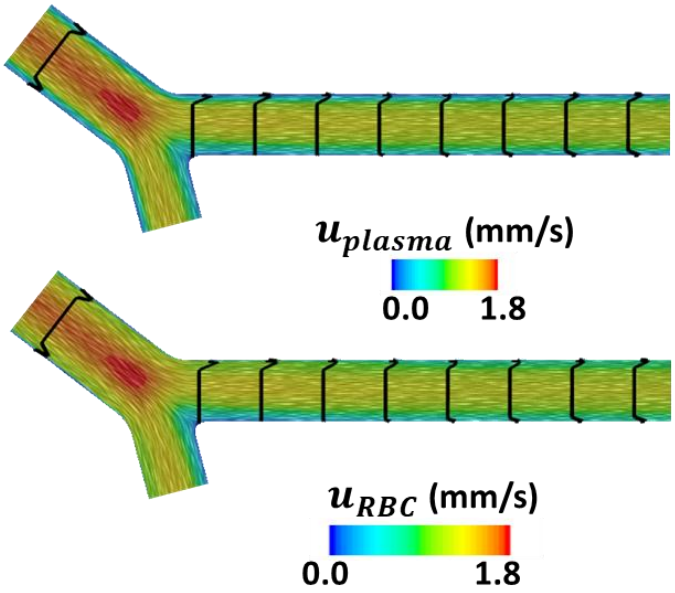

Figure A.3: Vector patterns of the RBC-rich region and plasma velocities, indicating that the flow is mostly parallel to the tube. The black line represents the slip velocity profile. The white lines represent the velocity vector, which paralleled to the axis.

A.3 The boundary and initial conditions for various scale.

Inlet boundary conditions were defined based on vessel scale. A pseudo shear rate (PSR = U/D) of 60 s^{-1} was imposed on the plasma-RBC component velocity ($u_{RBC-rich}$) for symmetric bifurcations with diameters of 20 μm, 200 μm, 1 mm, resulting in $u_{RBC-rich}$ of 1.2×10^{-3}, 1.2×10^{-2} and 6.0×10^{-2} mm/s, respectively (Table A.2). The initial pure plasma component velocity (u_{plasma}) was assigned slightly lower than that of RBC-rich core; and, the bulk velocity (u_{bulk}) was calculated using: $u_{bulk} = u_{RBC-rich}\alpha_{RBC-rich} + u_{plasma}\alpha_{plasma}$. The PSR for the bulk velocity values listed in Table A.2 correspond to RBC-rich velocities within the 55–60 s^{-1} range. The initial δ_{CFL} was assumed at 1.4 μm for all cases.

The densities for the 200-μm and 1-mm bifurcations were kept consistent with the 20-μm case, and apparent viscosity was maintained across all diameters. Plasma viscosity was fixed at 1.3 mPa·s, and RBC-rich phase viscosity was adjusted using Eq. 2.18, as shown in Table A.3.

Table A.2: Boundary conditions in the scaled bifurcations.

	u_{bulk} (m/s)	$u_{RBC-rich}$ (m/s)	u_{plasma} (m/s)	PSR (s^{-1})	Pressure outlet	
					(Pa)	(mmHg)
20 mm	$1.1\text{x}10^{-3}$	$1.2\text{x}10^{-3}$	$8.0\text{x}10^{-4}$	55	6666.12	50
200 mm	$1.2\text{x}10^{-2}$	$1.2\text{x}10^{-2}$	$8.0\text{x}10^{-3}$	60	6666.12	50
1 mm	$6.0\text{x}10^{-2}$	$6.0\text{x}10^{-2}$	$5.6\text{x}10^{-2}$	60	15998.7	120

Table A.3: Properties in the scaled bifurcations.

	μ_{app} (mPa·s)	$\mu_{RBC-rich}$ (mPa·s)	μ_{plasma} (mPa·s)	ρ_{bulk} (g/cm^3)	$\rho_{RBC-rich}$ (g/cm^3)	ρ_{plasma} (g/cm^3)
20 μm	2.90	3.45	1.3	1.060	1.125	1.025
200 μm	2.80	2.85	1.3	1.060	1.125	1.025
1 mm	2.88	2.88	1.3	1.060	1.125	1.025

A.4 The methods for non-Newtonian viscosity investigations

The computational domain was a three-dimensional straight tube of 20 μm diameter and 400 μm length. All EMP settings followed Chapter 2, except for the initial and boundary conditions, which were adjusted to examine the effects of feeding haematocrit, inflow rate, and two intrinsic pseudo-solid viscosities (3.45 and 6.50 mPa·s). The HF was set to 55%, 44%, 18% and 1%, with corresponding CFL thicknesses of 1.0, 1.4, 1.8, 3.3 and 5.0 μm, respectively. This range covered physiological norms (~44%) and haemotological disorders [237], as well as very dilute condition (1%) used in certain *in vitro* protocols [73]. The PSR lied within the physiological range for 20 μm microvessels, at 1 - 380 s^{-1} [89, 199]. Choosing pseudo-viscosity is based on the general blood viscosity (3.45 mPa-s) and cytoplasmic viscosity (6.5 mPa-s) [335].

Fig. A.4 outlined the data fitting with viscosity models. The apparent viscosity and discharge haematocrit were organised into μ_{eff}-PSR data and μ_{eff}-HD pairs and subsequently fitted to the rheological models specified in Table A.4. A non-linear least-squares method (lsqcurvefit) in MATLAB, informed by data-driven initial values, was employed for the Casson and Carreau-Yasuda models. In contrast, the Power-law model was linearised via logarithmic transformation and fitted using a linear polynomial function (polyfit). The performance of each optimised model was then quantitatively assessed by calculating the coefficient of determination (R^2).

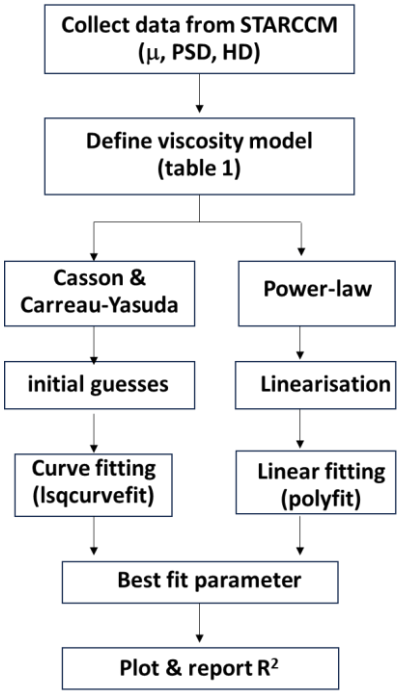

Figure A.4: Flow chart of curve fitting.

Table A.4: Chosen rheological models.

Constitutive equations governing	Model parameters	Initial guess
Power-law		
$\mu(\gamma) = K\gamma^{n-1}$	K consistency (Pa·s^n)	-
	n index	-
Casson		
$\mu(\gamma) = \left(\frac{\sqrt{\tau_0}}{\sqrt{\gamma}} + \sqrt{\mu_p}\right)^2$	τ_0 Yield Stress (Pa)	1x10^{-4}
	μ_p High shear viscosity (Pa·s)	5x10^{-4}
Carreau-Yasuda		
$\mu(\gamma)$	μ_0 Zero shear viscosity (Pa·s)	Lower
$= \mu_\infty + (\mu_0 - \mu_\infty)[1 + (\lambda\gamma)^\alpha]^{(n-1)/\alpha}$	μ_∞ Infinite shear viscosity (Pa·s)	Upper
	λ Time constant (s)	1
	n Power-law index	0.6
	α Transition sharpness	2

Note: The Lower and Upper received from the set of μ_{eff} from the multi-phase multi-component model. The initial guess values are roughly estimated based on known rheological ranges for blood.

A.5 The results for non-Newtonian viscosity investigations

In the Power-law model, the flow behaviour index (n) remained below unity for all cases (Table A.5), confirming the shear-thinning response, with a slight tendency towards more Newtonian behaviour at the lowest HF (n≈0.94). The Casson model demonstrated that the fluid's rheological properties were directly proportional to the HF. Decreasing the haematocrit consistently lowered both the yield stress (τ_0) and the plastic viscosity (μ_p). For instance, at the pseudo-solid viscosity of 3.4 mPa·s, τ_0 dropped from 0.50 to 0.13 mPa, while μ_p fell from 3.65 to 1.16 mPa·s. This was physically expected, as τ_0 represented the force to break RBC rouleaux network at rest, and μ_p reflected high-shear viscosity. Furthermore, the Carreau-Yasuda model suggested that viscosity was highly dependent on HF. Both zero-shear (μ_0) and infinite-shear (μ_∞) viscosities decreased as haematocrit was reduced. For example, in the pseudo-solid viscosity of 3.4 mPa·s, μ_0 decreased from 4.84 to 1.58 mPa·s while μ_∞ dropped from 3.45 to 1.14 mPa·s (Table A.5). The decrease in μ_0 with lower haematocrit reflected the reduced formation of RBC aggregates (rouleaux) at rest. At very high shear rates, the drop in μ_∞ occurred because of the low RBC fraction to generate flow resistance.

Table A.5: Rheological model fits.

	$\mu_{RBC-rich}$ =3.4				$\mu_{RBC-rich}$ =6.5			
HF	**55%**	**44%**	**18%**	**1%**	**55%**	**44%**	**18%**	**1%**
Power-Law								
K (mPa·s^n)	2.96	2.66	1.89	0.88	5.50	4.92	3.54	1.67
n	0.92	0.91	0.88	0.94	0.93	0.92	0.89	0.94
R^2	0.92	0.97	0.99	0.95	0.92	0.97	0.99	0.99
Casson								
τ_0 (mPa)	0.50	0.58	0.78	0.13	0.33	0.38	0.46	0.06
μ_p (mPa·s)	3.65	3.08	1.77	1.16	1.87	1.58	0.90	0.62
R^2	0.82	0.90	0.95	0.98	0.83	0.91	0.96	0.95
Carreau–Yasuda								
μ_∞ (mPa·s)	1.78	1.43	0.90	0.59	3.47	2.98	1.73	1.14
μ_0 (mPa·s)	2.57	2.40	1.59	0.88	4.84	4.30	2.98	1.58
λ (s)	0.02	0.07	0.05	0.15	0.02	0.03	0.04	0.09
n	0.10	0.50	0.10	0.50	0.10	0.10	0.10	0.37
α	2.00	1.25	2.00	1.00	2.00	2.00	2.00	1.64
R^2	0.98	0.98	1.00	0.96	0.98	1.00	1.00	1.00

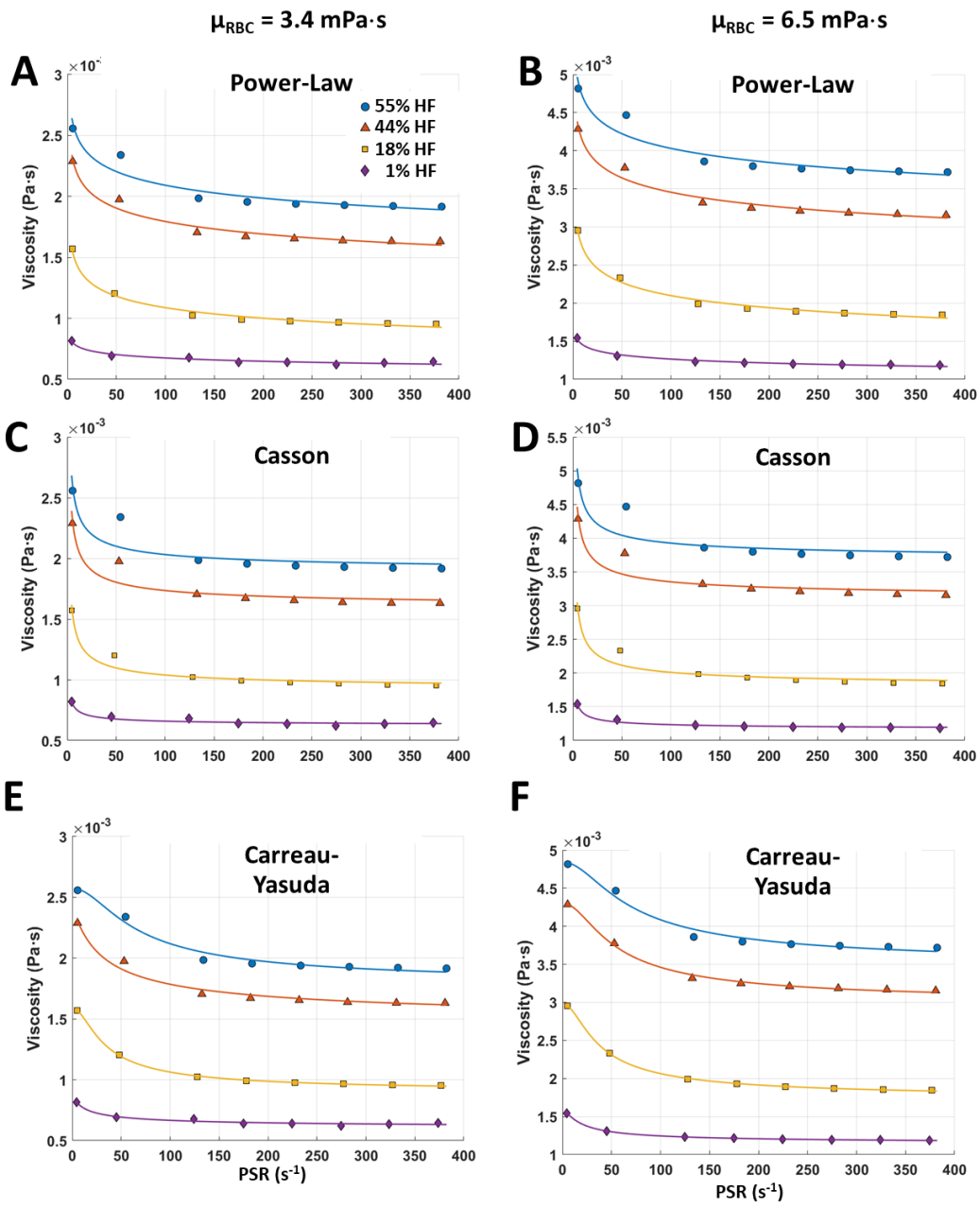

Figure A.5: Curve fitting of effective viscosity to pseudo shear rate (PSR = U/D) from the multi-phase, multi-component model. (A, B) Power-Law model. (C, D) Casson model. (E, F) Carreau Yasuda model for pseudo-solid viscosity of 3.45 and 6.50 mPa·s.

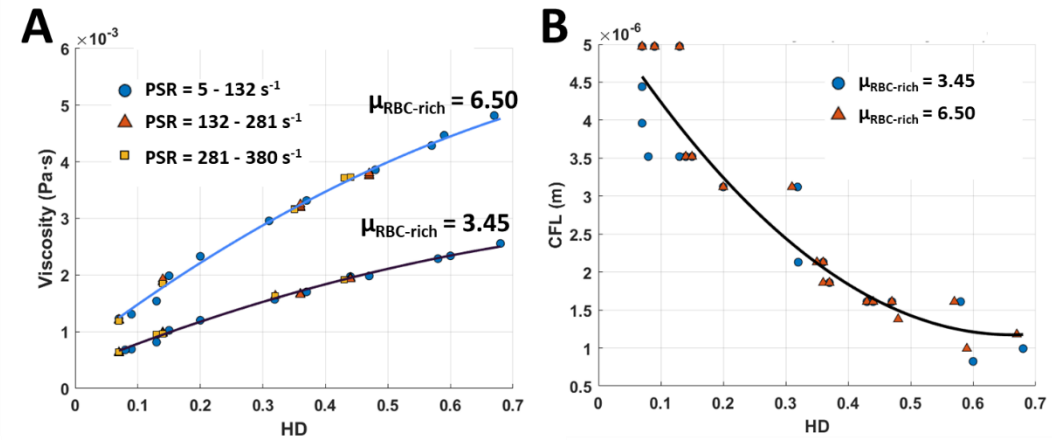

Figure A.6: Influence of haematocrit. (A) viscosity and (B) CFL dynamics with varying discharge haematocrit for pseudo-solid viscosities of 3.45 and 6.50 mPa·s.

A.6 Impact of CFL eccentricity on shear rate, viscosity, and WSS

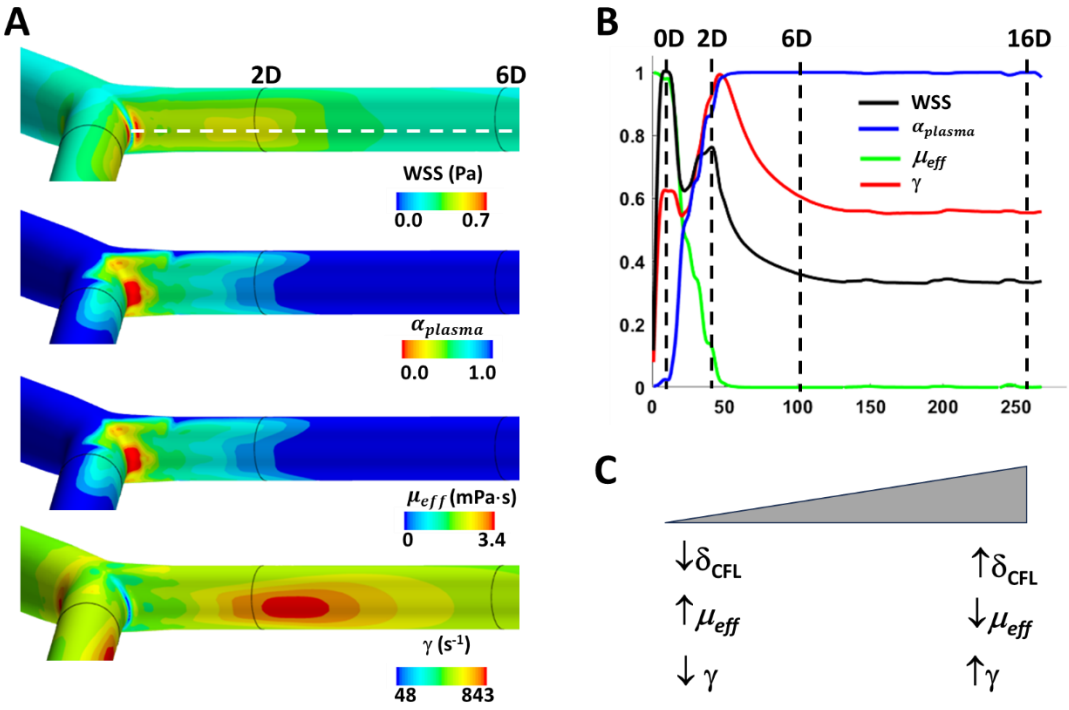

Figure A.7: Local rheology and flow dynamics. (A) Spatial distribution along the inner wall of WSS, volume fraction of plasma component, effective viscosity and shear rate. (B) Normalised profiles of these parameters relative to their maximum values, on the white dashed line in Fig. A.7. (C) Conceptual illustration showing that increased CFL thickness lowers near-wall effective viscosity and elevates near-wall shear rate during 0D to 2D.

Appendix B

Supplementary material for Chapter 3

B.1 Hydrodynamic forces in variation of feeding haematocrit

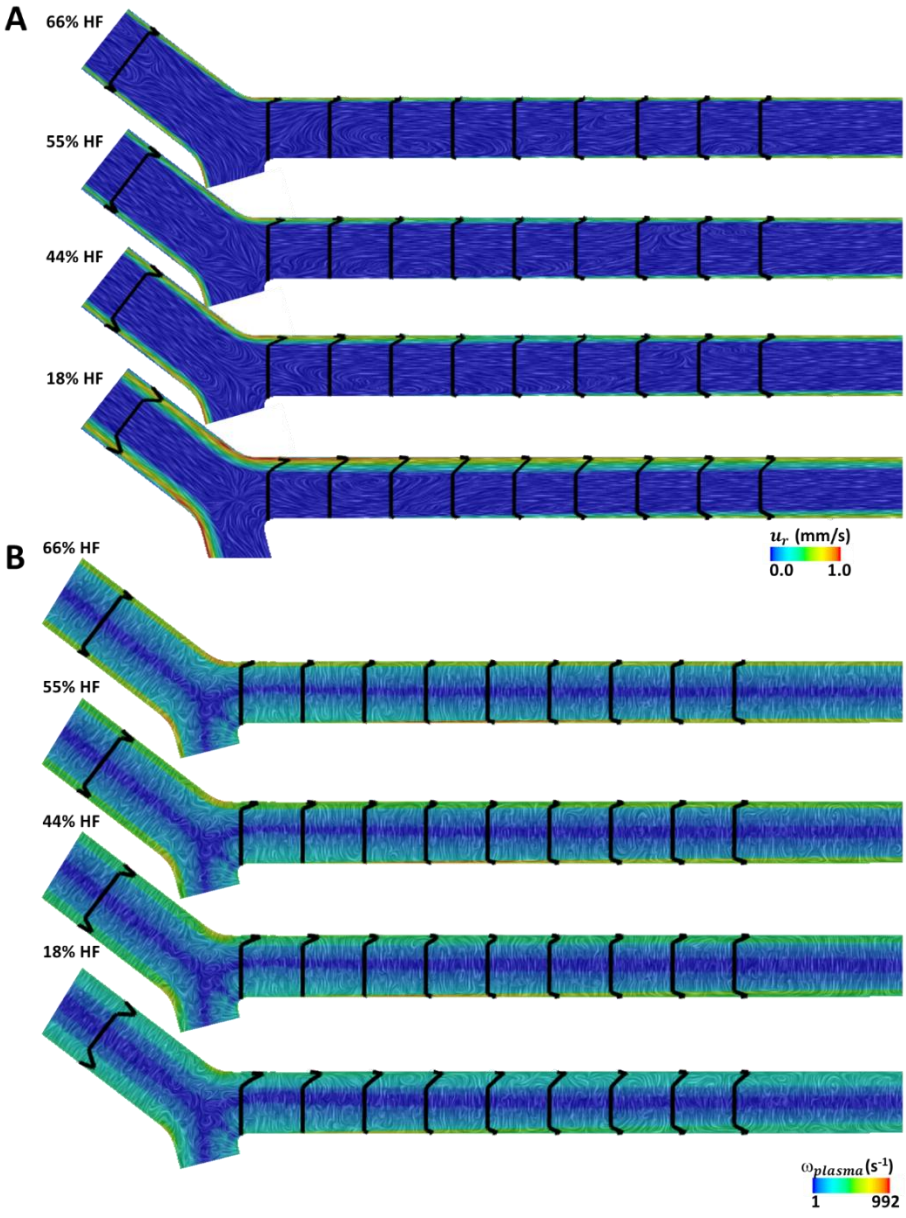

Figure B.1: Hydrodynamic forces including (A) slip velocity, (B) vorticity and (C) lift force in the symmetric bifurcation with different feeding haematocrit.

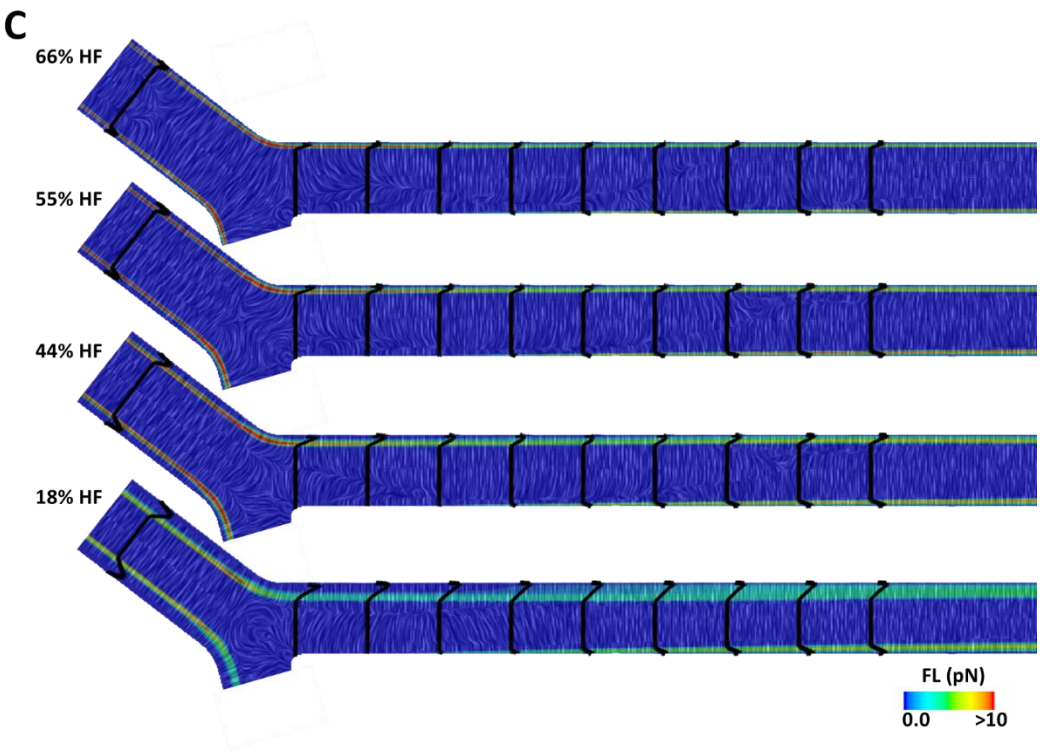

Figure B.1: Hydrodynamic forces including (A) slip velocity, (B) vorticity and (C) lift force in the symmetric bifurcation with different feeding haematocrit (continued).

B.2 Hydrodynamic forces in variation of inflow

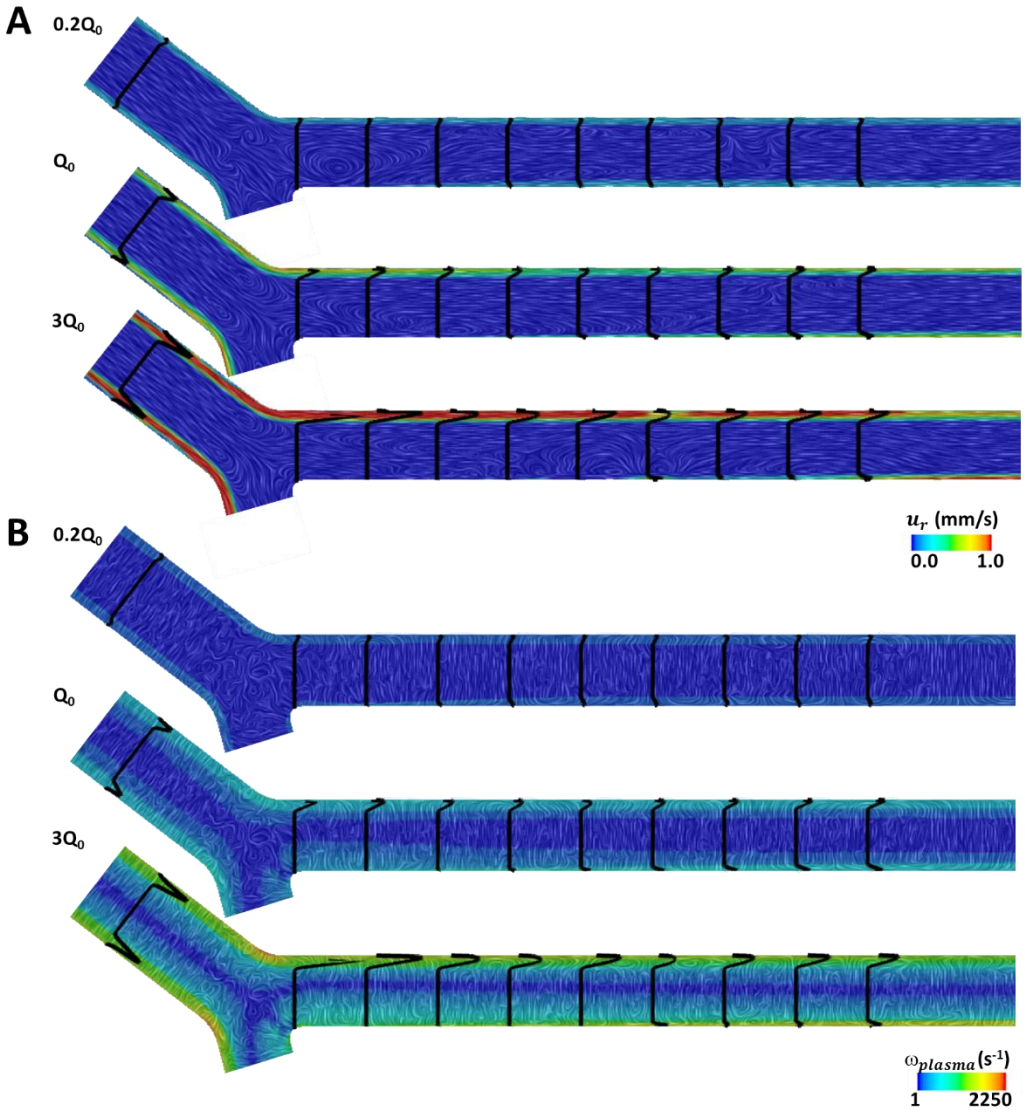

Figure B.2: Hydrodynamic forces including (A) Slip velocity, (B) vorticity and (C) lift force in the symmetric bifurcation with different inflow.

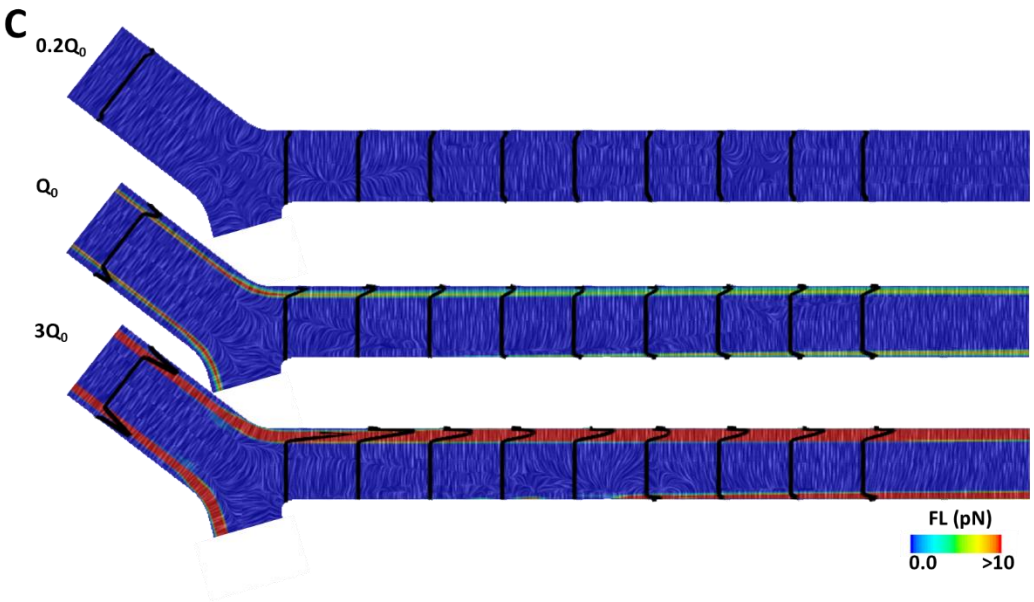

Figure B.2: Hydrodynamic forces including (A) Slip velocity, (B) vorticity and (C) lift force in the symmetric bifurcation with different inflow (continued).

B.3 Dividing streamline

The dividing streamline is the boundary that separates fluid destined for each daughter branch. It ends at the stagnation point, the location where flow impinges on the wall and velocity becomes zero (Fig. B.3A). While the true streamline typically curves near the bifurcation to meet this point, in this study, we use a straight dashed pink line (Fig. B.3B) as a simplified geometrical projection. The benefit of this common visualisation is that it clearly demonstrates our key finding: the eccentric origin of this streamline in the parent branch.

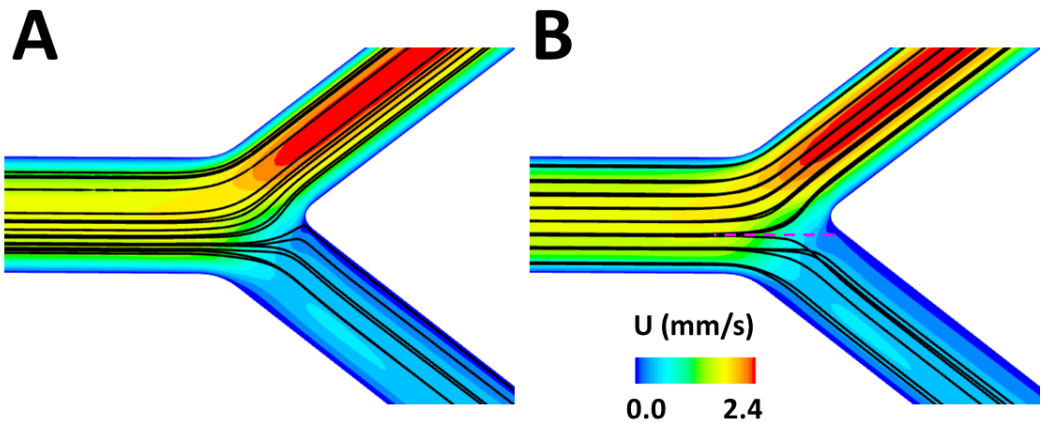

Figure B.3: Visualisation of dividing streamline. (A) Actual streamline curvature approaching the stagnation point. (B) Common simplified depiction (pink dashed line) showing its shift toward the low-flow branch under flow imbalance, highlighting the eccentric origin of the streamline.

B.4 Hydrodynamic forces in variation of biased outflow

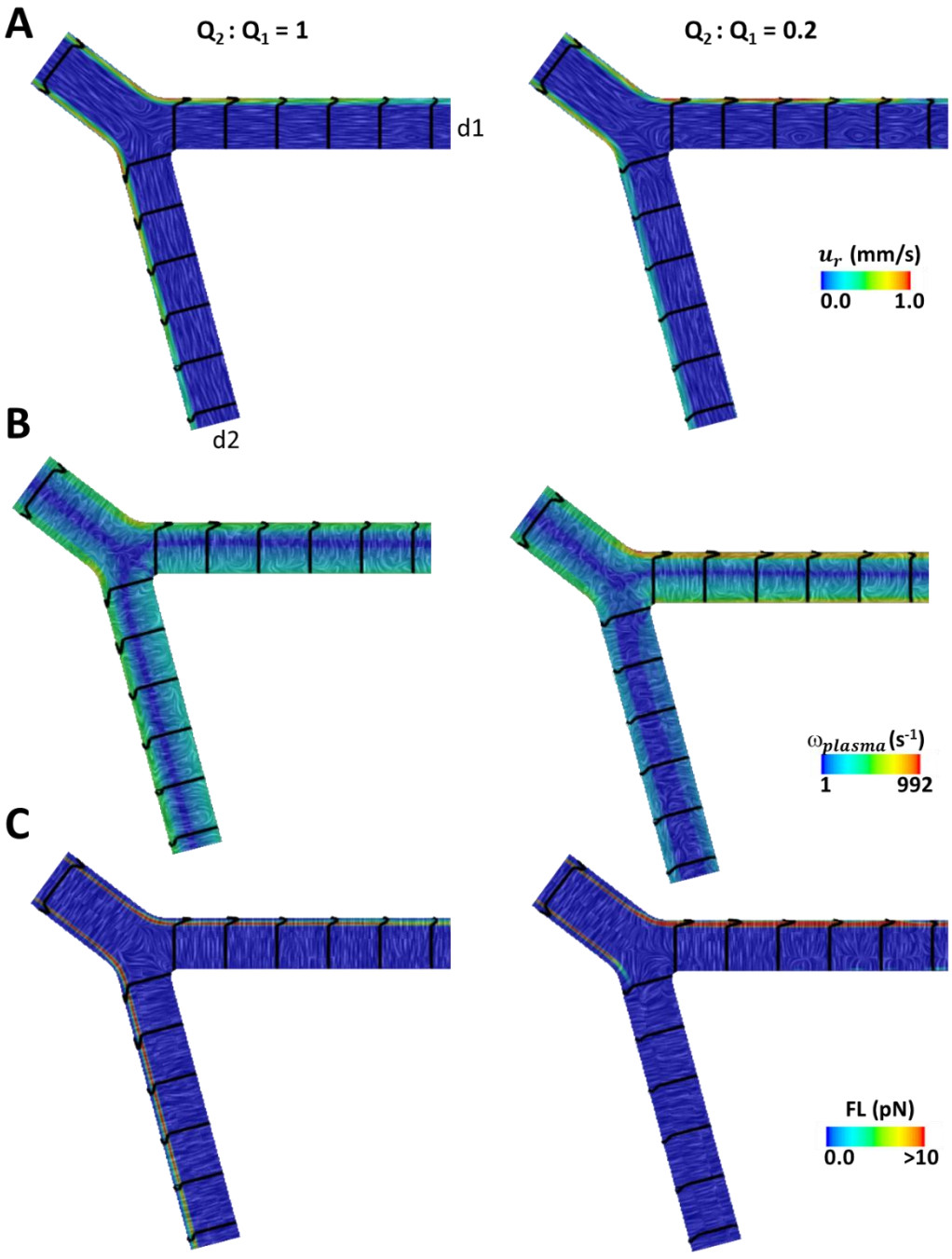

Figure B.4: Slip velocity, vorticity of plasma phase and lift force in the symmetric bifurcation with unbalanced outflow (Q_2/Q_1=0.2) compared to baseline.

B.5 Hydrodynamic forces in variation of asymmetric diameter bifurcation

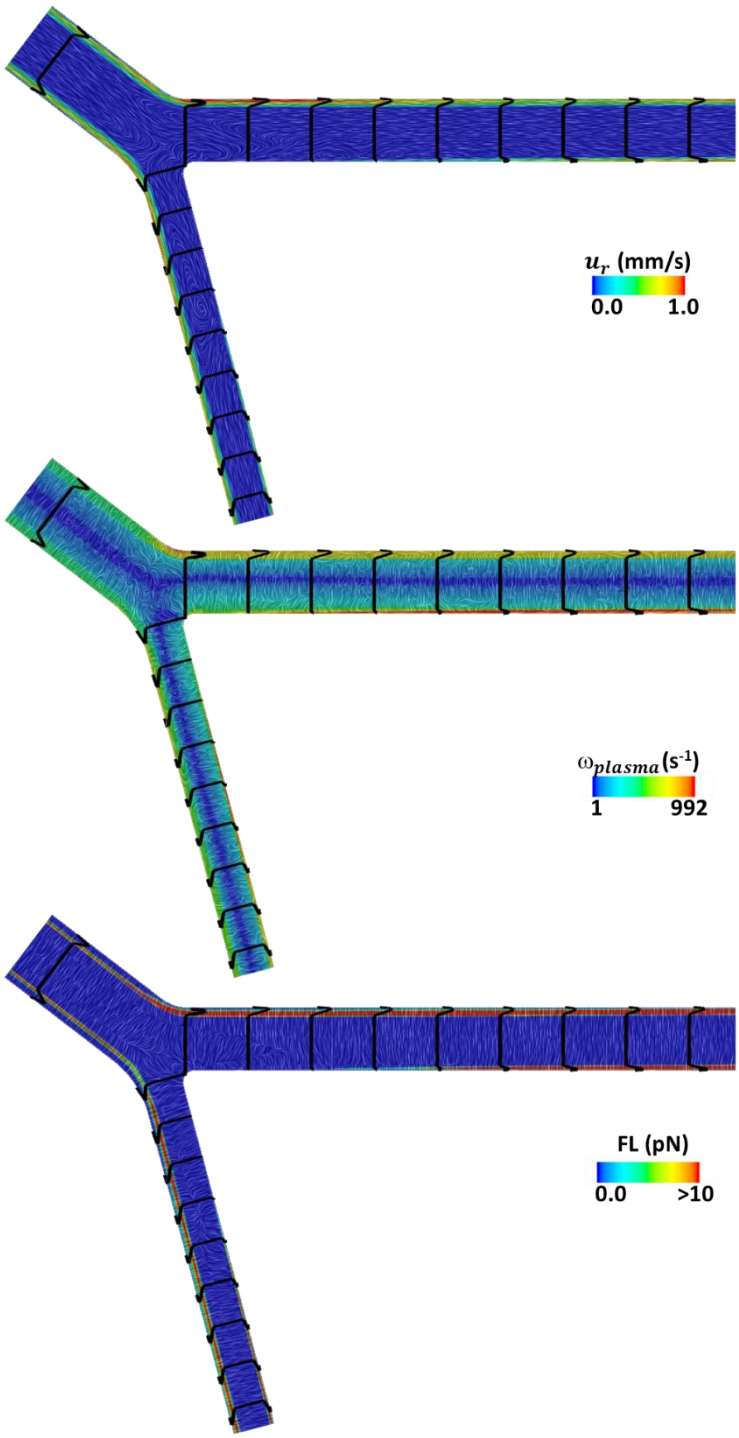

Figure B.5: Slip velocity, vorticity of plasma phase and lift force in the asymmetric diameter bifurcation (d2=0.7d1).

B.6 Hydrodynamic forces in variation of inter-bifurcation distance

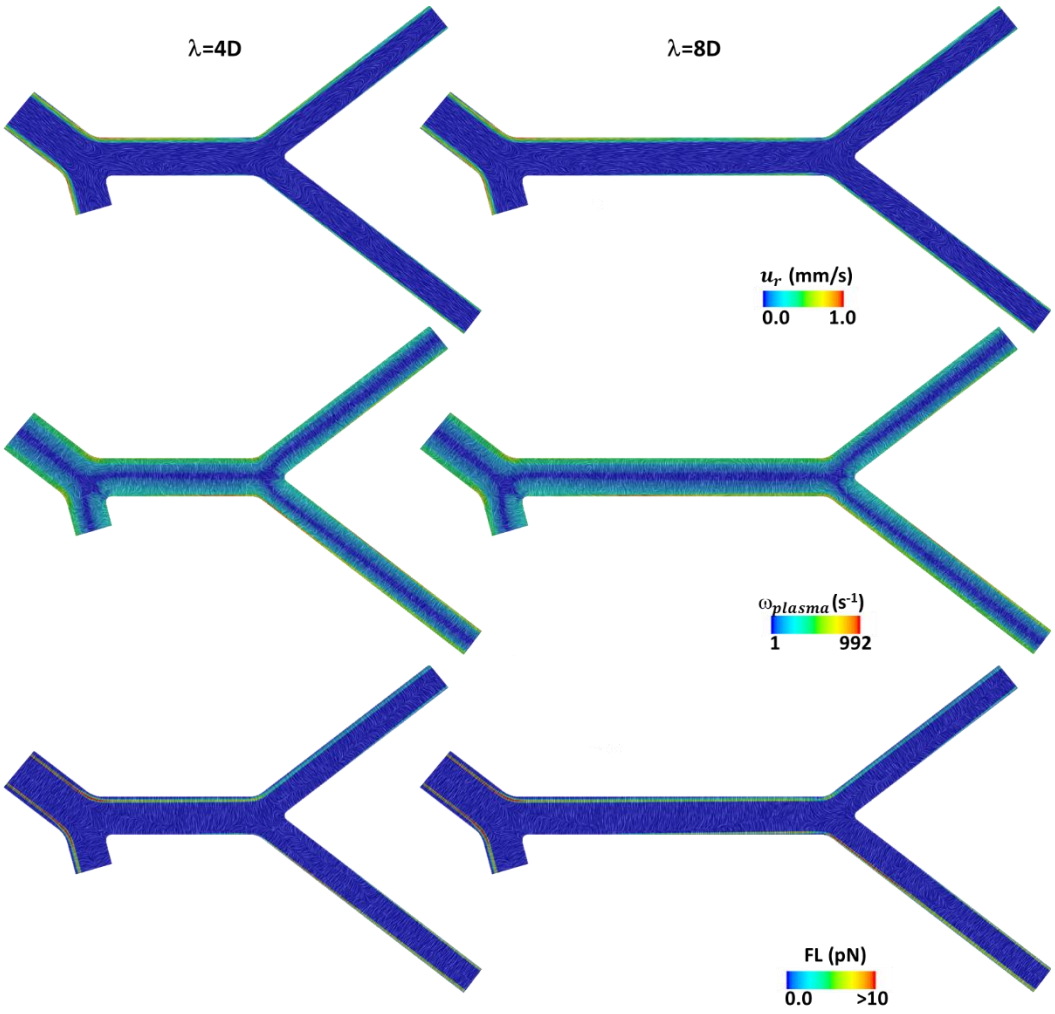

Figure B.6: Slip velocity, vorticity of plasma phase and lift force in the networks with different inter-bifurcation distance.

Appendix C

Supplementary material for Chapter 4

C.1 Meshing independence analysis.

A mesh independence study was performed on the bifurcation 'B', the 20-µm testicular bifurcation. This analysis was conducted using a single-phase, Newtonian laminar flow model with an inlet velocity of 1.0 mm/s. The parameters including cell-based size, number of prism layers and PLTT (prism layer total thickness) were varied as listed in Table C.1. Other meshing parameters were constant, including a relative surface size of 200%, minimum surface size of 10%, surface growth rate of 1.2, prism layer stretching of 1.1, volume growth rate of 1.2 and maximum Tet size of 100%. Based on the results (Fig. C.1), an optimal mesh with a base size of 8.5×10^{-7} m and 30 prism layers was chosen for subsequent analysis. The height of the 1st mesh layer was 3.08×10^{-8} m, which is lower than the theorical value of 5.75×10^{-8} m (see meshing section in Chapter 2). For bifurcations 'A' and 'C', mesh independence was not separately verified. The meshing relied on parameters consistent with bifurcation 'B', adopting a similar height for the first layer

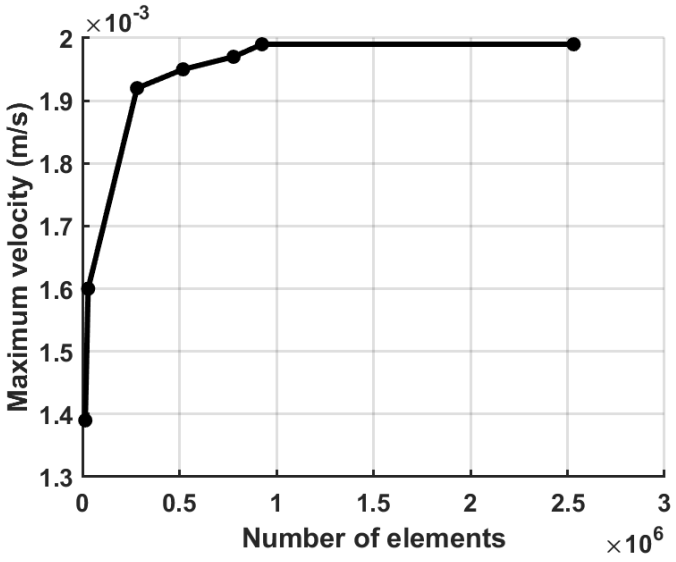

Figure C.1: Mesh independence based on maximum velocity on the bifurcation 'B'.

Table C.1: Mesh parameter variation for a mesh independence analysis of bifurcation 'B'.

Based size (m)	No. PL	PLTT (m)	No. cell	Max. u_{bulk} (m/s)
$4.3x10^{-7}$	20	$8.5x10^{-6}$	2531831	$1.99x10^{-3}$
$8.5x10^{-7}$	25	$8.5x10^{-6}$	778813	$1.97x10^{-3}$
$8.5x10^{-7}$	30	$8.5x10^{-6}$	925622	$1.99x10^{-3}$
$3.4x10^{-6}$	20	$4.3x10^{-6}$	518475	$1.95x10^{-3}$
$4.3x10^{-6}$	10	$2.1x10^{-6}$	281489	$1.92x10^{-3}$
$3.4x10^{-5}$	5	$4.3x10^{-7}$	29382	$1.60x10^{-3}$
$4.3x10^{-5}$	3	$2.1x10^{-7}$	14710	$1.39x10^{-3}$

Note: PL and PLTT stand for prism layer and prism layer total thickness, respectively.

C.2 Multi-phase, multi-component models on engineered capillary

The complexity of replicating functional vasculature in engineered constructs remains a major barrier to advancing tissue engineering, as current designs fail to establish a robust link between haemodynamics and biological outcomes. This limitation restricts construct size to below the cm^2 scale and compromises perfusion efficiency. To address this, the present study explores whether a multi-phase, multi-component model can accurately predict haematocrit behaviour and improve physiological relevance in engineered networks.

The model was applied to bio-artificial microvascular networks fabricated by culturing human umbilical vein endothelial cells (HUVECs) in collagen hydrogels. Two-dimensional images of the capillary networks, provided by Laure Vidal-Roussel were processed to reconstruct the vascular geometry for simulation. Meshing and Eulerian Multiphase (EMP) parameters followed the methodology outlined in Chapter 2, enabling the model to represent RBC-rich and plasma phases under laminar, time-dependent conditions.

Preliminary simulations on two capillary structures (Fig. C.3–C.4) successfully captured key haemodynamic parameters, including the spatial distribution of the RBC-rich component and WSS profiles, and hydrodynamic forces. These findings confirm the capability of the multi-phase, multi-component model to resolve microvascular flow behaviour under identical pressure outlet conditions. The next step will involve implementing diameter-based pressure outlet boundaries to achieve a more physiologically accurate representation of flow regulation and pressure gradients.

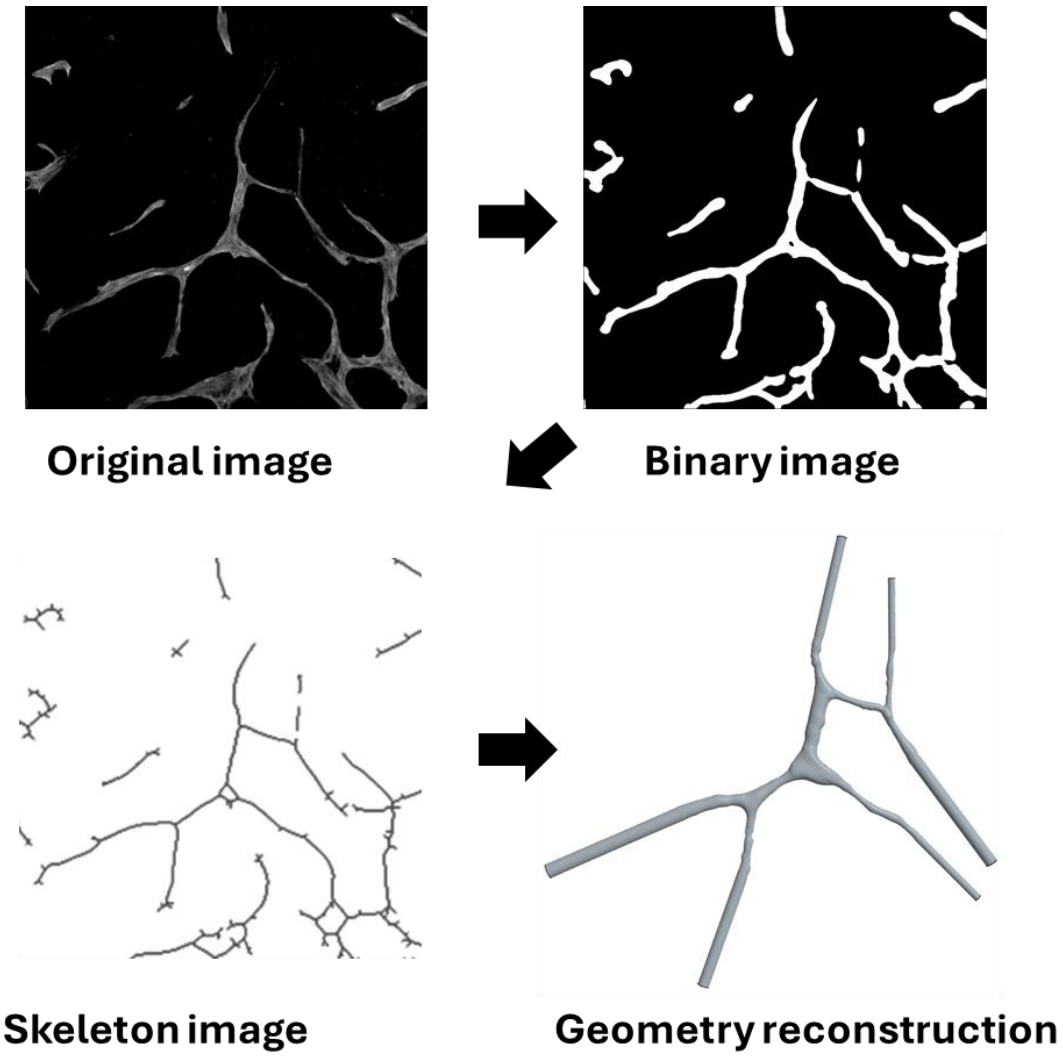

Figure C.2: Workflow for reconstructing vascular geometry from 2D imaging data.

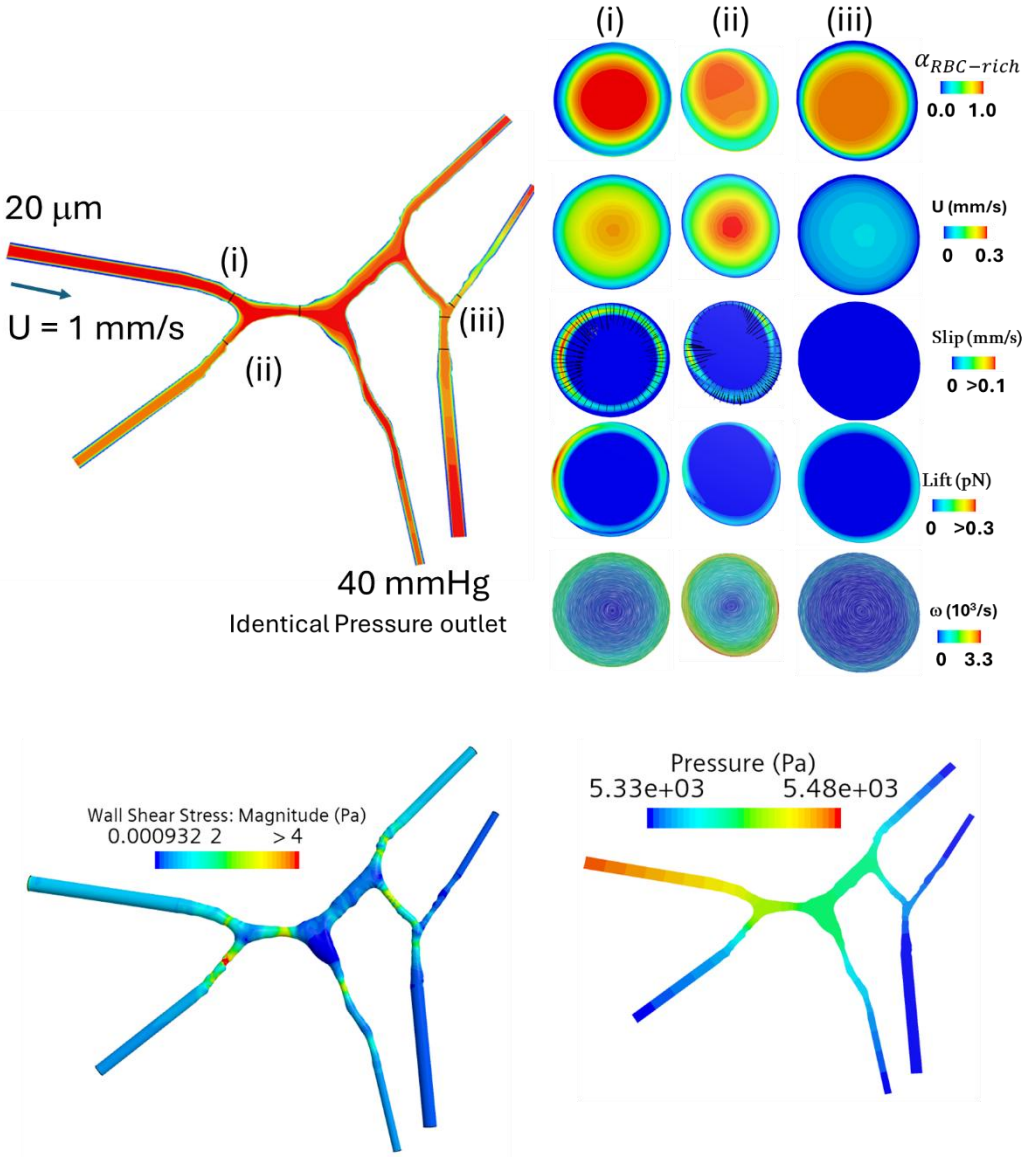

Figure C3.: Preliminary haemodynamic data of the capillary model 1.

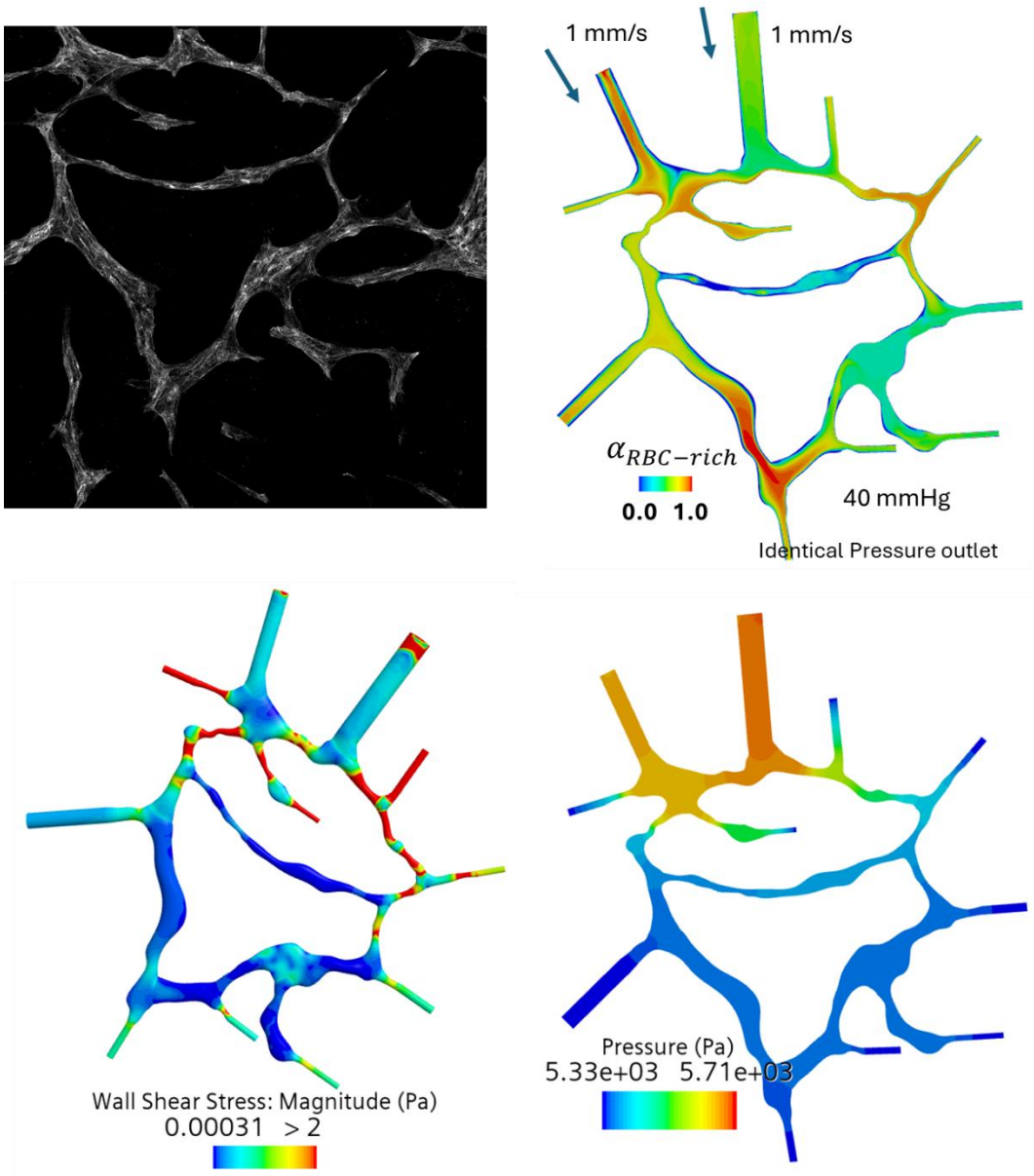

Figure C4.: Preliminary haemodynamic data of the capillary model 2.

Appendix D

Supplementary material for Chapter 5

D.1 Meshing independence analysis.

A mesh independence analysis was performed for testis control (89 μm) and atrophy (48 μm), applying a Newtonian laminar flow model with inlet velocities of 6.0 mm/s and 1.0 mm/s, respectively. For the testis control, parameter variations are provided in Table D.1, while the fixed parameters consisted of PLTT (prism layer total thickness) at 33%, volume growth rate at 1.3, surface growth rate at 1.3, and prism layer stretching at 1.3. For the testis atrophy, the PLTT (33%) and volume growth rate (1.3) were fixed, whilst other parameters were varied as shown in Table D.2.

As shown in Fig. D.1 and D.2, the suitable meshed selected for further analysis consisted of 3.7 million (control) and 1.9 million (atrophy) cells. The first mesh layer height (Δy_1) of these meshes was 3.82×10^{-8} and 3.53×10^{-8} m, which were shorter than the theoretical values (3.4×10^{-7} and 5.7×10^{-8} m, respectively) calculated using the viscous sublayer thickness equation:

$$\Delta y_1 = \frac{\mu y^+}{\rho U_T}; \quad U_T = \sqrt{wss/\rho}; \quad y^+ = U^+ = U/U_T.$$

,where the μ, wss and ρ was 0.00345 Pa·s, 60 dyn/cm^3 [43] and 1060 kg/m^3, respectively.

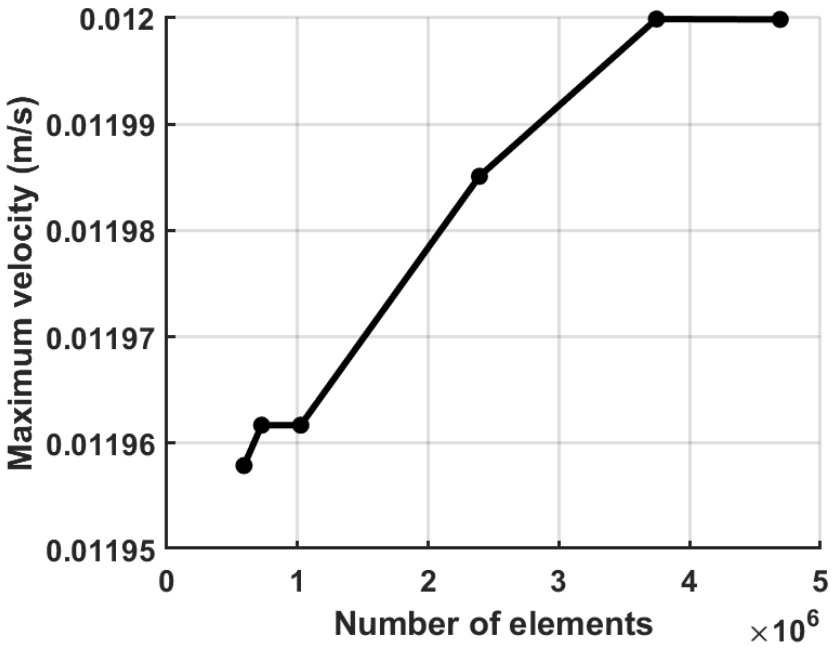

Figure D.1: Mesh independence based on maximum velocity on the testis control.

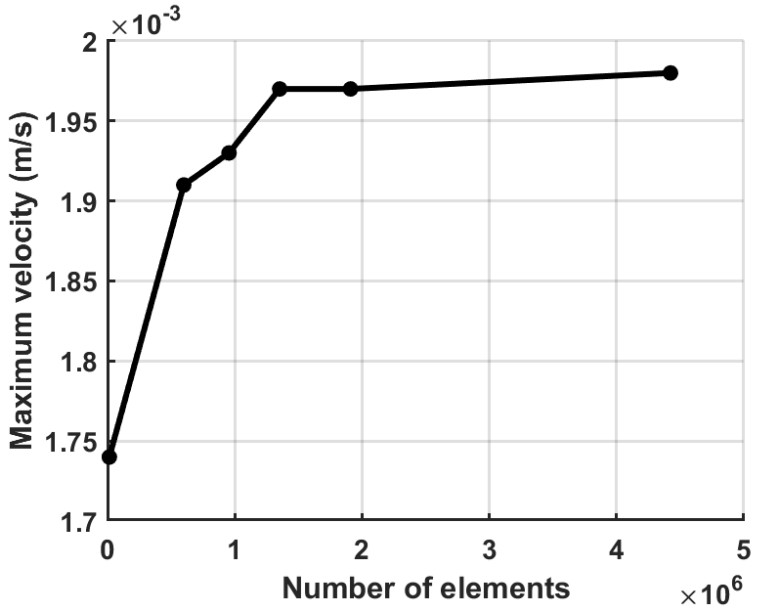

Figure D.2: Mesh independence based on maximum velocity on the testis atrophy.

Table D.1: Mesh parameter variation for a mesh independence analysis of testis control.

Based size (m)	Target surface size (%)	No. PL	PLTT (%)	No. cell	Max.u_{bulk} (m/s)
6.18×10^{-7}	500	7	100	4692345	1.2000×10^{-2}
6.66×10^{-7}	500	7	100	3745527	1.2000×10^{-2}
8.56×10^{-7}	500	7	100	2391666	1.1985×10^{-2}
8.56×10^{-6}	500	5	33	1024681	1.1962×10^{-2}
8.56×10^{-6}	500	3	10	725435	1.1962×10^{-2}
8.56×10^{-6}	100	2	10	581499	1.1958×10^{-2}

Note: PL and PLTT stand for prism layer and prism layer total thickness, respectively. The percentage value is relative to based size.

Table D.2: Mesh parameter variation for a mesh independence analysis of testis atrophy.

Based size (m)	Target surface size (%)	Surface growth	No. PL	PL-stretching	No. cell	Max.u_{bulk} (m/s)
1.35×10^{-6}	100	1.3	5	1.2	4424066	1.98×10^{-3}
1.35×10^{-6}	150	1.1	6	1.3	1909837	1.97×10^{-3}
1.35×10^{-6}	200	1.1	7	1.2	1352748	1.97×10^{-3}
2.03×10^{-6}	150	1.1	6	1.3	954744	1.93×10^{-3}
2.70×10^{-6}	200	1.1	7	1.2	599151	1.91×10^{-3}
1.35×10^{-4}	150	1.1	2	1.3	14176	1.74×10^{-3}

Note: PL and PLTT stand for prism layer and prism layer total thickness, respectively. The percentage value is relative to based size.

Appendix E

Supplementary material for Chapter 6

E.1 Meshing independence analysis.

A mesh independence analysis was performed for pulmonary artery TS1, applying a Newtonian laminar flow model with inlet velocities of 1.5 m/s. parameter variations are provided in Table E.1, while the fixed parameters consisted of surface growth rate of 1.1, prism layer stretching of 1.2 and volume growth rate of 1.2.

As shown in Fig. E.1, the suitable meshed selected for further analysis consisted of 0.5 million cells. The first mesh layer height (Δy_1) of these meshes was 4.67x10^{-5} m, which were shorter than the theoretical values (1.5x10^{-4} m, respectively) calculated using the viscous sublayer thickness equation as mentioned in Appendix D.1. The WSS used to calculate the Δy_1 is 4 dyn/cm^2 for MPA in healthy control [321].

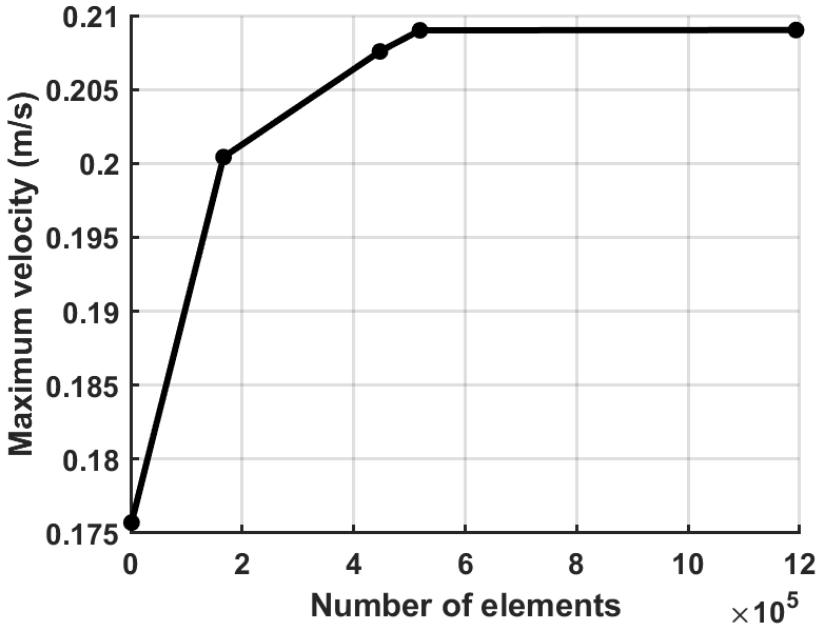

Figure E.1: Mesh independence based on maximum velocity on pulmonary artery TS1.

Table E.1: Mesh parameter variation for a mesh independence analysis of pulmonary artery TS1.

Based size (m)	Target surface size (%)	No. PL	PLTT (%)	No. cell	Max.u_{bulk} (m/s)
$3.0x10^{-4}$	200	7	100	1193438	0.209
$6.0\ x10^{-4}$	200	7	100	518803	0.209
$8.0\ x10^{-4}$	1000	7	100	446997	0.208
$4.0\ x10^{-3}$	200	3	10	166585	0.200
$8.0\ x10^{-2}$	200	2	1	1534	0.176

Note: PL and PLTT stand for prism layer and prism layer total thickness, respectively. The percentage value is relative to based size.

Bibliography

[1] Y. Çınar, G. Demir, M. Paç, and A. B. Çınar, "Effect of hematocrit on blood pressure via hyperviscosity," *American journal of hypertension,* vol. 12, no. 7, pp. 739-743, 1999.

[2] L. Allport *et al.*, "Elevated hematocrit is associated with reduced reperfusion and tissue survival in acute stroke," *Neurology,* vol. 65, no. 9, pp. 1382-1387, 2005.

[3] O. Oulaid and J. Zhang, "Cell-free layer development process in the entrance region of microvessels," *Biomechanics and modeling in mechanobiology,* vol. 14, no. 4, pp. 783-794, 2015.

[4] T. Ye, L. Peng, and G. Li, "Red blood cell distribution in a microvascular network with successive bifurcations," *Biomechanics and modeling in mechanobiology,* vol. 18, no. 6, pp. 1821-1835, 2019.

[5] M. O. Bernabeu *et al.*, "Abnormal morphology biases hematocrit distribution in tumor vasculature and contributes to heterogeneity in tissue oxygenation," *Proceedings of the National Academy of Sciences,* vol. 117, no. 45, pp. 27811-27819, 2020.

[6] S. S. Ye, M. Ju, and S. Kim, "Recovery of cell-free layer and wall shear stress profile symmetry downstream of an arteriolar bifurcation," *Microvascular Research,* vol. 106, pp. 14-23, 2016.

[7] M. Salame and M. Fenech, "Key contributors to cell-free layer formation: An experimental investigation of hematocrit and shear rate gradient," *Microvascular Research,* p. 104859, 2025.

[8] E. Yeom and S. J. Lee, "Microfluidic-based speckle analysis for sensitive measurement of erythrocyte aggregation: A comparison of four methods for detection of elevated erythrocyte aggregation in diabetic rat blood," *Biomicrofluidics,* vol. 9, no. 2, 2015.

[9] W. Reinke, P. Gaehtgens, and P. Johnson, "Blood viscosity in small tubes: effect of shear rate, aggregation, and sedimentation," *American Journal of Physiology-Heart and Circulatory Physiology,* vol. 253, no. 3, pp. H540-H547, 1987.

[10] T. W. Secomb, "Blood flow in the microcirculation," *Annual Review of Fluid Mechanics,* vol. 49, no. 1, pp. 443-461, 2017.

[11] J. Kim, H. Lee, and S. Shin, "Advances in the measurement of red blood cell deformability: A brief review," *Journal of Cellular Biotechnology,* vol. 1, no. 1, pp. 63-79, 2015.

[12] W. H. Organization. "The top 10 causes of death." https://www.who.int/news-room/fact-sheets/detail/the-top-10-causes-of-death (accessed.

[13] P. Gyawali *et al.*, "Whole blood viscosity is associated with baseline cerebral perfusion in acute ischemic stroke," *Neurological Sciences,* vol. 43, no. 4, pp. 2375-2381, 2022.

[14] Y. Pratumwal *et al.*, "Whole blood viscosity modeling using power law, Casson, and Carreau Yasuda models integrated with image scanning U-tube viscometer technique," *Songklanakarin Journal of Science & Technology,* vol. 39, no. 5, 2017.

[15] Z. J. Taylor *et al.*, "Microvascular basis for growth of small infarcts following occlusion of single penetrating arterioles in mouse cortex," *Journal of Cerebral Blood Flow & Metabolism,* vol. 36, no. 8, pp. 1357-1373, 2016.

[16] L. Zhu *et al.*, "Single-microvessel occlusion produces lamina-specific microvascular flow vasodynamics and signs of neurodegenerative change," *Cell Reports,* vol. 42, no. 5, 2023.
[17] Y. R. Nartsissov, "Geometries of vasculature bifurcation can affect the level of trophic damage during formation of a brain ischemic lesion," *Biochemical Society transactions,* vol. 45, no. 5, pp. 1097-1103, 2017.
[18] Y. Chen and R. J. Rivers, "Arteriolar occlusion causes independent cellular responses in endothelium and smooth muscle," *Microcirculation,* vol. 9, no. 5, pp. 353-362, 2002.
[19] W. R. Carroll and R. M. Esclamado, "Ischemia/reperfusion injury in microvascular surgery," *Head & Neck: Journal for the Sciences and Specialties of the Head and Neck,* vol. 22, no. 7, pp. 700-713, 2000.
[20] J. Kang *et al.*, "High blood viscosity in acute ischemic stroke," *Frontiers in Neurology,* vol. 14, p. 1320773, 2023.
[21] M. Harrison, B. Kendall, S. Pollock, and J. Marshall, "Effect of haematocrit on carotid stenosis and cerebral infarction," *The Lancet,* vol. 318, no. 8238, pp. 114-115, 1981.
[22] A. Y. Shih *et al.*, "The smallest stroke: occlusion of one penetrating vessel leads to infarction and a cognitive deficit," *Nature neuroscience,* vol. 16, no. 1, pp. 55-63, 2013.
[23] T. R. Weerasooriya and T. Yaniamoto, "Three-dimensional organisation of the vasculature of the rat spermatic cord and testis: A scanning electron-microscopic study of vascular corrosion casts," *Cell and tissue research,* vol. 241, no. 2, pp. 317-323, 1985.
[24] T. Murakami, Y. Uno, A. Ohtsuka, and T. Taguchi, "The blood vascular architecture of the rat testis: a scanning electron microscopic study of corrosion casts followed by light microscopy of tissue sections," *archives of histology and cytology,* vol. 52, no. 2, pp. 151-172, 1989.
[25] J. González and G. Ciancio, "Vascular Diseases of the Testis," *PanVascular Medicine,* pp. 3855-3886, 2015.
[26] P. K. Mittal *et al.*, "Role of imaging in the evaluation of male infertility," *Radiographics,* vol. 37, no. 3, pp. 837-854, 2017.
[27] S. Tarhan, B. Gümüs, İ. Gündüz, V. Ayyildiz, and C. Göktan, "Effect of varicocele on testicular artery blood flow in men color doppler investigation," *Scandinavian journal of urology and nephrology,* vol. 37, no. 1, pp. 38-42, 2003.
[28] H.-I. Choi, H. C. Kim, S. W. Kim, S. K. Moon, and J. W. Lim, "Small testes: clinical characteristics and ultrasonographic findings," *Ultrasonography,* vol. 40, no. 3, pp. 455-463, 2020.
[29] A. Abdelhalim *et al.*, "Testicular volume changes in laparoscopic staged Fowler-Stephens orchiopexy: studying the impact of testicular vessel division," *Urology,* vol. 127, pp. 113-118, 2019.
[30] V. S. Dogra, R. H. Gottlieb, M. Oka, and D. J. Rubens, "Sonography of the scrotum," *Radiology,* vol. 227, no. 1, pp. 18-36, 2003.
[31] S. J. Park, H. C. Kim, J. W. Lim, S. K. Moon, and S. E. Ahn, "Distribution of epididymal involvement in mumps epididymo‐orchitis," *Journal of Ultrasound in Medicine,* vol. 34, no. 6, pp. 1083-1089, 2015.
[32] H.-I. Choi, H. C. Kim, S. W. Kim, H. S. Jeong, S. K. Moon, and J. W. Lim, "Testicular atrophy after mumps orchitis: ultrasonographic findings," *Ultrasonography,* vol. 39, no. 3, pp. 266-271, 2020.

[33] D. A. Paduch and J. Niedzielski, "Repair versus observation in adolescent varicocele: a prospective study," *The Journal of urology,* vol. 158, no. 3, pp. 1128-1132, 1997.
[34] M. J. Colebank, M. U. Qureshi, S. Rajagopal, R. A. Krasuski, and M. S. Olufsen, "A multiscale model of vascular function in chronic thromboembolic pulmonary hypertension," *American Journal of Physiology-Heart and Circulatory Physiology,* vol. 321, no. 2, pp. H318-H338, 2021.
[35] M. J. Colebank and N. C. Chesler, "Efficient uncertainty quantification in a spatially multiscale model of pulmonary arterial and venous hemodynamics," *Biomechanics and modeling in mechanobiology,* vol. 23, no. 6, pp. 1909-1931, 2024.
[36] V. Sucato *et al.*, "Ischemia in patients with no obstructive coronary artery disease: classification, diagnosis and treatment of coronary microvascular dysfunction," *Coronary Artery Disease,* vol. 31, no. 5, pp. 472-476, 2020.
[37] B.-H. Zhao *et al.*, "The role and mechanisms of microvascular damage in the ischemic myocardium," *Cellular and Molecular Life Sciences,* vol. 80, no. 11, p. 341, 2023.
[38] J. A. Kloka, B. Friedrichson, P. Wülfroth, R. Henning, and K. Zacharowski, "Microvascular leakage as therapeutic target for ischemia and reperfusion injury," *Cells,* vol. 12, no. 10, p. 1345, 2023.
[39] A. R. Pries and T. W. Secomb, "Blood flow in microvascular networks," in *Microcirculation*: Elsevier, 2008, pp. 3-36.
[40] R. W. a. W. Hill, Gordon A. and Anderson, Margaret, *Animal Physiology*. Sinauer Associates, 2012.
[41] T. W. Secomb, "Blood flow in the microcirculation," *Annual Review of Fluid Mechanics,* vol. 49, pp. 443-461, 2017.
[42] R. S. Rawlani Shobha, *Chapter-08 Blood Vascular System*. 2013.
[43] A. S. Popel and P. C. Johnson, "Microcirculation and hemorheology," *Annu. Rev. Fluid Mech.,* vol. 37, no. 1, pp. 43-69, 2005.
[44] A. Tokarev, G. Panasenko, and F. Ataullakhanov, "Segregation of Flowing Blood: MathematicalDescription," *Mathematical modelling of natural phenomena,* vol. 6, no. 5, pp. 281-319, 2011.
[45] J. L. Poiseuille, *Recherches expérimentales sur le mouvement des liquides dans les tubes de très-petits diamètres*. Imprimerie Royale, 1844.
[46] R. Fåhraeus, "The suspension stability of the blood," *Physiological reviews,* vol. 9, no. 2, pp. 241-274, 1929.
[47] J. H. Barbee and G. R. Cokelet, "The fahraeus effect," *Microvascular research,* vol. 3, no. 1, pp. 6-16, 1971.
[48] T. W. Secomb, "Theoretical models for regulation of blood flow," *Microcirculation,* vol. 15, no. 8, pp. 765-775, 2008.
[49] A. Pries, D. Schonfeld, P. Gaehtgens, M. Kiani, and G. Cokelet, "Diameter variability and microvascular flow resistance," *American Journal of Physiology-Heart and Circulatory Physiology,* vol. 272, no. 6, pp. H2716-H2725, 1997.
[50] H. H. Lipowsky, "Microvascular rheology and hemodynamics," *Microcirculation,* vol. 12, no. 1, pp. 5-15, 2005.
[51] B. W. Zweifach, "Quantitative studies of microcirculatory structure and function: I. Analysis of pressure distribution in the terminal vascular bed in cat mesentery," *Circulation Research,* vol. 34, no. 6, pp. 841-857, 1974.
[52] T. Bodnár, A. Sequeira, and M. Prosi, "On the shear-thinning and viscoelastic effects of blood flow under various flow rates," *Applied Mathematics and Computation,* vol. 217, no. 11, pp. 5055-5067, 2011.

[53] S. Chien, S. Usami, R. J. Dellenback, M. I. Gregersen, L. B. Nanninga, and M. M. Guest, "Blood viscosity: influence of erythrocyte aggregation," *Science,* vol. 157, no. 3790, pp. 829-831, 1967.

[54] S. Chien, S. Usami, R. J. Dellenback, and M. I. Gregersen, "Blood viscosity: influence of erythrocyte deformation," *Science,* vol. 157, no. 3790, pp. 827-829, 1967.

[55] G. Vlastos, D. Lerche, and B. Koch, "The superposition of steady on oscillatory shear and its effect on the viscoelasticity of human blood and a blood-like model fluid," *Biorheology,* vol. 34, no. 1, pp. 19-36, 1997.

[56] A. R. Pries, "Microvascular hemodynamics: system properties," *Biorheology,* vol. 56, no. 1, pp. 1-13, 2019.

[57] A. R. Pries, T. W. Secomb, P. Gaehtgens, and J. F. Gross, "Blood Flow in Microvascular Networks Experiments and Simulation," *Circ Res,* vol. 67, no. 4, pp. 826-834, 1990, doi: 10.1161/01.Res.67.4.826.

[58] A. R. Pries, D. Neuhaus, and P. Gaehtgens, "Blood viscosity in tube flow: dependence on diameter and hematocrit," *American Journal of Physiology-Heart and Circulatory Physiology,* vol. 263, no. 6, pp. H1770-H1778, 1992.

[59] A. R. Pries, T. Secomb, T. Gessner, M. Sperandio, J. Gross, and P. Gaehtgens, "Resistance to blood flow in microvessels in vivo," *Circulation research,* vol. 75, no. 5, pp. 904-915, 1994.

[60] T. W. Secomb, C. Ellington, and T. Pedley, "Mechanics of blood flow in the microcirculation," *Biomedical flows at low Reynolds numbers,* vol. 9, pp. 9-10, 1995.

[61] S. Weber‐Fishkin, H. S. Seidner, G. Gunter, and M. D. Frame, "Erythrocyte aggregation in sudden flow arrest is linked to hyperthermia, hypoxemia, and band 3 availability," *Journal of Thrombosis and Haemostasis,* vol. 20, no. 10, pp. 2284-2292, 2022.

[62] C. Alonso, A. Pries, O. Kiesslich, D. Lerche, and P. Gaehtgens, "Transient rheological behavior of blood in low-shear tube flow: velocity profiles and effective viscosity," *American Journal of Physiology-Heart and Circulatory Physiology,* vol. 268, no. 1, pp. H25-H32, 1995.

[63] P. K. Ong, B. Namgung, P. C. Johnson, and S. Kim, "Effect of erythrocyte aggregation and flow rate on cell-free layer formation in arterioles," *American Journal of Physiology-Heart and Circulatory Physiology,* vol. 298, no. 6, pp. H1870-H1878, 2010.

[64] P. K. Ong, S. Jain, B. Namgung, Y. I. Woo, and S. Kim, "Cell‐free layer formation in small arterioles at pathological levels of erythrocyte aggregation," *Microcirculation,* vol. 18, no. 7, pp. 541-551, 2011.

[65] D. A. Fedosov, W. Pan, B. Caswell, G. Gompper, and G. E. Karniadakis, "Predicting human blood viscosity in silico," *Proceedings of the National Academy of Sciences,* vol. 108, no. 29, pp. 11772-11777, 2011.

[66] J. B. Freund and M. Orescanin, "Cellular flow in a small blood vessel," *Journal of Fluid Mechanics,* vol. 671, pp. 466-490, 2011.

[67] S. D. House and H. H. Lipowsky, "Microvascular hematocrit and red cell flux in rat cremaster muscle," *American Journal of Physiology-Heart and Circulatory Physiology,* vol. 252, no. 1, pp. H211-H222, 1987.

[68] G. R. Cokelet, "Rheology and hemodynamics," *Annu. Rev. Physiol.;(United States),* vol. 42, 1980.

[69] C. Desjardins and B. R. Duling, "Microvessel hematocrit: measurement and implications for capillary oxygen transport," *American Journal of Physiology-Heart and Circulatory Physiology,* vol. 252, no. 3, pp. H494-H503, 1987.

[70] M. W. Keller, D. Damon, and B. R. Duling, "Determination of capillary tube hematocrit during arteriolar microperfusion," *American Journal of Physiology-Heart and Circulatory Physiology,* vol. 266, no. 6, pp. H2229-H2238, 1994.
[71] H. H. Lipowsky and J. C. Firrell, "Microvascular hemodynamics during systemic hemodilution and hemoconcentration," *American Journal of Physiology-Heart and Circulatory Physiology,* vol. 250, no. 6, pp. H908-H922, 1986.
[72] M. Soutani, Y. Suzuki, N. Tateishi, and N. Maeda, "Quantitative evaluation of flow dynamics of erythrocytes in microvessels: influence of erythrocyte aggregation," *American Journal of Physiology-Heart and Circulatory Physiology,* vol. 268, no. 5, pp. H1959-H1965, 1995.
[73] Q. Zhou, J. Fidalgo, M. O. Bernabeu, M. S. Oliveira, and T. Krüger, "Emergent cell-free layer asymmetry and biased haematocrit partition in a biomimetic vascular network of successive bifurcations," *Soft Matter,* vol. 17, no. 13, pp. 3619-3633, 2021.
[74] B. Klitzman and B. R. Duling, "Microvascular hematocrit and red cell flow in resting and contracting striated muscle," *American journal of physiology-heart and circulatory physiology,* vol. 237, no. 4, pp. H481-H490, 1979.
[75] A. Bucciarelli, A. Mantegazza, A. Haeberlin, and D. Obrist, "Relation between hematocrit partitioning and red blood cell lingering in a microfluidic network," *Biophysical Journal,* vol. 123, no. 19, pp. 3355-3365, 2024.
[76] K. Giannokostas, Y. Dimakopoulos, A. Anayiotos, and J. Tsamopoulos, "Advanced constitutive modeling of the thixotropic elasto-visco-plastic behavior of blood: steady-state blood flow in microtubes," *Materials,* vol. 14, no. 2, p. 367, 2021.
[77] M. L. Ellsworth and R. N. Pittman, "Evaluation of photometric methods for quantifying convective mass transport in microvessels," *American Journal of Physiology-Heart and Circulatory Physiology,* vol. 251, no. 4, pp. H869-H879, 1986.
[78] Y. Rashidi *et al.*, "Red blood cell lingering modulates hematocrit distribution in the microcirculation," *Biophysical Journal,* vol. 122, no. 8, pp. 1526-1537, 2023.
[79] R. Lima, T. Ishikawa, Y. Imai, and T. Yamaguchi, "Blood flow behavior in microchannels: Past, current and future trends," *Single and two-phase flows on chemical and biomedical engineering,* pp. 513-547, 2012.
[80] A. R. Pries and T. W. Secomb, "Microvascular blood viscosity in vivo and the endothelial surface layer," *American Journal of Physiology-Heart and Circulatory Physiology,* vol. 289, no. 6, pp. H2657-H2664, 2005.
[81] P. C. Johnson, J. Blaschke, K. S. Burton, and J. Dial, "Influence of flow variations on capillary hematocrit in mesentery," *American Journal of Physiology-Legacy Content,* vol. 221, no. 1, pp. 105-112, 1971.
[82] R. Lima, T. Ishikawa, Y. Imai, M. Takeda, S. Wada, and T. Yamaguchi, "Radial dispersion of red blood cells in blood flowing through glass capillaries: the role of hematocrit and geometry," *Journal of biomechanics,* vol. 41, no. 10, pp. 2188-2196, 2008.
[83] A. N. Balachandran Nair, S. Pirker, and M. Saeedipour, "Resolved CFD-DEM simulation of blood flow with a reduced-order RBC model," *Computational Particle Mechanics,* vol. 9, no. 4, pp. 759-774, 2022.
[84] Y. Sugii, R. Okuda, K. Okamoto, and H. Madarame, "Velocity measurement of both red blood cells and plasma of in vitro blood flow using high-speed micro PIV technique," *Measurement science and Technology,* vol. 16, no. 5, p. 1126, 2005.
[85] C. J. Munoz, A. Lucas, A. T. Williams, and P. Cabrales, "A review on microvascular hemodynamics: the control of blood flow distribution and tissue oxygenation," *Critical care clinics,* vol. 36, no. 2, pp. 293-305, 2020.

[86] G. J. Tangelder, D. W. Slaaf, A. Muijtjens, T. Arts, M. Oude Egbrink, and R. S. Reneman, "Velocity profiles of blood platelets and red blood cells flowing in arterioles of the rabbit mesentery," *Circulation Research,* vol. 59, no. 5, pp. 505-514, 1986.

[87] H. Goldsmith, "Red cell motions and wall interactions in tube flow," in *Federation proceedings*, 1971, vol. 30, no. 5, pp. 1578-1590.

[88] M. Baker and H. Wayland, "On-line volume flow rate and velocity profile measurement for blood in microvessels," *Microvascular research,* vol. 7, no. 1, pp. 131-143, 1974.

[89] T. P. Santisakultarm *et al.*, "In vivo two-photon excited fluorescence microscopy reveals cardiac-and respiration-dependent pulsatile blood flow in cortical blood vessels in mice," *American Journal of Physiology-Heart and Circulatory Physiology,* vol. 302, no. 7, pp. H1367-H1377, 2012.

[90] Y. C. Ng, B. Namgung, S. L. Tien, H. L. Leo, and S. Kim, "Symmetry recovery of cell-free layer after bifurcations of small arterioles in reduced flow conditions: effect of RBC aggregation," *American Journal of Physiology-Heart and Circulatory Physiology,* vol. 311, no. 2, pp. H487-H497, 2016.

[91] M. Ishikawa, E. Sekizuka, K. Shimizu, N. Yamaguchi, and T. Kawase, "Measurement of RBC velocities in the rat pial arteries with an image-intensified high-speed video camera system," *Microvascular research,* vol. 56, no. 3, pp. 166-172, 1998.

[92] R. S. Reneman and A. P. Hoeks, "Wall shear stress as measured in vivo: consequences for the design of the arterial system," *Medical & biological engineering & computing,* vol. 46, no. 5, pp. 499-507, 2008.

[93] L. D. Casa, D. H. Deaton, and D. N. Ku, "Role of high shear rate in thrombosis," *Journal of vascular surgery,* vol. 61, no. 4, pp. 1068-1080, 2015.

[94] H. A. Baieth, "Physical parameters of blood as a non-Newtonian fluid," *International journal of biomedical science: IJBS,* vol. 4, no. 4, p. 323, 2008.

[95] K. Sriram, M. Intaglietta, and D. M. Tartakovsky, "Non‐Newtonian flow of blood in arterioles: Consequences for wall shear stress measurements," *Microcirculation,* vol. 21, no. 7, pp. 628-639, 2014.

[96] R. S. Reneman, B. Woldhuis, M. G. oude Egbrink, D. W. Slaaf, and G. J. Tangelder, "Concentration and velocity profiles of blood cells in the microcirculation," in *Advances in cardiovascular engineering*: Springer, 1992, pp. 25-40.

[97] A. R. Pries, T. W. Secomb, and P. Gaehtgens, "Design principles of vascular beds," *Circulation research,* vol. 77, no. 5, pp. 1017-1023, 1995.

[98] E. Bakker *et al.*, "Differential structural adaptation to haemodynamics along single rat cremaster arterioles," *The Journal of physiology,* vol. 548, no. 2, pp. 549-555, 2003.

[99] R. S. Reneman, T. Arts, and A. P. Hoeks, "Wall shear stress–an important determinant of endothelial cell function and structure–in the arterial system in vivo: discrepancies with theory," *Journal of vascular research,* vol. 43, no. 3, pp. 251-269, 2006.

[100] B. Namgung, L. H. Liang, and S. Kim, "Physiological significance of cell-free layer and experimental determination of its width in microcirculatory vessels," *Visualization and simulation of complex flows in biomedical engineering,* pp. 75-87, 2014.

[101] S. Kim, R. L. Kong, A. S. Popel, M. Intaglietta, and P. C. Johnson, "Temporal and spatial variations of cell-free layer width in arterioles," *Am J Physiol Heart Circ Physiol,* vol. 293, no. 3, pp. 1526-1535, 2007, doi: 10.1152/ajpheart.01090.2006.

[102] N. Maeda, Y. Suzuki, J. Tanaka, and N. Tateishi, "Erythrocyte flow and elasticity of microvessels evaluated by marginal cell-free layer and flow resistance," *American journal of physiology. Heart and circulatory physiology,* vol. 271, no. 6, pp. H2454-H2461, 1996, doi: 10.1152/ajpheart.1996.271.6.h2454.

[103] D. Katanov, G. Gompper, and D. A. Fedosov, "Microvascular blood flow resistance: Role of red blood cell migration and dispersion," *Microvasc Res,* vol. 99, pp. 57-66, 2015, doi: 10.1016/j.mvr.2015.02.006.

[104] S. Kim, P. K. Ong, O. Yalcin, M. Intaglietta, and P. C. Johnson, "The cell-free layer in microvascular blood flow," *Biorheology,* vol. 46, no. 3, pp. 181-189, 2009.

[105] O. K. Baskurt and H. J. Meiselman, "Blood rheology and hemodynamics," in *Seminars in thrombosis and hemostasis*, 2003, vol. 29, no. 05: Copyright© 2003 by Thieme Medical Publishers, Inc., 333 Seventh Avenue, New …, pp. 435-450.

[106] G. R. Cokelet and H. L. Goldsmith, "Decreased Hydrodynamic Resistance in the Two-Phase Flow of Blood Through Small Vertical Tubes at Low Flow Rates," *Circ Res,* vol. 68, no. 1, pp. 1-17, 1991, doi: 10.1161/01.Res.68.1.1.

[107] B. Das, P. C. Johnson, and A. S. Popel, "Effect of nonaxisymmetric hematocrit distribution on non-Newtonian blood flow in small tubes," *Biorheology,* vol. 35, no. 1, pp. 69-87, 1998, doi: 10.1016/s0006-355x(98)00018-3.

[108] W. Reinke, P. C. Johnson, and P. Gaehtgens, "Effect of shear rate variation on apparent viscosity of human blood in tubes of 29 to 94 microns diameter," *Circulation research,* vol. 59, no. 2, pp. 124-132, 1986.

[109] O. Yalcin, Q. Wang, P. C. Johnson, A. F. Palmer, and P. Cabrales, "Plasma expander viscosity effects on red cell-free layer thickness after moderate hemodilution," *Biorheology,* vol. 48, no. 5-6, pp. 277-291, 2011.

[110] P. Cabrales and M. Intaglietta, "Blood substitutes: evolution from non-carrying to oxygen and gas carrying fluids," *ASAIO Journal (American Society for Artificial Internal Organs: 1992),* vol. 59, no. 4, p. 337, 2013.

[111] D. Dias, D. Sampaio, G. Silva, V. Semiao, and M. N. De Pinho, "The effect of hemicylindrical disruptors on the cell free layer thickness in animal blood flows inside microchannels," *Experimental Results,* vol. 1, p. e55, 2020.

[112] C. Makena Hightower *et al.*, "Integration of cardiovascular regulation by the blood/endothelium cell‐free layer," *Wiley Interdisciplinary Reviews: Systems Biology and Medicine,* vol. 3, no. 4, pp. 458-470, 2011.

[113] C. Munoz, F. Aletti, K. Govender, P. Cabrales, and E. B. Kistler, "Resuscitation after hemorrhagic shock in the microcirculation: targeting optimal oxygen delivery in the design of artificial blood substitutes," *Frontiers in Medicine,* vol. 7, p. 691, 2020.

[114] B. M. Fenton, R. T. Carr, and G. R. Cokelet, "Nonuniform red cell distribution in 20 to 100 µm bifurcations," *Microvascular research,* vol. 29, no. 1, pp. 103-126, 1985.

[115] S. Chien, C. D. Tvetenstrand, M. Epstein, and G. W. Schmid-Schonbein, "Model studies on distributions of blood cells at microvascular bifurcations," *American Journal of Physiology-Heart and Circulatory Physiology,* vol. 248, no. 4, pp. H568-H576, 1985.

[116] A. R. Pries, K. Ley, M. Claassen, and P. Gaehtgens, "Red cell distribution at microvascular bifurcations," *Microvascular research,* vol. 38, no. 1, pp. 81-101, 1989.

[117] T. Hyakutake and S. Nagai, "Numerical simulation of red blood cell distributions in three-dimensional microvascular bifurcations," *Microvascular research,* vol. 97, pp. 115-123, 2015.

[118] J. O. Barber, J. P. Alberding, J. M. Restrepo, and T. W. Secomb, "Simulated two-dimensional red blood cell motion, deformation, and partitioning in microvessel bifurcations," *Annals of biomedical engineering,* vol. 36, no. 10, pp. 1690-1698, 2008.
[119] S. K. Sanjeevi, J. Kuipers, and J. T. Padding, "Drag, lift and torque correlations for non-spherical particles from Stokes limit to high Reynolds numbers," *International Journal of Multiphase Flow,* vol. 106, pp. 325-337, 2018.
[120] F. Yilmaz and M. Y. Gundogdu, "Analysis of conventional drag and lift models for multiphase CFD modeling of blood flow," *Korea-Australia Rheology Journal,* vol. 21, no. 3, pp. 161-173, 2009.
[121] M. Madadelahi, L. F. Acosta-Soto, S. Hosseini, S. O. Martinez-Chapa, and M. J. Madou, "Mathematical modeling and computational analysis of centrifugal microfluidic platforms: a review," *Lab on a Chip,* vol. 20, no. 8, pp. 1318-1357, 2020.
[122] D. Huber, A. Oskooei, X. Casadevall i Solvas, A. Demello, and G. V. Kaigala, "Hydrodynamics in cell studies," *Chemical reviews,* vol. 118, no. 4, pp. 2042-2079, 2018.
[123] L. Zhang, A. S. Jebakumar, and J. Abraham, "Lattice Boltzmann method simulations of Stokes number effects on particle motion in a channel flow," *Physics of Fluids,* vol. 28, no. 6, 2016.
[124] R.-J. Yang, H.-H. Hou, Y.-N. Wang, C.-H. Lin, and L.-M. Fu, "A hydrodynamic focusing microchannel based on micro-weir shear lift force," *Biomicrofluidics,* vol. 6, no. 3, 2012.
[125] A. Farahinia, W. Zhang, and I. Badea, "Recent developments in inertial and centrifugal microfluidic systems along with the involved forces for cancer cell separation: A review," *Sensors,* vol. 23, no. 11, p. 5300, 2023.
[126] Y. Zhang and T. G. Fai, "Influence of the vessel wall geometry on the wall-induced migration of red blood cells," *PLoS computational biology,* vol. 19, no. 7, p. e1011241, 2023.
[127] E. E. Michaelides, "Hydrodynamic force and heat/mass transfer from particles, bubbles, and drops—The Freeman scholar lecture," *J. Fluids Eng.,* vol. 125, no. 2, pp. 209-238, 2003.
[128] H. L. Goldsmith, "The microcirculatory society Eugene M. Landis award lecture: The microrheology of human blood," *Microvascular research,* vol. 31, no. 2, pp. 121-142, 1986.
[129] P. Aarts, S. Van Den Broek, G. W. Prins, G. Kuiken, J. J. Sixma, and R. M. Heethaar, "Blood platelets are concentrated near the wall and red blood cells, in the center in flowing blood," *Arteriosclerosis: An Official Journal of the American Heart Association, Inc.,* vol. 8, no. 6, pp. 819-824, 1988.
[130] F. Moukalled, L. Mangani, and M. Darwish, *The Finite Volume Method in Computational Fluid Dynamics: An Advanced Introduction with OpenFOAM® and Matlab®* (Fluid Mechanics and Its Applications). Cham: Springer International Publishing, 2016.
[131] C. González-Abós, R. Molina, S. Almirante, M. Vázquez, and F. Ausania, "Computational fluid dynamics for vascular assessment in hepatobiliopancreatic surgery: a pilot study and future perspectives," *Surgical Endoscopy,* pp. 1-10, 2025.
[132] Y. Hohri *et al.*, "Blood flow assessment technology in aortic surgery: a narrative review," *Journal of Thoracic Disease,* vol. 16, no. 4, p. 2623, 2024.
[133] N. K. R. Pandian *et al.*, "Three-dimensional modeling of flow through microvascular beds and surrounding interstitial spaces," *bioRxiv,* p. 2024.02. 28.582152, 2025.

[134] R. Dong *et al.*, "Revisiting hemodynamics and blood oxygenation in a microfluidic microvasculature replica," *Microvascular Research,* vol. 152, p. 104640, 2024.
[135] B.-J. Lai, L.-T. Zhu, Z. Chen, B. Ouyang, and Z.-H. Luo, "Review on blood flow dynamics in lab-on-a-chip systems: An engineering perspective," *Chem & Bio Engineering,* vol. 1, no. 1, pp. 26-43, 2024.
[136] J. H. Ferziger and M. Perić, *Computational methods for fluid dynamics*. Springer, 2002.
[137] K. Timm, H. Kusumaatmaja, A. Kuzmin, O. Shardt, G. Silva, and E. Viggen, "The lattice Boltzmann method: principles and practice," *Cham, Switzerland: Springer International Publishing AG,* 2016.
[138] Siemens Digital Industries Software, "Mesh Construction," in *Simcenter STAR-CCM+ User Guide, Version 18.02.010-R8Pressure Outlet*, 18.02.010 ed.: Siemens 2023.
[139] T. Defraeye, B. Blocken, and J. Carmeliet, "CFD analysis of convective heat transfer at the surfaces of a cube immersed in a turbulent boundary layer," *International Journal of Heat and Mass Transfer,* vol. 53, no. 1-3, pp. 297-308, 2010.
[140] T. Cebeci, "General Behavior of Turbulent Boundary Layers," in *Analysis of Turbulent Flows with Computer Programs* Elsevier, 2013.
[141] H. Lei, D. A. Fedosov, B. Caswell, and G. E. Karniadakis, "Blood flow in small tubes: quantifying the transition to the non-continuum regime," *Journal of fluid mechanics,* vol. 722, pp. 214-239, 2013.
[142] S. Zhou *et al.*, "A review on low-dimensional physics-based models of systemic arteries: application to estimation of central aortic pressure," *Biomedical engineering online,* vol. 18, pp. 1-25, 2019.
[143] Y. Shi, P. Lawford, and R. Hose, "Review of zero-D and 1-D models of blood flow in the cardiovascular system," *Biomedical engineering online,* vol. 10, pp. 1-38, 2011.
[144] D. Loganathan, C.-H. Cheng, and C.-Y. Chen, "Hemodynamic analysis of mean arterial pressure on cerebral arteries for embolic ischemic stroke using a lumped parameter model," *IEEE Access,* 2024.
[145] H. F. Frasch, J. Y. Kresh, and A. Noordergraaf, "Two-port analysis of microcirculation: an extension of windkessel," *American Journal of Physiology-Heart and Circulatory Physiology,* vol. 270, no. 1, pp. H376-H385, 1996.
[146] Q. Pan *et al.*, "Pulsatility damping in the microcirculation: Basic pattern and modulating factors," *Microvascular Research,* vol. 139, p. 104259, 2022.
[147] N. Safaeian and T. David, "A computational model of oxygen transport in the cerebrocapillary levels for normal and pathologic brain function," *Journal of Cerebral Blood Flow & Metabolism,* vol. 33, no. 10, pp. 1633-1641, 2013.
[148] D. A. Fedosov, B. Caswell, A. S. Popel, and G. E. Karniadakis, "Blood flow and cell-free layer in microvessels," *Microcirculation,* vol. 17, no. 8, pp. 615-628, 2010.
[149] T. R. Lee, J. A. Hong, S. S. Yoo, and D. W. Kim, "A computational modeling of blood flow in asymmetrically bifurcating microvessels and its experimental validation," *International journal for numerical methods in biomedical engineering,* vol. 34, no. 6, p. e2981, 2018.
[150] C. Psevdos, K. Giannokostas, P. Moschopoulos, Y. Dimakopoulos, and J. Tsamopoulos, "Incorporating the complex rheological behavior of blood in microvascular network simulations: Two-phase modeling and a model reduction approach," *Journal of Non-Newtonian Fluid Mechanics,* vol. 322, p. 105134, 2023.
[151] A. Tiwari and S. S. Chauhan, "Effect of varying viscosity on two-fluid model of pulsatile blood flow through porous blood vessels: A comparative study," *Microvascular research,* vol. 123, pp. 99-110, 2019.

[152] M. Sharan and A. S. Popel, "A two‐phase model for flow of blood in narrow tubes with increased effective viscosity near the wall," *Biorheology,* vol. 38, no. 5-6, pp. 415-428, 2001.
[153] B. Namgung, M. Ju, P. Cabrales, and S. Kim, "Two-phase model for prediction of cell-free layer width in blood flow," *Microvascular research,* vol. 85, pp. 68-76, 2013.
[154] R. Chebbi, "A two-zone shear-induced red blood cell migration model for blood flow in microvessels," *Frontiers in Physics,* vol. 7, p. 206, 2019.
[155] L. Achab and F. Iachachene, "A new numerical approach using the VOF method to model the two-layered Herschel-Bulkley blood flow in microvessels," *Computers & Mathematics with Applications,* vol. 190, pp. 154-169, 2025.
[156] J. U. Brackbill, D. B. Kothe, and C. Zemach, "A continuum method for modeling surface tension," *Journal of computational physics,* vol. 100, no. 2, pp. 335-354, 1992.
[157] S. P. Yadav, A. Sharma, and A. Agrawal, "Modeling of three-dimensional blood flow in microchannels using a two-fluid method," *Physics of Fluids,* vol. 36, no. 2, 2024.
[158] H. Valtchanov, R. Cecere, and R. Mongrain, "Effect of intercellular collisions on red blood cell membrane damage," *Scientific Reports,* vol. 15, no. 1, p. 20698, 2025.
[159] A. Jafari, S. Mousavi, and P. Kolari, "Numerical investigation of blood flow. Part I: In microvessel bifurcations," *Communications in Nonlinear Science and Numerical Simulation,* vol. 13, no. 8, pp. 1615-1626, 2008.
[160] Y. Mendygarin, L. R. Rojas-Solórzano, N. Kussaiyn, R. Supiyev, and M. Zhussupbekov, "Eulerian-Eulerian multiphase modeling of blood cells segregation in flow through microtubes," in *ASME International Mechanical Engineering Congress and Exposition*, 2017, vol. 58363: American Society of Mechanical Engineers, p. V003T04A020.
[161] X. Yin, T. Thomas, and J. Zhang, "Multiple red blood cell flows through microvascular bifurcations: cell free layer, cell trajectory, and hematocrit separation," *Microvascular research,* vol. 89, pp. 47-56, 2013.
[162] J. Zhang, P. C. Johnson, and A. S. Popel, "An immersed boundary lattice Boltzmann approach to simulate deformable liquid capsules and its application to microscopic blood flows," *Physical biology,* vol. 4, no. 4, p. 285, 2007.
[163] P. Hoogerbrugge and J. M. Koelman, "Simulating microscopic hydrodynamic phenomena with dissipative particle dynamics," *Europhysics letters,* vol. 19, no. 3, p. 155, 1992.
[164] K. Lykov, X. Li, H. Lei, I. V. Pivkin, and G. E. Karniadakis, "Inflow/outflow boundary conditions for particle-based blood flow simulations: application to arterial bifurcations and trees," *PLoS computational biology,* vol. 11, no. 8, p. e1004410, 2015.
[165] X. Li, A. S. Popel, and G. E. Karniadakis, "Blood-plasma separation in Y-shaped bifurcating microfluidic channels: a dissipative particle dynamics simulation study," *PhysBio,* vol. 9, no. 2, pp. 026010-026010, 2012, doi: 10.1088/1478-3975/9/2/026010.
[166] C. Bächer *et al.*, "Antimargination of microparticles and platelets in the vicinity of branching vessels," *Biophysical journal,* vol. 115, no. 2, pp. 411-425, 2018.
[167] M. Ishii, "Thermo-fluid dynamic theory of two-phase flow," *NASA Sti/recon Technical Report A,* vol. 75, p. 29657, 1975.
[168] G. B. Wallis, *One-dimensional two-phase flow*. Courier Dover Publications, 2020.

[169] D. A. Drew and S. L. Passman, *Theory of multicomponent fluids*. Springer Science & Business Media, 2006.
[170] Siemens Digital Industries Software, "Eulerian Multiphase (EMP) Flow," in *Simcenter STAR-CCM+ User Guide, Version 18.02.010-R8Pressure Outlet*, 18.02.010 ed.: Siemens, 2023.
[171] Siemens Digital Industries Software, "Particulate Flows," in *Simcenter STAR-CCM+ User Guide, Version 18.02.010-R8Pressure Outlet*, 18.02.010 ed.: Siemens, 2023.
[172] Siemens Digital Industries Software, "Momentum Transfer," in *Simcenter STAR-CCM+ User Guide, Version 18.02.010-R8Pressure Outlet*, 18.02.010 ed.: Siemens, 2023.
[173] Siemens Digital Industries Software, "Segregated Flow Solver," in *Simcenter STAR-CCM+ User Guide, Version 18.02.010-R8Pressure Outlet*, 18.02.010 ed.: Siemens, 2023.
[174] Siemens Digital Industries Software, "Boundary Type Reference," in *Simcenter STAR-CCM+ User Guide, Version 18.02.010-R8Pressure Outlet*, 18.02.010 ed.: Siemens, 2023.
[175] A. Pries, T. W. Secomb, and P. Gaehtgens, "Biophysical aspects of blood flow in the microvasculature," *Cardiovascular research,* vol. 32, no. 4, pp. 654-667, 1996.
[176] A. Krogh, "Studies on the physiology of capillaries: II. The reactions to local stimuli of the blood-vessels in the skin and web of the frog," *The Journal of physiology,* vol. 55, no. 5-6, p. 412, 1921.
[177] K. Svanes and B. Zweifach, "Variations in small blood vessel hematocrits produced in hypothermic rats by micro-occlusion," *Microvascular Research,* vol. 1, no. 2, pp. 210-220, 1968.
[178] Y.-C. Fung, "Stochastic flow in capillary blood vessels," *Microvascular research,* vol. 5, no. 1, pp. 34-48, 1973.
[179] T. W. Secomb, B. Styp-Rekowska, and A. R. Pries, "Two-dimensional simulation of red blood cell deformation and lateral migration in microvessels," *Annals of biomedical engineering,* vol. 35, pp. 755-765, 2007.
[180] B. Namgung, L. H. Liang, and S. Kim, "Physiological significance of cell-free layer and experimental determination of its width in microcirculatory vessels," in *Visualization and Simulation of Complex Flows in Biomedical Engineering*: Springer, 2013, pp. 75-87.
[181] G. R. Cokelet and H. L. Goldsmith, "Decreased hydrodynamic resistance in the two-phase flow of blood through small vertical tubes at low flow rates," *Circulation research,* vol. 68, no. 1, pp. 1-17, 1991.
[182] P. K. Ong, S. Jain, and S. Kim, "Spatio-temporal variations in cell-free layer formation near bifurcations of small arterioles," *Microvascular research,* vol. 83, no. 2, pp. 118-125, 2012.
[183] X. Han *et al.*, "In vivo two-photon imaging reveals acute cerebral vascular spasm and microthrombosis after mild traumatic brain injury in mice," *Frontiers in neuroscience,* vol. 14, p. 210, 2020.
[184] J. L. Fan *et al.*, "High-speed volumetric two-photon fluorescence imaging of neurovascular dynamics," *Nature communications,* vol. 11, no. 1, p. 6020, 2020.
[185] C. D. Murray, "The physiological principle of minimum work: I. The vascular system and the cost of blood volume," *Proceedings of the National Academy of Sciences,* vol. 12, no. 3, pp. 207-214, 1926.
[186] M. Zamir, "Nonsymmetrical bifurcations in arterial branching," *The Journal of general physiology,* vol. 72, no. 6, pp. 837-845, 1978.

[187] A. Pries, T. W. Secomb, and P. Gaehtgens, "Structure and hemodynamics of microvascular networks: heterogeneity and correlations," *American Journal of Physiology-Heart and Circulatory Physiology,* vol. 269, no. 5, pp. H1713-H1722, 1995.
[188] R. I. Grant, D. A. Hartmann, R. G. Underly, A.-A. Berthiaume, N. R. Bhat, and A. Y. Shih, "Organizational hierarchy and structural diversity of microvascular pericytes in adult mouse cortex," *Journal of Cerebral Blood Flow & Metabolism,* vol. 39, no. 3, pp. 411-425, 2019.
[189] T. L. Haas and B. R. Duling, "Morphology favors an endothelial cell pathway for longitudinal conduction within arterioles," *Microvascular research,* vol. 53, no. 2, pp. 113-120, 1997.
[190] Y. Imai, T. Omori, Y. Shimogonya, T. Yamaguchi, and T. Ishikawa, "Numerical methods for simulating blood flow at macro, micro, and multi scales," *Journal of biomechanics,* vol. 49, no. 11, pp. 2221-2228, 2016.
[191] S. Yamakawa and K. Shimada, "Converting a tetrahedral mesh to a prism-tetrahedral hybrid mesh for FEM accuracy and efficiency," in *Proceedings of the 2008 ACM symposium on Solid and physical modeling*, 2008, pp. 287-294.
[192] T. J. Baker, "Mesh generation: Art or science?," *Progress in aerospace sciences,* vol. 41, no. 1, pp. 29-63, 2005.
[193] O. Yalcin, D. Ortiz, A. T. Williams, P. C. Johnson, and P. Cabrales, "Perfusion pressure and blood flow determine microvascular apparent viscosity," *Experimental physiology,* vol. 100, no. 8, pp. 977-987, 2015.
[194] L. Zarrinkoob *et al.*, "Aging alters the dampening of pulsatile blood flow in cerebral arteries," *Journal of Cerebral Blood Flow & Metabolism,* vol. 36, no. 9, pp. 1519-1527, 2016.
[195] S. Kim, S. Yang, and D. Lim, "Effect of dextran on rheological properties of rat blood," *Journal of mechanical science and technology,* vol. 23, pp. 868-873, 2009.
[196] Y. Tomonaga, M. S. Brennwald, D. M. Livingstone, G. Tomonaga, and R. Kipfer, "Determination of natural in vivo noble-gas concentrations in human blood," *Plos one,* vol. 9, no. 5, p. e96972, 2014.
[197] Y. I. Cho and K. R. Kensey, "Effects of the non-Newtonian viscosity of blood on flows in a diseased arterial vessel. Part 1: Steady flows," *Biorheology,* vol. 28, no. 3-4, pp. 241-262, 1991.
[198] M. Diez-Silva, M. Dao, J. Han, C.-T. Lim, and S. Suresh, "Shape and biomechanical characteristics of human red blood cells in health and disease," *MRS bulletin,* vol. 35, no. 5, pp. 382-388, 2010.
[199] S. Kim, R. L. Kong, A. S. Popel, M. Intaglietta, and P. C. Johnson, "Temporal and spatial variations of cell-free layer width in arterioles," *American Journal of Physiology-Heart and Circulatory Physiology,* vol. 293, no. 3, pp. H1526-H1535, 2007.
[200] Siemens Digital Industries Software, "Drag," in *Simcenter STAR-CCM+ User Guide, Version 18.02.010-R8Pressure Outlet*, 18.02.010 ed.: Siemens, 2023.
[201] G. G. Stokes, "On the effect of the internal friction of fluids on the motion of pendulums," 1851.
[202] J. Richardson and W. Zaki, "Sedimentation and fluidisation: Part I," *Chemical Engineering Research and Design,* vol. 75, pp. S82-S100, 1997.
[203] S. Connolly, D. Newport, and K. McGourty, "The mechanical responses of advecting cells in confined flow," *Biomicrofluidics,* vol. 14, no. 3, 2020.
[204] W. H. Graf, *Hydraulics of sediment transport*. Water Resources Publication, 1984.

[205] O. Khare, A. H. Huijgen, M. Davids, J. Kuipers, and M. W. Baltussen, "A closure based on Direct Numerical Simulations for virtual mass force in dense liquid-solid systems," *Chemical Engineering Science,* p. 122452, 2025.
[206] Siemens Digital Industries Software, "Multiphase Flow," in *Simcenter STAR-CCM+ User Guide, Version 18.02.010-R8Pressure Outlet*, 18.02.010 ed.: Siemens, 2023.
[207] H. K. Versteeg and W. Malalasekera, *An Introduction to Computational Fluid Dynamics: The Finite Volume Method*. 1995.
[208] Siemens Digital Industries Software, "(Pseudo-) Time-Marching Approach," in *Simcenter STAR-CCM+ User Guide, Version 18.02.010-R8Pressure Outlet*, 2003.
[209] V. Leble *et al.*, "Asymmetry of red blood cell motions in a microchannel with a diverging and converging bifurcation," *Biomicrofluidics,* vol. 5, no. 4, 2011.
[210] X. Hu *et al.*, "A time-dependent power law viscosity model and its application in modelling semi-solid die casting of 319s alloy," *Acta Materialia,* vol. 124, pp. 410-420, 2017.
[211] K. Yasuda, "Investigation of the analogies between viscometric and linear viscoelastic properties of polystyrene fluids," Massachusetts Institute of Technology, 1979.
[212] M. Manjunatha and M. Singh, "Digital blood flow analysis from microscopic images of mesenteric microvessel with multiple branching," *Clinical hemorheology and microcirculation,* vol. 27, no. 2, pp. 91-106, 2002.
[213] J. M. Sherwood, D. Holmes, E. Kaliviotis, and S. Balabani, "Spatial distributions of red blood cells significantly alter local haemodynamics," *PloS one,* vol. 9, no. 6, p. e100473, 2014.
[214] J. Zhang *et al.*, "Fundamentals and applications of inertial microfluidics: A review," *Lab on a Chip,* vol. 16, no. 1, pp. 10-34, 2016.
[215] E. S. Asmolov, "The inertial lift on a spherical particle in a plane Poiseuille flow at large channel Reynolds number," *Journal of fluid mechanics,* vol. 381, pp. 63-87, 1999.
[216] P. G. Saffman, "The lift on a small sphere in a slow shear flow," *Journal of fluid mechanics,* vol. 22, no. 2, pp. 385-400, 1965.
[217] T. M. Geislinger and T. Franke, "Hydrodynamic lift of vesicles and red blood cells in flow—from Fåhræus & Lindqvist to microfluidic cell sorting," *Advances in colloid and interface science,* vol. 208, pp. 161-176, 2014.
[218] M. Salame and M. Fenech, "A Two-Phase Core-Plasma Model for Microvascular Blood Flow: Comparative Analysis of Hemodynamic Models," *bioRxiv,* p. 2025.06. 25.661657, 2025.
[219] R. Mehri, C. Mavriplis, and M. Fenech, "Red blood cell aggregates and their effect on non-Newtonian blood viscosity at low hematocrit in a two-fluid low shear rate microfluidic system," *Plos one,* vol. 13, no. 7, p. e0199911, 2018.
[220] S. A. Mahrous, N. A. C. Sidik, and K. M. Saqr, "Newtonian and non-Newtonian CFD models of intracranial aneurysm: a review," *CFD Letters,* vol. 12, no. 1, pp. 62-86, 2020.
[221] A. Marcinkowska-Gapińska, J. Gapinski, W. Elikowski, F. Jaroszyk, and L. Kubisz, "Comparison of three rheological models of shear flow behavior studied on blood samples from post-infarction patients," *Medical & biological engineering & computing,* vol. 45, no. 9, pp. 837-844, 2007.
[222] B. Behir, A. Benslimane, H. Mehdaoui, and B. Mehdi, "Impact of hematocrit on pulsatile blood flow in stenosed arteries: a computational study in healthy, diabetic, and anemic models," *Computer Methods in Biomechanics and Biomedical Engineering,* vol. 28, no. 6, pp. 764-776, 2025.

[223] L. Méndez-Mora *et al.*, "Microrheometer for biofluidic analysis: Electronic detection of the fluid-front advancement," *Micromachines,* vol. 12, no. 6, p. 726, 2021.
[224] P. Cabrales, J. Martini, M. Intaglietta, and A. G. Tsai, "Blood viscosity maintains microvascular conditions during normovolemic anemia independent of blood oxygen-carrying capacity," *American Journal of Physiology-Heart and Circulatory Physiology,* vol. 291, no. 2, pp. H581-H590, 2006.
[225] R. E. Wells and E. W. Merrill, "Influence of flow properties of blood upon viscosity-hematocrit relationships," *The Journal of clinical investigation,* vol. 41, no. 8, pp. 1591-1598, 1962.
[226] S. Subramaniam, "Lagrangian–Eulerian methods for multiphase flows," *Progress in Energy and Combustion Science,* vol. 39, no. 2-3, pp. 215-245, 2013.
[227] C. Porcaro and M. Saeedipour, "Hemolysis prediction in bio-microfluidic applications using resolved CFD-DEM simulations," *Computer Methods and Programs in Biomedicine,* vol. 231, p. 107400, 2023.
[228] S. Cho, B. Namgung, H. S. Kim, H. L. Leo, and S. Kim, "Effect of erythrocyte aggregation at pathological levels on NO/O2 transport in small arterioles," *Clinical hemorheology and microcirculation,* vol. 59, no. 2, pp. 163-175, 2015.
[229] Y. C. Ng, B. Namgung, and S. Kim, "Two-dimensional transient model for prediction of arteriolar NO/O2 modulation by spatiotemporal variations in cell-free layer width," *Microvascular Research,* vol. 97, pp. 88-97, 2015.
[230] J. S. Olson, "Lessons learned from 50 years of hemoglobin research: unstirred and cell-free layers, electrostatics, baseball gloves, and molten globules," *Antioxidants & redox signaling,* vol. 32, no. 4, pp. 228-246, 2020.
[231] O. Yalcin, P. Ulker, U. Yavuzer, H. J. Meiselman, and O. K. Baskurt, "Nitric oxide generation by endothelial cells exposed to shear stress in glass tubes perfused with red blood cell suspensions: role of aggregation," *American Journal of Physiology-Heart and Circulatory Physiology,* vol. 294, no. 5, pp. H2098-H2105, 2008.
[232] W. D. Haselden, R. T. Kedarasetti, and P. J. Drew, "Spatial and temporal patterns of nitric oxide diffusion and degradation drive emergent cerebrovascular dynamics," *PLoS computational biology,* vol. 16, no. 7, p. e1008069, 2020.
[233] P. K. Ong, S. Jain, and S. Kim, "Modulation of NO bioavailability by temporal variation of the cell-free layer width in small arterioles," *Annals of biomedical engineering,* vol. 39, no. 3, pp. 1012-1023, 2011.
[234] B. Das, P. Johnson, and A. Popel, "Effect of nonaxisymmetric hematocrit distribution on non-Newtonian blood flow in small tubes," *Biorheology,* vol. 35, no. 1, pp. 69-87, 1998.
[235] R. Busse and I. Fleming, "Regulation of endothelium-derived vasoactive autacoid production by hemodynamic forces," *Trends in pharmacological sciences,* vol. 24, no. 1, pp. 24-29, 2003.
[236] J. C. Liao, T. W. Hein, M. W. Vaughn, K.-T. Huang, and L. Kuo, "Intravascular flow decreases erythrocyte consumption of nitric oxide," *Proceedings of the National Academy of Sciences,* vol. 96, no. 15, pp. 8757-8761, 1999.
[237] S. Kishimoto *et al.*, "Hematocrit, hemoglobin and red blood cells are associated with vascular function and vascular structure in men," *Scientific reports,* vol. 10, no. 1, p. 11467, 2020.
[238] N. Maeda, Y. Suzuki, J. Tanaka, and N. Tateishi, "Erythrocyte flow and elasticity of microvessels evaluated by marginal cell-free layer and flow resistance," *American Journal of Physiology-Heart and Circulatory Physiology,* vol. 271, no. 6, pp. H2454-H2461, 1996.

[239] D. Katanov, G. Gompper, and D. A. Fedosov, "Microvascular blood flow resistance: Role of red blood cell migration and dispersion," *Microvascular research,* vol. 99, pp. 57-66, 2015.
[240] J. O. Barber, J. P. Alberding, J. M. Restrepo, and T. W. Secomb, "Simulated two-dimensional red blood cell motion, deformation, and partitioning in microvessel bifurcations," *Annals of biomedical engineering,* vol. 36, pp. 1690-1698, 2008.
[241] R. D. Jäggi, R. Sandoz, and C. S. Effenhauser, "Microfluidic depletion of red blood cells from whole blood in high-aspect-ratio microchannels," *Microfluidics and Nanofluidics,* vol. 3, no. 1, pp. 47-53, 2007.
[242] X. Li, A. S. Popel, and G. E. Karniadakis, "Blood–plasma separation in Y-shaped bifurcating microfluidic channels: a dissipative particle dynamics simulation study," *Physical biology,* vol. 9, no. 2, p. 026010, 2012.
[243] A. Pskowski, P. Bagchi, and J. D. Zahn, "Investigation of red blood cell partitioning in an in vitro microvascular bifurcation," *Artificial organs,* vol. 45, no. 9, pp. 1083-1096, 2021.
[244] V. Doyeux, T. Podgorski, S. Peponas, M. Ismail, and G. Coupier, "Spheres in the vicinity of a bifurcation: elucidating the Zweifach–Fung effect," *Journal of Fluid Mechanics,* vol. 674, pp. 359-388, 2011.
[245] K. Chandran, I. S. Dalal, K. Tatsumi, and K. Muralidhar, "Numerical simulation of blood flow modeled as a fluid-particulate mixture," *Journal of Non-Newtonian Fluid Mechanics,* vol. 285, p. 104383, 2020.
[246] A. Pskowski, P. Bagchi, and J. D. Zahn, "Hematocrit skewness along sequential bifurcations within a microfluidic network induces significant changes in downstream red blood cell partitioning," *Biomicrofluidics,* vol. 16, no. 6, 2022.
[247] A. Pries, K. Ley, M. Claassen, and P. Gaehtgens, "Red cell distribution at microvascular bifurcations," *Microvascular research,* vol. 38, no. 1, pp. 81-101, 1989.
[248] G. Schmid-Schönbein, R. Skalak, S. Usami, and S. Chien, "Cell distribution in capillary networks," *Microvascular research,* vol. 19, no. 1, pp. 18-44, 1980.
[249] T. Hyakutake *et al.*, "In vitro study on the partitioning of red blood cells using a microchannel network," *Microvascular Research,* vol. 140, p. 104281, 2022.
[250] E. D. McGAHREN, K. Dora, D. N. Damon, and B. R. Duling, "A test of the role of flow-dependent dilation in arteriolar responses to occlusion," *American Journal of Physiology-Heart and Circulatory Physiology,* vol. 272, no. 2, pp. H714-H721, 1997.
[251] J. C. Frisbee, R. J. Roman, J. R. Falck, J. R. Linderman, and J. H. Lombard, "Impairment of flow-induced dilation of skeletal muscle arterioles with elevated oxygen in normotensive and hypertensive rats," *Microvascular research,* vol. 60, no. 1, pp. 37-48, 2000.
[252] M. Jacob, D. Chappell, and B. F. Becker, "Regulation of blood flow and volume exchange across the microcirculation," *Critical care,* vol. 20, no. 1, p. 319, 2016.
[253] S. Trzeciak and E. P. Rivers, "Clinical manifestations of disordered microcirculatory perfusion in severe sepsis," *Critical Care,* vol. 9, no. Suppl 4, p. S20, 2005.
[254] W. M. Bayliss, "On the local reactions of the arterial wall to changes of internal pressure," *The Journal of physiology,* vol. 28, no. 3, p. 220, 1902.
[255] E. Saldívar, P. Cabrales, A. G. Tsai, and M. Intaglietta, "Microcirculatory changes during chronic adaptation to hypoxia," *American Journal of Physiology-Heart and Circulatory Physiology,* vol. 285, no. 5, pp. H2064-H2071, 2003.
[256] L. Li *et al.*, "Hormone regulation in testicular development and function," *International Journal of Molecular Sciences,* vol. 25, no. 11, p. 5805, 2024.

[257] S. Yoshida, M. Sukeno, and Y.-i. Nabeshima, "A vasculature-associated niche for undifferentiated spermatogonia in the mouse testis," *science,* vol. 317, no. 5845, pp. 1722-1726, 2007.
[258] H. Lan, A. Updegrove, N. M. Wilson, G. D. Maher, S. C. Shadden, and A. L. Marsden, "A re-engineered software interface and workflow for the open-source simvascular cardiovascular modeling package," *Journal of biomechanical engineering,* vol. 140, no. 2, p. 024501, 2018.
[259] L. Antiga and D. A. Steinman, "Robust and objective decomposition and mapping of bifurcating vessels," *IEEE transactions on medical imaging,* vol. 23, no. 6, pp. 704-713, 2004.
[260] H.-C. Han, "Twisted blood vessels: symptoms, etiology and biomechanical mechanisms," *Journal of vascular research,* vol. 49, no. 3, pp. 185-197, 2012.
[261] M. Li *et al.*, "Non-invasive ultrasound localization microscopy (ULM) in azoospermia: connecting testicular microcirculation to spermatogenic functions," *Theranostics,* vol. 14, no. 13, p. 4967, 2024.
[262] M. A. A. Pour and W. Mao, "Numerical Investigation of Hemodynamic Factors in Cellular Blood Flow: Insights From Curved Microvessels," *Microcirculation,* vol. 32, no. 4, p. e70013, 2025.
[263] P. Balogh and P. Bagchi, "Direct numerical simulation of cellular-scale blood flow in 3D microvascular networks," *Biophysical journal,* vol. 113, no. 12, pp. 2815-2826, 2017.
[264] T. Niizawa *et al.*, "Spatiotemporal analysis of blood plasma and blood cell flow fluctuations of cerebral microcirculation in anesthetized rats," *Journal of Cerebral Blood Flow & Metabolism,* vol. 43, no. 1, pp. 138-152, 2023.
[265] A. Gloria, A. Carluccio, L. Wegher, D. Robbe, C. Valorz, and A. Contri, "Pulse wave Doppler ultrasound of testicular arteries and their relationship with semen characteristics in healthy bulls," *Journal of Animal Science and Biotechnology,* vol. 9, no. 1, p. 14, 2018.
[266] M. B. de Souza *et al.*, "Regional differences of testicular artery blood flow in post pubertal and pre-pubertal dogs," *BMC veterinary research,* vol. 11, no. 1, p. 47, 2015.
[267] M. Zouache, I. Eames, and P. Luthert, "Blood flow in the choriocapillaris," *Journal of Fluid Mechanics,* vol. 774, pp. 37-66, 2015.
[268] M. Ooms *et al.*, "Blood pressure and microvascular free flap perfusion in head and neck reconstruction–a retrospective analysis," *Oral and Maxillofacial Surgery,* vol. 29, no. 1, p. 85, 2025.
[269] M. M. N. Hossain, N. W. Hu, A. Kazempour, W. L. Murfee, and P. Balogh, "Hemodynamic characteristics of a tortuous microvessel using high‐fidelity red blood cell resolved simulations," *Microcirculation,* vol. 31, no. 7, p. e12875, 2024.
[270] T. E. Sweeney, J. S. Rozum, C. Desjardins, and R. W. Gore, "Microvascular pressure distribution in the hamster testis," *American Journal of Physiology-Heart and Circulatory Physiology,* vol. 260, no. 5, pp. H1581-H1589, 1991.
[271] R. Hu *et al.*, "Microfluidic analysis of pressure drop and flow behavior in hypertensive micro vessels," *Biomedical Microdevices,* vol. 17, no. 3, p. 60, 2015.
[272] N.-W. Hu *et al.*, "Identification of shear stress as a potential vasoconduction signal across microvascular networks," *Microvascular Research,* p. 104855, 2025.
[273] W. S. Kamoun *et al.*, "Simultaneous measurement of RBC velocity, flux, hematocrit and shear rate in vascular networks," *Nature methods,* vol. 7, no. 8, pp. 655-660, 2010.

[274] S. S. Segal, "Regulation of blood flow in the microcirculation," *Microcirculation,* vol. 12, no. 1, pp. 33-45, 2005.
[275] F. Goirand, T. Le Borgne, and S. Lorthois, "Network-driven anomalous transport is a fundamental component of brain microvascular dysfunction," *Nature communications,* vol. 12, no. 1, p. 7295, 2021.
[276] P. K. Ong, S. Cho, B. Namgung, and S. Kim, "Effects of cell-free layer formation on NO/O2 bioavailability in small arterioles," *Microvascular Research,* vol. 83, no. 2, pp. 168-177, 2012.
[277] S. Sakadžić *et al.*, "Large arteriolar component of oxygen delivery implies a safe margin of oxygen supply to cerebral tissue," *Nature communications,* vol. 5, no. 1, p. 5734, 2014.
[278] M. Moeini *et al.*, "Compromised microvascular oxygen delivery increases brain tissue vulnerability with age," *Scientific reports,* vol. 8, no. 1, p. 8219, 2018.
[279] O. Azu, "Testicular morphology in spontaneously hypertensive rat model: oxidant status and stereological implications," *Andrologia,* vol. 47, no. 2, pp. 123-137, 2015.
[280] A. Bergh, O. Collin, and E. Lissbrant, "Effects of acute graded reductions in testicular blood flow on testicular morphology in the adult rat," *Biology of reproduction,* vol. 64, no. 1, pp. 13-20, 2001.
[281] M. A. Hassan *et al.*, "Morphological and ultrasonographic characterization of the three zones of supratesticular region of testicular artery in Assaf rams," *Scientific Reports,* vol. 12, no. 1, p. 8334, 2022.
[282] E. Becker, H. Prillaman, and T. Turner, "Microvascular blood flow is altered after repair of testicular torsion in the rat," *The Journal of urology,* vol. 157, no. 4, pp. 1493-1498, 1997.
[283] A. Pries, B. Reglin, and T. Secomb, "Structural adaptation of microvascular networks: functional roles of adaptive responses," *American Journal of Physiology-Heart and Circulatory Physiology,* vol. 281, no. 3, pp. H1015-H1025, 2001.
[284] J. M. Ortiz-Rodriguez *et al.*, "Pulse Doppler ultrasound as a tool for the diagnosis of chronic testicular dysfunction in stallions," *PLoS One,* vol. 12, no. 5, p. e0175878, 2017.
[285] N. M. Tsoukias, D. Goldman, A. Vadapalli, R. N. Pittman, and A. S. Popel, "A computational model of oxygen delivery by hemoglobin-based oxygen carriers in three-dimensional microvascular networks," *Journal of theoretical biology,* vol. 248, no. 4, pp. 657-674, 2007.
[286] A. A. Mendelson *et al.*, "Capillary module haemodynamics and mechanisms of blood flow regulation in skeletal muscle capillary networks: Experimental and computational analysis," *The Journal of Physiology,* vol. 600, no. 8, pp. 1867-1888, 2022.
[287] P. M. Rasmussen, T. W. Secomb, and A. R. Pries, "Modeling the hematocrit distribution in microcirculatory networks: a quantitative evaluation of a phase separation model," *Microcirculation,* vol. 25, no. 3, p. e12445, 2018.
[288] D. Liu, N. Wood, N. Witt, A. Hughes, S. Thom, and X. Xu, "Computational analysis of oxygen transport in the retinal arterial network," *Current eye research,* vol. 34, no. 11, pp. 945-956, 2009.
[289] W. H. Reinhart, N. Z. Piety, and S. S. Shevkoplyas, "Influence of feeding hematocrit and perfusion pressure on hematocrit reduction (Fåhraeus effect) in an artificial microvascular network," *Microcirculation,* vol. 24, no. 8, p. e12396, 2017.
[290] S. Milanovic, K. Shaw, C. Hall, and S. Payne, "Investigating the role of pericytes in cerebral autoregulation: a modeling study," *Physiological Measurement,* vol. 42, no. 5, p. 054003, 2021.

[291] K. Pappelis, L. Choritz, and N. M. Jansonius, "Microcirculatory model predicts blood flow and autoregulation range in the human retina: in vivo investigation with laser speckle flowgraphy," *American Journal of Physiology-Heart and Circulatory Physiology,* vol. 319, no. 6, pp. H1253-H1273, 2020.
[292] P. M. Rasmussen, "Blood flow simulation and uncertainty quantification in extensive microvascular networks: Application to brain cortical networks," *Microcirculation,* vol. 32, no. 7, p. e70027, 2025.
[293] C. A. Bondy and T. S. C. S. Group, "Care of girls and women with Turner syndrome: a guideline of the Turner Syndrome Study Group," *The Journal of Clinical Endocrinology & Metabolism,* vol. 92, no. 1, pp. 10-25, 2007.
[294] A. Cockwell, M. MacKenzie, S. Youings, and P. Jacobs, "A cytogenetic and molecular study of a series of 45, X fetuses and their parents," *Journal of medical genetics,* vol. 28, no. 3, pp. 151-155, 1991.
[295] J. Nielsen and M. Wohlert, "Chromosome abnormalities found among 34910 newborn children: results from a 13-year incidence study in Århus, Denmark," *Human genetics,* vol. 87, no. 1, pp. 81-83, 1991.
[296] V. P. Sybert, "Cardiovascular malformations and complications in Turner syndrome," *Pediatrics,* vol. 101, no. 1, pp. e11-e11, 1998.
[297] L. Mazzanti, E. Cacciari, and I. S. G. f. T. Syndrome, "Congenital heart disease in patients with Turner's syndrome," *The Journal of pediatrics,* vol. 133, no. 5, pp. 688-692, 1998.
[298] T. M. Völkl, K. Degenhardt, A. Koch, D. Simm, H. G. Dörr, and H. Singer, "Cardiovascular anomalies in children and young adults with Ullrich‐Turner syndrome—the erlangen experience," *Clinical Cardiology: An International Indexed and Peer‐Reviewed Journal for Advances in the Treatment of Cardiovascular Disease,* vol. 28, no. 2, pp. 88-92, 2005.
[299] M. Silberbach *et al.*, "Cardiovascular health in Turner syndrome: a scientific statement from the American Heart Association," *Circulation: Genomic and Precision Medicine,* vol. 11, no. 10, p. e000048, 2018.
[300] I. Gutmark‐Little and P. F. Backeljauw, "Cardiac magnetic resonance imaging in T urner syndrome," *Clinical endocrinology,* vol. 78, no. 5, pp. 646-658, 2013.
[301] V. B. Ho *et al.*, "Major vascular anomalies in Turner syndrome: prevalence and magnetic resonance angiographic features," *Circulation,* vol. 110, no. 12, pp. 1694-1700, 2004.
[302] A. V. B. d. Castro *et al.*, "Cardiovascular assessment of patients with Ullrich-Turner's Syndrome on Doppler echocardiography and magnetic resonance imaging," *Arquivos Brasileiros de Cardiologia,* vol. 78, pp. 55-58, 2002.
[303] H. K. Kim *et al.*, "Cardiovascular anomalies in Turner syndrome: spectrum, prevalence, and cardiac MRI findings in a pediatric and young adult population," *American Journal of Roentgenology,* vol. 196, no. 2, pp. 454-460, 2011.
[304] K. De Groote *et al.*, "Arterial hypertension in Turner syndrome: a review of the literature and a practical approach for diagnosis and treatment," *Journal of Hypertension,* vol. 33, no. 7, pp. 1342-1351, 2015.
[305] B. Donato and M. J. Ferreira, "Cardiovascular risk in Turner syndrome," *Revista portuguesa de cardiologia,* vol. 37, no. 7, pp. 607-621, 2018.
[306] W. Tan, K. Madhavan, K. S. Hunter, D. Park, and K. R. Stenmark, "Vascular stiffening in pulmonary hypertension: cause or consequence?(2013 Grover Conference series)," *Pulmonary circulation,* vol. 4, no. 4, pp. 560-580, 2014.

[307] N. Galie *et al.*, "Guidelines on diagnosis and treatment of pulmonary arterial hypertension: The Task Force on Diagnosis and Treatment of Pulmonary Arterial Hypertension of the European Society of Cardiology," *European heart journal,* vol. 25, no. 24, pp. 2243-2278, 2004.
[308] J. D. Humphrey, "Mechanisms of arterial remodeling in hypertension: coupled roles of wall shear and intramural stress," *Hypertension,* vol. 52, no. 2, pp. 195-200, 2008.
[309] F. Capuano, Y.-H. Loke, and E. Balaras, "Blood flow dynamics at the pulmonary artery bifurcation," *Fluids,* vol. 4, no. 4, p. 190, 2019.
[310] L. Louvelle, M. Doyle, G. Van Arsdell, and C. Amon, "The effect of geometric and hemodynamic parameters on blood flow efficiency in repaired tetralogy of Fallot patients," *Annals of Biomedical Engineering,* vol. 49, no. 9, pp. 2297-2310, 2021.
[311] H. N. Ntsinjana *et al.*, "3D morphometric analysis of the arterial switch operation using in vivo MRI data," *Clinical Anatomy,* vol. 27, no. 8, pp. 1212-1222, 2014.
[312] M.-J. Chern, M.-T. Wu, and S.-W. Her, "Numerical study for blood flow in pulmonary arteries after repair of tetralogy of Fallot," *Computational and mathematical methods in medicine,* vol. 2012, no. 1, p. 198108, 2012.
[313] M. Boumpouli, E. L. Sauvage, C. Capelli, S. Schievano, and A. Kazakidi, "Characterization of flow dynamics in the pulmonary bifurcation of patients with repaired tetralogy of Fallot: a computational approach," *Frontiers in Cardiovascular Medicine,* vol. 8, p. 703717, 2021.
[314] M. Boumpouli, S. M. Black, and A. Kazakidi, "Computational analysis of blood flow in healthy pulmonary arteries in comparison to repaired Tetralogy of Fallot results: a small cohort study," *Fluids,* vol. 9, no. 4, p. 85, 2024.
[315] M. Sabry *et al.*, "Vortex duration in the pulmonary artery does not depend on vascular Afterload: a sign of adaptation?," *Computers in Biology and Medicine,* vol. 196, p. 110717, 2025.
[316] L. Johnston, R. Allen, A. Mason, and A. Kazakidi, "Morphological characterisation of pediatric Turner syndrome aortae: Insights from a small cohort study," *Medical Engineering & Physics,* vol. 120, p. 104045, 2023.
[317] M. Dong *et al.*, "Image-based scaling laws for somatic growth and pulmonary artery morphometry from infancy to adulthood," *American Journal of Physiology-Heart and Circulatory Physiology,* vol. 319, no. 2, pp. H432-H442, 2020.
[318] N. M. Wilson, A. K. Ortiz, and A. B. Johnson, "The vascular model repository: a public resource of medical imaging data and blood flow simulation results," *Journal of medical devices,* vol. 7, no. 4, p. 040923, 2013.
[319] G. Biglino, C. Capelli, J. Bruse, G. M. Bosi, A. M. Taylor, and S. Schievano, "Computational modelling for congenital heart disease: how far are we from clinical translation?," *Heart,* vol. 103, no. 2, pp. 98-103, 2017.
[320] A. Updegrove, N. M. Wilson, J. Merkow, H. Lan, A. L. Marsden, and S. C. Shadden, "SimVascular: an open source pipeline for cardiovascular simulation," *Annals of biomedical engineering,* vol. 45, no. 3, pp. 525-541, 2017.
[321] A. J. Barker *et al.*, "Four‐dimensional flow assessment of pulmonary artery flow and wall shear stress in adult pulmonary arterial hypertension: Results from two institutions," *Magnetic resonance in medicine,* vol. 73, no. 5, pp. 1904-1913, 2015.
[322] F. R. Menter, M. Kuntz, and R. Langtry, "Ten years of industrial experience with the SST turbulence model," *Turbulence, heat and mass transfer,* vol. 4, no. 1, pp. 625-632, 2003.

[323] K. H. Mortensen, D. Gopalan, B. L. Nørgaard, N. H. Andersen, and C. H. Gravholt, "Multimodality cardiac imaging in Turner syndrome," *Cardiology in the Young,* vol. 26, no. 5, pp. 831-841, 2016.
[324] C. Devlin *et al.*, "Patient-specific 3D in vitro modeling and fluid dynamic analysis of primary pulmonary vein stenosis," *Frontiers in Cardiovascular Medicine,* vol. 11, p. 1432784, 2024.
[325] H. Baumgartner *et al.*, "2020 ESC Guidelines for the management of adult congenital heart disease: The Task Force for the management of adult congenital heart disease of the European Society of Cardiology (ESC). Endorsed by: Association for European Paediatric and Congenital Cardiology (AEPC), International Society for Adult Congenital Heart Disease (ISACHD)," *European heart journal,* vol. 42, no. 6, pp. 563-645, 2021.
[326] M. H. Yacoub *et al.*, "Criss-cross pulmonary arteries in common arterial trunk–Implications to management and outcome," *International Journal of Cardiology Congenital Heart Disease,* vol. 13, p. 100471, 2023.
[327] G. Mastromoro *et al.*, "Crossed pulmonary arteries: an underestimated cardiovascular variant with a strong association with genetic syndromes—a report of 74 cases with systematic review of the literature," *American Journal of Medical Genetics Part A,* vol. 188, no. 8, pp. 2351-2359, 2022.
[328] J. Chen and Y. Feng, "A rare case of crossed pulmonary arteries in an infant-case report," *Journal of Cardiothoracic Surgery,* vol. 8, no. 1, p. 79, 2013.
[329] A. A. Alhassan *et al.*, "A neonate with crossed pulmonary arteries: a case report and literature review of 115 cases worldwide," *Cardiology in the Young,* vol. 32, no. 8, pp. 1196-1201, 2022.
[330] B. S. Ebrahimi, H. Kumar, M. H. Tawhai, K. S. Burrowes, E. A. Hoffman, and A. R. Clark, "Simulating multi-scale pulmonary vascular function by coupling computational fluid dynamics with an anatomic network model," *Frontiers in Network Physiology,* vol. 2, p. 867551, 2022.
[331] I. Gutmark-Little, K. N. Hor, J. Cnota, W. M. Gottliebson, and P. F. Backeljauw, "Partial anomalous pulmonary venous return is common in Turner syndrome," *Journal of Pediatric Endocrinology & Metabolism,* vol. 25, 2012.
[332] N. R. Pillalamarri, S. Piskin, S. S. Patnaik, S. Murali, and E. A. Finol, "Patient-specific computational analysis of hemodynamics in adult pulmonary hypertension," *Annals of biomedical engineering,* vol. 49, no. 12, pp. 3465-3480, 2021.
[333] Y. Bazilevs, M.-C. Hsu, D. J. Benson, S. Sankaran, and A. L. Marsden, "Computational fluid–structure interaction: methods and application to a total cavopulmonary connection," *Computational Mechanics,* vol. 45, no. 1, pp. 77-89, 2009.
[334] A. Malka-Markovitz *et al.*, "Multiscale modeling of drug-induced liver injury from organ to lobule," *npj Digital Medicine,* vol. 8, no. 1, p. 383, 2025.
[335] T. Somer and H. J. Meiselman, "Disorders of blood viscosity," *Annals of medicine,* vol. 25, no. 1, pp. 31-39, 1993.